LASER INDUCED NUCLEAR PHYSICS

Iain Spencer
Department of Physics and Astronomy
University of Glasgow
Glasgow G12 8QQ
Scotland

UNIVERSITY
of
GLASGOW

Presented as a thesis for the degree of
Doctor of Philosophy

February 2002

ProQuest LLC.
789 East Eisenhower Parkway
P.O. Box 1346
Ann Arbor, MI 48106 – 1346

To Mum and Dad

Acknowledgements

In addition to the thesis dedication, I would like to express thanks to the following people, without whom this thesis would not exist:

- My supervisor Prof. Kenneth W.D. Ledingham for his knowledge, leadership, enthusiasm, guidance, friendship and for believing in me. The above does not come close to expressing the extent of my gratitude.

- My second supervisor Dr. Ravi P. Singhal for his constant availability and guidance.

- My colleagues and friends at Glasgow, Paul McKenna, Tom McCanny, Andy Tasker, Lynne Robson and Catherine MacIntyre.

- My fellow experimenters with whom it was a pleasure to work with and for their invaluable knowledge, input and help: Peter Norreys, Eugene Clark, Marko Santala, Karl Krushelnick, Matt Zepf, Ian Watts, Michalis Tatarakis, Antonin Machacek, Cristina Escoda, Farhat Beg and Bucker Dangor.

- The staff at the Central Laser Facility for their expertise, dedication and sharing of knowledge: Ric Allott, Rob Clarke, David Neely, Colin Danson, John Collier, Mike Poulter, Rob Kraty, Edwin Divall, Andrew Langley, Phil Taday, Chris Hooker, Norma Prior, Donna Shepherd, Lisa Coffey and Mark Harman.

- EPSRC for receipt of a research studentship.

- My high school Physics teacher, Mr. Rothwell W. Glen, for getting me into this game in the first place.

- My sisters, Janice and Heather, and my Aunts, Jenny and Janette.

- Sara

- All of my friends but especially Stevie, Stuart, Scott, Iain, Roy, Liz, Victoria, Vaila, Stephen and Nicky.

Publications and Presentations

Papers

1) **Quantitative Measurement of Suprathermal Electron Temperature in Ultra-Intense Laser-Solid Interactions via Nuclear Activation Techniques**
I Spencer, K W D Ledingham, T McCanny, R P Singal, M I K Santala, E L Clark, I Watts, F N Beg, M Zepf, K Krushelnick, M Tatarakis, A E Dangor, P A Norreys, R M Allott, D Neely, R J Clarke, A C Machacek, J S Wark, A J Cresswell, D C W Sanderson, J Magill.
Rutherford Appleton Laboratory, Cental Laser Facility Annual Report 1998/99, pp 31.

2) **Studies of Novel Laser-Solid Interactions at High Intensities on Vulcan using Nuclear Techniques**
K W D Ledingham, I Spencer, T McCanny, R P Singal, M I K Santala, E L Clark, I Watts, F N Beg, M Zepf, K Krushelnick, M Tatarakis, A E Dangor, P A Norreys, R M Allott, D Neely, R J Clarke, A C Machacek, J S Wark, A J Cresswell, D C W Sanderson, J Magill.
Rutherford Appleton Laboratory, Cental Laser Facility Annual Report 1998/99, pp 35.

3) **Measurement of the Direction of Fast Electrons versus Plasma Scale-Length**
M I K Santala, E L Clark, F N Beg, M Tatarakis, M Zepf, K Krushelnick, A E Dangor, T McCanny, I Spencer, R P Singhal, K W D Ledingham, S C Wilks, A C Machacek, J S Wark, R M Allott, R J Clarke, P A Norreys.
Rutherford Appleton Laboratory, Cental Laser Facility Annual Report 1998/99, pp 27.

4) **Photonuclear Physics when a Multiterawatt Laser Pulse Interacts with Solid Targets**
K W D Ledingham, I Spencer, T McCanny, R P Singal, M I K Santala, E L Clark, I Watts, F N Beg, M Zepf, K Krushelnick, M Tatarakis, A E Dangor, P A Norreys, R M Allott, D Neely, R J Clarke, A C Machacek, J S Wark, A J Cresswell, D C W Sanderson, J Magill.
Physical Review Letters, **84,** 899 (2000).

5) **The Effect of the Plasma Density Scale-Length on the Direction of Fast Electrons in Relativistic Laser-Solid Interactions**
M I K Santala, E L Clark, F N Beg, M Tatarakis, M Zepf, K Krushelnick, A E Dangor, T McCanny, I Spencer, R P Singhal, K W D Ledingham, S C Wilks, A C Machacek, J S Wark, R M Allott, R J Clarke, P A Norreys.
Physical Review Letters, **84,** 1459 (2000).

6) **Energetic Proton Production and Plasma Jet Formation from Ultra-Intense Laser-Plasma Interactions with Solids**
E L Clark, M Zepf, F N Beg, M Tatarakis, C Escoda, M Norrefeldt, A E Dangor, K Krushelnick, R J Clarke, P A Norreys, I Spencer, K W D Ledingham.
Rutherford Appleton Laboratory, Cental Laser Facility Annual Report 1999/2000, pp 30.

7) **Observations of Heavy-Ion Fusion during High Intensity Laser Plasma Interactions using Nuclear Activation Techniques**
M I K Santala, M Zepf, F N Beg, E L Clark, A E Dangor, K Krushelnick, M Tatarakis, I Watts, K W D Ledingham, T McCanny, I Spencer, R M Allott, R J Clarke, P A Norreys, A C Machacek.
Rutherford Appleton Laboratory, Cental Laser Facility Annual Report 1999/2000, pp 25.

8) **Proton Induced Nuclear Reactions from Intense Laser-Plasma Interactions**
M I K Santala, M Zepf, F N Beg, E L Clark, A E Dangor, K Krushelnick, M Tatarakis, I Watts, K W D Ledingham, T McCanny, I Spencer, R M Allott, R J Clarke, P A Norreys, A C Machacek.
Rutherford Appleton Laboratory, Cental Laser Facility Annual Report 1999/2000, pp 23.

9) **Proton Production from a Terawatt, Compact, High-Repetition Rate Laser Interacting with Thin Solid Targets**
I Spencer, K W D Ledingham, T McCanny, R P Singhal, E L Clark, K Krushelnick, M Zepf, A E Dangor, R M Allott, D Neely, R J Clarke, A J Langley, P F Taday, E J Divall, P A Norreys.
Rutherford Appleton Laboratory, Cental Laser Facility Annual Report 1999/2000, pp 92.

10) **Production of Radioactive Nuclides by Energetic Protons Generated from Intense Laser-Plasma Interactions**
M I K Santala, M Zepf, F N Beg, E L Clark, A E Dangor, K Krushelnick, M Tatarakis, I Watts, K W D Ledingham, T McCanny, I Spencer, A C Machacek, R M Allott, R J Clarke, P A Norreys.
Applied Physics Letters, **78,** 19 (2001).

11) **High Intensity Laser Generation of Proton Beams for the Production of β^+ Sources used in Positron Emission Tomography**
I Spencer, K W D Ledingham, R P Singhal, T McCanny, E L Clark, K Krushelnick, M Zepf, F N Beg, M Tatarakis, C Escoda, M Norrefeldt, P A Norreys, R J Clarke, R M Allott.
RIS-2000 Conference Proceedings, AIP Publishing, in press 2001.

12) **Fast Particle Generation and Energy Transport in Laser-Solid Interactions**
M Zepf, E L Clark, K Krushelnick, F N Beg, A E Dangor, M I K Santala, M Tatarakis, I Watts, P A Norreys, R J Clarke, J R Davies, M Sinclair, R Edwards, T Goldsack, I Spencer, K W D Ledingham.
Physics of Plasmas, **8,** 2323 (2001).

13) **Laser Generation of Proton Beams for the Production of Short-Lived Positron Emitting Radioisotopes**
I Spencer, K W D Ledingham, R P Singhal, T McCanny, P McKenna, E L Clark, K Krushelnick, M Zepf, F N Beg, M Tatarakis, A E Dangor, P A Norreys, R J Clarke, R M Allott, I N Ross.
Nuclear Instrumentation and Methods in Physics Research Section B, **183,** 449 (2001)

Poster Presentations

1) **Laser Induced Nuclear Reactions**
Friday 12th November 1999.
Highlights of Physics Research and R&D in 1999 by Younger Physicists
CLRC Rutherford Appleton Laboratory, Oxfordshire, UK.

2) **Particle Acceleration and Nuclear Physics with Lasers**
Wednesday 23rd August 2000.
Lasers and Electro-Optics Society – Scottish Branch Meeting
University of St. Andrews, UK.

Oral Presentations

1) **Production of Energetic Proton Beams and Radioisotopes on VULCAN**
Wednesday 27th September 2000.
Invited talk, Imperial College of Science, Technology and Medicine, University of London, UK.

2) **High Intensity Laser Generation of Proton Beams for the Production of PET Radioisotopes**
9th October 2000.
RIS 2000 - Laser Ionisation and Applications Incorporating RIS, The 10th International Symposium on Resonance Ionisation Spectroscopy, University of Tennessee, Knoxville, TN, USA.

3) **Laser Generation of Proton Beams for Medical Isotope Production**
18th December 2000.
Annual High Power Laser Users Meeting
Coseners' House, Abingdon, UK.

4) **PET Isotope Production Using Ultra-Intense Lasers**
21st February 2001.
Invited Talk, Department of Biomedical Physics, University of Aberdeen, UK.

5) **Particle Acceleration and Nuclear Physics Using Ultra-Intense Lasers**
6th June 2001.
3rd Year Postgraduate Talk, Department of Physics and Astronomy,
University of Glasgow, UK.

Abstract

This thesis describes the first systematic study of laser induced nuclear physics. When the VULCAN ultra-intense laser pulse interacts with a solid target, electron and proton beams of energies up to 40 MeV are generated. These particles were used to induce nuclear reactions in materials.

The electron beams, being inefficient in inducing nuclear reactions were converted to energetic γ-rays via bremsstrahlung in a tantalum converter. These γ-rays were then used to induce photo-nuclear reactions in different materials via (γ,mn) reactions. Evidence of reactions occurring was obtained by measuring the radiation emitted by the product nuclei. The γ-rays produced in the laser-solid interaction were used to fission a sample of ^{238}U, the first observation of laser induced fission. Photo-nuclear reactions were used to measure the number and angular distribution of photons above 10 MeV produced in the interaction and to measure the temperature of the fast electrons generated.

Protons can directly interact with nuclei to take part in nuclear reactions. In particular (p,n) and (p,α) reactions were used to produce positron emitting nuclei, specifically ^{11}C and ^{13}N which are used in Positron Emission Tomography, a form of medical imaging. Nuclear reactions were also used to measure the spectrum of the proton beams produced in the laser-solid interaction.

Preliminary measurements of proton production on a much smaller laser system, ASTRA were performed as a possible extension of the above techniques to table-top laser systems.

Thesis Summary

This thesis reports on the generation of energetic particles (up to 40 MeV) and subsequent nuclear phenomena when an ultra-intense laser pulse interacts with solids. This work was carried out using the VULCAN and ASTRA laser facilities at the Rutherford Appleton Laboratory, UK. The content therefore brings together the study of high-power lasers and nonlinear optics, laser-solid interactions and nuclear physics.

The first chapter discusses the history of how this subject came about. In doing this, the motivation behind the work is made clear. It also serves as an introduction, and some basic concepts are discussed.

Chapter 2 deals with the theory behind laser-solid interactions, and how MeV electrons, γ-rays and protons are generated when an ultra-intense laser interacts with a solid target. This deals with aspects of plasma physics, since this is how these particles are generated in the interaction.

Chapter 3 describes the operational characteristics of the VULCAN laser system and the generation of ultra-intense laser pulses.

Chapter 4 discusses the physics of energetic particle interactions with nuclei, specifically photo-nuclear physics and proton-induced nuclear reactions. In addition, the radiation detectors used to provide evidence of nuclear events are described in detail.

The next four chapters are the results section of the thesis. Chapter 5 describes the use of the VULCAN laser to perform photo-nuclear physics. This technique is used to measure the angular distribution of the fast electrons produced in the interaction, the production of radioactive isotopes, measurements of the γ-rays produced and the temperature of the electrons and to perform laser-induced nuclear fission of ^{238}U.

Chapter 6 reports on the generation of energetic proton beams and subsequent nuclear physics using the VULCAN laser. This technique is used to generate positron emitting radioisotopes, specifically ^{11}C and ^{13}N via (p,n) and (p,α) reactions. These isotopes are of relevance to the nuclear medicine community, specifically Positron Emission Tomography, a form of medical imaging. The possibility of using lasers for the commercial production of these isotopes is discussed.

Chapter 7 describes preliminary results of proton production on the ASTRA laser system – a much smaller scale facility than VULCAN. The operation of the ASTRA laser is briefly described. The implications these results have on the possibility of re-producing the results described in Chapters 5 and 6 are discussed.

Chapter 8 reports on measurements of the temperature of the fast electrons produced in VULCAN interactions with materials via higher-order photo-nuclear reactions using tantalum targets.

The final chapter discusses the implications the results have, and puts the findings into context. In addition, some experiments to be performed in the immediate future are outlined.

Author's Contribution

The experimental work was carried out at the Central Laser Facility, Rutherford Appleton Laboratory, UK, on the VULCAN Nd: Glass laser facility, and the ASTRA Ti: Sapphire laser system.

On the VULCAN experiments, target alignment and setting up of the target chamber was carried out by Ian Watts, Antonin Machacek, Michalis Tatarakis and Matt Zepf, with the author helping out whenever possible. Detection and measurement of radiation following nuclear events was carried out by the author, in close collaboration with Marko Santala and with useful help from Cristina Escoda and Tom McCanny.

The analysis and interpretation of the data taken from the VULCAN runs is completely the work of the author, with guidance from Ken Ledingham. The work on measurement of the fast electron temperature (Section 5.4 and Chapter 8) was carried out with guidance from Ravi Singhal. One exception to this is Section 5.2, the angular distribution measurements, which was mostly the work of Marko Santala, with useful input from the author regarding data collection and interpretation. Measurement of the proton spectra in Section 6.3 was carried out using a technique developed by Eugene Clark.

On the ASTRA experiments, the laser was operated by the RAL staff of Edwin Divall, Andrew Langley, Phil Taday and Chris Hooker. Setting up of the target chamber and diagnostics was carried out by the author, Tom McCanny, Paul McKenna, Rob Clarke, Ric Allott and Rob Kraty. Analysis and interpretation of the results is solely the work of the author, again with useful guidance from Ken Ledingham.

Contents

List of Figures and Tables

Chapter 1

History, Background and Introduction

The purpose of this Chapter is to provide the reader with introductory information regarding the subject matter with the emphasis on ease of reading. The concepts discussed here will be described in more detail in later chapters. A brief history of how this area of study evolved is given.

1.1 Introduction

This thesis is concerned with the use of high power lasers to accelerate charged particles to multi-MeV energies. In this regime, these particles can induce nuclear reactions, coining the phrase "laser induced nuclear physics". Given the novelty of the results described, the history of this field is described in Section 1.3, but firstly in Section 1.2 basic principles and parameters are discussed regarding high power pulsed laser systems.

1.2 High Power Pulsed Laser Characteristics

The power of a pulsed laser is defined by the energy contained in a pulse divided by the pulse length. The highest pulse powers achievable today are of the order 10^{12}-10^{15} Watts (Terawatt-Petawatt). For example, the VULCAN laser at the Rutherford Appleton Laboratory, UK packs 100 J of energy into a 1 picosecond (1 ps=10^{-12} s) pulse, giving a pulse power of 100 TW. To put this into some sort of perspective, the total electrical power generated in the USA is about 10^{12} W. When laser pulses of this magnitude are focused to spot sizes of the order 12 μm, the power density, or the intensity can be in excess of 10^{20} Wcm^{-2}. Laser intensities are usually quoted in the non-SI unit of Wcm^{-2}.

$$PulsePower = \frac{PulseEnergy}{PulseLength} \qquad \text{Eqn (1.1)}$$

$$Intensity = \frac{Energy}{PulseLength \times FocalSpotArea} \qquad \text{Eqn (1.2)}$$

Laser light, like any other electromagnetic wave has associated with it perpendicular electric and magnetic fields with the direction of wave propagation being the vector cross product of these. The electric (E) and magnetic (B) fields associated with a laser pulse are defined as

$$E_{\perp} = \sqrt{\frac{2I}{\varepsilon_0 c}} \qquad \text{Eqn (1.3)}$$

$$B = \sqrt{\frac{2I\mu_0}{c}} \qquad \text{Eqn (1.4)}$$

where I is the intensity of the laser pulse, c is the velocity of light, ε_0 is the permittivity of free space and μ_0 is the permeability of free space.

It is the (E) and (B) fields that are responsible for charged particle acceleration. Since the magnitudes of these fields are dependant on the laser intensity, it is vital to achieve the maximum laser intensity possible. For a laser pulse of intensity $I=10^{20}$ Wcm^{-2}, the associated electric field is $2.7x10^{11}$ Vcm^{-1}. This is a huge accelerating gradient and a factor of some × 400 greater than the field experienced by the electron of the hydrogen atom in its K-shell. At the same time the varying magnetic field is also very large being close to 10^9 G. This is only a factor of 1000 smaller than the magnetic field of a typical black hole. These parameters will be discussed in more detail in later chapters, but at this stage it is necessary to review the history of this field of study to gain some insight into how the work detailed in this thesis evolved.

1.3 History

The work described in this thesis has been possible due to the remarkable upsurge in short pulse laser technology from the 1970s onwards, leading to higher and higher achievable peak powers – hence peak focused intensities. Running parallel to this revolution has been the outstanding theoretical and experimental work by researchers who have developed the applications of these ever-increasing laser intensities by studying the interaction of these laser pulses with matter. The object of this section is to comment on some of the highlights of these two areas.

1.3.1 High-Power Pulsed Lasers

In the 1960s, the peak power available from pulsed laser systems was a few kilowatts (10^3 W) leading to a peak intensity of 10^9 Wcm^{-2}. Since then, the techniques of Q-switching (Wilson & Hawkes 1987), first achieved in the early 1970s, then mode locking (mid 70s) meant that by the early 80s, powers in the gigawatt (10^9 W) regime were obtainable, and when focused yielded intensities in the region 10^{16} Wcm^{-2}.

To achieve efficient amplification of the radiation in a laser cavity, the waves circulating within it must undergo constructive interference. For constructive interference, the phase change produced be the wave passing once around the cavity must be $2\pi m$, where m=1,2,3,etc. Thus, only certain wavelengths (or frequencies) can oscillate. These allowed frequencies are called longitudinal modes.

If the bandwidth ($\Delta\nu$) of the amplifying medium is large enough, a large number of mode frequencies can experience gain. These modes would in general oscillate more or less independently of each other and produce radiation that exhibits random fluctuations of intensity. However, if the modes are made to oscillate in phase, the output becomes a regular sequence of pulses whose duration is determined by the number of modes which can oscillate. This is defined by the bandwidth of the medium and is the principle behind mode locking (Hutchinson 1989).

These oscillators can, in principle produce pulses whose duration is defined by the inverse of the bandwidth of the amplifying medium. Hence it is desirable to use an amplifying medium with a large bandwidth in order to produce pulses of short duration and hence high power. Materials with large bandwidths include organic dyes ($\Delta\nu$~20-40 nm) and rare gas excimers ($\Delta\nu$~20-40 nm). These materials can be used to generate pulses in the picosecond regime, as can solid state media such as glass doped with neodymium ($\Delta\nu$~22 nm). Titanium: sapphire crystals ($\Delta\nu$~120 nm) can be used to generate pules as short as 8 femtoseconds ($1\mathrm{fs}=10^{-15}$ s). The intensity of light passing through an amplifying medium will increase exponentially (assuming no losses) with distance provided the intensity is kept low enough such that there is still an excess of atoms/molecules that can excite/de-excite. However, the probability of stimulated emission increases with the intensity of radiation, so a point is reached where the fraction of the stored energy which is converted into radiation becomes significant. The intensity increases at a lower rate, and the amplifying medium is said to have reached its saturation point.

From the above, it would be reasonable to assume that there is a minimum intensity required to extract (say) half the stored energy. For this to occur, it is required that at least one photon (of energy hf where h is Planck's constant and f is the laser frequency) to interact with each atom/molecule, each having an interaction cross section σ (the cross section for stimulated emission, usually given in cm^2). Hence, the energy/unit area required to extract a significant fraction of the stored energy, or the Saturation Energy Density is defined by

$$E_s = \frac{hf}{\sigma} Jcm^{-2} \qquad \text{Eqn (1.5)}$$

Dyes and excimers have relatively high stimulated emission cross sections with $\sigma \sim 10^{-16}$ cm^2 (Hutchinson 1989). Therefore the saturation energy densities of these materials are relatively low, in the regime ~$mJcm^{-2}$. These materials can only be used in amplifying pulses of high energy if the area of the aperture of the amplifier is large.

Solid state materials on the other hand have much smaller stimulated emission cross sections (~10^{-19}-10^{-20} cm^2) (Hutchinson 1989). This gives very high saturation energy densities of around 20 Jcm^{-2}. In addition, the number of excited species per unit volume in these materials is very large hence the energy that can be stored when the material is excited is high with values around 1 Jcm^{-3}. Another advantage is that the lifetimes of the excited species are long (~100 μs) so energy can be accumulated over a relatively long period compared to other amplifying media. From this point of view, solid-state materials are again the most favourable lasing media.

The major disadvantage regarding solid state media is that the intensities achieved are well above the level at which catastrophic damage to the amplifier would occur. For this reason, solid state materials are more suited to the amplification of nanosecond pulses as opposed to picosecond or sub-picosecond pulses.

Another problem with amplifying intense laser pulses is that of self focusing. Put simply, when an intense laser pulse travels through a medium, its presence induces a change in the refractive index of the medium and hence the pulse is "self-focused" (Hutchinson 1989). This obviously increases the power density of the pulse and can lead to irreversible damage of the amplifier medium.

The critical intensity at which a beam is significantly distorted is $\sim 10^{10}$ Wcm^{-2}. For a 1 ps pulse amplified in a dye or excimer medium, the saturation intensity is 10^{9} Wcm^{-2}, so self focusing is not an issue for these media. However for solid state media, the saturation intensity is 10^{14} Wcm^{-2} for a 1 ps pulse. This means that the full potential of solid state media as amplifiers cannot be realised due to self-focusing.

The latest revolution in laser technology came about in the mid 80s, with the technique known as Chirped Pulse Amplification (CPA) (Perry & Mourou 1994;Strickland & Morou 1985). This technique resolved the problems of saturation intensity and self focusing and released the full potential of solid state amplifiers. A full account of this technique as applied to the VULCAN laser system at the Rutherford Appleton Laboratory, UK is given in Chapter 3. In simple terms, CPA involves stretching a pulse in time prior to amplification and then recompressing it back to its original duration. A stretched pulse of long duration can be passed through an amplifying medium without causing damage to the amplifier, due to the lower power density of the stretched pulse. Self focusing also becomes less of an issue as long as the intensity of the stretched pulse is sufficiently low. After recompression, much higher powers can be obtained than before the advent of CPA. Hence by 1990, peak laser powers soared to the terawatt regime (10^{12} W) with focused intensities of 10^{18} Wcm^{-2}. To date, pulses powers of 1 petawatt (10^{15} W) have been generated, yielding intensities of up to 10^{21} Wcm^{-2}. Excellent reviews of the state-of-art in high-power laser technology and future possibilities are given in (Hutchinson 1989;Mourou 1997;Perry & Mourou 1994). Figure 1.1 displays the evolution of peak laser power from the 1960s – present day.

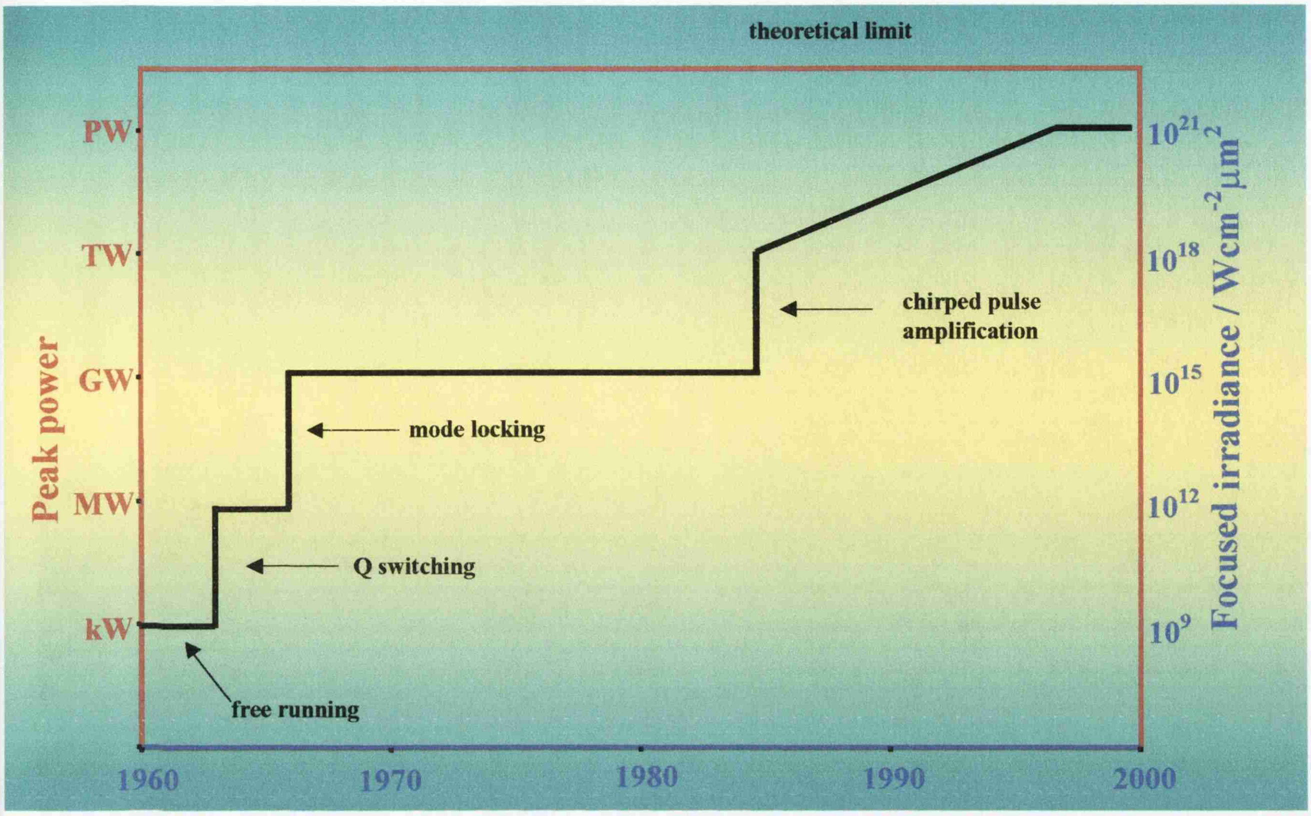

Figure 1.1 Increase in peak laser powers and focused irradiances from 1960 – present day.

The highest power laser systems in the world today can be loosely categorised into one of two sections: large scale, low repetition rate lasers, and smaller scale, high repetition rate systems. The larger systems have a high pulse energy of tens of joules - few kJ. This characteristic requires large beam diameters and hence large optics and amplifiers to minimise the energy density and hence avoid damage to the system. The smaller-scale laser systems have less energy in the pulse, but with a reduced pulse duration compared to the larger systems can now reach comparable powers and intensities.

The highest pulse power achieved to date was delivered by the Petawatt branch of the NOVA laser facility at the Lawrence Livermore National Laboratory, USA. Before its decommission in 1999, this system achieved 10^{15} W, or 1 PW with a focused intensity of 10^{21} Wcm^{-2}. This system consisted of a Nd: Glass amplifier with CPA and delivered a pulse of 1 kJ in 1 ps every 30 minutes. This was an extremely large scale system as can be seen in Figure 1.2.

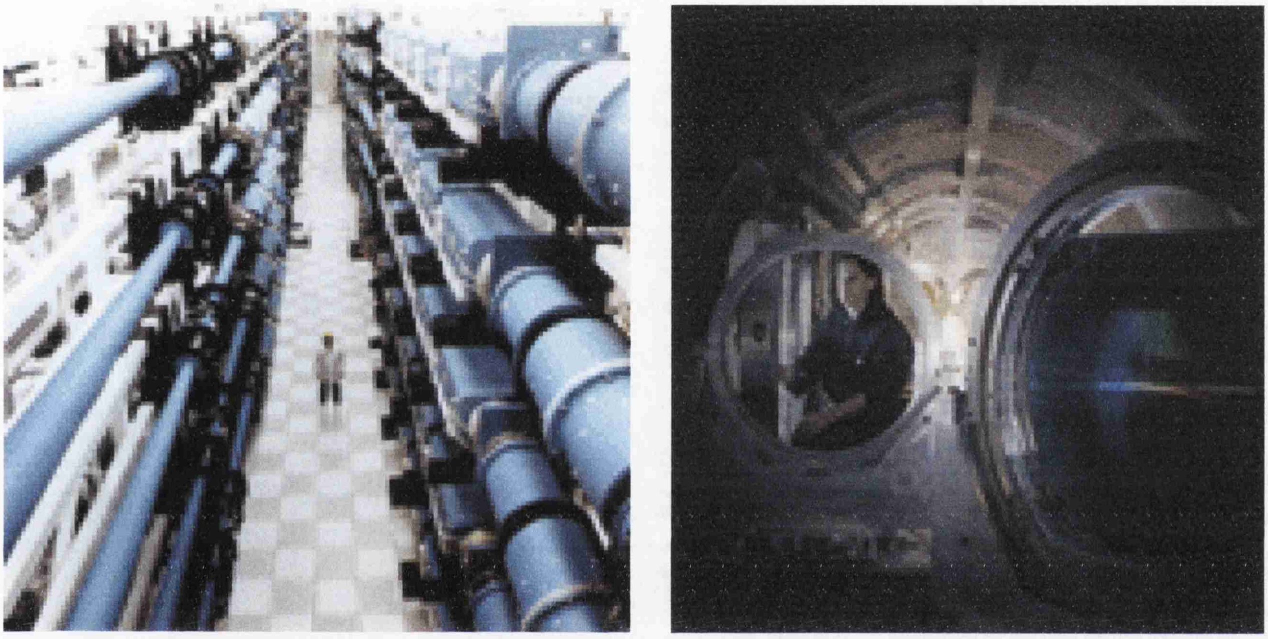

Figure 1.2 The NOVA Laser system at LLNL. (Left) The power amplifiers of the system. (Right) The inside of the CPA pulse compression chamber.

Many other facilities throughout the world have similar designs to NOVA i.e. large scale, low-rep-rate systems. The VULCAN laser at the Rutherford Appleton Laboratory, UK where most of the experiments described in this thesis were carried out is of this type. The pulse characteristics of VULCAN are described in Section 1.2 and a full description of this facility is given in Chapter 3. For an idea of the scale of VULCAN, Figure 1.3 shows the VULCAN amplifier chain and target chamber. The upgrade to the VULCAN laser is currently underway incorporating components of the decommissioned NOVA project and will increase its power to 1 PW with intensities exceeding 10^{21} Wcm^{-2}. The GEKKO M11 laser in Japan is again a Nd: Glass system, with a pulse energy of 25 J in 700 femtoseconds (1 fs=10^{-15} s) with a pulse power of 30 TW and a focused intensity of 10^{18-19} Wcm^{-2}. The p102 laser at Lemeil in France is a similar system reaching intensites in the 10^{19} Wcm^{-2} regime, with pulses of energy 20 J in 400 fs. LULI, also in France is now capable of 100 TW (10^{20} Wcm^{-2}). The wavelength of Nd: Glass lasers is 1.053 μm which is in the infra-red region of the electromagnetic spectrum. Systems of this type currently under construction are the PHELIX (Petawatt High Energy Laser for Heavy Ion EXperiments) in Darmstadt, and the NIF (National Ignition Facility) in the USA. PHELIX will deliver 1 PW and NIF when completed will exceed this current record. The OMEGA laser at the University of Rochester, USA is a 30 kJ, 60 beam ultra-violet laser used for fusion studies.

Smaller-scale, high-repetition rate lasers have been yielding higher and higher peak powers in recent years. The most common laser of this type is titanium: sapphire. These systems have less energy in their pulses, but much shorter pulse lengths than their larger counterparts described above and hence yield comparable powers and intensities. Ti: sapphire lasers operate between 780-1100 nm. Recently a system has been developed at LOA in France which delivers 1 J in 30 fs providing 100 TW with a 10 Hz repetition rate. Intensities of 10^{20} Wcm^{-2} have been measured. A 10 TW hybrid Ti: sapphire/ Nd: phosphate laser has been developed at the Centre for Ultrafast Optical Science, University of Michigan. This system delivers 4 J in 400 fs at 1.053 μm with a focused intensity of 6×10^{18} Wcm^{-2}. Other facilities similar to these systems throughout the world are the ATLAS laser at the Max Planck Institute, Garching, Germany, and The Max Born Institute (MBI), Berlin, Germany. The ASTRA laser system at the Rutherford Appleton Laboratory which was used in the experiments described in Chapter 7 is of this type. The newly constructed JANUS system at LLNL and the Trident Facility at Los Alamos, USA are also very impressive high-power lasers. The characteristics of all of these laser systems are summarised in Table 1.1.

With laser intensities of this magnitude, new regimes of study are possible, including the subject of this thesis. The next section goes through the history of the study of laser interactions with matter then describes the experiments that can be carried out with the ever-increasing intensities available throughout the years and into the future.

Laser	Type	Pulse Energy (J)	Pulse Duration (s)	Power (W)	Focused Intensity (Wcm^{-2})	Repetition Rate
Petawatt – NOVA	Nd: Glass	1000	10^{-12}	10^{15}	10^{21}	1/30 mins
VULCAN	Nd: Glass	100	10^{-12}	10^{14}	10^{20}	1/20 mins
P102, Lemeil	Nd: Glass	20	$0.4\text{x}10^{-12}$	$30\text{x}10^{12}$	10^{19}	1/20 mins
LULI	Nd: Glass	30	$0.3\text{x}10^{-12}$	$100\text{x}10^{12}$	10^{20}	1/20 mins
GEKKO M11	Nd Glass	25	$0.7\text{x}10^{-12}$	$30\text{x}10^{12}$	10^{19}	1/20 mins
LOA	Ti:sapphire	1	$30\text{x}10^{-15}$	$30\text{x}10^{12}$	10^{20}	10 Hz
Michigan	Ti:sapphire Nd: phosphate	4	$0.4\text{x}10^{-12}$	$10\text{x}10^{12}$	$6\text{x}10^{18}$	1 Hz
ATLAS	Ti:sapphire	1	$130\text{x}10^{-15}$	$8\text{x}10^{12}$	10^{18-19}	10 Hz
PHELIX*	Nd: glass	5000	$< 1\text{x}10^{12}$ s	10^{15}	10^{21}	Low
Berlin	Ti:sapphire	1.5	$50\text{x}10^{-15}$	30 TW	10^{19}	10 Hz
ASTRA	Ti:sapphire	1	$70\text{x}10^{-15}$	$10\text{x}10^{12}$	10^{19}	2 Hz
JANUS		10	$600\text{x}10^{-15}$	100 TW	10^{20}	1/3mins
Trident		800 mJ	$150\text{x}10^{-15}$	5 TW	$\sim10^{19}$	1 Hz
NIF*				$>10^{15}$	$>10^{21}$	Low

Table 1.1 Characteristics of the world's highest power lasers. Systems marked with a * are currently in construction.

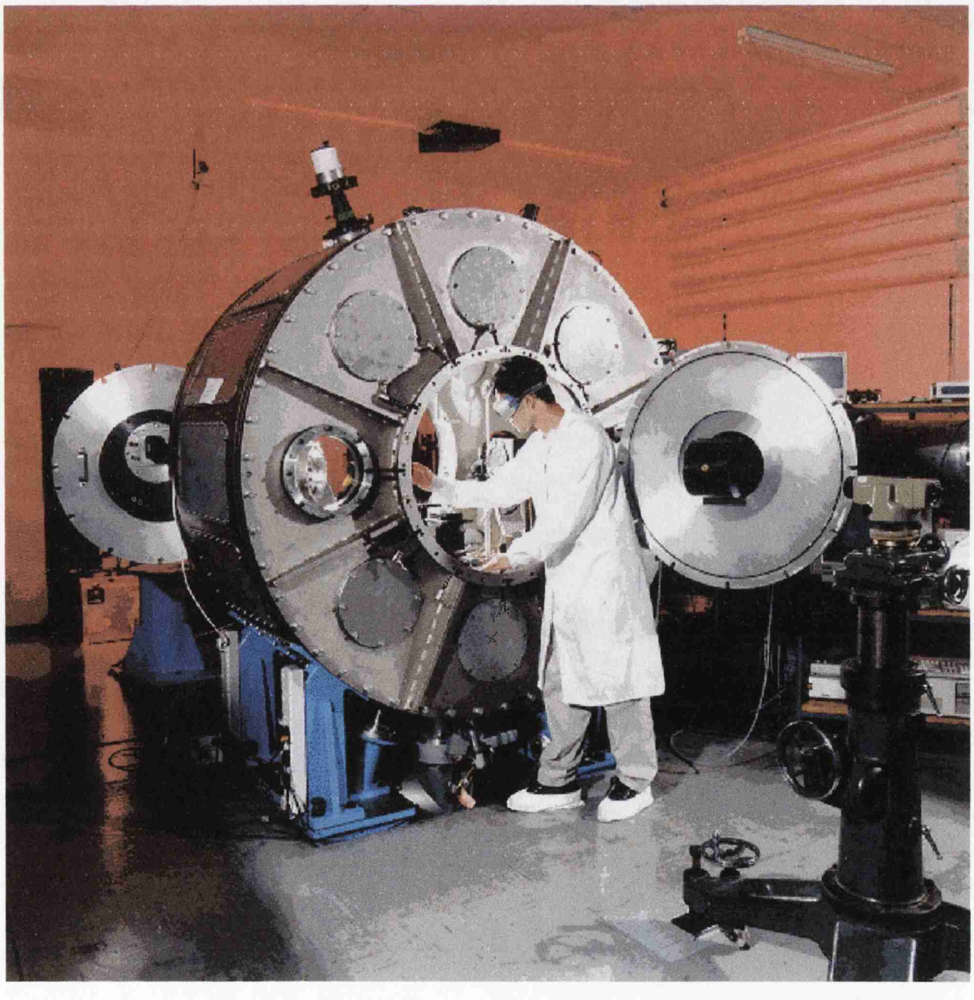

Figure 1.3 The VULCAN Nd: glass laser system. (Top) The amplifier chain. (Bottom) The laser-target interaction chamber.

1.3.2 Interaction of charged particles in intense electromagnetic fields

The mechanism of the interaction of charged particles in intense electromagnetic fields has been considered for more than fifty years. In 1948, Menzel and Salisbury (Menzel & Salisbury 1948) postulated that cosmic rays are the product of charged particles (electrons and ions) being accelerated by transient electric fields in space which arise from the solar corona. This idea was developed further by McMillan in 1950 (McMillan 1950) who attempted to explain that both "ordinary" cosmic rays and the intense rays following solar flares are due to the presence of low frequency electromagnetic waves. Meanwhile, Fermi (Fermi 1949) proposed that cosmic rays are originated and accelerated primarily in the interstellar space of the galaxy by collisions against moving magnetic fields.

As mentioned previously, an electromagnetic wave has associated with it perpendicular electric and magnetic fields with the direction of propagation being the vector cross product of these. The basic principle behind the groundbreaking work noted above is as follows: a charged particle in an intense electromagnetic field is accelerated initially along the direction of the electric field. The Lorentz force, $-e(\mathbf{v} \times \mathbf{B})$ causes the particle to be bent in the direction of the wave propagation. In intense fields the charged particle can be accelerated rapidly to close to the speed of light, and tends to travel with the EM wave gaining energy from it. The idea behind Menzel and Salisbury's theory was that charged particles become entrained in a low frequency (a few cycles per second) wave and can be accelerated to energies as high as 10^{19} eV. This concept is a counterpart of the machines built on earth at that time to accelerate particles to high energies, the predecessors of modern day facilities such as CERN.

Laser light is an electromagnetic wave and hence it may not be surprising that if the fields associated with the laser are intense enough, that laser beams can be used to accelerate particles. This concept was first proposed by Feldman and Chiao in 1971 (Feldman & Chiao 1971), twenty years after the idea was first applied to astrophysical phenomena. They showed theoretically that an electron could gain energies as high as

30 MeV after a single pass through the focus of a diffraction limited laser beam of power 10^{12} W and wavelength 1 μm. Chan (Chan 1971) similarly calculated that an intense laser beam could be used as an energy booster for relativistic charged particles showing that a 10 MeV electron can absorb 40 MeV from a laser beam of 1 μm wavelength and an electric field of 3×10^{10} Vcm^{-1} in a distance of 1.3 mm. It is interesting to note that the potential of laser-induced particle acceleration was realised in these early works, since it is largely dependant on the peak power of the laser pulse. "These results are especially encouraging considering that peak laser power might possibly become several orders of magnitude higher than at present; peak powers have been increasing by orders of magnitude in the past few years and there seems to be no fundamental limit on these peak powers" (Feldman & Chiao 1971). The problem with these schemes is that it is still not possible to maintain the required intensities over the necessary distances in vacuum, even with the highest power laser systems which exist today.

This problem was overcome in the late seventies by the seminal work of Tajima and Dawson (Tajima & Dawson 1979) who realised that by focusing laser light into a plasma medium (a plasma is an electrified gas with the atoms dissociated into positive ions and electrons), much higher accelerating fields could be generated than by focusing into the vacuum alone.

It is often said that 99 % of the matter in the universe exists in the plasma state (Chen 1983), and in fact the solar corona is a plasma. Referring back to the early work on the origin of cosmic rays, the accelerating fields were thought to originate from the solar corona, and hence the analogies between this mechanism and laser-plasma acceleration are clear.

Tajima and Dawson proposed the construction of a laser-electron accelerator which could be created when an intense laser pulse produced a wake of plasma oscillations (volumes of high and low densities of electrons). Similar to a boat creating a bow wave or wake as it moves through water, a bunch or cloud of high velocity electrons creates a wake of plasma waves as it passes through the plasma. They demonstrated with computer simulations that with the most powerful lasers at that time capable of 10^{18}

Wcm^{-2} incident on plasmas of densities 10^{18} cm^{-3} could yield electrons of GeV per cm of acceleration. This concept is known as wakefield acceleration and is an area of great interest today. It is known that conventional accelerators are limited by electrical breakdown at fields of around 20 MVm^{-1}; at these fields the electrons are torn from the nuclei in the accelerator's support structure. Plasma particle accelerators are seen as an alternative to conventional accelerators and also as particle beam injectors for high-energy physics experiments.

More recently the importance of Raman forward scattering and plasma wave breaking in short pulse high intensity laser produced plasmas has been realised by a number of authors, (Joshi, Tajima, & Dawson 1981;Modena et al. 1995;Mori et al. 1994;Sheng & Meyer-ter-Vehn 1997) in generating electrons of very high energies in very short distances. In these papers the authors considered the probability of using this technology for the construction of compact accelerators which might find applications where 2-200 MeV electrons or photons are required.

There has been a plethora of experimental data from the 90s onwards with evidence of electron acceleration using intense laser pulses (Amiranoff et al. 1998;Clayton et al. 1993;Esarey et al. 1997;Everett et al. 1994;Malka, Lefebvre, & Miquel 1997;Malka & Miquel 1996;Modena et. al. 1995;Ting et al. 1997;Wagner et al. 1997). The reason for the current and thriving interest in high intensity laser plasma interactions is not only their relevance to advanced concepts of plasma high energy particle accelerators described above, but also to a number of other fields.

The plasma conditions in a laser produced plasma resemble the inside of a brown dwarf star. The ability to produce plasmas previously only found in space has proved to be hugely beneficial to the astrophysics community – again the analogies with the origin of cosmic rays is apparent.

Laser-plasma interactions also have their part to play in the search for a renewable, safe, environmentally friendly source of energy. The sun produces energy via thermonuclear fusion reactions. Of course these reactions are only possible under the extreme pressure and temperature conditions found in stars. Laser-plasma interactions are a possible route to achieving these conditions and inducing thermonuclear reactions on Earth, a branch of physics known as inertial confinement fusion (ICF). In this scheme, a deuterium-tritium target is rapidly heated by several incident laser pulses, which leads to compression of the fuel to twenty times the density of lead. The compression and heating of the pulse leads to ignition of the fuel core and thermonuclear burn. Ignition conditions have yet to be achieved, and although fusion neutrons have been observed (Norreys et al. 1998;Norreys et al. 2000), the energy input by the laser still far exceeds the fusion energy output. Recently the "fast ignitor" scheme was proposed (Tabak et al. 1994) which could lead to fusion conditions with much lower laser requirements than originally envisaged. The National Ignition Facility in the USA is currently being constructed for this purpose.

In 1988, Boyer Luk and Rhodes published a seminal theoretical paper discussing the possibility of inducing nuclear fission using intense laser-plasma interactions (Boyer, Luk, & Rhodes 1988). They predicted that by focusing a laser of intensity 10^{21} Wcm^{-2} on to a sample of uranium-238 that fission of the uranium nuclei would occur with a probability 10^{-5}. This paper dealt with the mechanism of electrofission, where the energetic (in fact relativistic) electrons produced by the laser-matter interaction couple to the fission mode of nuclear decay. Prior to this, many probes had been used to induce fission, particularly neutrons, both fast and slow. Other nuclear probes had also been used e.g. protons, deuterons and heavy ions as well as non nuclear beams e.g. gamma rays, electrons and muons. It is perhaps not surprising for a sufficiently intense light source to induce fission, albeit indirectly by means of accelerated electrons from the laser interacting with matter. Lynn (Lynn 1988) reviewed the work of Boyer, Luk and Rhodes and commented that as well as electrofission, the relativistic electrons could generate bremsstrahlung ("braking radiation") high energy photon beams causing photofission to occur. Lynn calculated that around 10^6 fission events could occur under the criteria set out by Boyer, Luk and Rhodes. In fact at this time, Ken Ledingham and Ravi Singhal of the University of Glasgow, together with Joe Magill (Kalshrue) submitted a proposal to the EC seeking support to carry out laser-induced nuclear fission of uranium experimentally. Although the proposal was short listed for funding, it was eventually turned down because it was felt that at that time no laser in Europe had a sufficiently high intensity. The peak intensity available at the time was around 10^{18} Wcm^{-2} and Boyer, Luk and Rhodes were looking at intensities around three orders of magnitude greater than this.

In the last three years, electrons of energies up to 100 MeV have been generated using the highest intensity lasers available, up to and in excess of 10^{20} Wcm^{-2}. Hence a high intensity laser can produce energetic electrons similar to that of a low-energy linear accelerator. If the laser interacts with a thick high Z solid target, bremsstrahlung conversion takes place and gamma rays of energies up to 100 MeV are produced (Cowan et al. 2000;Ledingham et al. 2000;Ledingham & Norreys 1999;Norreys et al. 1999;Phillips et al. 1999). The subject matter of Chapter 5 is the use of these laser-generated gamma-rays to produce radioactive nuclei (decaying by electron capture/positron emission) via (γ,mn) reactions (m=1,2,3..), and the first experimental observation of fission of uranium-238 via (γ,f) reactions, ten years after the technique was first postulated. The physics of photo-nuclear reactions is discussed in Chapter 4. This branch of laser-induced nuclear physics also has applications in measuring the angular distribution and temperature of the hot electrons produced, again described in detail in Chapter 5. To this date these results have only been obtained using large-scale, low repetition rate laser systems such as VULCAN at the Rutherford Appleton Laboratory, UK and the Petawatt branch of the NOVA facility at the Lawerence Livermore National Laboratory, USA. The development of this technique for "table-top" production of radionuclides is the natural extension of this work. With the ongoing advancements in laser technology, table-top lasers capable of 10^{19-20} Wcm^{-2} are currently being developed and will soon be available.

One of the potential applications of this new technology is to produce short lived (2 minutes-2 hours) positron emitters for Positron Emission Tomography (PET). This is a form of medical imaging where a patient receives by injection a pharmaceutical labelled with a short-lived β^+ emitting source. This radio-pharmaceutical is taken up wherever it is used in the body, and specific sites in the body can be imaged by detecting the back-to-back 511 keV positron-electron annihilation gamma rays emitted. Among the principal applications for this important diagnostic technique are imaging: blood flow, amino acid transport and brain tumours. The main positron emitting nuclei used as tracers are ^{11}C, ^{13}N, ^{15}O and ^{18}F, with the latter being the most widely used positron source. These sources are usually produced using energetic proton beams produced by cyclotrons or van de Graaffs via (p,n) or (p,α) reactions. The nuclear reaction physics involved here is covered in Chapter 4. The reason that proton induced nuclear reactions are favoured is because the isotope produced has a different atomic number than the reactant, and hence these can be separated using fast chemistry. This makes it possible to produce carrier free sources allowing patients to be injected with the minimum of foreign material. With (γ,mn) reactions, the reactant and the product have the same atomic number.

So far only the acceleration of electrons in laser-plasma interactions has been discussed. Of course, ions are also present in a plasma, and in fact it is possible to produce beams of energetic protons using intense laser pulses.

The mechanisms responsible for ion acceleration are currently the subject of intensive research by many groups throughout the world. The main mechanism though to be responsible for the generation of proton beams is the production of electrostatic fields due to space charge effects when the fast electrons exit the target. For this reason, thin (few micron) low Z targets are favoured to accelerate protons and heavier ions, to allow the electrons to escape and set up these fields. The acceleration mechanisms for both ions and electrons are the subject of Chapter 2.

Measurements of proton emission from laser-solid interactions have been made as early as the 1980s (Gitomer et al. 1986;Kishimoto et al. 1983) using nanosecond CO_2 lasers. In these early works it was thought that the protons originated from a hydrocarbon impurity layer on the metal target surface. Later measurements, using picosecond pulsed lasers with intensities 10^{18}-10^{19} Wcm^{-2} (Beg et al. 1997;Fews et al. 1994) showed that protons of energies in the MeV range can be generated. In more recent experiments (Clark et al. 2000;Krushelnick et al. 1999;Santala et al. 2001;Snavely et al. 2000), multi-MeV protons have been observed at intensities up to 10^{20} Wcm^{-2}. Again the targets were metallic and the protons were believed to originate from impurity layers on the target surface. This issue will be addressed in later chapters.

Multi-MeV protons can induce nuclear reactions in materials, and Chapter 6 reports on the production of the PET isotopes ^{11}C and ^{13}N using proton beams generated via ultra-intense laser-solid interactions.

It is instructive to show what experiments can be carried out with regards to laser intensity. Figure 1.4 presents some of the events that can occur with intensity plotted on the x-axis. There is no significance to the y-coordinate apart from spatially separating the events to ease viewing. With a 1 ps pulse of 1 μm wavelength, helium gas is ionised at around 3×10^{14} Wcm^{-2}. As the intensity increases, the inert gas becomes multiply ionised and at 10^{19} Wcm^{-2} and above, photon-induced nuclear reactions are energetically possible. Close to 10^{21} Wcm^{-2}, pion production can take place – the first of the elementary particles. After its upgrade, VULCAN will achieve this intensity. Between 10^{22-23} Wcm^{-2}, it is predicted that it will be possible to strip 36 electrons from an atom of krypton, Kr^{36+}, and to produce U^{90+}. Above 10^{23} Wcm^{-2} it has been proposed that the ultra-intense laser field will promote nuclear transitions directly and hence possibly modify the half-lives of long-lived radioisotopes. At the very high

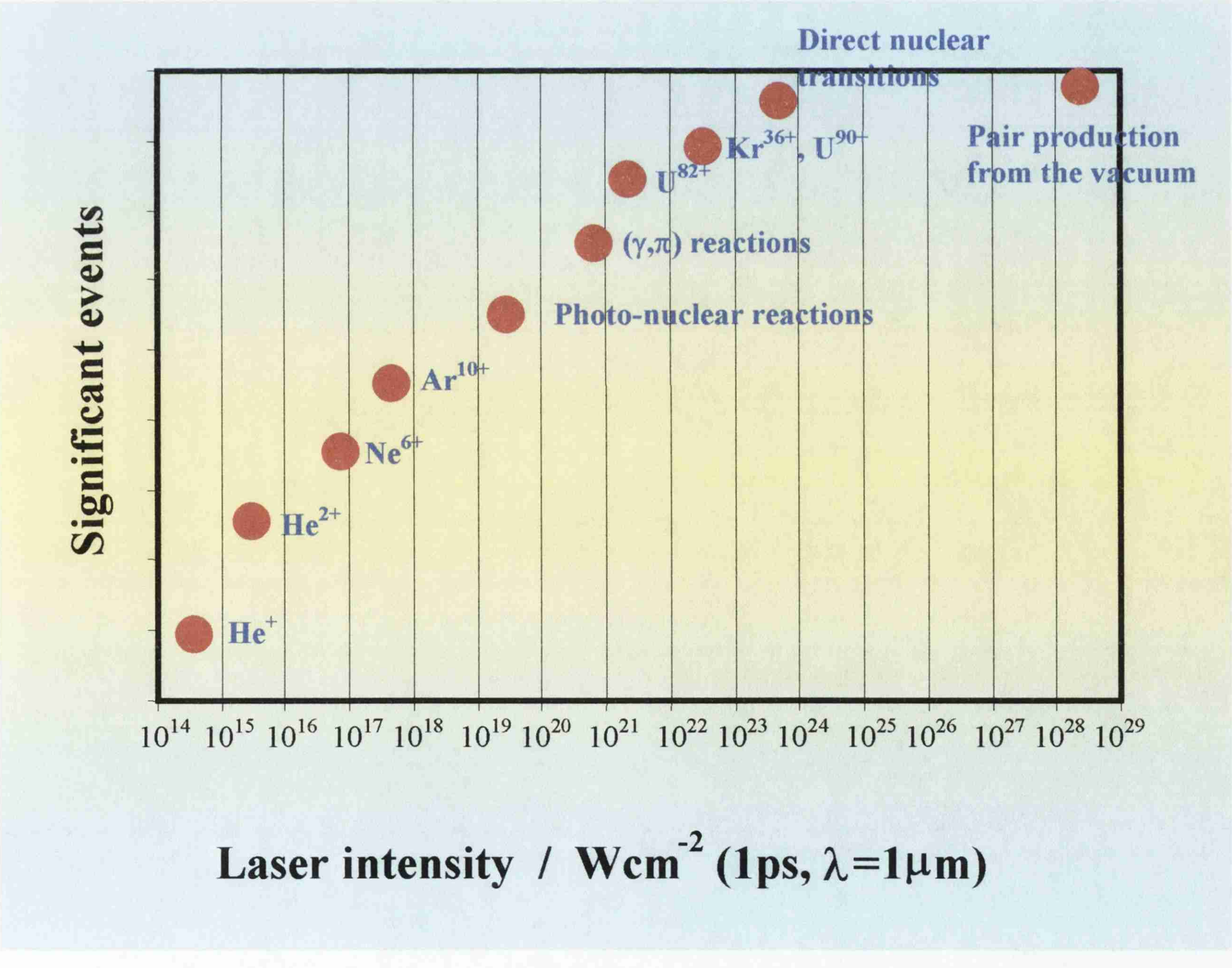

Figure 1.4 The significant atomic and nuclear events as a function of intensity for a laser of wavelength 1 μm and pulse length 1 ps. At present the highest laser intensity achieved is 10^{21} Wcm^{-2}. Plans are already in place to build lasers 100 times more intense.

intensities of 10^{28} Wcm^{-2}, it can be shown that electron-positron pairs can be created from the vacuum simply using the ultra-intense electric field associated with the laser. However pair production can take place in the presence of matter at very much lower laser intensities, around 10^{20-21} Wcm^{-2}.

References

Amiranoff, F., Baton, S., Bernard, D., Cros, B., Descamps, D., Dorchies, F., Jaquet, F., Malka, V., Marquès, J. R., Matthieussent, G., Miné, P., Modena, A., Mora, P., Morillo, J., & Najmudin, Z. 1998, "Observation of laser wakefield acceleration of electrons", *Physical Review Letters*, vol. 81, p. 995.

Beg, F. N., Bell, A. R., Dangor, A. E., Danson, C. N., Fews, A. P., Glinsky, M. E., Hammel, B. A., Lee, P., Norreys, P. A., & Tatarakis, M. 1997, "A study of picosecond laser-solid interactions up to 10^{19} Wcm^{-2}", *Physics of Plasmas*, vol. 4, p. 447.

Boyer, K., Luk, T. S., & Rhodes, C. K. 1988, "Possibility of Optically Induced Nuclear Fission", *Physical Review Letters*, vol. 60, p. 557.

Chan, Y. W. 1971, "Ultra-intense laser radiation as a possible energy booster for relativistic charged particles", *Physics Letters*, vol. 35A, p. 305.

Chen, F. F. 1983, *Introduction to Plasma Physics and Controlled Fusion*, pp 1, Second edn, Plenum Publishing Corporation.

Clark, E. L., Krushelnick, K., Davies, J. R., Zepf, M., Tatarakis, M., Beg, F. N., Machacek, A., Norreys, P. A., Santala, M. I. K., Watts, I., & Dangor, A. E. 2000, "Measurements of energetic proton transport through magnetized plasma from intense laser interactions with solids", *Physical Review Letters*, vol. 84, p. 670.

Clayton, C. E., Marsh, K. A., Dyson, A., Everett, M., Lal, A., Leemans, W. P., Williams, R., & Joshi, C. 1993, "Ultrahigh-gradient acceleration of injected electrons by laser-excited relativistic electron plasma waves", *Physical Review Letters*, vol. 70, p. 37.

Cowan, T. E., Hunt, A. W., Phillips, T. W., Wilks, S. C., Perry, M. D., Brown, C., Fountain, W., Hatchett, S. P., Johnson, J., Key, M. H., Parnell, T., Pennington, D. M., Snavely, R. A., & Takahashi, Y. 2000, "Photonuclear fission from high energy electrons from ultra-intense laser-solid interactions", *Physical Review Letters*, vol. 84, p. 903.

Esarey, E., Hubbard, R. F., Leemans, W. P., Ting, A., & Sprangle, P. 1997, "Electron injection into plasma wake fields by colliding laser pulses", *Physical Review Letters*, vol. 79, p. 2682.

Everett, M., Lal, A., Gordon, D., Clayton, C. E., Marsh, K. A., & Joshi, C. 1994, "Trapped electron acceleration by a laser-driven relativistic plasma wave", *Nature*, vol. 368, p. 527.

Feldman, M. J. & Chiao, R. Y. 1971, "Single-cycle electron acceleration in focused laser fields", *Physical Review A*, vol. 4, p. 352.

Fermi, E. 1949, "On the origin of cosmic radiation", *Physical Review*, vol. 75, p. 1169.

Fews, A. P., Norreys, P. A., Beg, F. N., Bell, A. R., Dangor, A. E., Danson, C., Lee, P., & Rose, S. J. 1994, "Plasma ion emission from high intensity picosecond laser pulse interactions with solid targets", *Physical Review Letters*, vol. 73, p. 1801.

Gitomer, S. J., Jones, R. D., Begay, F., Ehler, A. W., Kephart, J. F., & Kristal, R. 1986, "Fast ions and hot electrons in the laser-plasma interaction", *Physics of Fluids*, vol. 29, p. 2679.

Hutchinson, M. H. R. 1989, "Terawatt lasers", *Contemporary Physics*, vol. 30, p. 355.

Joshi, C., Tajima, T., & Dawson, J. M. 1981, "Forward Raman instability and electron acceleration", *Physical Review Letters*, vol. 47, p. 1285.

Kishimoto, Y., Mima, K., Watanabe, T., & Nishikawa, K. 1983, "Analysis of fast-ion velocity distributions in laser plasmas with a truncated Maxwellian velocity distribution of hot electrons", *Physics of Fluids*, vol. 26, p. 2308.

Krushelnick, K., Clark, E. L., Najmudin, Z., Salvati, M., Santala, M. I. K., Tatarakis, M., & Dangor, A. E. 1999, "Multi-MeV Ion Production from high-intensity laser interactions with underdense plasmas", *Physical Review Letters*, vol. 83, p. 737.

Ledingham, K. W. D. & Norreys, P. A. 1999, "Nuclear physics merely using a light source", *Contemporary Physics*, vol. 40, p. 367.

Ledingham, K. W. D., Spencer, I., McCanny, T., Singhal, R. P., Santala, M., Clark, E. L., Watts, I., Beg, F. N., Zepf, M., Krushelnick, K., Tatarakis, M., Dangor, A. E., Norreys, P. A., Allott, R. M., Neely, D., Clarke, R. J., Machacek, A., Wark, J. S., Creswell, A., Sanderson, D. C. W., & Magill, J. 2000, "Photo-nuclear physics when a multiterawatt laser pulse interacts with solid targets", *Physical Review Letters*, vol. 84, p. 899.

Lynn, J. E. 1988, "Laser-induced fission", *Nature*, vol. 333, p. 116.

Malka, G., Lefebvre, E., & Miquel, J. L. 1997, "Experimental observation of electrons accelerated in vacuum to relativistic energies by a high intensity laser", *Physical Review Letters*, vol. 78, p. 3314.

Malka, G. & Miquel, J. L. 1996, "Experimental confirmation of ponderomotive-force electrons produced by an ultra-relativistic laser pulse on a solid target", *Physical Review Letters*, vol. 77, p. 75.

McMillan, E. M. 1950, "The origin of cosmic rays", *Physical Review*, vol. 79, p. 498.

Menzel, D. H. & Salisbury, W. W. 1948, "The origin of cosmic rays", *Nucleonics*, vol. 2, p. 67.

Modena, A., Najmudin, Z., Dangor, A. E., Clayton, C. E., Marsh, K. A., Joshi, C., Malka, V., Darrow, C. B., Danson, C., Neely, D., & Walsh, F. N. 1995, "Electron acceleration from the breaking of relativistic plasma-waves", *Nature*, vol. 377, p. 606.

Mori, W. B., Decker, C. D., Hinkel, D. E., & Katsouleas, T. 1994, "Raman forward scattering of short-pulse high intensity lasers", *Physical Review Letters*, vol. 72, p. 1994.

Mourou, G. 1997, "The ultrahigh-peak-power laser: present and future", *Applied Physics B*, vol. 65, p. 205.

Norreys, P. A., Allott, R. M., Clarke, R. J., Collier, J., Neely, D., Rose, S. J., Zepf, M., Santala, M., Bell, A. R., Krushelnick, K., Dangor, A. E., Woolsey, N. C., Evans, R. G., Habara, H., Norimatsu, T., & Kodama, R. 2000, "Experimental studies of the advanced fast ignitor scheme", *Physics of Plasmas*, vol. 7, p. 3721.

Norreys, P. A., Fews, A. P., Beg, F. N., Bell, A. R., Dangor, A. E., Lee, P., Nelson, M. B., Schmidt, H., Tatarakis, M., & Cable, M. D. 1998, "Neutron production from picosecond laser irradiation of deuterated targets at intensities of 10^{19} Wcm^{-2}", *Plasma Physics and Controlled Fusion*, vol. 40, p. 175.

Norreys, P. A., Santala, M., Clark, E. L., Zepf, M., Watts, I., Beg, F. N., Krushelnick, K., Tatarakis, M., Dangor, A. E., Fang, X., Graham, P., McCanny, T., Singhal, R. P., Ledingham, K. W. D., Creswell, A., Sanderson, D. C. W., Magill, J., Machacek, A., Wark, J. S., Allott, R. M., Kennedy, B., & Neely, D. 1999, "Observation of a Highly Directional γ-ray Beam from Ultra-short, Ultra-intense Laser Pulse Interactions with Solids", *Physics of Plasmas*, vol. 6, p. 2150.

Perry, M. D. & Mourou, G. 1994, "Terawatt to Petawatt Subpicosecond Lasers", *Science*, vol. 264, p. 917.

Phillips, T. W., Cable, M. D., Cowan, T. E., Hatchett, S. P., Henry, E. A., Key, M. H., Perry, T., Sangster, C., & Stoyer, M. A. 1999, "Diagnosing hot electron production by short pulse, high intensity lasers using photonuclear reactions", *Review of Scientific Instruments*, vol. 70, p. 1213.

Santala, M. I. K, Zepf, M,, Beg, F. N., Clark, E.L., Dangor, A. E., Krushelnick, K., Ledingham, K. W.D., McCanny, T., Spencer, I., Machacek, A. C., Allott, R., Clarke, R.J., Norreys, P. A. 2001, "Production of radioactive nuclides by energetic protons generated from intense laser-plasma interactions", *Applied Physics Letters*, vol. 78, p. 19.

Sheng, Z. M. & Meyer-ter-Vehn, J. 1997, "Relativistic wave breaking in warm plasmas", *Physics of Plasmas*, vol. 4, p. 493.

Snavely, R. A., Key, M. H., Hatchett, S. P., Cowan, T. E., Roth, M., Phillips, T. W., Stoyer, M. A., Henry, E. A., Sangster, C., Singh, M. S., Wilks, S. C., Mackinnon, A. J., Offenberger, A. A., Pennington, D. M., Yasuike, K., Langdon, A. B., Lasinski, B. F., Johnson, J., Perry, M. D., & Campbell, E. M. 2000, "Intense high-energy proton beams from petawatt-laser irradiation of solids", *Physical Review Letters*, vol. 85, p. 2945.

Strickland, D. & Morou, G. 1985, "Compression of Amplified Chirped Optical Pulses", *Optics Communications*, vol. 56, p. 219.

Tabak, M., Hammer, J., Glinsky, M. E., Kruer, W. L., Wilks, S. C., Woodworth, J., Campbell, E. M., & Perry, M. D. 1994, "|gnition and high gain with ultrapowerful lasers", *Physics of Plasmas*, vol. 1, p. 1626.

Tajima, T. & Dawson, J. M. 1979, "Laser Electron Accelerator", *Physical Review Letters*, vol. 43, p. 267.

Ting, A., Moore, C. I., Krushelnick, K., Manka, C., Esarey, E., Sprangle, P., Hubbard, R. F., Burris, H. R., Fischer, R., & Baine, M. 1997, "Plasma wakefield generation and electron acceleration in a self-modulated laser wakefield accelerator experiment", *Physics of Plasmas*, vol. 4, p. 1889.

Wagner, R., Chen, S. Y., Maksimchuk, A., & Umstadter, D. 1997, "Electron acceleration by a laser wakefield in a relativistically self-guided channel", *Physical Review Letters*, vol. 78, p. 3125.

Wilson, J. & Hawkes, J. F. B. 1987, "Q-Switching," in *Lasers: Principles and Applications*, 1 edn, Prentice Hall, pp. 108-114.

Chapter 2

Theoretical Electron and Proton Acceleration in Ultra-Intense Laser-Solid Interactions

This chapter provides a theoretical background in the physics of ultra-intense laser-solid interactions. From this, a description of electron acceleration due to the various absorption mechanisms in the interaction follows. The chapter concludes with a description of how ions, in particular protons can be accelerated in these interactions.

2.1 Introduction

So far the concept of particle acceleration in laser-matter interactions has only been discussed tentatively. In fact, the physics of the laser-matter interaction is highly complicated and gives rise to a number of physical phenomena. The study of these interactions both theoretically and experimentally is currently an area of huge interest. To date, there is no single theoretical model that can adequately describe all the main aspects of the interaction physics. Excellent reviews of this subject are given in (Gibbon & Förster 1996;Joshi & Corkum 1995;Umstadter 2001;Witte et al. 1999).

Recall from Chapter 1 that for a laser pulse of intensity $I=10^{20}$ Wcm^{-2}, the associated electric field is $2.7\text{x}10^{11}$ Vcm^{-1}. This field is some × 400 greater than the field experienced by the electron of the hydrogen atom in its K-shell. This means that a gaseous or solid target placed at the laser focus will undergo rapid ionisation. The plasma formed in this manner will comprise of the usual fluid-like mixture of electrons and ions, but many of its basic properties will be governed by the laser field, rather than by its own density and temperature. The experiments described in this thesis involve the interaction of high intensity ($>10^{19}$ Wcm^{-2}) laser pulses with solid targets and hence the discussion focuses on this type of interaction.

Whether the target medium placed at the focus is gaseous or solid, short-pulse, high intensity interactions with matter generally involve a number of physical processes: ionisation, propagation and refraction, generation of plasma waves and the subsequent thermal and hydrodynamic evolution of the target material. The importance of any one of these processes depends heavily on the laser parameters. The evolution in laser technology described in Chapter 1 has shifted the research emphasis from atomic physics and linear laser-plasma wave coupling to extremely nonlinear collective behaviour.

When a high-power laser is focused onto a solid or gaseous target at ultra-high intensities, the motion of an electron in the electric field of the laser becomes relativistic, with a "quiver velocity", v_{osc}. Under these conditions, the average kinetic energy of the electron oscillating in the laser field is equivalent to the electron rest mass.

The onset of this "relativistic regime" is around $I\lambda^2 = 1.3\mathrm{x}10^{18}$ $\mathrm{Wcm^{-2}\mu m}$, where I is the intensity of the laser (Watts per centimetre^2) and λ is the wavelength (microns). As stated previously, VULCAN operates at around 10^{20} $\mathrm{Wcm^{-2}}$ and at a wavelength of 1.053 μm. A characteristic parameter (a) of this quiver motion is the normalised momentum (p) defined by $a = p/m_o c$ where m_o is the rest mass of the electron (Malka & Miquel 1996;Wilks & Kruer 1997).

$$a = \frac{p_{osc}}{m_o c} = \frac{\gamma v_{osc}}{c} = \frac{eE_o}{m_o c \omega_o} = \left(\frac{I\lambda^2}{1.37x10^{18}}\right)^{\frac{1}{2}} \qquad \text{Eqn (2.1)}$$

γ is the relativistic factor $1/[1-(v/c)^2]^{1/2}$, E_o is the amplitude of the electric field vector of the laser, ω_o is the laser angular frequency, I is the laser intensity ($\mathrm{Wcm^{-2}}$) and λ is the wavelength in microns.

Note that this parameter scales as $I\lambda^2$, known as the irradiance (or normalised intensity) of the laser. The energy associated with this quiver velocity can easily reach MeV levels for irradiances of 10^{19} $\mathrm{Wcm^{-2}\mu m^2}$. Of course, the E-field of the laser and hence the direction of this quiver motion is perpendicular to the direction of laser propagation and hence no significant charged particle acceleration can take place in this direction (Hora et al. 2000). However, in this relativistic regime, a nonlinear effect known as the "ponderomotive force" becomes important. The physical mechanism for the ponderomotive force is as follows (Chen 1983): electrons oscillate in the direction of **E**, but the Lorentz force $-e(\mathbf{v}\times\mathbf{B})$ distorts their orbits and pushes the electrons in the direction of laser propagation, called the **k** vector. The phases of **v** and **E** are such that the motion does not average to zero over an oscillation but there is a secular drift over **k**. If the wave has uniform amplitude, no force is needed to maintain this drift; but if the wave amplitude varies, the electrons will pile up in regions of small amplitude and a force is required to overcome the space charge. It can be shown (Chen 1983) that the ponderomotive force along the direction of laser propagation is proportional to the gradient of $E_\perp$. The relativistic expression for the ponderomotive potential, U_p using Eqn (2.1) is:

$$U_p = m_o c^2(\gamma - 1) = m_o c^2\left(\sqrt{1+a^2} - 1\right) = 0.511\left(\sqrt{1+\frac{I\lambda^2}{1.37x10^{18}}} - 1\right)MeV \quad \text{Eqn (2.2)}$$

Assuming the electron energy distribution can be described by the relativistic equation $E^2\exp(-E/kT)$ where k is the Boltzmann constant and T is the electron temperature (Ledingham et al. 2000), the average value of kT is found to be U_p (Malka & Miquel 1996) and for a laser intensity of 10^{20} Wcm^{-2} using equation (2.2) is around 4 MeV. The importance of this acceleration mechanism in context with the various other mechanisms will be described in detail later.

Another interesting effect is that the light pressure can easily be larger than the plasma pressure, even for extremely dense plasmas. This pressure is defined as

$$P_L = 330\frac{I}{10^{18}Wcm^{-2}}\frac{\lambda^2}{\mu m^2}Mbar \qquad \text{Eqn (2.3)}$$

For example, a laser with $I\lambda^2=10^{19}$ $Wcm^{-2}\mu m$ has a pressure of 33 Gbar. This light pressure is sufficient to accelerate ions inward, and for solid targets the plasma can be driven to densities above the original solid density, an effect known as "hole boring" (Wilks et al. 1992;Zepf et al. 1996). This will be discussed in detail below.

2.1.1 The Plasma Frequency

If electrons in a plasma are displaced from their equilibrium position by a laser field, then they will experience a restoring field generated by charge separation. They oscillate sinusoidally at a frequency known as the plasma frequency ω_p (Chen 1983)

$$\omega_p = \left(\frac{n_e e^2}{\varepsilon_0 m_e}\right)^{\frac{1}{2}} \qquad \text{Eqn (2.4)}$$

where n_e is the electron density, e is the electronic charge and m_e is the electronic mass.

2.1.2 Overdense and Underdense Plasmas

The density of a laser-produced plasma depends heavily on the type of target and the parameters of the laser. For example, when a picosecond pulse interacts with a gaseous target, the pulse can propagate through the gas over millimetres, during which time it can ionise, distort, refract and accelerate particles. A plasma produced in this manner is termed underdense. Gaseous targets are usually used in the study of wakefield acceleration (Amiranoff et al. 1998;Dorchies et al. 1999;Tajima & Dawson 1979;Ting et al. 1997;Wagner et al. 1997) to accelerate particles above the ponderomotive potential since acceleration can take place over longer distances than for solids. A simple picture of wakefield acceleration is: an intense laser pulse focused on a target can produce a wake of plasma oscillations (or plasma waves). These are volumes of low and high densities of electrons. Similar to a boat creating a bow wave or wake as it moves through water, a population of high velocity electrons creates a wake of plasma waves as it propagates through a plasma. Electrons can "ride" on these waves similar to a surfer riding on a wave in water and can gain energy. Energies higher than the ponderomotive potential can also be obtained in underdense plasmas via scattering instabilities (Estabrook & Kruer 1982;Joshi, Tajima, & Dawson 1981;Mori et al. 1994) and plasma wave breaking (Kato et al. 1993;Modena et al. 1995;Sheng & Meyer-ter-Vehn 1997).

When the same pulse interacts with a solid target, a plasma is formed on the target surface, but there is not enough time for a substantial region of "coronal" plasma to form. Hence a plasma with a steep density gradient, or scale length is produced, ranging from solid density to a density defined by the interaction time. At $\omega_p=\omega_0$ the laser cannot propagate through the plasma and is reflected. Since ω_p is dependent on the electron density (Eqn 2.4), there is a certain density at which this occurs known as the critical density, N_c and is given by (Wilks and Kruer 1997)

$$N_c = \frac{1.1\times 10^{21}}{\lambda^2} cm^{-3} \qquad \text{Eqn (2.5)}$$

where λ is the laser wavelength in microns. Above this density, a plasma is termed overdense. For a plasma with a density gradient ranging from underdense to overdense, the point at which the laser can no longer propagate and is reflected is known as the critical surface.

2.2 Ultra-Intense Laser-Solid Interactions

One of the reasons that ultra-short (femtosecond-picosecond), ultra-intense laser pulses have become such important research tools is that before their advent, it was not possible to deposit so much laser energy in such a short time scale, in such a tiny volume in front of a solid target. Previously, using nanosecond intense pulses obtained with CO_2 lasers, large preformed plasmas with shallow density gradients were created that the laser had to interact with. That is, due to the long pulse length, ionisation has already taken place during the rising edge of the pulse and a plasma formed on the target surface that expands outwards, before the peak of the pulse can interact with the target. This led to a considerable amount of absorption of laser energy in the underdense part of the plasma, as well as enough time for the laser beam to filament on its way to the critical surface (Wilks & Kruer 1997). This, in turn led to a large fraction (>10 %) of the laser energy to be converted into hot electrons, which were thought to be created via various laser-plasma interactions (Priedhorsky et al. 1981).

However, ultra-intense pulses of picoseconds or shorter have the ability to create an overdense plasma (sometimes several times the critical density and up to solid densities) and interact with it. However, real laser systems have an associated pre-pulse arriving on target prior to the main pulse. If this pre-pulse is intense enough, it can create a plasma, which the main pulse interacts with. The laser is thus interacting with a preformed plasma, making the modelling of the interaction even more complicated. In the next section, the laser pulse structure will be discussed and the various relevant plasma parameters that are generated in the laser-solid interaction. The remaining sections will discuss the possible absorption and hence acceleration mechanisms, firstly for electrons and subsequently ions. Of course in laser-plasma interactions, the electrons are accelerated preferentially to ions; the heavier ions are initially left behind due to inertia and are subsequently accelerated due to charge separation.

2.3 Laser Pulse Characteristics

Let us assume that an ultra-intense pulse is described by a perfect Gaussian with temporal pulse length (FWHM) of τ_o=1 ps and a peak intensity of $I_o=10^{20}$ Wcm^{-2} as shown in Figure 2.1.

This pulse propagates through vacuum and is focused on to a solid target. Assume that the interface between vacuum and the solid target is step-like. Once the laser intensity exceeds around 10^{12} Wcm^{-2}, ionisation occurs and a plasma is formed on the target surface. Typical ion densities are $\eta_i \sim 10^{23}$ cm^{-3} and electron densities $\eta_e = Z\eta_i$ where Z is the atomic number of the target material. For a pulse of 10^{20} Wcm^{-2}, plasma formation occurs quite early in the interaction, and so most of the pulse interacts with a plasma as opposed to an unionised solid.

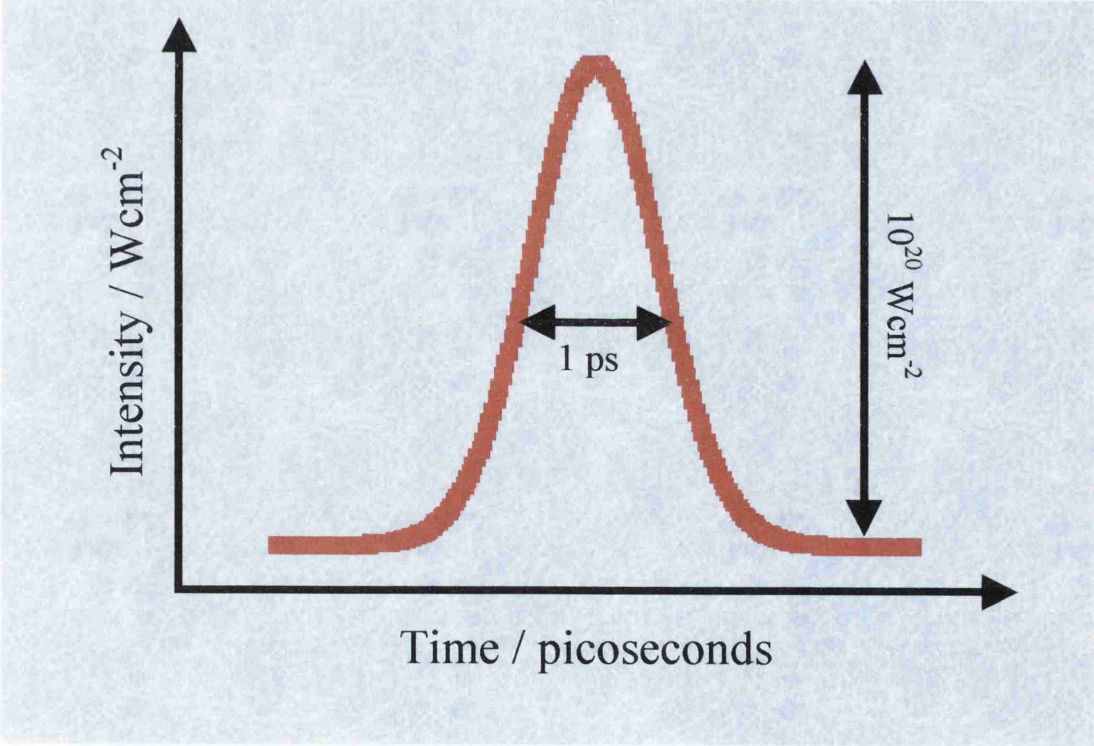

Figure 2.1 An ideal Gaussian laser pulse.

As stated previously, the laser light interacting with the plasma will propagate up to the critical density, but after which it is reflected. More precisely, the laser penetrates slightly past critical, but falls of exponentially in a distance determined by the plasma density. This distance is known as the collisionless skin depth and is given by c/ω_p in the nonrelativistic case where $\omega_p=(\eta_e e^2/\varepsilon_0 m_e)^{1/2}$ is the plasma frequency (Eqn 2.4). For example, for a solid target of carbon (Z=6) the skin depth is about 60 Å. For the relativistic case ($\gamma>1$) the effective density at which the light will be reflected is increased by the factor γ, hence the light can penetrate even further into the overdense plasma. This is due to the relativistic increase in the electron mass. The plasma formed in front of the target expands thermally into the vacuum, and accounts for the electron and ion beams in this direction. This is also known as "blow-off" plasma. Extensive studies of laser ablation of materials at lower laser intensities have shown that this plasma always expands along the target normal independent of angle of incidence (Zheng et al. 1989).

Real laser pulses are however more complex, and have a prepulse, or pedestal present, due to the Chirped Pulse Amplification process (Chapter 3) (Hutchinson 1989;Mourou 1997;Perry, Ditmire, & Stuart 1994). The VULCAN prepulse has an intensity of 10^{-6} that of the main pulse (10^{20} Wcm^{-2}), and can be several nanoseconds long. At 10^{14} Wcm^{-2} this is sufficient to ionise the target prior to the arrival of the main pulse. A sketch of a pulse of this type is shown if Figure 2.2.

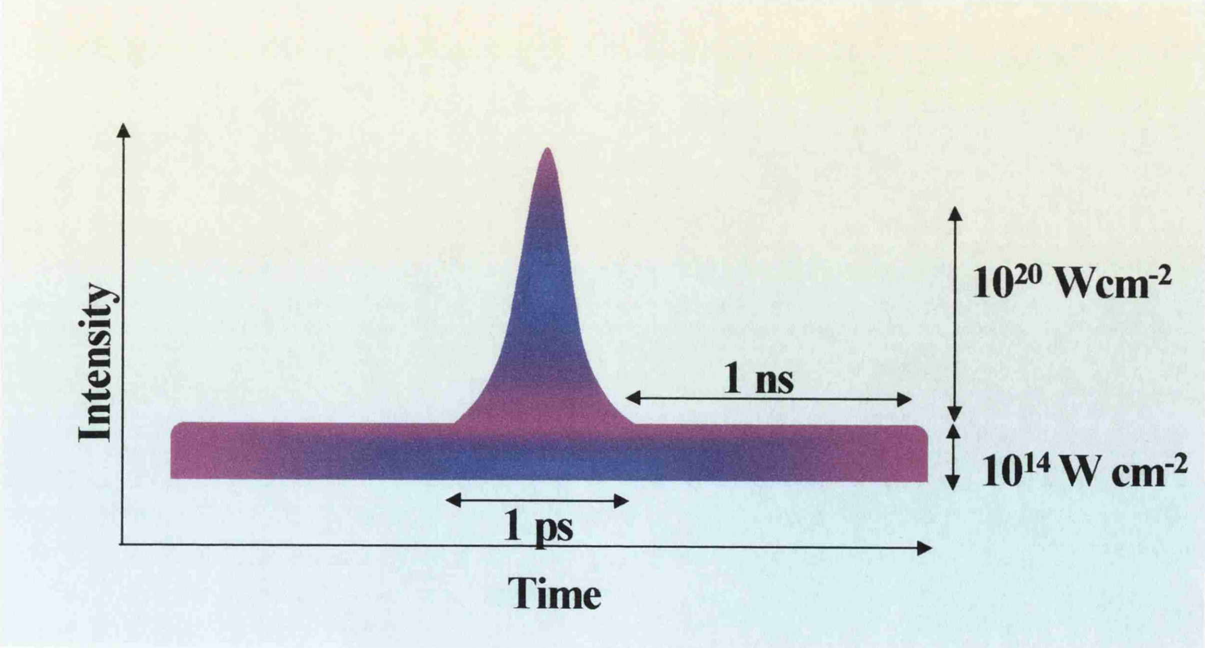

Figure 2.2 Sketch of a real CPA laser pulse with a pre-pulse or "pedestal".

The density scale length of this pre-plasma generated by the pedestal is defined by (Wilks & Kruer 1997)

$$L_n = \eta \frac{dn}{dx} \sim C_s \tau_L \qquad \text{Eqn (2.6)}$$

where η is the plasma density, $d\eta/dx$ is the slope of the density at the density η, $C_s=[k(ZT_e+T_i)/M_I]^{1/2}$ is the ion sound speed, M_i is the ion mass, k is Boltzmann's constant and τ_L is the duration of the ionising laser. The fact that the laser interacts with a small sphere of pre-formed plasma can influence the interaction physics greatly. Chapter 5 describes experiments carried out that show the effect the plasma density scale length has on the dominance of the various electron absorption and hence acceleration mechanisms that are described below.

2.4 Classical Resonance Absorption

The resonance absorption process has been discussed since as early as 1977 (Estabrook & Kruer 1978;Forslund, Kindel, & Lee 1977) since it is a dominant mechanism in nanosecond, $10^{12} < I\lambda^2 < 10^{17}$ Wcm$^{-2}\mu$m^2 experiments. This is because it predominately takes place in plasmas with a shallow density gradient. However, it is still present in picosecond or less, $I\lambda^2 > 10^{19}$ Wcm$^{-2}\mu$m^2 laser-solid interactions, hence it is necessary to review the physics of this process.

Consider a plasma expanding into vacuum from a solid surface as described in Section 2.2. A laser is incident at some angle θ from the normal of the target plane. Using Snell's Law, it can be shown that the laser light will propagate up to the density $\eta_{cr}\cos^2\theta$ before it is reflected. If the electric field vector, **E** of the laser light is in the direction of the density gradient $\nabla\eta$, or the target normal (the case known as p-polarisation) then an electron plasma wave will be resonantly excited when the plasma frequency ω_p is equal to the laser frequency ω_o. That is, at the critical surface, a plasma wave is generated due to resonance. The electrostatic field associated with this resonant wave is capable of accelerating electrons. Wilks and Kruer (Wilks & Kruer 1997) showed that the temperature of the hot electrons produced by resonance absorption scales as

$$T_{hot} \sim 10[T_{keV} I_{15} \lambda^2]^{\frac{1}{3}} keV \qquad \text{Eqn (2.7)}$$

where T_{keV} is the background electron temperature in keV, I_{15} is the laser intensity in units of 10^{15} Wcm^{-2} and λ is the laser wavelength in μm. If we assume a background electron temperature of 4 keV, the hot electron temperature due to resonance absorption for $I\lambda^2=10^{20}$ Wcm^{-2} is around 740 keV. Note that this is far less than the ponderomotive potential for this irradiance, which, from Section 2.1 is around 4 MeV.

This absorption mechanism accelerates electrons along the direction of the target normal and can contribute to the total absorption in $I\lambda^2 > 10^{19}$ Wcm^{-2}μm^2 interactions, but is not the dominant process. This will be discussed further via the experimental results found in Chapter 5.

2.5 "Not-so-Resonant", Resonance Absorption

This absorption mechanism was first discussed by Brunel in 1987 (Brunel 1987) and is also known as "vacuum heating" or the Brunel effect. Since then, a number of theoretical and numerical studies have developed the understanding of this effect (Bonnaud et al. 1991;Brunel 1988;Gibbon & Bell 1992;Kato et. al. 1993). More recently, many authors have provided experimental evidence of vacuum heating (Chen et al. 2001;Grimes et al. 1999;Maksimchuk et al. 2000).

This effect is related to classical resonance absorption in that the electric field of the laser light accelerates electrons across a density gradient. The difference between the two is that in classical resonance absorption the laser light is assumed to be incident on a plasma of gently increasing density (the density scale-length is many ×laser wavelength). The electric field of the laser can hence drive a large plasma wave at the critical surface resonantly. In vacuum heating, the density scale length is taken to be much less than a wavelength of the incident laser light (i.e. the plasma density is greater than critical or overdense), and hence no such resonance exists. Therefore, the light non-resonantly couples into an electrostatic plasma wave. It has been shown that the electric field of a laser of $I\lambda^2=10^{20}$ Wcm^{-2} is very large and so a significant amount of energy can be transferred to the plasma electrons. The electrons are dragged away from the target surface, turned around and accelerated back into the solid all within half a laser cycle. These electrons are absorbed simply because the laser only penetrates to a skin depth or so due to the steep plasma density gradient. It can be shown (Gibbon & Förster 1996) that the hot electron temperature due to vacuum heating is

$$T_{hot} \sim 8(I_{16}\lambda^2)^{\frac{1}{3}}\, keV \qquad \text{Eqn (2.8)}$$

Where I_{16} is the laser intensity in units of 10^{16} Wcm^{-2} and λ is again the laser wavelength in μm. So for a laser pulse of $I\lambda^2=10^{20}$ Wcm^{-2}μm^2, the hot electron temperature due to vacuum heating is only 172 keV. This is somewhat less than the temperature inferred from resonance absorption, although this value depends heavily on the plasma scale length since this strongly affects the absorption efficiency (Gibbon & Bell 1992).

This process, like its classical counterpart accelerates electrons along the target normal, since it too drives the plasma electrons via a plasma wave generated across the plasma density gradient, albeit in the overdense region. This mechanism is considered to be a major factor in the acceleration of electrons in ultra-intense laser-solid interactions.

2.6 Relativistic j×B Heating

This absorption mechanism is due to the oscillating compoment of the ponderomotive force of the laser (Section 2.1, Eqn 2.2). It depends on the large gradient in the laser light near the vacuum-plasma interface, due to the penetration of the laser electric and magnetic fields, a skin depth into the overdense plasma. In 1996, Malka and Miquel (Malka & Miquel 1996) measured the energy distribution of hot electrons escaping from a solid target and found a scaling in good agreement with Equation (2.2) (Wilks et. al. 1992;Wilks & Kruer 1997) for laser pulses of $I\lambda^2=2\text{x}10^{19}$ Wcm^{-2}μm^2.

For an electron fluid element in the plasma, near the vacuum-plasma interface, Wilks and Kruer (Wilks & Kruer 1997) showed that in the non-relativistic case, the force felt by this element is given by

$$f_p = -\frac{\partial}{\partial x}\left(\frac{m v^2_{osc}}{2}\frac{4\omega_o^{\ 2}}{\omega^2_{pe}}e^{-2\omega_{pe}x/c}\left[\frac{1+\cos 2\omega_o t}{2}\right]\right) \qquad \text{Eqn (2.9).}$$

This is the force felt by an electron a depth x inside the plasma (as measured from the vacuum-plasma boundary). Heating is a result of that component of the **j**×**B** force that oscillates the electrons at the vacuum-plasma interface with a frequency of twice the laser frequency. So twice every laser cycle electrons are accelerated into the target. If the magnitude of the force is great enough, as is the case for $I\lambda^2 > 10^{19}$ Wcm$^{-2}\mu$m^2, all the electrons at the boundary will oscillate in this non-resonant wave. The direction of oscillation is of course **j**×**B,** the direction of propagation of the laser (also known as the **k**-vector of the laser). This is different from the two previous processes where the acceleration is along the direction of the plasma density gradient target (target normal for p-polarised light), independent of the laser angle of incidence. The phases of some of the electrons oscillating in this wave may be such that they gain energy from this oscillation, i.e. they are given a nonadiabatic "kick" into the overdense plasma. However, only a fraction of the electrons may escape the wave, and the number of escapees will depend on the strength of the oscillating force. This mechanism is considered dominant in $I\lambda^2 > 10^{19}$ Wcm$^{-2}\mu$m^2 laser-solid interactions, although it is believed that these interactions involve a mixture of resonant absorption, vacuum heating and **j**×**B** acceleration. For example, it is important to point out that vacuum heating is more important than **j**×**B** heating when the driving field (in particular, the component of the E-field that is normal to the surface) is greater than the magnitude of the **j**×**B** driving term. That is, when $2E_L\sin\theta > v_{osc}B_L$, or equivalently, when $\sin\theta > (v_{osc}/c)(\omega_o/\omega_{pe})$, as discussed by Denavit (Denavit 1992). Chapter 5 discusses experimental evidence of the dependence of the direction of fast electrons on the plasma density scale length. From the direction of fast electrons, the dominance of the various absorption mechanisms can be inferred.

2.7 The "Hole Boring" Phenomenon

This effect takes place only in laser-solid interactions for $I\lambda^2 > 10^{18}$ $Wcm^{-2}\mu m^2$. It was first discussed theoretically by Wilks *et al.* in 1992 (Wilks et. al. 1992) and verified experimentally by Zepf *et al.* in 1996 (Zepf et. al. 1996).

"Hole boring" results from a combination of three effects. (1), the huge light pressure as discussed in Section 2.1 causes the plasma to be pushed inwards preferentially at the centre of the focal spot. (2), a radial ponderomotive force due to the transverse intensity gradient $\nabla_r I$ pushes electrons away from the centre of the beam, creating a charge separation which pulls the ions out. Hence hole boring is considered to be one of the mechanisms responsible for ion acceleration and indeed inward ion acceleration has been observed in simulations as a result of this process (Wilks et. al. 1992). (3), The relativistic increase in the skin depth as discussed previously can lead to "induced transparency", where the laser beam is transmitted through a nominally overdense plasma instead of being reflected (Lefebvre & Bonnaud 1995). As a hole is formed, the absorption efficiency and temperature of the hot electrons both increase because density gradients are formed parallel to the laser electric field (Wilks et. al. 1992). Hence the hole boring effect can result in electron energies above that of the ponderomotive potential.

2.8 "B-Loop" Acceleration

This mechanism was first found in simulations by Pukhov and Meyer-ter-Vehn (Pukhov & Meyer-ter-Vehn 1998) and was given the above name by these authors. It has been shown in simulations that magnetic fields of up to 100 Mega Gauss are generated during interactions involving laser pulses in the $I\lambda^2 = 10^{20}$ $Wcm^{-2}\mu m^2$ regime (Pukhov & Meyer-ter-Vehn 1996). Experimentally, magnetic fields of 30 MG have been inferred via measurements of the collimation of ion beams (Clark et al. 2000a). It is believed that these fields are generated by the beam of fast electrons, produced in the manner described above.

Pukhov and Meyer-ter-Vehn incorporated into their simulations an azimuthal dc magnetic field of this type to investigate the behaviour of electrons in the presence of such a field. What they found was that an electron quivering inside a relativistically intense laser pulse is scattered in the transverse direction with a non-zero energy gain, (Hartemann et al. 1995) makes a loop in the surrounding azimuthal B-field and is re-injected back into the laser pulse. At the same time the **v×B** force is pushing electrons in the direction of $\mathbf{k}_{\mathbf{laser}}$. This picture could be described simply as a "corkscrew" type motion. Figure 2.3. shows a simple sketch of this electron motion. A chain of such acceleration stages produces electrons with energies many times higher than the ponderomotive potential. The simulations also showed that this mechanism is dominant in near-critical plasma, or when plasma waves disappear due to wave-breaking.

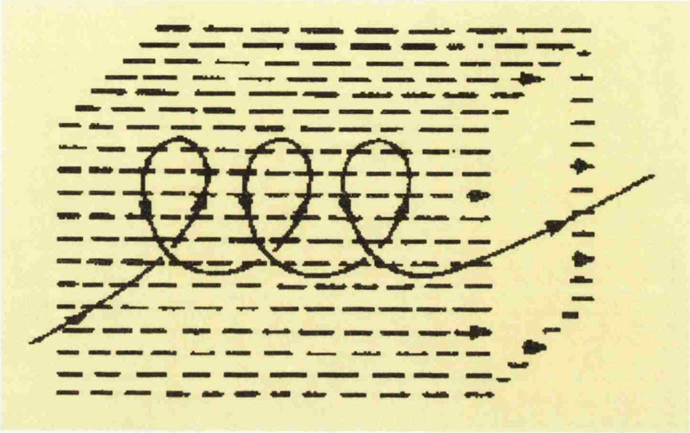

Figure 2.3 Motion of an electron in a dc magnetic field.

2.9 Proton Acceleration in Laser-Solid Interactions

A laser-produced plasma contains both free electrons and ions, and for a solid target, the type of ion depends on the target. Of current interest is the production of energetic proton beams, (Chapter 6) where the protons are of course ionised hydrogen atoms.

Measurements of proton emission from laser-solid interactions has been made as early as the 1980s (Gitomer et al. 1986;Kishimoto et al. 1983) using nanosecond CO_2 lasers. Later measurements, using picosecond pulsed lasers (Beg et al. 1997;Fews et al. 1994) showed that protons of energies in the MeV range can be generated at $I\lambda^2$ up to 10^{19} $Wcm^{-2}\mu m^2$. In more recent experiments (Clark et al. 2000b;Clark et. al.

2000a;Krushelnick et al. 1999;Santala et al. 2001;Snavely et al. 2000), multi-MeV protons have been observed for $I\lambda^2$ up to 10^{20} $\text{Wcm}^{-2}\mu\text{m}^2$.

The mechanisms responsible for ion acceleration are currently the subject of intensive research by many groups around the world.

In front of the target, ion beams are observed from the expansion of the plasma generated on the target surface, produced either by a prepulse (Pukhov & Meyer-ter-Vehn 1998;Yu et al. 2000) or by the rising edge of the main pulse itself, also known as "blow-off" plasma, directed normal to the target surface. The principal area of study at the moment however is how the ion beam observed at the rear of the solid target is generated.

The main mechanism thought to be responsible for the generation of this beam is the production of electrostatic fields due to space charge effects when the fast electrons, accelerated via the mechanisms described above, exit the target. Inward ion acceleration via hole boring (Pukhov & Meyer-ter-Vehn 1997;Wilks et. al. 1992;Zepf et. al. 1996) should lead to ions of the order of a few MeV (Zepf et al. 2000) and hence cannot explain the recent experimental observations.

The major area of debate has been on where the proton beam at the rear of the target originates. The hydrogen atoms responsible for proton production are either from the bulk hydrocarbon molecules in typically CH (plastic) targets, or from hydrocarbon impurities on target surfaces when metallic targets are used. In the latter case, Clark *et al.* (Clark et. al. 2000a) and Maksimchuk *et al.* (Maksimchuk et. al. 2000) stated that the energetic protons are generated from hydrocarbon impurity layers on the front of the target, then travel through the target and out the rear. Snavely *et al.* (Snavely et. al. 2000) on the other hand argued that the protons originate at the rear of the target. Nemoto *et al.* (Nemoto et al. 2001) have shown recently that using deuterated targets that the accelerated deuterons appear to originate from the front surface. This issue has been discussed by Zepf *et al.* (Zepf et. al. 2000) in detail.

The most viable model to date however has been offered by Wilks *et al*. (Wilks et al. 2001). What is believed to happen is as follows. A population of hot electrons, generated in the blow-off plasma created by the laser prepulse interacting with the front target surface, is accelerated into the target via the mechanisms described above. This electron beam travels through the target and ionises the hydrogen-containing impurity layer on the back surface. Plasmas on the front and back surfaces of solid targets have been observed experimentally (Tatarakis et al. 1998). These protons are then pulled off

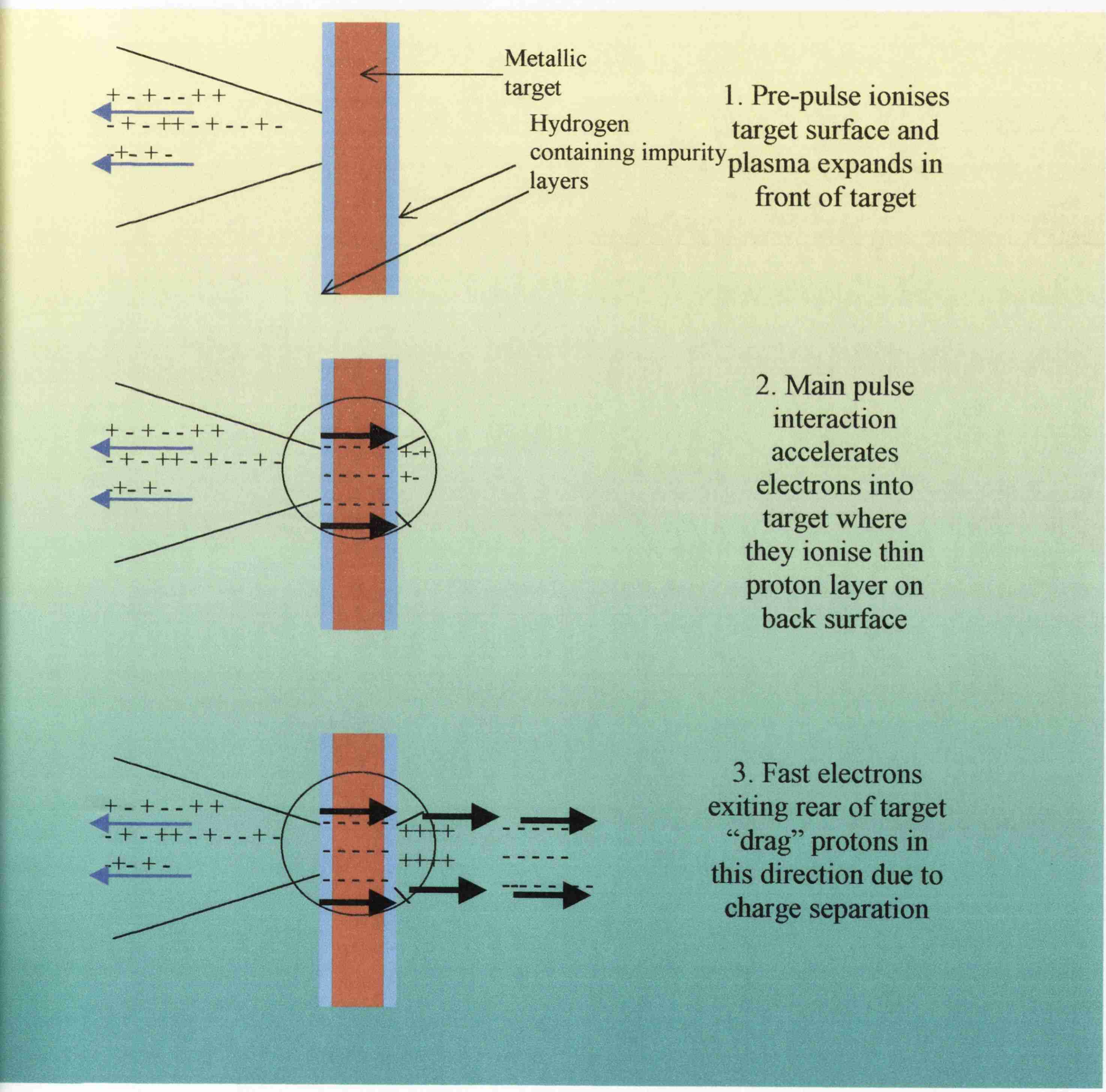

Figure 2.3 Simplistic view of the proton acceleration model.

the target surface by this cloud of electrons, due to charge separation, and accelerated to the multi-MeV energies reported in recent experiments. Chapter 6 describes experimental evidence of the production of around 8×10^{12} protons with a maximum energy of around 40 MeV. Figure 2.3 shows a simplified picture of this ion acceleration model. This mechanism means that the protons at the rear are always directed normal to the target surface, independent of the direction of this fast electrons. This has been observed experimentally (Snavely et al. 2000).

References

Amiranoff, F., Baton, S., Bernard, D., Cros, B., Descamps, D., Dorchies, F., Jaquet, F., Malka, V., Marquès, J. R., Matthieussent, G., Miné, P., Modena, A., Mora, P., Morillo, J., & Najmudin, Z. 1998, "Observation of laser wakefield acceleration of electrons", *Physical Review Letters*, vol. 81, p. 995.

Beg, F. N., Bell, A. R., Dangor, A. E., Danson, C. N., Fews, A. P., Glinsky, M. E., Hammel, B. A., Lee, P., Norreys, P. A., & Tatarakis, M. 1997, "A study of picosecond laser-solid interactions up to 10^{19} Wcm^{-2}", *Physics of Plasmas*, vol. 4, p. 447.

Bonnaud, G., Gibbon, P., Kindel, J. M., & Williams, E. 1991, "Laser interaction with a sharp-edged overdense plasma", *Laser and Particle Beams*, vol. 9, p. 339.

Brunel, F. 1987, "Not-so-resonant, resonant absorption", *Physical Review Letters*, vol. 59, p. 52.

Brunel, F. 1988, "Anomalous absorption of high intensity sub-picosecond laser pulses", *Physics of Fluids*, vol. 31, p. 2714.

Chen, F. F. 1983, *Introduction to Plasma Physics and Controlled Fusion*, Second edn, Plenum Publishing Corporation.

Chen, L. M., Zhang, J., Dong, Q. L., Teng, H., Liang, T. J., Zhao, L. Z., & Wei, Z. Y. 2001, "Hot electron generation via vacuum heating process in femtosecond laser-solid interactions", *Physics of Plasmas*, vol. 8, p. 2925.

Clark, E. L., Krushelnick, K., Davies, J. R., Zepf, M., Tatarakis, M., Beg, F. N., Machacek, A., Norreys, P. A., Santala, M. I. K., Watts, I., & Dangor, A. E. 2000a, "Measurements of energetic proton transport through magnetized plasma from intense laser interactions with solids", *Physical Review Letters*, vol. 84, p. 670.

Clark, E. L., Krushelnick, K., Zepf, M., Beg, F. N., Tatarakis, M., Machacek, A., Santala, M. I. K., Watts, I., Norreys, P. A., & Dangor, A. E. 2000b, "Energetic heavy-ion and proton generation from ultra-intense laser-plasma interactions with solids", *Physical Review Letters*, vol. 85, p. 1654.

Denavit, J. 1992, "Absorption of high-intensity subpicosecond lasers on solid-density targets", *Physical Review Letters*, vol. 69, p. 3052.

Dorchies, F., Amiranoff, F., Baton, S., Bernard, D., Cros, B., Descamps, D., Jacquet, F., Malka, G., Marquès, J. R., Matthieussent, G., Miné, P., Modena, A., Mora, P., Morillo, J., Najmudin, Z., & Solodov, A. 1999, "Electron acceleration in laser wakefield experiment at Ecole Polytechnique", *Laser and Particle Beams*, vol. 17, p. 299.

Estabrook, K. & Kruer, W. L. 1978, "Properties of resonantly heated electron distributions", *Physical Review Letters*, vol. 40, p. 42.

Estabrook, K. & Kruer, W. L. 1982, "Theory and simulation of one-dimensional Raman backward and forward scattering", *Physics of Fluids*, vol. 26, p. 1892.

Fews, A. P., Norreys, P. A., Beg, F. N., Bell, A. R., Dangor, A. E., Danson, C., Lee, P., & Rose, S. J. 1994, "Plasma ion emission from high intensity picosecond laser pulse interactions with solid targets", *Physical Review Letters*, vol. 73, p. 1801.

Forslund, D. W., Kindel, J. M., & Lee, K. 1977, "Theory of hot-electron spectra at high laser intensity", *Physical Review Letters*, vol. 39, p. 284.

Gibbon, P. & Bell, A. R. 1992, "Collisionless absorption in sharp-edged plasmas", *Physical Review Letters*, vol. 68, p. 1535.

Gibbon, P. & Förster, E. 1996, "Short-pulse laser-plasma interactions", *Plasma Physics and Controlled Fusion*, vol. 38, p. 769.

Gitomer, S. J., Jones, R. D., Begay, F., Ehler, A. W., Kephart, J. F., & Kristal, R. 1986, "Fast ions and hot electrons in the laser-plasma interaction", *Physics of Fluids*, vol. 29, p. 2679.

Grimes, M. K., Rundquist, A. R., Lee, Y.-S., & Downer, M. C. 1999, "Experimental identification of "Vacuum Heating" at femtosecond-laser-irradiated metal surfaces", *Physical Review Letters*, vol. 82, p. 4010.

Hartemann, F. V., Fochs, S. N., Le Sage, G. P., Luhmann, N. C. J., Woodworth, J. G., Perry, M. D., Chen, Y. J., & Kerman, A. K. 1995, "Nonlinear ponderomotive scattering of relativistic electrons by an intense laser field at focus", *Physical Review E*, vol. 51, p. 4833.

Hora, H., Hoelss, M., Wang, W., Ho, Y. K., Osman, F., & Castillo, R. 2000, "Principle of high accuracy for the nonlinear theory of the acceleration of electrons in a vacuum by lasers at relativistic intensities", *Laser and Particle Beams*, vol. 18, p. 135.

Hutchinson, M. H. R. 1989, "Terawatt lasers", *Contemporary Physics*, vol. 30, p. 355.

Joshi, C. & Corkum, P. 1995, "Interactions of ultra-intense laser light with matter", *Physics Today*, vol. January, p. 36.

Joshi, C., Tajima, T., & Dawson, J. M. 1981, "Forward Raman instability and electron acceleration", *Physical Review Letters*, vol. 47, p. 1285.

Kato, S., Bhattacharyya, B., Nishiguchi, A., & Mima, K. 1993, "Wave breaking and absorption efficiency for short pulse p-polarised laser light in a very steep density gradient", *Physics of Fluids B*, vol. 5, p. 564.

Kishimoto, Y., Mima, K., Watanabe, T., & Nishikawa, K. 1983, "Analysis of fast-ion velocity distributions in laser plasmas with a truncated Maxwellian velocity distribution of hot electrons", *Physics of Fluids*, vol. 26, p. 2308.

Krushelnick, K., Clark, E. L., Najmudin, Z., Salvati, M., Santala, M. I. K., Tatarakis, M., & Dangor, A. E. 1999, "Multi-MeV Ion Production from high-intensity laser interactions with underdense plasmas", *Physical Review Letters*, vol. 83, p. 737.

Ledingham, K. W. D., Spencer, I., McCanny, T., Singhal, R. P., Santala, M., Clark, E. L., Watts, I., Beg, F. N., Zepf, M., Krushelnick, K., Tatarakis, M., Dangor, A. E., Norreys, P. A., Allott, R. M., Neely, D., Clarke, R. J., Machacek, A., Wark, J. S., Creswell, A., Sanderson, D. C. W., & Magill, J. 2000, "Photo-nuclear physics when a multiterawatt laser pulse interacts with solid targets", *Physical Review Letters*, vol. 84, p. 899.

Lefebvre, E. & Bonnaud, G. 1995, "Transparency/Opacity of a solid target illuminated by an ultrahigh intensity laser pulse", *Physical Review Letters*, vol. 74, p. 2002.

Maksimchuk, A., Gu, S., Flippo, K., & Umstadter, D. 2000, "Forward ion acceleration in thin films driven by a high-intensity laser", *Physical Review Letters*, vol. 84, p. 4108.

Malka, G. & Miquel, J. L. 1996, "Experimental confirmation of ponderomotive-force electrons produced by an ultra-relativistic laser pulse on a solid target", *Physical Review Letters*, vol. 77, p. 75.

Modena, A., Najmudin, Z., Dangor, A. E., Clayton, C. E., Marsh, K. A., Joshi, C., Malka, V., Darrow, C. B., Danson, C., Neely, D., & Walsh, F. N. 1995, "Electron acceleration from the breaking of relativistic plasma-waves", *Nature*, vol. 377, p. 606.

Mori, W. B., Decker, C. D., Hinkel, D. E., & Katsouleas, T. 1994, "Raman forward scattering of short-pulse high intensity lasers", *Physical Review Letters*, vol. 72, p. 1994.

Mourou, G. 1997, "The ultrahigh-peak-power laser: present and future", *Applied Physics B*, vol. 65, p. 205.

Nemoto, K., Maksimchuk, A., Banerjee, S., Flippo, K., Umstadter, D., & Bychenkov, V. Y. 2001, "Laser-triggered ion acceleration and table top isotope production", *Applied Physics Letters*, vol. 78, p. 595.

Perry, M. D., Ditmire, T., & Stuart, B. C. 1994, "Self phase modulation in chirped pulse amplification", *Optics Letters*, vol. 19, p. 2149.

Priedhorsky, W., Lier, D., Day, R., & Gerke, D. 1981, "Hard X-ray measurements of 10.6 μm laser-irradiated targets", *Physical Review Letters*, vol. 47, p. 1661.

Pukhov, A. & Meyer-ter-Vehn, J. 1996, "Relativistic magnetic self-channeling of light in near-critical plasma: three-dimensional particle-in-cell simulation", *Physical Review Letters*, vol. 76, p. 3975.

Pukhov, A. & Meyer-ter-Vehn, J. 1997, "Laser hole boring into overdense plasma and relativistic electron currents for fast ignition of ICF targets", *Physical Review Letters*, vol. 79, p. 2686.

Pukhov, A. & Meyer-ter-Vehn, J. 1998, "Relativistic laser-plasma interaction by multi-dimensional particle-in-cell simulations", *Physics of Plasmas*, vol. 5, p. 1880.

Santala, M. I. K, Zepf, M,, Beg, F. N., Clark, E.L., Dangor, A. E., Krushelnick, K., Ledingham, K. W.D., McCanny, T., Spencer, I., Machacek, A. C., Allott, R., Clarke, R.J., Norreys, P. A. 2001, "Production of radioactive nuclides by energetic protons generated from intense laser-plasma interactions", *Applied Physics Letters*, vol. 78, p. 19.

Sheng, Z. M. & Meyer-ter-Vehn, J. 1997, "Relativistic wave breaking in warm plasmas", *Physics of Plasmas*, vol. 4, p. 493.

Snavely, R. A., Key, M. H., Hatchett, S. P., Cowan, T. E., Roth, M., Phillips, T. W., Stoyer, M. A., Henry, E. A., Sangster, C., Singh, M. S., Wilks, S. C., Mackinnon, A. J., Offenberger, A. A., Pennington, D. M., Yasuike, K., Langdon, A. B., Lasinski, B. F., Johnson, J., Perry, M. D., & Campbell, E. M. 2000, "Intense high-energy proton beams from petawatt-laser irradiation of solids", *Physical Review Letters*, vol. 85, p. 2945.

Tajima, T. & Dawson, J. M. 1979, "Laser Electron Accelerator", *Physical Review Letters*, vol. 43, p. 267.

Tatarakis, M., Davies, J. R., Lee, P., Norreys, P. A., Kassapakis, N. G., Beg, F. N., Bell, A. R., Haines, M. G., & Dangor, A. E. 1998, "Plasma fromation on the front and rear of plastic targets due to high intensity laser-generated fast electrons", *Physical Review Letters*, vol. 81, p. 999.

Ting, A., Moore, C. I., Krushelnick, K., Manka, C., Esarey, E., Sprangle, P., Hubbard, R. F., Burris, H. R., Fischer, R., & Baine, M. 1997, "Plasma wakefield generation and electron acceleration in a self-modulated laser wakefield accelerator experiment", *Physics of Plasmas*, vol. 4, p. 1889.

Umstadter, D. 2001, "Review of physics and applications of relativistic plasmas driven by ultra-intense lasers", *Physics of Plasmas*, vol. 8, p. 1774.

Wagner, R., Chen, S. Y., Maksimchuk, A., & Umstadter, D. 1997, "Electron acceleration by a laser wakefield in a relativistically self-guided channel", *Physical Review Letters*, vol. 78, p. 3125.

Wilks, S. C. & Kruer, W. L. 1997, "Absorption of ultrashort, ultra-intense laser light by solids and overdense plasmas", *IEEE Journal of Quantum Electronics*, vol. 33, p. 1954.

Wilks, S. C., Kruer, W. L., Tabak, M., & Langdon, A. B. 1992, "Absorption of Ultra-Intense Laser Pulses", *Physical Review Letters*, vol. 69, p. 1383.

Wilks, S. C., Langdon, A. B., Cowan, T. E., Roth, M., Singh, M. S., Hatchett, S. P., Key, M. H., Pennington, D. M., Mackinnon, A. J., & Snavely, R. A. 2001, "Energetic proton generation in ultra-intense laser-solid interactions", *Physics of Plasmas*, vol. 8, p. 542.

Witte, K. J., Gahn, C., Meyer-ter-Vehn, J., Pretzler, G., Pukhov, A., & Tsakiris, G. D. 1999, "Physics of ultra-intense laser-plasma interaction", *Plasma Physics and Controlled Fusion*, vol. 41, p. B221.

Yu, W., Bychenkov, V. Y., Sentoku, Y., Yu, M. Y., Sheng, Z. M., & Mima, K. 2000, "Electron acceleration by a short relativistic laser pulse at the front of solid targets", *Physical Review Letters*, vol. 85, p. 570.

Zepf, M., Castro-Colin, M., Chambers, D., Preston, S. G., Wark, J. S., Zhang, J., Danson, C., Neely, D., Norreys, P. A., Dangor, A. E., Dyson, A., Lee, P., Fews, A. P., Gibbon, P., Moustaizis, S., & Key, M. H. 1996, "Measurements of the hole boring velocity from Doppler shifted harmonic emission from solid targets", *Physics of Plasmas*, vol. 3, p. 3242.

Zepf, M., Clark, E. L., Krushelnick, K., Beg, F. N., Dangor, A. E., Santala, M., Tatarakis, M., Watts, I., Norreys, P. A., Clarke, R. J., Davies, J. R., Sinclair, M., Edwards, R., Goldsack, T., Spencer, I., & Ledingham, K. W. D. 2000, "Fast particle generation and energy transport in laser-solid interactions", *Physics of Plasmas*.

Zheng, J. P., Huang, Z. Q., Shaw, D. T., & Kwok, H. S. 1989, "Generation of high-energy atomic-beams in laser-superconducting target interactions", *Applied Physics Letters*, vol. 54, p. 280.

Chapter 3

The VULCAN Nd: Glass Laser System

This chapter describes the operating characteristics of the laser system employed in the experiments, namely the VULCAN Nd: Glass system at the Rutherford Appleton Laboratory, UK. The Chirped Pulse Amplification (CPA) technique as applied to VULCAN is described, and the chapter concludes with a description of the various laser pulse diagnostics.

3.1 Introduction

In Chapter 1, the history of high-intensity pulsed lasers was discussed. To recap, in the 1960s, the highest available intensity was 10^9 Wcm^{-2}. Since then, the techniques of Q-switching and mode-locking made intensities of 10^{16} Wcm^{-2} possible by the early 80s. Excellent descriptions of these techniques can be found in (Davis 1996;Hutchinson 1989;Svelto 1989;Wilson & Hawkes 1987).

The implementation of Chirped Pulse Amplification (CPA) (Strickland & Morou 1985) brought about a dramatic increase in the output power and focused intensities (Perry & Mourou 1994). The highest power achieved to date is 10^{15} W, yielding intensities of 10^{21} Wcm^{-2}. All of the highest power laser systems today incorporate this technique, including VULCAN.

Over the past eight years or so, there have been two principal directions of high power laser development. The first has been the realisation of table-top multi-terawatt CPA systems using Ti: Sapphire as the gain medium where the large gain bandwidth enables pulses to be generated in the 10-100 fs regime (Barty et al. 1996;Barty, Gordon, & Lemoff 1994;Chambaret et al. 1996;Langley et al. 1999a;Langley et al. 1999b;Yamakawa et al. 1998;Zhou et al. 1995). The second is towards increased power and focused intensity using large-scale, single pulse, high energy lasers operating in the picosecond regime. Systems of this type usually employ Nd: glass as the amplifying medium (Danson et al. 1998;Danson et al. 1999a;Irion 1998;Mourou 1997), equipped for the CPA mode of operation. This is because Nd: glass has a saturation energy density (recall from Chapter 1), E_s~7 Jcm^{-2}, compared to Ti: sapphire's E_s~0.6 Jcm^{-2} (Mourou 1997). Ti: sapphire however has a broader bandwidth of ($\Delta\nu$~120 nm) compared to ($\Delta\nu$~20 nm) for Nd: glass so Ti: sapphire can support shorter pulses (Chapter 1, Section 1.3.1, "Mode-Locking"). So there is a trade-off between shorter pulses but at lower energies, and longer pulses but at higher energies. The highest power achieved with a Ti: sapphire system to date is in the 25 TW regime, compared to 1000 TW for Nd: Glass.

This chapter describes the VULCAN laser operating characteristics as it was for the experiments carried out herein, operating at 10-100 TW in CPA mode with focused intensities of 10^{19}-10^{20} Wcm^{-2}. At present, the VULCAN laser is being upgraded to operate at 1 PW, with focused intensities of 10^{21} Wcm^{-2}, incorporating slightly different operating characteristics. Figure 3.1 shows a floor plan of the VULCAN facility; the target area used for the experiments was Target Area West.

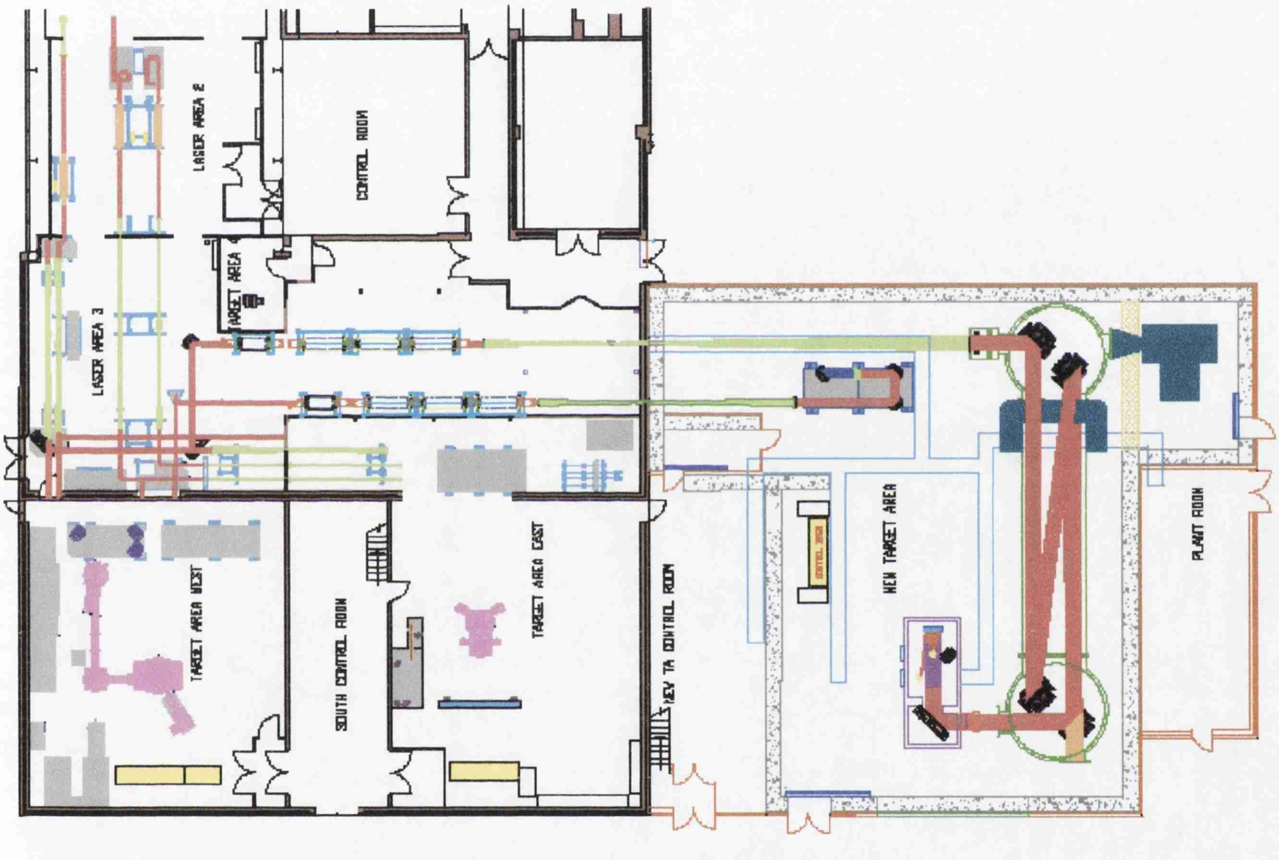

Figure 3.1 Floor plan of the VULCAN facility.

3.2 System Architecture

VULCAN is an 8 beam 2.5 kJ Nd: Glass laser of which six beams typically deliver long pulses (80 ps – 2 ns) and one beam a synchronised ultra-high power, ultra-short pulse using the CPA mode of operation. The final eighth beam is also available with the CPA set-up, but at a reduced power level. This thesis is concerned with the ultra-high power CPA beam-line (TA West) and the architecture of this is shown in Figure 3.2. It essentially comprises of three areas; the Front End, the Amplifier and the Compression/Target Interaction Area.

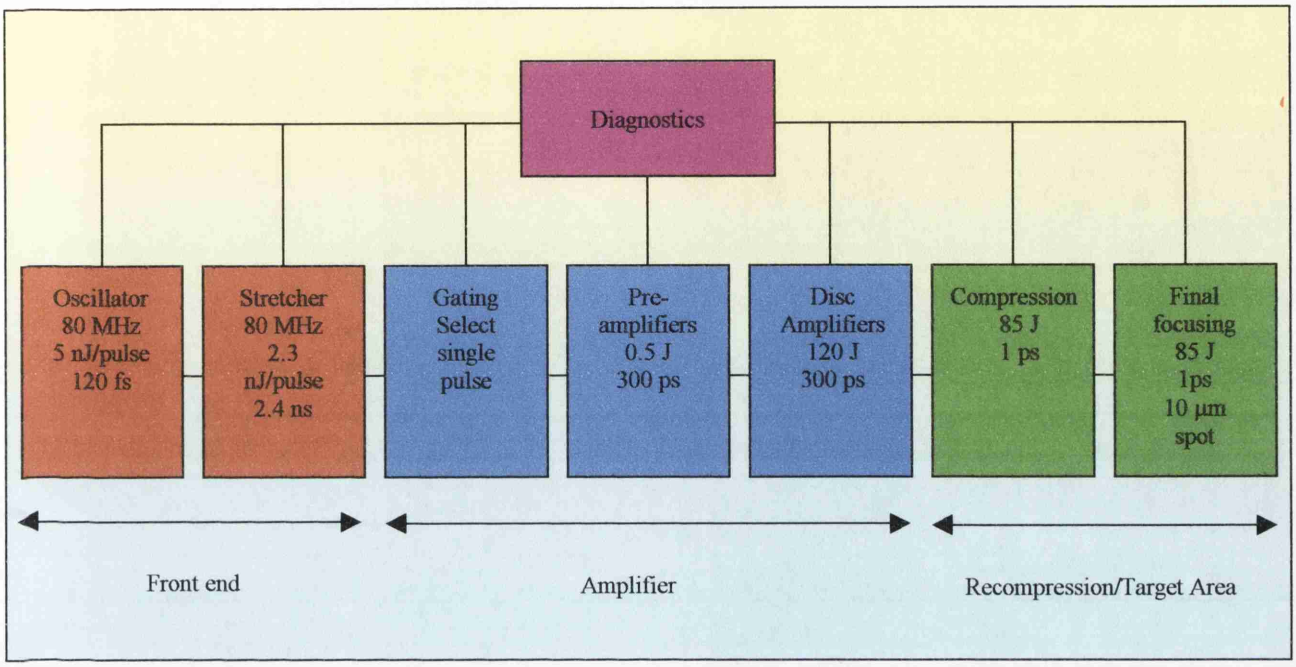

Figure 3.2 Block diagram of the VULCAN system architecture.

3.2.1 The Front End

The ultra-short seed pulses are generated from a commercial Tsunami oscillator (Spectra-Physics Lasers – see http://www.spectra-physics.com). The system is Kerr Lens Mode-locked (Spence, Kean, & Sibbet 1991) and the active medium is Ti: sapphire, pumped by all lines of a stabilised Argon Ion laser.

Figure 3.3 shows the absorption and emission spectroscopic properties of the Ti:Al_2O_3 material (Davis 1996). The Ar-ion laser wavelength was suitably in the middle and most intense part of the absorption spectrum of the Ti: sapphire crystal. The Ti: sapphire laser is a four level lasing system based on the schematic illustration shown in Figure 3.4. Ground state particles are optically excited into an absorption band (4) followed by a rapid non-radiative transfer into the upper laser level (3) such that a population inversion will result between levels 3 and 2 and laser action can be obtained. Then a fast drain transition (2-to-1) occurs.

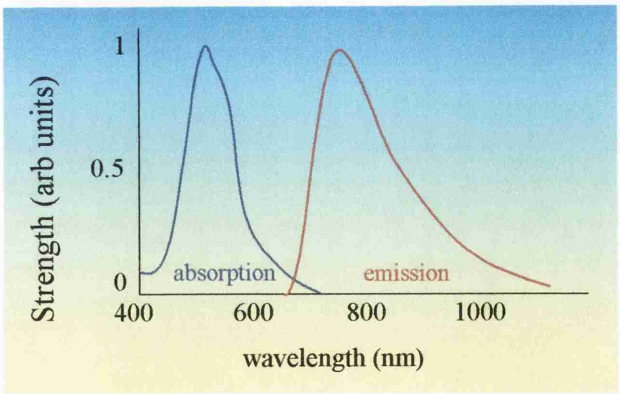

Figure 3.3 Absorption and emission properties of Ti: sapphire.

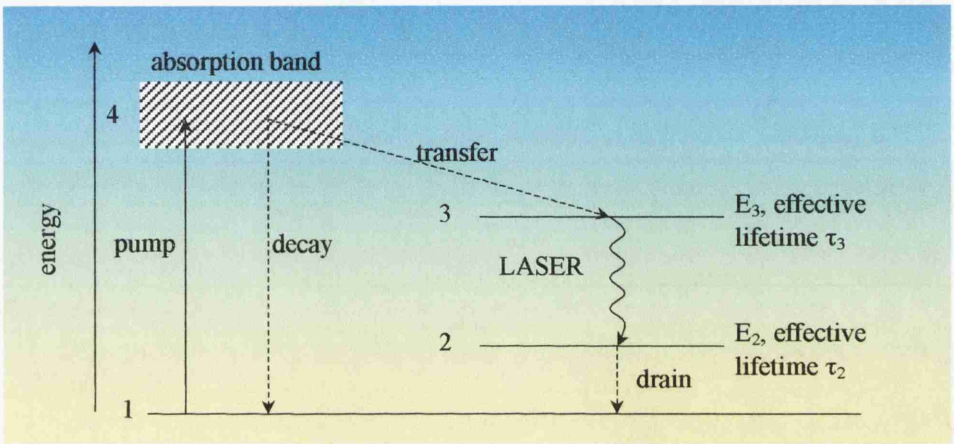

Figure 3.4 Schematic of an optically pumped four-level laser system.

The Tsunami oscillator is tuneable to the entire broad bandwidth range (~300 nm) of Ti: sapphire and hence it is tuned to a wavelength of 1053 nm ($\Delta\nu$~12 nm FWHM), the optimum wavelength of the Nd: glass. Nd: glass has a very narrow bandwidth of ~20 nm which means that gain narrowing can take place, the problems associated with this will be demonstrated later. When operated in this manner, the oscillator produces 5 nJ pulses of 120 fs duration at 80 MHz.

In order to successfully amplify the seed pulses produced by the oscillator, the pulses must be stretched in time to reduce its intensity, primarily to avoid damage to the optical components, while maintaining the frequency spectrum of the initial pulse. Stretching also limits nonlinear distortion to the spatial and temporal profile of the beam, which happens at higher intensities. Nonlinear self focusing is also prevented as stated previously.

The pulse stretching system employed is shown in Figure 3.5. It involves the use of two diffraction gratings. When a laser pulse containing a spectrum of frequencies is incident on such a grating, the higher frequencies within the pulse are diffracted through smaller angles at the gratings. The higher frequencies then follow a longer path than the lower frequencies and hence the pulse is stretched, or "chirped" with the lower frequencies leading the higher frequencies in time. This is shown in Figure 3.6.

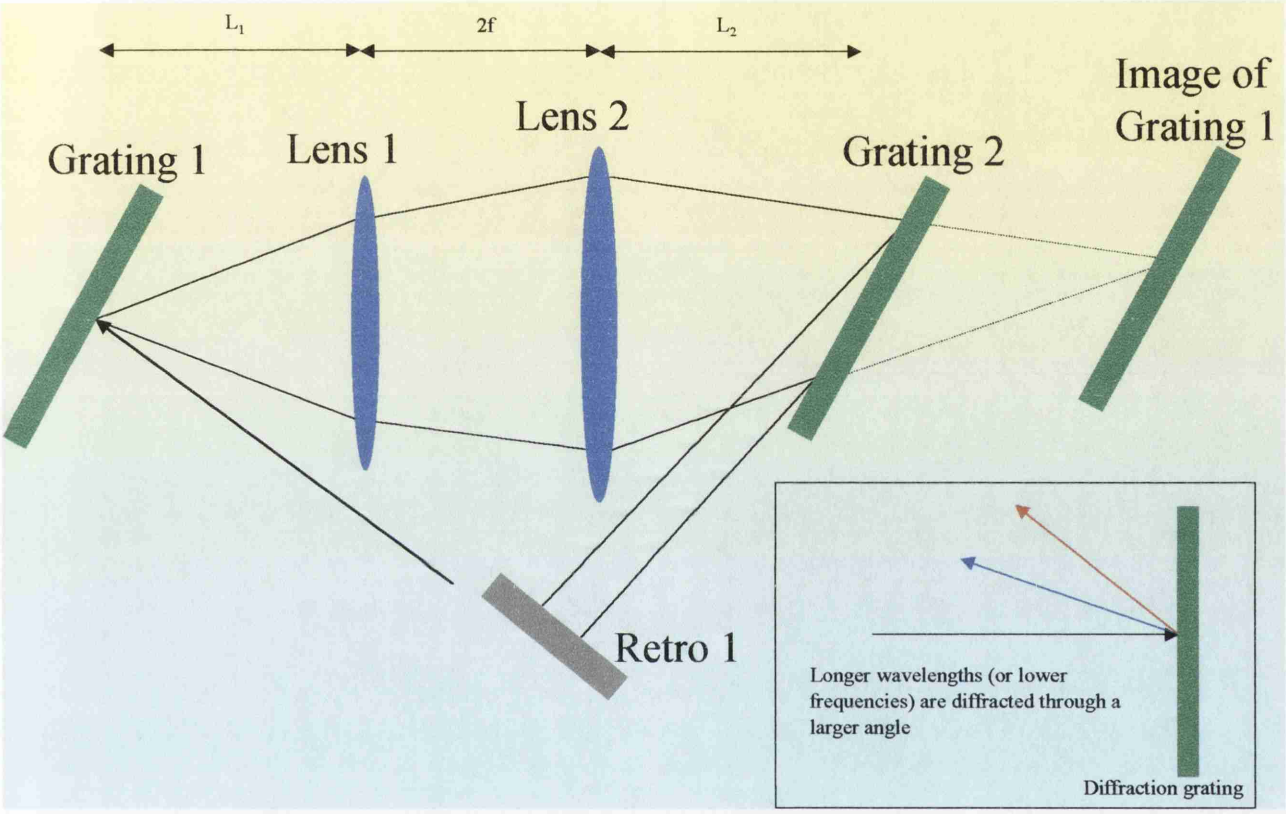

Figure 3.5 The VULCAN CPA pulse stretcher. (Inset) the effect a diffraction grating has on a pulse containing a spectrum of frequencies.

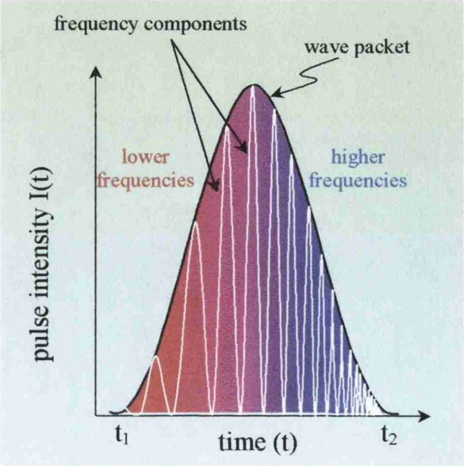

Figure 3.6 Pulse with a frequency chirp.

The stretcher design is that of a refractive telescope, operated in double pass mode. The pulses from the oscillator are incident at 73° on a 1740 lines mm^{-1} diffraction grating (Grating 1). This grating is imaged using a 4f telescope to a point 6 m away using a pair of 1.5 m focal length lenses separated by 3 m. The first lens is located ~300 mm away from Grating 1. A second grating (Grating 2), aligned parallel to the image of Grating 1 is situated ~300 mm from the second lens, producing a separation of Grating 2 to the image of Grating 1 of ~2.4 m. The beam exiting from Grating 2 is reflected at normal incidence back into the system to double the effective grating separation and to eliminate the spectral dispersion imposed after the single pass. The maximum bandwidth that can pass through the stretcher is 16 nm. After passing through the stretcher, the pulse is elongated to 2.4 ns – a stretch factor of ×20 000. The stretcher is around 50 % efficient and so the pulse energy after the stretcher is ~2.5 nJ.

The chirp can be undone and the frequency coded pulse restored to its original form, again using diffraction gratings. The red-shifted leading edge is delayed by a suitable amount relative to the blue-shifted trailing edge. This is done after amplification.

3.2.2 Amplifier

A single 2.5 nJ pulse from the Front End is selected when required using the optical gating system and injected into the VULCAN amplifier chain. Pre-amplification of the pulse is performed by 3 double-passed Nd: glass amplifiers each with a 9 mm aperture. Each amplifier has a gain of ~×600 resulting in a pulse energy of ~0.5 J. The pulse is then propagated through one of the main VULCAN amplifier chains where it is initially amplified in a series of single-pass, flashlamp pumped, rod amplifiers. This chain consists of one rod of 16 mm aperture (gain×25), one of 25 mm aperture (gain×16) and one of 45 mm aperture (gain×8). The 45 mm beam is then passed to the final amplifier stages which consist of a double-pass 108 mm aperture disc amplifier (gain×90) followed by a single pass 150 mm aperture disc amplifier (gain×4). This would result in an overall gain of $\sim 2.5\times10^{14}$ however static losses are ~×2000 so the overall gain is $\sim 10^{11}$ (Collier 2001). This results a pulse of up to 250 J although the limit is defined by the laser induced damage threshold of the compressor gratings as will be demonstrated later. This at the moment limits the maximum pulse energy exiting the amplifier chain to 120 J. Figure 3.7 shows Chris Edwards of the Central Laser Facility inspecting one of the large-aperture disc amplifiers.

The laser beam quality is maintained to high fidelity by passing the beam through a system of vacuum spatial filters (VSF) which act to eliminate phase distortions in the beam as it passes through the different optics. A spatial filter is essentially a pinhole through which the laser beam passes. The final VSF can be seen in Figure 3.8.

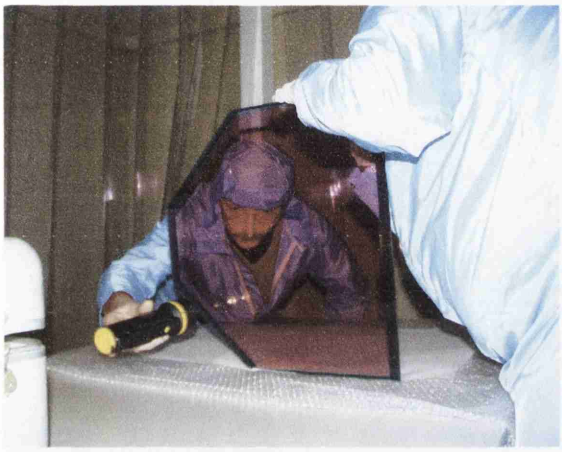

Figure 3.7 A VULCAN Nd: glass disc amplifier.

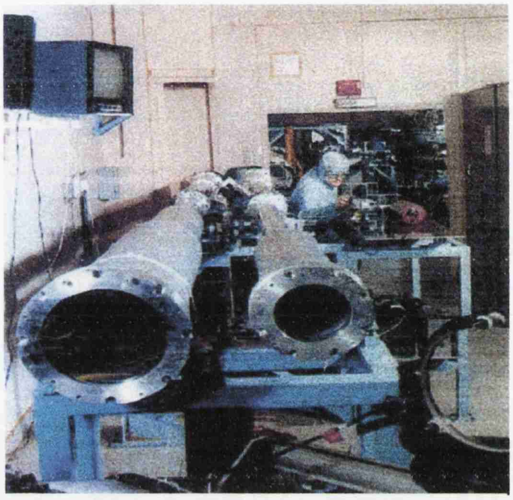

Figure 3.8 The final vacuum spatial filter of the CPA beamilne of VULCAN.

As the oscillator pulse propagates through the amplifiers, the spectral peak of the pulse is shifted to shorter wavelengths (Danson et al. 1998). This is due to the narrow bandwidth of Nd: glass. The 12 nm FHWM pulse spectrum is narrowed to only ~2 nm and hence the pulse length is shortened to 300 ps during and after amplification.

3.2.3 Recompression

After amplification, the pulse is compressed using the system shown in Figure 3.9. It consists of a pair of large aperture diffraction gratings separated by 3.5 m. The 420 × 210 mm, (880 cm^2) 1740 lines mm^{-1} gratings are operated at an incidence angle of 73°.

To maximise the intensity to target, the beam has to be as uniform as possible and completely filling the first grating (Ross, Trentelman, & Danson 1997). To achieve this, the aperture of the output laser beam was increased by modifying the vacuum spatial filter in the system. The 135 mm beam at the output of the 150 mm amplifier was expanded to 200mm in the final VSF then apertured to give a rectangular beam of 200×130 mm, which is of suitable dimensions for the acceptance aperture of the first grating.

The maximum energy that can be delivered to target is limited by the laser-induced damage threshold (LIDT) of the compressor gratings. This has been measured (Danson et al. 1999a) to be ~0.45 Jcm^{-2}. This means that the maximum energy incident on the gratings must not exceed 120 J. The transmission efficiency of the compressor system and transport optics to target has been measured to be 70 % which includes single grating efficiencies of ~89 %. This gives a maximum energy to target of ~85 J.

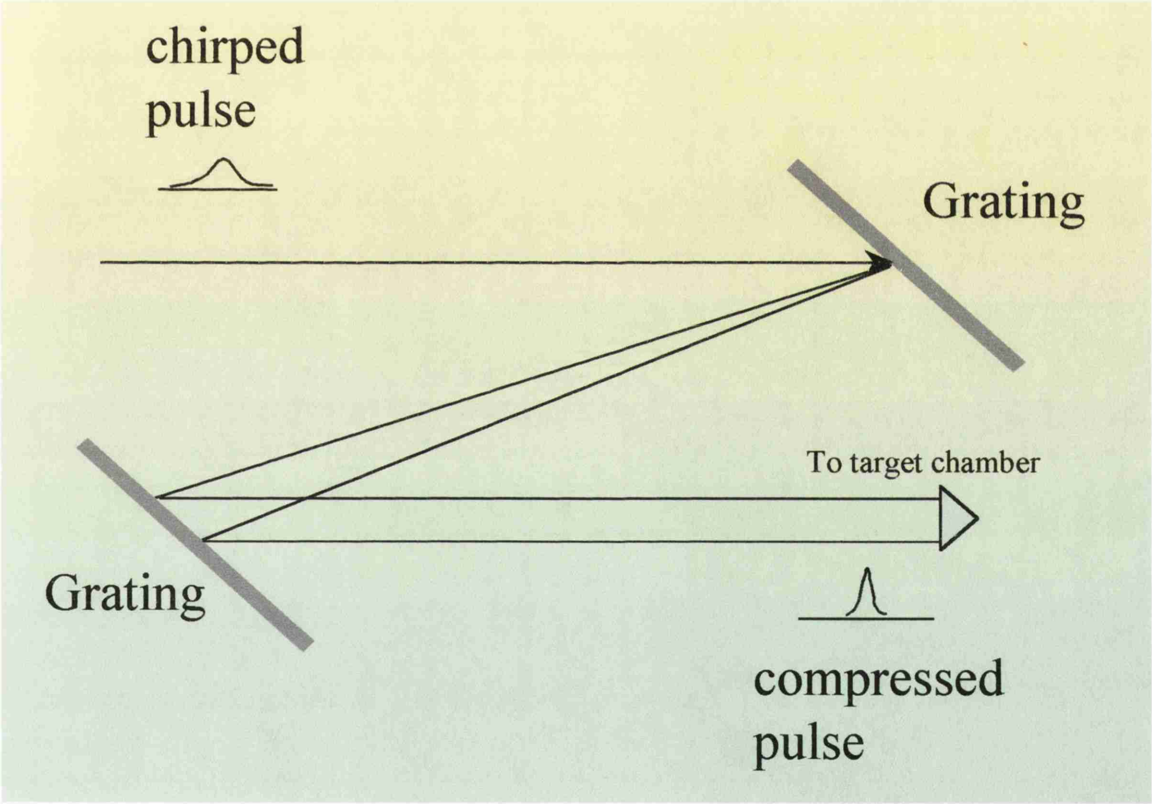

Figure 3.9 The VULCAN compressor. The longer wavelengths are delayed relative to the shorter wavelengths. If the alignment corresponding to the stretcher is exact, complete recompression occurs.

3.2.4. Target Area

After the compressor, the pulse enters the target chamber, which is also held in vacuum. A 95 % reflectivity turning mirror is used to steer the beam onto target. The 5 % leakage is then transported to a separate diagnostics suite for measurement, as described in Section 3.4. The pulse is then focused using a parabolic mirror as shown in Figure 3.10. Lenses cannot be used to focus at this stage due to the nonlinear nature of the pulse. More detailed descriptions of the target area arrangements are given for the respective experiments in Chapters 5 and 6.

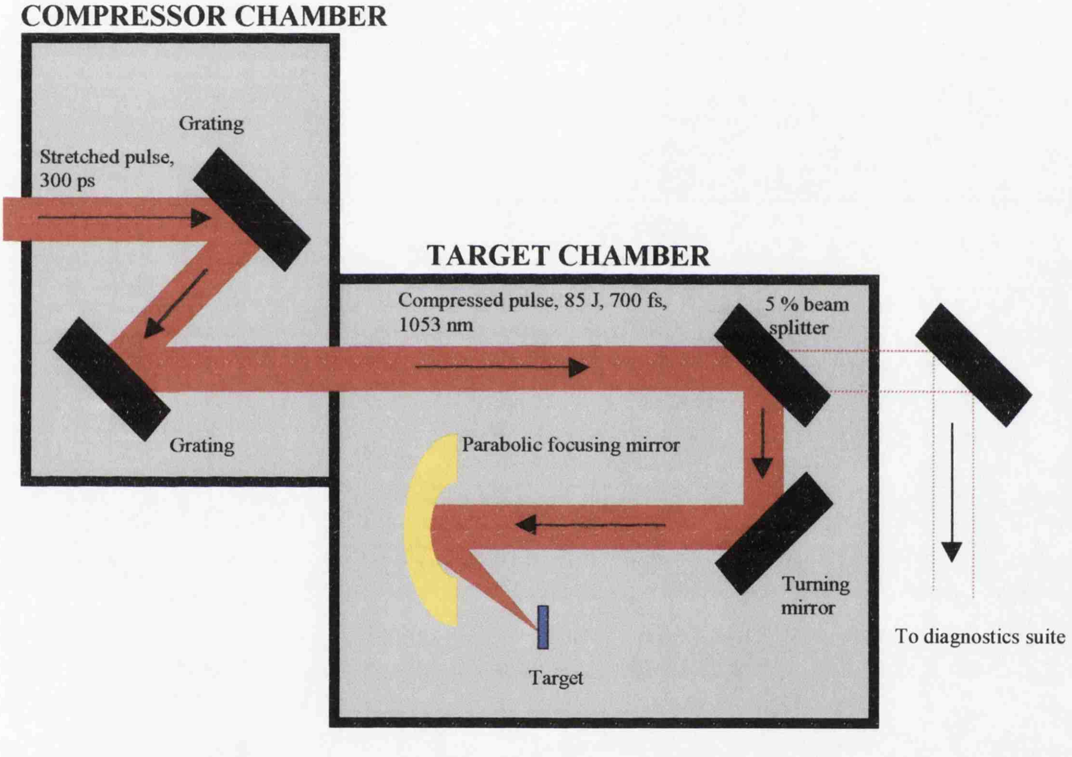

Figure 3.10 Schematic of the compressor / target chambers.

In order to generate the highest intensities, the beam must be focused to the smallest spot possible. Theoretically, the minimum focal spot possible is defined by the diffraction limit (Svelto 1989). For a parabolic mirror of focal length f, and a beam diameter D of wavelength λ, the minimum spot diameter limited by diffraction is given by

$$SpotDiameter = \frac{1.22 f\lambda}{D}. \qquad \text{Eqn (3.1)}$$

So it is obvious that a parabola with a shorter focal length can produce a smaller spot and hence higher intensities.

Focusing optics such as parabolic mirrors are usually defined by their F-number. If we assume that the light exactly fills the aperture of the parabola, the F-number is given by F=f/D. This means that Eqn (3.1) can be re-written as

$$\text{Spot Diameter} = 1.22F\lambda. \qquad \text{Eqn (3.2)}$$

Hence, the smaller the F-number of the focusing optic, the greater its focusing capabilities.

Focusing optics employed on VULCAN are either an F1.5 on-axis parabola, dimensions 255 mm x 130 mm, focal length 225 mm or an F4 off-axis parabola, focal length 450 mm. It is possible to manufacture an F1 on-axis parabola, which has the advantage of producing smaller spot sizes. A disadvantage of using an on-axis parabola however is that the incoming beam is clipped by the target before being focused by the mirror as shown in Figure 3.11, which can lead to distortion of the beam and a loss of energy. Off-axis parabolas do not have this problem as shown in Figure 3.11 however it is not possible to manufacture off-axis parabolas with F-numbers as low as on-axis.

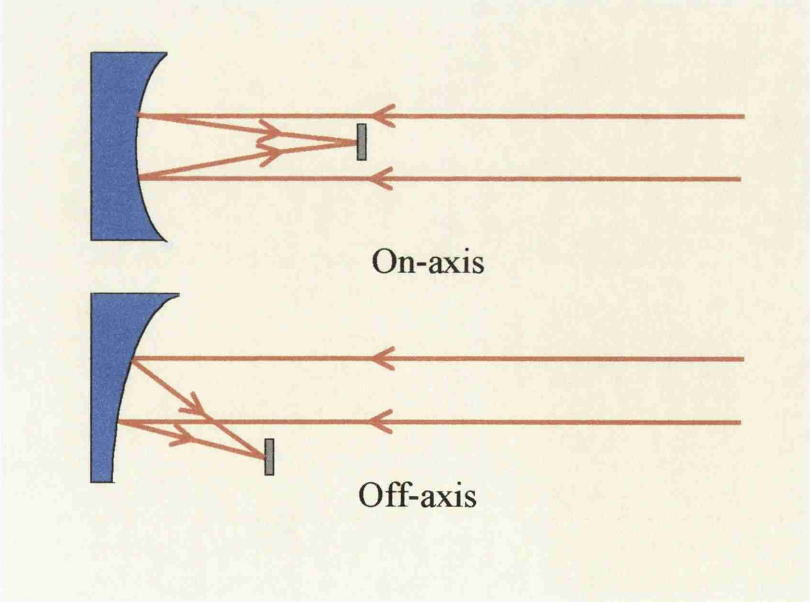

Figure 3.11 Focusing by on and off axis parabolas. Use of an on-axis parabola can result in clipping of the incoming beam by the target.

3.3 Laser Diagnostics

To say with confidence what the intensity on target is, three parameters must be measured; the pulse energy, pulse duration, and focal spot size. The measurement of these is described in Sections 3.3.1, 3.3.2 and 3.3.3.

Another characteristic that it is important to diagnose is the contrast ratio between any low level optical activity and the main pulse. This is also known as the "pedestal" or the pre-pulse. It is important to measure this since a pedestal of sufficient intensity can ionise a target prior to the arrival of the main pulse, and thus affect drastically the interaction physics (Chapter 2).

The limit in contrast of any conventional laser system is Amplified Spontaneous Emission (ASE) and is present on target for a time determined by the optical gate of the system. There are two main sources of pre-pulse; the amplifier system through poor choice of amplifier elements / poor alignment strategy, and the oscillator that is used to seed the amplifier system. The contrast ratio, i.e. the ratio of the main pulse to any background activity in the amplifier system has is well known and has been measured to be ~10^6 (Danson et al. 1993) using the third order cross correlation technique (Luan et al. 1993). Tight optical gating ensures that long time scale pre-pulse activity occurring at times greater than 300 ps from the main pulse is effectively removed. It is possible to increase the timing of the gating to allow longer pre-pulses through, to investigate the effect this has on the interaction physics (Santala et al. 2000) (Chapter 5). Section 3.3.4. describes the measurement of the contrast ratio in the oscillator, again using the third order cross correlation technique.

3.3.1 Measurement of Pulse Energy

In order to measure the pulse energy of the amplified pulse for every shot, a 2 % leakage of the beam is taken after the final VSF using a 98 % reflectivity turning mirror. This leakage beam is incident on a calibrated calorimeter which converts the energy incident on it to an electrical pulse. The meter is cross calibrated with a direct energy measurement of the full beam energy which is taken periodically using a large aperture NPL calibrated joule meter. Using the calibration, the calorimeter measurement of the 2 % leakage beam provides information on the pulse energy before the compressor for every shot. To calculate the energy in the target area, the 70 % efficiency of the compressor system must be taken into account, plus any leakage from mirrors in the target chamber (e.g. the 5 % leakage for the diagnostics suite).

3.3.2 Measurement of Pulse Duration

The direct measurement of pulses in the fs-few ps regime is not yet possible since the response times of detectors e.g. streak cameras are at the moment too slow.

Ultrashort pulses are usually measured using the technique of second harmonic generation (SHG) autocorrelation (Fujimoto, Weiner, & Ippen 1984;Salin et al. 1987;Singhal 1995;Yariv 1997). It is desirable to measure the pulse length on a single shot basis, and the design of one such system can be found in (Salin, Georges, Roger, & Brun 1987). A number of designs for such systems have been demonstrated, e.g. the above references plus (Clements, Taylor, & Kane 1995) but all have a multiaxial nature, both spatially and temporally leading to difficulties of alignment. This means that systems of this type are more suited to measurements of pulse length on high-repetition rate systems, but can prove awkward for low-repetition rate systems such as VULCAN, where the repetition rate is typically one shot every twenty minutes.

Single shot autocorrelation is usually achieved by splitting the beam to be measured into two parts and delaying one arm by a certain time. The two beams are then focused on to a nonlinear frequency mixing crystal. If the group delay from the splitter to the crystal is the same for each arm, then a sum frequency signal is generated in the crystal where the arms spatially and temporally overlap.

The sum frequency signal is generated at all points in the overlap region and at each point it is proportional to the product of the local intensity in each arm at that point. The emission of the sum frequency signal occurs for all points in the overlap region in a direction that bisects the crossover angle. For any line parallel to this bisector, a measurement of the total amount of sum frequency signal occurring along that line represents the time integral of the local intensity products. The beams cross at an angle and thus for different measurement lines the intensity product integral occurs for a different relative delay between each arm. Therefore, the spatial distribution of the emitted light is the time integrated intensity product of the two pulses evaluated at different delays. This is known as the intensity autocorrelation, and details of this function can be found in (Collier et al. 1999;Davis 1996).

Traditional designs to implement this autocorrelation process generally use a 50 % reflectivity mirror for the splitting process to generate the two arms from the input beam thereby forcing a biaxial design. The need to carefully match the optical path length of the two arms provides a third, temporal degree of freedom and the usual introduction of a retroreflector for this purpose produces a beam height change and thus a fourth axis of alignment. The multiaxial design of these types of autocorrelator can make them difficult to work with.

A system has been designed in-house at RAL for use on VULCAN which overcomes these problems in alignment by being uniaxial in nature (Collier, Danson, Johnson, & Mistry 1999). This system is shown schematically in Figure 3.12.

Precise details of the characteristics of the autocorrelator can be found in (Collier, Danson, Johnson, & Mistry 1999). Basically, the pulses are injected off a diffraction grating, which can be rotated to select the zeroth, first or second diffraction order which selects the autocorrelation range. The pulses are then split by a Woolaston prism, and recombined by a biprism. The autocorrelation takes place in the frequency mixing crystal and is recorded by a CCD camera. Using dedicated software, the autocorrelation signal intensity as a function of time can be extracted.

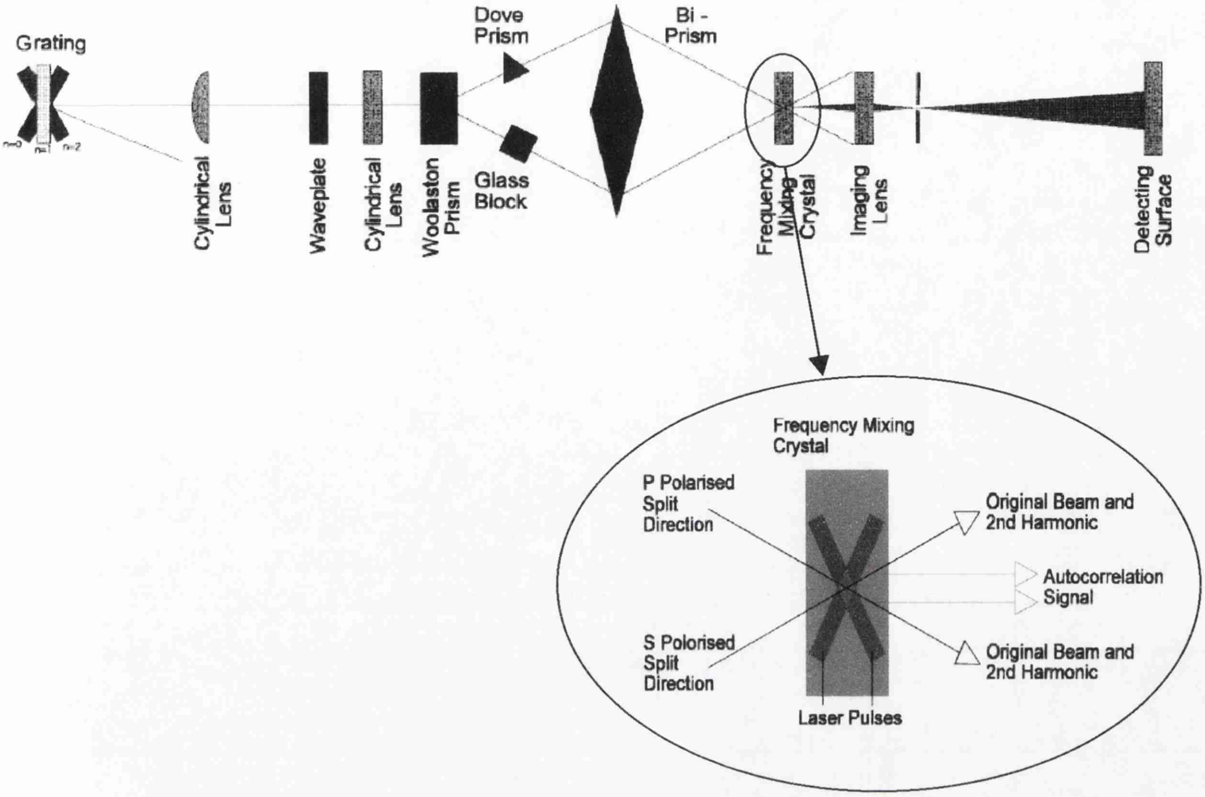

Figure 3.12 Design of the uniaxial autocorrelator used for pulse duration measurements on VULCAN. The magnified picture of the frequency mixing crystal shows how the autocorrelation signal is produced (Courtesy of Collier, J *et al,* 1999).

Figure 3.13 shows the autocorrelation signal intensity as a function of time. It can be seen that the FWHM of the pulse is ~ 700 fs. When combined with the maximum energy possible on target of 85 J, this gives a pulse power of ~120 TW.

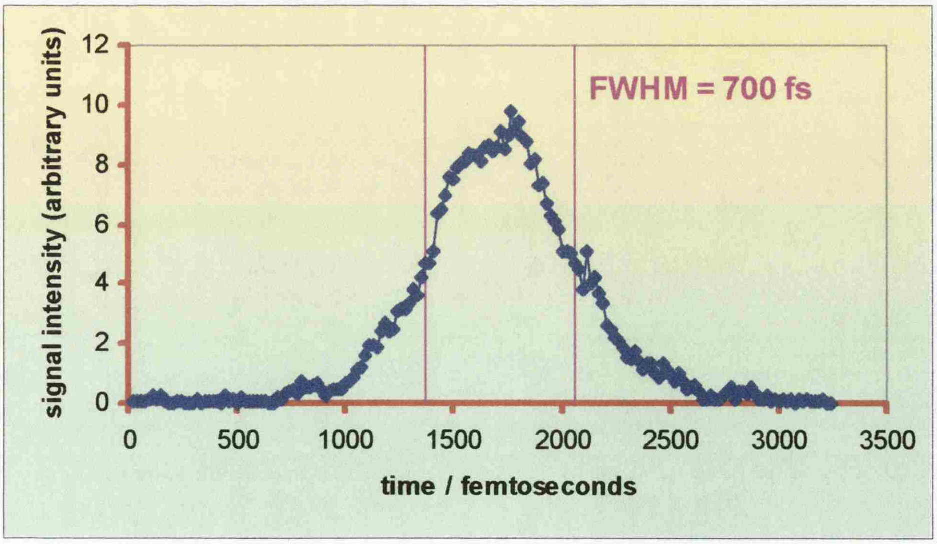

Figure 3.13 Autocorrelation measurement of the VULCAN CPA pulse.

3.3.3 Measurement of Focal Spot Size

The dimensions of the focal spot can be estimated using Equations (3.1) and (3.2), however these give the dimensions of the best focal spot obtainable theoretically. In operation, it is unlikely that the spot will be so ideal, since many factors can affect the focusability of the beam, such as the wave-front uniformity of the system (Danson et al. 1999a). Hence it is important to measure the focal spot dimensions and the intensity distribution of the spot i.e. the fraction of total intensity contained in the focal spot.

This is achieved using what is known as an equivalent plane monitor (EPM). The EPM uses part of the leakage beam, focused by a 9.6 m focal length lens producing a magnified image of the target plane. This image is captured via a CCD camera and a commercial frame grabber on a shot-to-shot basis.

The CCD image is calibrated by placing a transmission grating in the beam at normal incidence. The angular changes to the beam direction due to diffraction will be converted to a positional change on the equivalent plane by the lens (Poulter 2001). The theoretical separation of the spots can be calculated using well known diffraction equations (Jenkins & White 1981). This provides a calibration for the image of the spot captured by the CCD camera. The FWHM can be obtained using dedicated software.

Now that the focal spot dimensions in the equivalent plane are known, the dimensions of the parabola focus is calculated by scaling linearly between the 9.6 m focal length lens and the focal length of the parabola in use (Equation (3.1)) i.e. the ratio of the focal length of the lens to the focal length of the parabola. Figure 3.14 shows the intensity distribution of the VULCAN CPA pulse, with the x-axis calibrated to the F1.5 on-axis parabola. The FWHM of the focal spot is ~5 μm. Assuming that the focal spot is a square of 5×5 μm, where 25 % of the intensity lies in this region (Danson et al. 1999b) and the pulse power is 120 TW as stated previously, the intensity on target is $\sim 10^{20}$ $\mathrm{Wcm^{-2}}$.

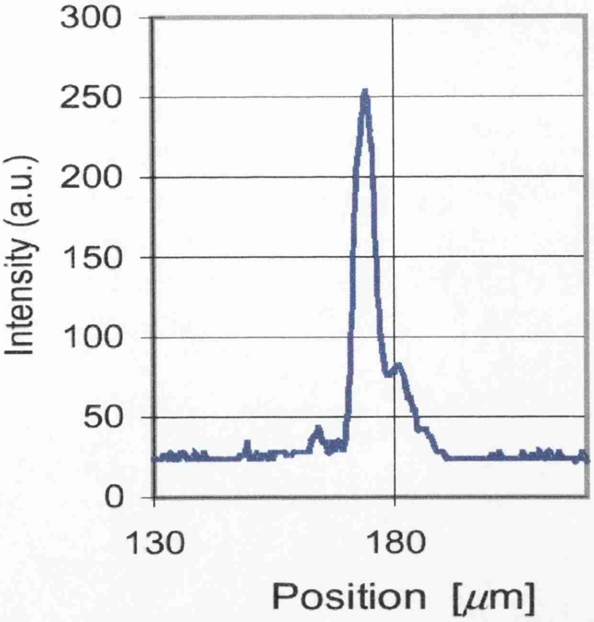

Figure 3.14 Equivalent plane intensity distribution of the VULCAN CPA beam, calibrated to the focal dimensions of the F1.5 on-axis parabola.

3.3.4 Measurement of Contrast Ratio in the Tsunami Oscillator

The SHG autocorrelation technique described in Section 3.3.2 is insufficient to measure pulse contrasts for several reasons. First, the scattered light from an SHG crystal limits the dynamic range to about 10^5. As a result, an acceptable contrast ratio (of~10^6) for high-power solid target experiments cannot be monitored using this technique. Secondly, second-order autocorrelations are symmetric. It is not possible to determine whether structures in the wings of an autocorrelation occur before or after the main pulse. Since it is the pre-pulse that affects the interaction physics more than the post-pulse, it is important to know if any background activity is occurring before the main pulse.

These disadvantages are overcome by using the 3rd order cross correlation technique (Luan, Hutchinson, Smith, & Zhou 1993). This technique (Figure 3.15) provides an autocorrelation between a pulse at its fundamental wavelength and the same pulse at its second harmonic wavelength (Collier et al. 1997).

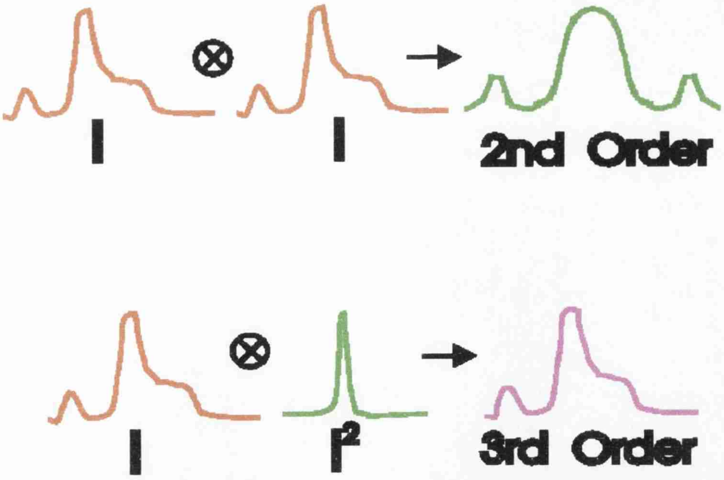

Figure 3.15 2nd and 3rd order cross correlation.

A main advantage of the 3rd order technique is that the incident pulse is initially frequency doubled. This nonliear process effectively “cleans up” the pulse with any low level activity being effectively removed as shown in Figure 3.15. Therefore the autocorrelation process becomes assymetrical and effectively provides a cross correlation of a pulse sequence with a single “clean” pulse. This enables one to determine whether any detected low level pulse activity occurs in front of or behind the main pulse in addition to providing a more accurate measurement of the pulse shape. A secondary advantage of this technique is that one detects the third harmonic light derived from the frequency mixing of the first and second harmonic input pulses. This is therefore a technique capable of high dynamic range operation and the detection systems can be set up to be sensitive to third harmonic light only.

A schematic of the device (Collier, Hitchcock, Danson, & Weingarten 1997) is shown in Figure 3.16. The incident beam from the Tsunami (Section 3.2) at 1053 nm is partially converted into a 526 nm beam with an approximate 20 % conversion efficiency. The frequency doubling is performed in a 1 mm length crystal of lithium triborate (LBO). The 1053 nm and 526 nm beams are then separated by a di-choric splitter and directed to a focusing lens via mirrors. The 526 nm beam is directed via a retro-reflector as shown to provide variability of arm length and thus the scanning range. The two beams are focused into a β-barium borate (BBO) frequency mixing crystal and phase matched by angle tuning. The 3rd harmonic mixed signal is detected by a photomultiplier tube.

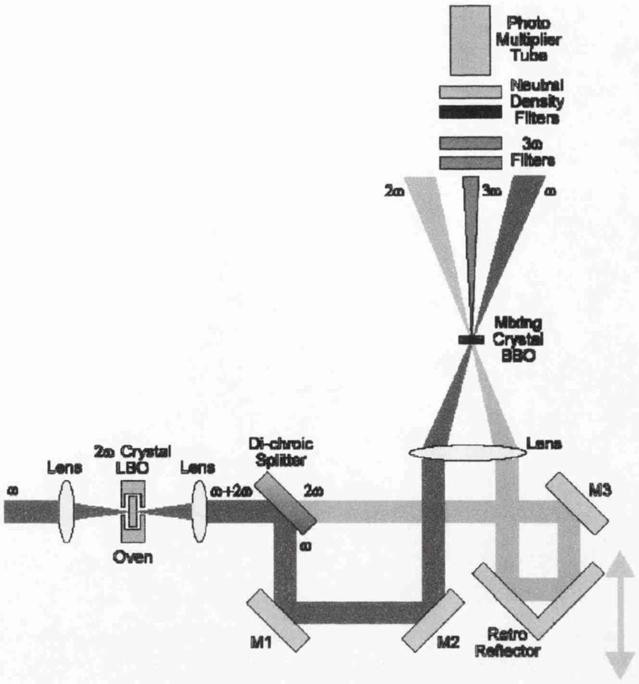

Figure 3.16 A third order cross correlator (courtesy of Collier, J *et al,* 1997).

Figure 3.17 shows the results for the Tsunami oscillator over a 40 ps and a 5 ps range respectively. The source of each one of the low-level pulses in Figure 3.17a has been identified as Frensel reflections generated within the instrument from the frequency doubling crystal, the mixing crystal and the splitter. The oscillator is therefore shown to be pre-pulse free over seven orders of magnitude. This is an order of magnitude better than the contrast of the amplifier system, which has been measured using the same technique to be 10^6 (Danson et al. 1993). The slight wings observed in Figure 3.17b, starting at ~10^{-4} level are consistent with previous observations (Braun et al. 1995) in KLM cavities indicating an incorrect amount of negative dispersion. From these measurements it can be said with confidence that the pulse contrast of VULCAN is 10^6, with this pre-pulse lasting for the duration that the optical gate is open i.e. a minimum of 300 ps. The 10^{-4} wings from the Tsunami may play a part in the interaction, after the 300 ps pedestal has arrived on target.

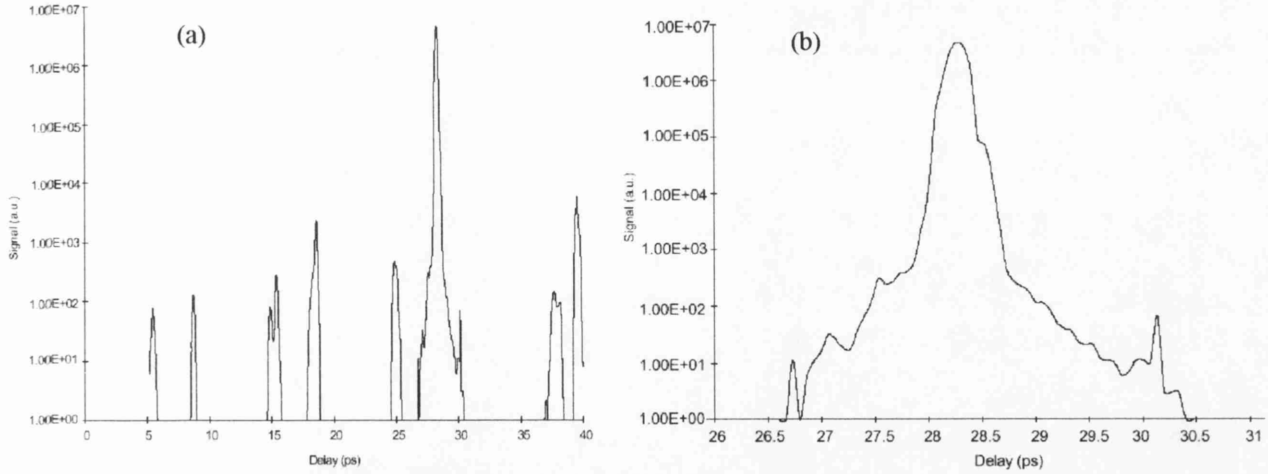

Figure 3.17 Third order cross-correlation of the Tsunami oscillator on (a) 40 ps and (b) 5 ps time scales.

References

Barty, C. P. J., Gordon, C. L., & Lemoff, B. E. 1994, "Multiterawatt 30-fs Ti-sapphire laser system", *Optics Letters*, vol. 19, p. 1442.

Barty, C. P. J., Guo, T., LeBlanc, C., Raksi, F., RosePetruck, C., Squier, C., Wilson, K. R., Yakovlev, V. V., & Yamakawa, K. 1996, "Generation of 18-fs, multiterawatt pulses by regenerative pulse shaping and chirped-pulse amplification", *Optics Letters*, vol. 21, p. 668.

Braun, A., Rudd, J. V., Cheng, H., Mourou, G., Kopf, D., Jung, I. D., Weingarten, K., & Keller, U. 1995, "Characterisation of short-pulse oscillators by means of a high-dynamic range autocorrelation measurement", *Optics Letters*, vol. 20, p. 1889.

Chambaret, J. P., LeBlanc, C., Cheriaux, G., Curley, P., Darpentigny, G., Rosseau, P., Hamoniaux, G., Antonetti, A., & Salin, F. 1996, "Generation of 25-TW, 32-fs pulses at 10 Hz", *Optics Letters*, vol. 21, p. 1921.

Clements, T. S., Taylor, A. J., & Kane, D. J. 1995, "Single shot measurement of the amplitude and phase of ultrashort laser-pulses in the violet", *Optics Letters*, vol. 20,no. 70.

Collier, J., Danson, C. N., Johnson, C., & Mistry, C. 1999, "Uniaxial single shot autocorrelator", *Review of Scientific Instruments*, vol. 70, p. 1599.

Collier, J., Hitchcock, D., Danson, C. N., & Weingarten, K. 1997, "Pulse contrast measurements of the VULCAN CPA front end oscillators", *Rutherford Appleton Laboratory Central Laser Facility Annual Report 1996/1997* p. 190.

Collier, J. 2001. Personal Communication.

Danson, C., Collier, J., Neely, D., Barzanti, L. J., Damerell, A., Edwards, C. B., Hutchinson, M. H. R., Key, M. H., Norreys, P. A., Pepler, D. A., Ross, I. N., Taday, P. F., Toner, W. T., Trentelman, M., Walsh, F. N., Winstone, T. B., & Wyatt, R. W. W. 1998, "Well characterized 10^{19} Wcm^{-2} operation of VULCAN - an ultra-high power Nd: glass laser", *Journal of Modern Optics*, vol. 45, p. 1653.

Danson, C. N., Allott, R. M., Booth, G., Collier, J., Edwards, C. B., Flintoff, P. S., Hawkes, S. J., Hutchinson, M. H. R., Hernandez-Gomez, C., Leach, J., Neely, D., Norreys, P. A., Notley, M., Pepler, D. A., Ross, I. N., Walczak, J. A., & Winstone, T. B. 1999a, "Generation of focused intensities of $5x10^{19}$ Wcm^{-2}", *Laser and Particle Beams*, vol. 17, p. 341.

Danson, C. N., Allott, R. M., Collier, J., Edwards, C. B., Neely, D., Norreys, P. A., Winstone, T. B., Child, N. S., Harris, W. P., & Mathers, J. H. 1999b, "An F1 on-axis parabola producing focal spots of less than 10 microns on VULCAN", *Rutherford Appleton Laboratory Central Laser Facility Annual Report 1998/1999* p. 183.

Danson, C. N., Barzanti, L. J., Chang, Z., Damerell, A., Edwards, C. B., Hancock, S., Hutchinson, M. H. R., Key, M. H., Luan, S., Mahadeo, R. R., Mercer, I. P., Norreys, P. A., Pepler, D. A., Rodkiss, D. A., Ross, I. N., Smith, R. A., Taday, P. F., Toner, W. T., Wigmore, K. W. M., Winstone, T. B., Wyatt, R. W. W., & Zhou, F. 1993, "High contrast multi-terawatt pulse generation using chirped pulse amplification on the VULCAN laser facility", *Optics Communications*, vol. 103, p. 392.

Davis, C. C. 1996, *Lasers and Electro-Optics, Fundamentals and Engineering* Cambridge University Press, Trumpington St, Cambridge CB2 1RP.

Fujimoto, J. G., Weiner, A. M., & Ippen, E. P. 1984, "Generation and measurement of pulses as short as 16 fs", *Applied Physics Letters*, vol. 44, p. 832.

Hutchinson, M. H. R. 1989, "Terawatt lasers", *Contemporary Physics*, vol. 30, p. 355.

Irion, R. "Supernova". *New Scientist* 18 April 1998, pp 30.

Jenkins, F. A. & White, H. E. 1981, "The Diffraction Grating," in *Fundamentals of Optics*, Fourth edn, McGraw-Hill, pp. 355-377.

Langley, A. J., Divall, E. J., Girard, N., Hooker, C. J., Hutchinson, M. H. R., Lecot, A., Marshall, A., Neely, D., & Taday, P. F. 1999a, "Development of a multi-terawatt, femtosecond laser facility - ASTRA", *Central Laser Facility, Rutherford Appleton Laboratory Annual Report 1998-99* p. 186.

Langley, A. J., Girard, N., Mohammed, I., Ross, I. N., & Taday, P. F. 1999b, "Astra Development Phase 1 - a femtosecond terawatt laser", *Central Laser Facility, Rutherford Appleton Laboratory Annual Report 1998-99* p. 187.

Luan, S., Hutchinson, M. H. R., Smith, R. A., & Zhou, F. 1993, "High dynamic range third-order correlation measurement of picosecond laser pulse shapes", *Measurement Science and Technology*, vol. 4, p. 1426.

Mourou, G. 1997, "The ultrahigh-peak-power laser: present and future", *Applied Physics B*, vol. 65, p. 205.

Perry, M. D. & Mourou, G. 1994, "Terawatt to Petawatt Subpicosecond Lasers", *Science*, vol. 264, p. 917.

Poulter, M. J. 2001 Personal Communication.

Ross, I. N., Trentelman, M., & Danson, C. N. 1997, "Optimization of a chirped-pulse amplification Nd: glass laser", *Applied Optics*, vol. 36, p. 9348.

Salin, F., Georges, P., Roger, G., & Brun, A. 1987, "Single-shot measurement of a 52-fs pulse", *Applied Optics*, vol. 26,no. 4528.

Santala, M. I. K., Zepf, M., Watts, I., Beg, F. N., Clark, E. L., Tatarakis, M., Krushelnick, K., Dangor, A. E., McCanny, T., Spencer, I., Singhal, R. P., Ledingham, K. W. D., Machacek, A., Wark, J. S., Allott, R. M., Clarke, R. J., & Norreys, P. A. 2000, "Effect of the plasma density scale length on the direction of fast electrons in relativistic laser-solid interactions", *Physical Review Letters*, vol. 84, p. 1459.

Singhal, R. P. 1995, "Nonlinear Optics," in *An Introduction to Laser Spectroscopy*, D. L. Andrews, ed., Plenum Press Spring Street, New York 10013.

Spence, D. E., Kean, P. N., & Sibbet, W. 1991, "60 fsec pulse generation from a self-mode-locked Ti:sapphire laser", *Optics Letters*, vol. 16, p. 42.

Strickland, D. & Morou, G. 1985, "Compression of Amplified Chirped Optical Pulses", *Optics Communications*, vol. 56, p. 219.

Svelto, O. 1989, *Principles of Lasers* Plenum Press, Spring St, New York.

Wilson, J. & Hawkes, J. F. B. 1987, "Q-Switching," in *Lasers: Principles and Applications*, 1 edn, Prentice Hall, pp. 108-114.

Yamakawa, K., Aoyama, M., Matsuoka, S., Takuma, H., Barty, C. P. J., & Fittinghoff, D. 1998, "Generation of 16-fs, 10-TW pulses at 10-Hz repetition rate with efficient Ti: sapphire amplifiers", *Optics Letters*, vol. 23, p. 525.

Yariv, A. 1997, *Optical Electronics in Modern Communications* Oxford University Press, Oxford, UK.

Zhou, J. P., Huang, C. P., Murnane, M. M., & Kapteyn, H. C. 1995, "Amplification of 26-fs, 2-TW pulses near the gain-narrowing linit in Ti: Sapphire", *Optics Letters*, vol. 20, p. 64.

Chapter 4

Background Nuclear Physics

This chapter provides the reader with the relevant nuclear physics necessary for the next three chapters. Full descriptions of the radiation detectors used in the experiments are also given.

4.1 Introduction

In Chapter 2, it was shown that energetic electron and proton beams can be generated from ultra-intense laser-solid interactions. Chapter 3 showed how these ultra-intense laser pulses are produced. Chapters 5, 6 and 8 provide evidence of these energetic particles inducing nuclear reactions and so first it is necessary to provide the reader with the necessary background in the various nuclear processes that can take place when energetic particles interact with nuclei. The physics of these processes are of course well established, but have never before been systematically applied to laser-matter interactions. A comprehensive guide to the concepts discussed in this chapter is given in “Introductory Nuclear Physics” (Krane 1988) at the appropriate level. It is assumed however that the reader has a basic knowledge of atomic and nuclear structure. Useful information can also be found in “Physics of the Atom” (Wehr, Richards Jr, & Adair III 1983), pp 225 and Chapters 10, 11 and 12.

Energetic electrons are inefficient in generating nuclear reactions. However, electrons can be converted into gamma-ray photons in high Z targets, via a process known as bremsstrahlung, discussed in Section 4.2. These energetic photons can then induce nuclear reactions. In this case, the reaction is termed photo-nuclear, and this is described in Section 4.3. Protons can directly participate in nuclear reactions, and the reaction physics is discussed in Section 4.4.

As will be shown later, depending on the target material, the product of a nuclear reaction can be unstable, and decays back to a stable isotope via the emission of radiation. The methods employed to detect various forms of radiation, i.e. positrons and gamma-rays in the present study are discussed in Section 4.5.

4.1.1 Overview of Nuclear Reactions

In a nucleus, protons and neutrons (known as nucleons) are bound in shells similar to the electrons in Bohr’s picture of the atom. The study of nuclear structure and the forces between nucleons is still today a huge area of research.

Nuclides can either be found naturally or can be man-made in reactors or accelerators. In addition, these nuclides can either be stable or radioactive. Radioactive nuclei decay to stable nuclei by emitting radiation; α, β^-, β^+ or γ decay (Krane 1988, Chapters 6-10). A complete listing of all known nuclides both stable and radioactive can be found in "Table of Isotopes",(Firestone, Shirley, & Chu 1998). It is instructive to plot all known nuclides on a chart with their neutron number as a function of proton number. This is known as a Segre Chart, named after its inventor and is shown in Figure 4.1. Stable isotopes are shown in black, and it can be seen that a line of stability exists. It can be seen that for light stable nuclei, the number of protons and neutrons are equal, however as the mass increases, many more neutrons must be added to reduce the unstable effect of many repulsive protons. Above the line of stability lies a sea of isotopes which are neutron rich (shown in blue). These isotopes have the ability to transform themselves back to stability by emitting β^- radiation in which a neutron decays to a proton plus an electron (with an accompanying antineutrino). Below the line of stability there is a sea of proton rich isotopes (shown in red) which achieve stability via β^+ emission where a proton transforms into a neutron plus a positron (plus a neutrino). An alternative process involves a proton capturing one of its orbiting electrons to form a neutron (plus a neutrino) (electron capture). In heavier unstable nuclei, stability can be achieved via α-decay where the heavy nucleus emits an α-particle, which is now known to be a ^{4}He nucleus. The four processes are summarised below:

$$\alpha \text{ decay: } {}^{A}_{Z}X \longrightarrow {}^{A-4}_{Z-2}X' + {}^{4}_{2}He$$

$$\beta^- \text{ decay: } (n) \rightarrow (p) + e^- + \overline{\nu}$$

$$\beta^+ \text{ decay: } (p) \rightarrow (n) + e^+ + \nu$$

$$\text{electron capture: } (p) + e^- \rightarrow (n) + \nu.$$

( ) denotes that
the particle is
bound in the
nucleus

The other type of radioactive decay is of course γ-emission, analagous to the emission of atomic radiations such as optical or X-ray transitions. An excited nuclear state decays to a lower excited state or possibly the ground state by the emission of a photon of energy equal to the difference in energy between the nuclear states. Gamma emission usually follows α and β decays since these decays will often lead to excited states in the product (or daughter) nucleus.

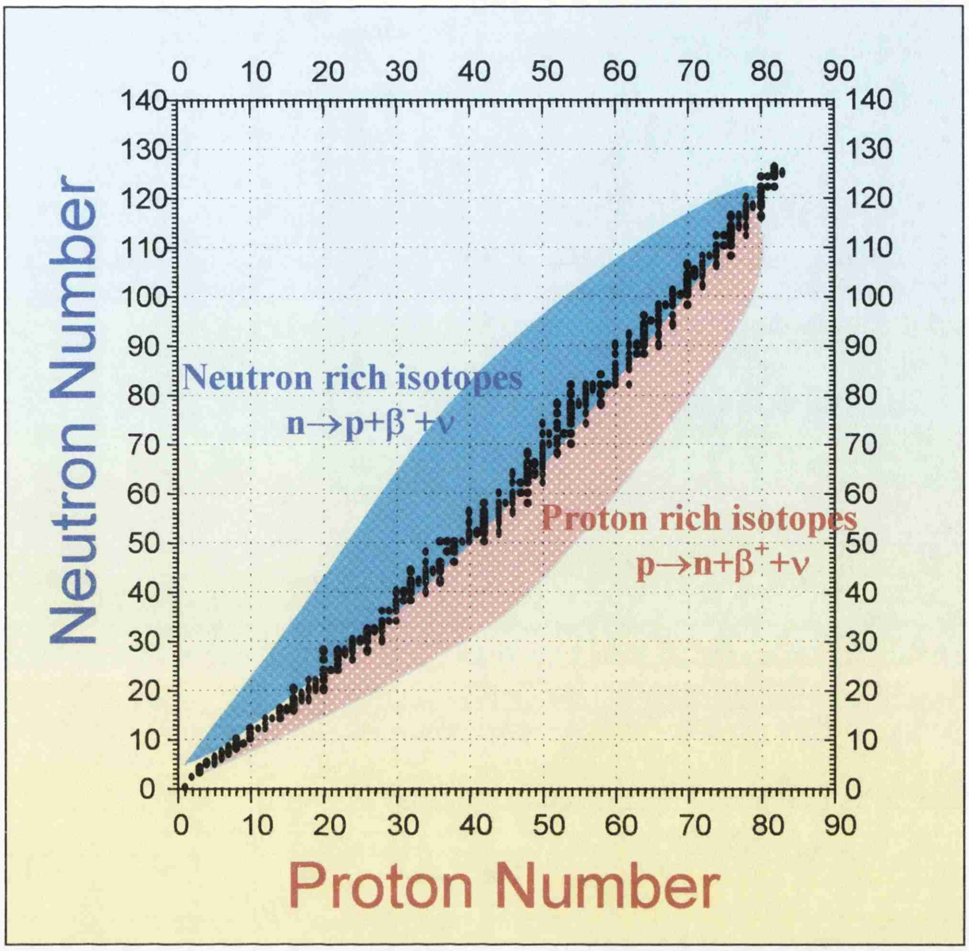

Figure 4.1 Segre plot of the nuclides. Stable isotopes are shown in black, neutron rich radioactive isotopes in blue, and proton rich radioisotopes in red.

The number of radioactive nuclei in any sample of radioactive material decreases continuously as some of the nuclei disintegrate via the above processes. The rate at which the number decreases varies widely for different nuclei, and is unique for a given radioisotope. For N radioactive nuclei present in a sample at time t, the rate of decay is given by

$$\frac{dN}{dt} = -\lambda N \qquad \text{Eqn (4.1).}$$

Where λ is a constant known as the *decay constant*. If the number of nuclei at time t=0 is denoted by N_0, the solution of this equation is

$$N = N_0 e^{-\lambda t} \qquad \text{Eqn (4.2).}$$

The *half-life* of a radioactive sample is defined as the time at which the number of radioactive nuclei has decreased to one half the number at t=0. Each unstable nuclide has its own characteristic half-life $t_{1/2}$, and it can be easily shown that

$$t_{1/2} = \frac{\ln(2)}{\lambda} \qquad \text{Eqn (4.3).}$$

If energetic particles from a reactor or an accelerator (in the present case the accelerator is of the novel laser-plasma variety discussed in Chapter 2) or even from a radioactive source are allowed to fall upon bulk matter, there is the possibility of a nuclear reaction taking place. The first such nuclear reactions were performed by Ernest Rutherford (Krane 1988 pp 378) in the early 1900s, using α particles from a radioactive source. In some of these early and now famous experiments, the α particles merely rebounded elastically from the target nuclei; this phenomenon, known ever since as Rutherford Scattering, gave us the first evidence for the existence of atomic nuclei. This picture, where atomic electrons orbit a dense nucleus consisting of protons and neutrons is of course now universally accepted. Rutherford also showed from these experiments that the α particle is in fact a doubly ionised helium atom.

In other experiments, Rutherford was able to observe a change or transmutation of nuclear species, as in this reaction carried out in 1919:

$$\alpha + {}^{14}\mathrm{N} \rightarrow {}^{17}\mathrm{O} + \mathrm{p}.$$

The nuclear reaction was observed by detecting the emitted proton in a cloud chamber. The product therefore must be ^{17}O by balancing the nuclear equation.

The general form of the above nuclear reaction is

$$\mathrm{a} + \mathrm{X} \rightarrow \mathrm{Y} + \mathrm{b}$$

where a is the accelerated projectile, X is the target (usually stationary in the laboratory) and Y and b are the reaction products. An alternative and compact way of indicating the same reaction is

$$X(a,b)Y.$$

This form is convenient because it provides a classification for a general type of reaction with common properties; in this study (γ,n) and (p,n) reactions are discussed in detail.

Depending on the target material, the product of a nuclear reaction (Y) can be stable or unstable. In the latter case, it will decay back to stability with a characteristic half-life via the processes described earlier.

4.1.2 Energetics of Nuclear Reactions

Conservation of total relativistic energy in our basic reaction gives

$$m_Xc^2 + T_X + m_ac^2 + T_a = M_Yc^2 + T_Y + m_bc^2 + T_b \qquad \text{Eqn (4.4)}$$

where the T denotes kinetic energy and m denotes rest mass. The *reaction Q-value* is defined as the initial mass energy minus the final mass energy:

$$\begin{aligned} Q &= (m_{\text{initial}} - m_{\text{final}})c^2 \\ &= (m_X + m_a - m_Y - m_b)c^2, \qquad \text{Eqn (4.5)} \end{aligned}$$

which is the same as the excess kinetic energy of the final products

$$\begin{aligned} Q &= T_{\text{final}} - T_{\text{initial}} \\ &= T_Y + T_b - T_X - T_a \qquad \text{Eqn (4.6)} \end{aligned}$$

The Q value may be positive, negative, or zero. If $Q>0$, the reaction is said to be *exothermic;* the nuclear mass or binding energy is released as kinetic energy of the final products. When Q<0, the reaction is *endothermic;* initial kinetic energy is converted into nuclear mass or binding energy. The changes in mass and energy must of course be related by the familiar expression from special relativity, $\Delta E = \Delta mc^2$, i.e. any change in the kinetic energy of the system of reacting particles must be balanced by an equal change in its rest energy.

4.1.3 Reaction Cross Sections

The cross section is a measure of the relative probability for a reaction to occur. Figure 4.2 shows the experimental set-up for measuring a differential cross section. If we have a detector placed to record particle b emitted in a direction (θ,ϕ) with respect to the beam direction, the detector defines a small solid angle dΩ at the target nucleus. To obtain the total cross section, one must integrate over all angles; i.e. rotate the position of the detector to measure the flux of outgoing particles over 4π stradians. In fact, there are a few facilities in the world today which have detectors that can measure over 4π stradians, the KLAS detector at the Jefferson Laboratory, USA to name one. Let the current of particles be I_a particles per unit time, and let the target show to the beam N target nuclei per unit area. If the outgoing particles appear at a rate R_b, then the total reaction cross section, σ is:

$$\sigma = \frac{R_b}{I_a N} \qquad \text{Eqn (4.10).}$$

Defined in this way, σ has the dimension of area per nucleus, but it may be very much larger or smaller than the geometrical area of the disc of the target nucleus seen by the incoming beam. For a typical nucleus of radius R = 6 fm ($R=1.1A^{1/3}$), the geometrical area πR^2 is about 100 fm^2 = 1 barn (b). For neutron capture by ^{135}Xe, the cross section is about 10^6 b, while for other more improbable reactions such as (γ,mn), (p,n) and (p,α) reactions discussed in this study, the cross section is measured in millibarns or even microbarns. The reaction cross section should be thought of as a quantity which has the dimension of area, but which is proportional to the reaction probability.

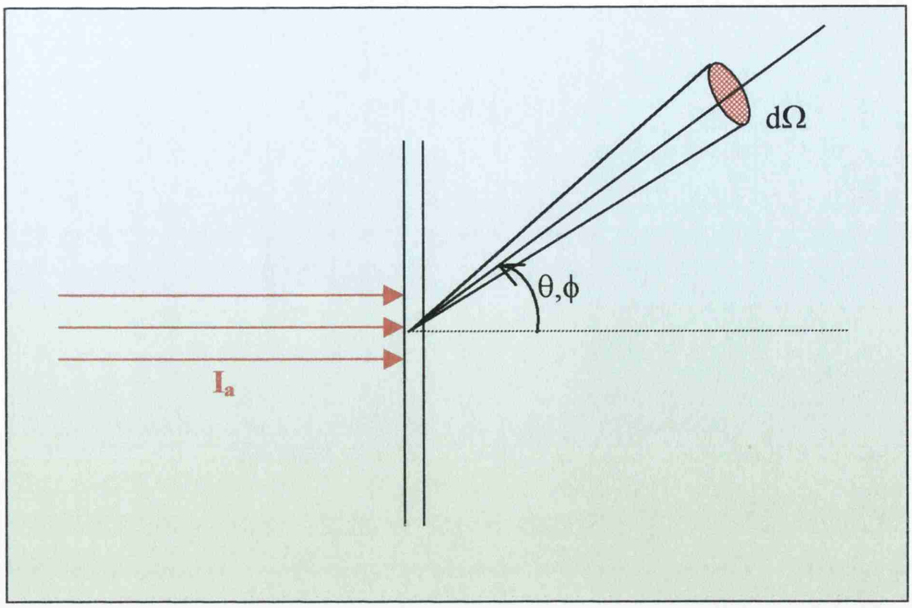

Figure 4.2 Differential reaction cross section geometry showing incoming beam I_a, target and products going into solid angle dΩ at θ,φ. To obtain the total cross section, one must integrate over Ω from 0 to 4π stradians.

Cross sections are measured experimentally, and the results of these measurements are stored in a database maintained by the International Atomic Energy Authority (IAEA). This database, called EXFOR, can be accessed via the internet (IAEA) and hence one can asses the probabilities of reactions of interest occurring and then make a judgement on choice of target and which reactions to carry out based on this information, as performed in this study.

4.2 Bremsstrahlung Generation

In Chapter 5, it is shown that high-energy gamma rays are used to generate photo-nuclear reactions in target nuclei, producing radioisotopes. However, as shown in Chapter 2, the laser-solid interaction generates fast (relativistic) electrons as well as energetic ions, so the intermediate process is the conversion of relativistic electrons into energetic gamma-rays. This process is known as bremsstrahlung, a German word meaning "braking radiation".

The term is quite literal since when electrons are incident on matter, they interact through Coulomb scattering from atomic electrons and ions and are decelerated. Some of the energy lost is converted into electromagnetic radiation (bremsstrahlung X or γ-rays) and the rest is given to the background electrons in the form of heat energy. Bremsstrahlung is emitted in a cone with a continuous spectrum of energies up to the initial kinetic energy of the electron decelerating in the target.

The energy loss to bremsstrahlung when electrons are incident on a target was calculated by Bethe, and can be found in (Krane 1988 pp 196). The expression has a Z^2 dependence, and hence high-Z targets are more efficient in generating bremsstrahlung. In the present study, tantalum (Z=73) was chosen as the bremsstrahlung converter.

Bremsstrahlung spectra can be calculated using Monte Carlo simulations, which are complicated and require considerable computing power. However, D J S Findlay (Findlay 1989) working in the Harwell Laboratory, UK at the time, developed a useful and relatively simple analytical expression for evaluating bremsstrahlung yield as a function of energy and angle to complement the Monte Carlo codes. This expression works well and yields results close to that of the Monte Carlo simulations for the energy range ~5-30 MeV which as will be shown later is the energy range of electrons produced in the experiments.

Bremsstrahlung spectra produced from the equation derived by Findlay are shown in Figure 4.3. for a tantalum target of thickness 1.75 mm (the target used in the experiments) for electrons of energies 10, 15 and 20 MeV for angles along the incident electron direction and at 15° and 30° to the incident electron direction. These results can be used as part of a broader study to measure the temperature of the fast electrons produced in the laser-plasma interaction, as will be shown in Chapter 5, Section 5.4.

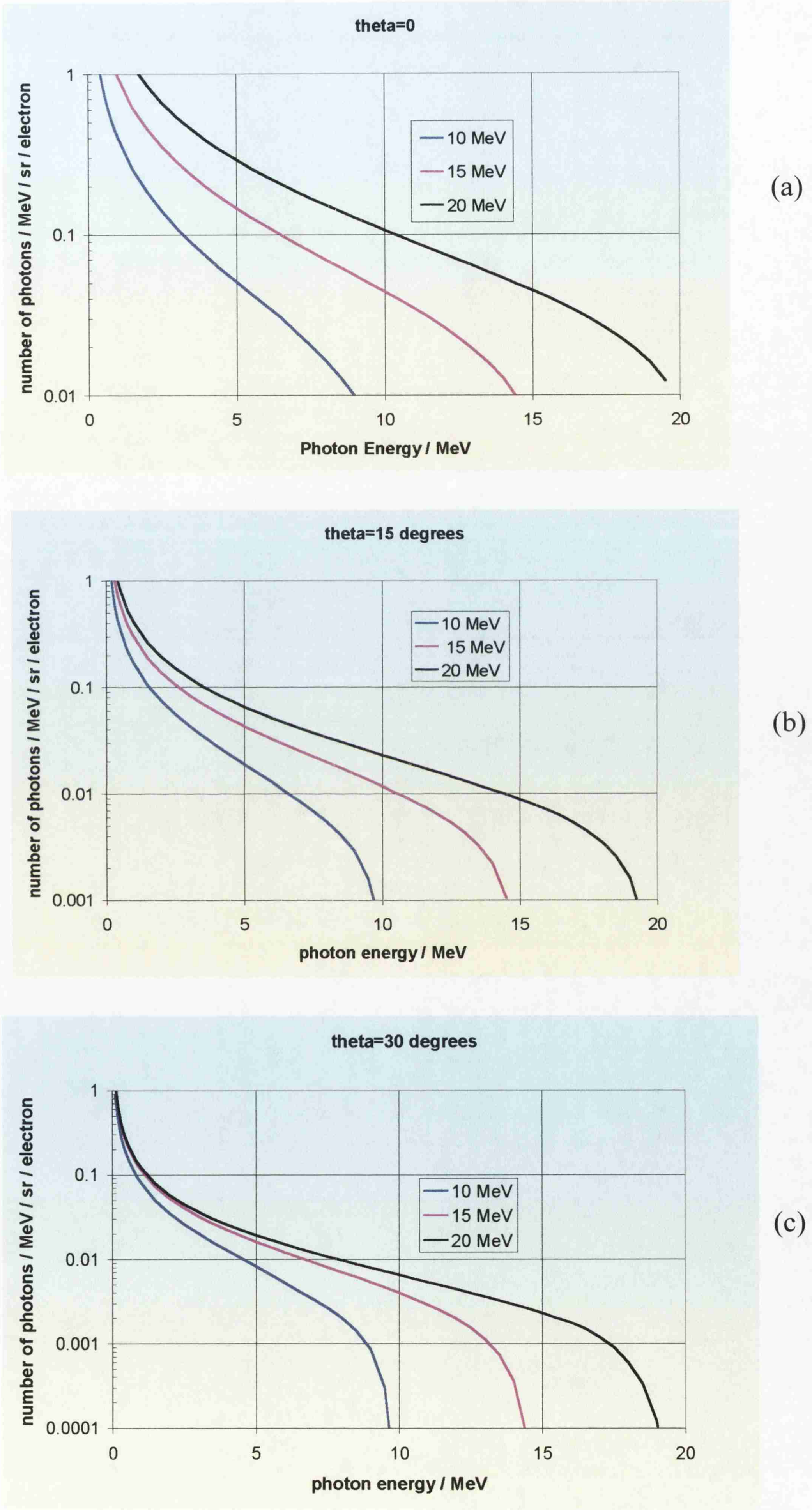

Figure 4.3 Bremsstrahlung spectra for electrons of energy 10, 15 and 20 MeV at angles (a) along electron direction, (b) at 15° and (c) at 30° to electron direction.

4.3 Photo-Nuclear Reactions

The most weakly bound neutron in a typical medium mass nucleus is around 10 MeV. If a nucleon absorbs energy from a beam of incident γ-rays of energy >10 MeV, it can escape from the nucleus. Neutrons can escape much more readily from a nucleus than protons since protons in addition must burrow through a positive Coulomb barrier before being liberated as illustrated in Figure 4.4 for a copper nucleus. Thus, photon-induced nuclear reactions generate large numbers of neutrons. These reactions are called (γ,n) processes and can take place when the incident γ-ray energy exceeds the (γ,n) reaction threshold energy for that target.

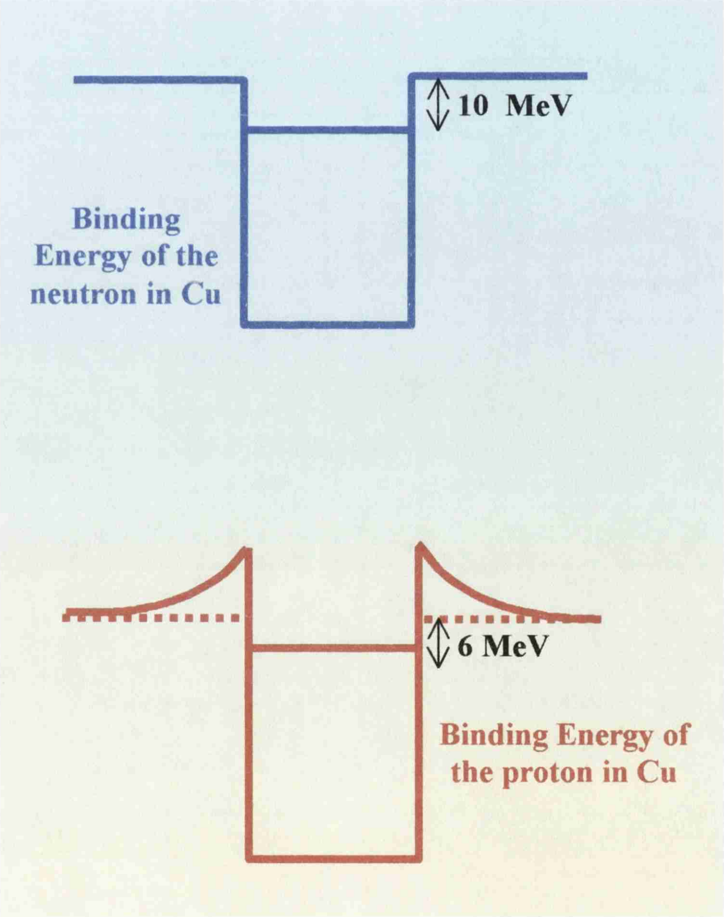

Figure 4.4 Binding energy of the neutron and proton in a ^{63}Cu nucleus. In order to escape from the nucleus, the proton has to overcome an additional Coulomb barrier due to its charge, unlike the neutron.

Let us take for example the reaction ^{63}Cu(γ,n)^{62}Cu, which is one of the reactions studied in Chapter 5. The rest masses of ^{63}Cu, ^{62}Cu and the neutron are well known, and the γ-ray mass can be assumed to be negligible since it is an electromagnetic wave. The Q-value for this reaction is thus calculated as -9.8 MeV using Equation (4.5). This means that if the ^{63}Cu nucleus absorbs a photon of energy exceeding this value, a neutron can be liberated from the nucleus.

The product nucleus, ^{62}Cu is proton rich and decays predominately via β^+ decay to either the ground state or excited states of ^{62}Ni with a half-life of 9.8 minutes. The ground state of ^{62}Ni is then achieved via the emission of γ-rays, with the longest lifetime of these excited states being 1.7 picoseconds. Figure 4.5 shows the nuclear decay scheme for ^{62}Cu and the relevant excited states of ^{62}Ni. The energies quoted are in MeV.

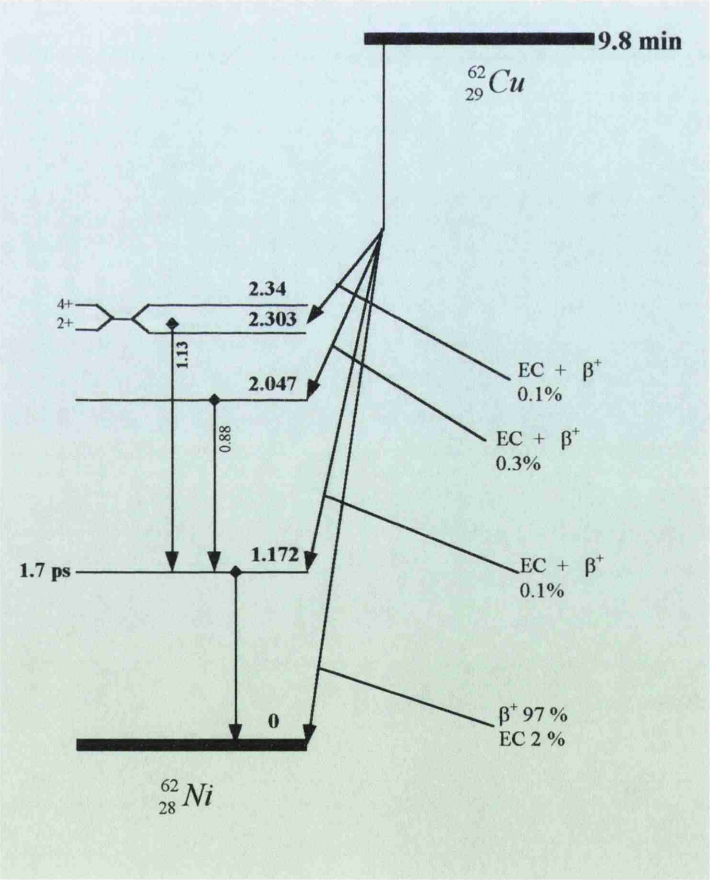

Figure 4.5 Decay scheme for ^{62}Cu.

The evidence of such a reaction taking place can therefore be obtained by either detecting the neutron emitted from the target nucleus, or by detecting the positrons emitted from the product. The techniques employed for detecting positron emission are described in Section 4.5. In other cases, especially in heavier nuclei, the nucleus decays via electron capture, resulting in the emission of the characteristic X-rays of the element of (Z-1). These X-rays can be detected using a germanium detector, the operation of which is described in Section 4.5.

If the energy of the incident photon is great enough, then more than one neutron can escape from the nucleus. These are known as higher order photo-nuclear reactions and can be written as (γ,mn) where $m=2,3,4,\ldots$ The Q-values for these reactions can again be calculated using the rest masses for the target and products. Higher order reactions obviously yield greater fluxes of neutrons for increasing m. For this study in particular, higher order reactions in tantalum were found to have useful applications in measuring the temperature of the fast electrons produced in the laser-tantalum interaction, as will be shown in Chapter 8.

4.3.1 Photo-Nuclear Fission

It is well known that nuclear fission occurs when a heavy nucleus such as uranium (Z=92) is bombarded with neutrons. This process results in the release of nuclear energy and is the basis of nuclear reactors which generate electricity.

The word "fission" is taken from biology, where it describes the division of a cell. When a uranium nucleus is fissioned, it splits into two fragments, one light and one heavy, along with the emission of neutrons. This is demonstrated in Figure 4.6. The nuclear energy is generally released as kinetic energy in the fission fragments. The neutrons released can then be made to induce further fission reactions, known as a "chain reaction" resulting in the release of huge amounts of energy. Nuclear reactors employ the use of controlled chain reactions, where ^{235}U is the fuel and using typically cadmium or boron which are efficient in absorbing neutrons and thus control the rate of or stop the chain reaction. Since thermal neutrons are most efficient in generating fission in ^{235}U, "moderators" (typically rods of carbon) are employed to slow down the fast neutrons emitted from previous fissions to thermal energies, thus generating further fission events.

Fission results primarily from the competition between the nuclear and Coulomb forces in heavy nuclei. The total nuclear binding energy increases roughly in proportion to A, while the Coulomb repulsion energy of the protons increases faster, approximately as Z^2. The nuclear forces of a uranium nucleus only just holds it together and so the absorption of a neutron is sufficient to cause it to split. In fact, any nucleus will fission if enough excitation energy is provided, although as a practical matter the process is only important for heavy nuclei (thorium and beyond).

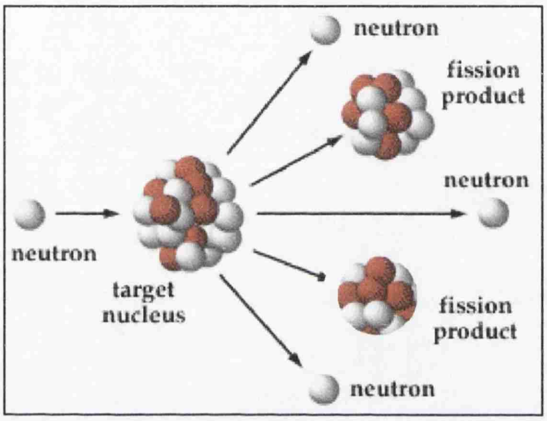

Figure 4.6 Neutron-induced nuclear fission.

In commercial reactors, thermal neutrons are the preferred probe, with enriched uranium (uranium samples which contain more ^{235}U than naturally occurring uranium) as the fuel. However, γ-rays of energy > 4 MeV can also provide sufficient excitation energy to induce fission in uranium. Thus it is feasible that an ultra-intense laser pulse, generating energetic electrons which are then converted to energetic γ-rays via a high Z bremsstrahlung radiator, can induce the fission of uranium.

Every fission reaction results in two fragments. The fission products are not determined uniquely – there is a distribution of masses of the two fission products. The distribution must be symmetric about the centre – for every heavy fragment, there must be a corresponding light fragment, however the probability that the fission event will result in two equal or nearly equal fragments is extremely low. This probability increases with the energy of the projectile.

The fission yield from ^{235}U of nuclides of different mass numbers (Dilorio 1979) is shown in Figure 4.7. The fission yield curve for ^{238}U, the isotope in question in Chapter

5, does not differ significantly from that of ^{235}U. It can be seen that the most abundant isotopes obtained from fission events occur at mass numbers around 95 and 140, corresponding to the neutron "magic numbers" 50 and 82.

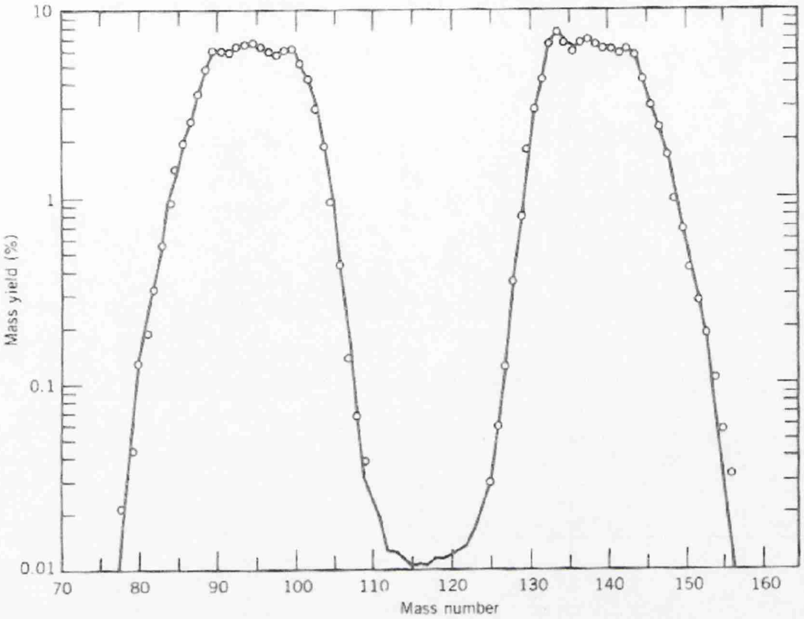

Figure 4.7 Mass distribution of fission fragments from thermal neutron fission of ^{235}U (Dilorio 1979).

The principal (most abundant) fission fragments amount to about 5-6 % of the total fission mass yield. Fission fragments are usually radioactive and constitute the radioactive waste from reactors – one of the present unsolved problems associated with the nuclear energy industry. Evidence for fission events can be carried out by detecting the characteristic γ-rays from the principal fission products, which was the technique used in this study. The detection of γ-rays using an intrinsic germanium detector is described in Section 4.5, and the results in Chapter 5, Section 5.5. Other techniques for providing evidence of fission events include the detection of fission neutrons and detection of fission tracks. The former can lead to ambiguities since there can be many sources of neutrons, in this case for example from (γ,mn) reactions in the bremsstrahlung radiator. The latter can prove complicated also, since the range of the fission fragments is so short that most of the fragments are stopped in the uranium sample and hence only fission events that occurred close to the surface of the uranium sample could be detected. This is why the measurement of the characteristic γ-rays of the fission products was the chosen technique in this case.

A useful reference for finding the most abundant fission fragments for the photofission of different nuclei is "High Resolution γ spectra of 40-44 MeV photon activation products" (Williams 1978). This is a list of spectra of different elements which have been bombarded with photons in the energy regime 40-44 MeV – extremely relevant in the present study. It shows that for ^{238}U, the principal fission fragments include ^{134}I, ^{138}Cs, ^{92}Sr. This will be discussed further in Chapter 5, Section 5.5.

4.4 Proton-Induced Nuclear Reactions

In Chapter 2, it was shown theoretically that energetic protons are produced in ultra-intense laser-solid interactions. In this case, the target is usually a thin, low-Z target, typically CH to maximise the H^+ ions (protons), as opposed to the thick, high-Z bremsstrahlung radiators described in the previous sections. Chapter 6 provides evidence of these proton beams, and also observations of proton-induced nuclear reactions, so firstly it is necessary to review the interaction of protons with nuclei.

Depending on the energy of the incident proton, it can interact with a nucleus in different ways. Put simply, the proton simply collides with nucleons in the nucleus, imparting energy to the nucleus in the form of photons via the Coulomb interaction (Krane 1988, pp 396-405).

The reactions studied in Chapter 6 are (p,n) and (p,α) reactions. These reactions can be brought about by one of two mechanisms, known as *compound nuclear reactions and direct nuclear reactions.* The dominance of either reaction is defined by the energy of the incident proton, as described below.

4.4.1 Compound Nucleus Reactions

The first of these is known as a *compound-nucleus reaction* (Krane 1988, pp 416-418) and can occur for incident proton energies in the 1 MeV-15 MeV regime provided the incident energy exceeds the reaction threshold energy. This is because a 1 MeV proton has a de Broglie wavelength of ~28 fm, much greater than the radius of a nucleon (~1 fm), and hence does not "see" individual nucleons, but rather the nucleus as a whole.

(The de Broglie wavelength is based on the wave-particle duality concept: a particle moving with momentum p can be thought of as a wave "packet" of wavelength $\lambda=h/p$ where h is Planck's constant). In this model, a proton enters a nucleus with a high probability of interacting with one of the nucleons in the target, possibly through a simple scattering. The recoiling struck nucleon and the incident proton (now with less energy) can each make successive collisions with other nucleons, and after several such interactions, the incident energy is shared among many of the nucleons of the combined system of projectile + target. The average increase in energy of any single nucleon is not enough to free it from the nucleus, but as many (essentially) random collisions occur, there is a statistical distribution in energies and a small probability for a single nucleon to gain a large enough share of the energy to escape.

Such reactions have a definite intermediate state, after the absorption of the proton but before the emission of the outgoing particle or particles (again the emission of a neutron is the most energetically feasible). The reaction can thus be written as

$$p + X \rightarrow C^{*} \rightarrow Y + b$$

where C^{*} indicates the compound nucleus in an excited state.

The reaction can therefore be thought of as a two-step process: the formation and then the subsequent decay of the compound nucleus.

A given compound nucleus may decay in many different ways. The decay products formed are defined by the total energy given to the system, i.e. the energy of the incident proton. That is, the more energy given to the compound nucleus, the more particles are likely to escape from the nucleus.

The compound nucleus model works well for low incident energies (up to 20 MeV), where the incident proton has a small chance of escaping from the nucleus with its identity and most of its energy intact. It also works best for medium weight and heavy nuclei, where the nuclear interior is large enough to absorb the incident energy.

4.4.2 Direct Nuclear Reactions

A 20 MeV incident nucleon has a de Broglie wavelength of a few fm, and therefore can "see" single nucleons and hence can interact with one or possibly very few valence nucleons near the surface of the nucleus, directly (Krane 1988, pp 419). If it exchanges its energy directly with a nucleon in the target nucleus, then that nucleon can gain sufficient energy to escape from the nucleus. At the same time, the projectile can lose sufficient energy to be stopped in the target nucleus. A 20 MeV or above proton interacting with a neutron on the surface of a target nucleus would generate a (p,n) reaction. Of course, as discussed previously, (p,n) reactions can also be generated via the production and subsequent decay of a compound nucleus.

Hence it may be possible to have direct and compound nucleus processes contribute to a given reaction. The processes can be distinguished by (1) the reaction time; direct processes occur on the order of 10^{-22} s, compound nucleus reactions slower at 10^{-16}-10^{-18} s, and (2) the angular distributions of the outgoing particles in direct reactions tend to be more sharply peaked that for compound nucleus reactions. To measure these quantities takes careful and dedicated nuclear physics experiments, and since the object of this study was not to confirm which nuclear process was contributing, rather it was to show that nuclear reactions can be performed using a laser and to show which nuclear reactions were induced and also to produce radioisotopes, the dominance of either process is of little relevance in the results, although knowledge of the processes provides a useful theoretical overview.

4.5 Radiation Detectors

It has been shown in the previous sections that evidence of nuclear reactions occurring can be obtained by detecting the radiation emitted by the product nuclei; in this study, specifically β^+ and γ-radiation. This section therefore deals with the devices and techniques used for the detection of such radiation. An excellent review of all the topics discussed in this section can be found in "Techniques for Nuclear and Particle Physics Experiments", (Leo 1994).

4.5.1 Sodium Iodide Scintillation Detectors

Scintillation detectors are one of the most often and widely used particle detection devices in nuclear and particle physics experiments today. This is partly due to the cost of these devices, and partly due to their versatility. One of the most common types of scintillator is made from a crystal of sodium iodide (NaI), doped with thallium (Tl).

When ionising radiation is incident on this material, the energy is absorbed and re-emitted after ~230 ns as photons in the visible region. The spectrum of photons emitted is centred around 400 nm (blue) with a FWHM bandwidth of $\Delta\nu$~100 nm (Leo 1994, pp 165). In fact, when a radioactive source is placed close to a NaI(Tl) crystal, the crystal can be seen to glow, or "scintillate". The number of scintillation photons generated is directly proportional to the energy absorbed in the detector. That is, the amount of light emitted from the scintillator is a direct measurement of the energy of the incident radiation.

The basic elements of a scintillation detector are shown in Figure 4.8. The NaI(Tl) crystal is optically coupled to a photomultiplier tube The scintillation crystal must of course be sealed in a light-tight container. Scintillation photons generated in the crystal strike a photocathode at the entrance to the photomultipler tube where they eject electrons via the photoelectric effect. These electrons are accelerated in a high potential towards a series of dynodes. At each dynode, the incident electrons release more electrons (about 3 to 5 each) and so the electron flux multiplies. After 8 to 12 dynodes (depending on the photomultiplier type) the avalanche of electrons is detectable as a small electrical pulse. The height of this pulse is directly proportional to the number of scintillation photons striking the photocathode and hence the energy of the incident radiation. The photomultipliers used had a shielding of mu-metal which reduces detrimental effects caused by any nearby magnetic fields. More information on photomultipliers can be found in (Leo 1994, Chapter 8, pp 176-198).

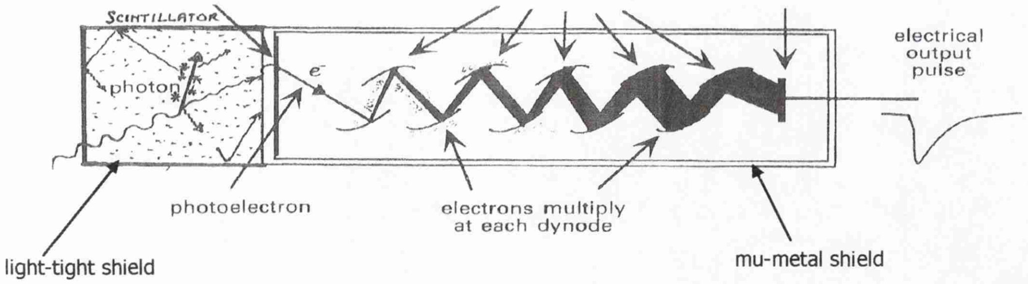

Figure 4.8 Basic components of a scintillation detector.

The pulse obtained from the photomultiplier is then inverted and amplified electronically. A typical output pulse from a scintillator is shown in Figure 4.9. Information on the energy and intensity of the incident radiation can then be obtained by analysing these pulse heights electronically. Specifically, the use of scintillators for positron detection is described below.

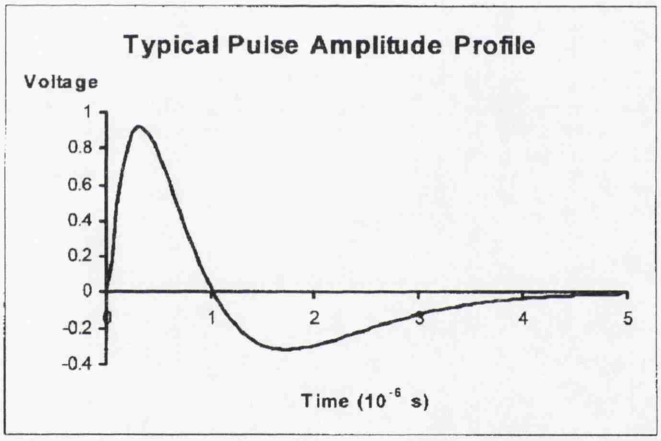

Figure 4.9 Typical output pulse from a NaI(Tl) detector.

4.5.2 *Detection of β^+ Radiation using Scintillation Detectors*

Positrons slow down in materials via collisions with atomic electrons and ions and at rest annihilate with electrons to produce two γ-ray photons of energy 511 keV via conservation of energy since the rest mass energy of the electron and the positron is 511 keV:

$$e^-_{\text{rest}} + \beta^+_{\text{rest}} \rightarrow \gamma_{511\text{keV}} + \gamma_{511\text{keV}}.$$

These photons are generated at 180° to each other to conserve angular momentum. These annihilation γ-rays can be detected unambiguously using NaI(Tl) scintillators. This technique is known as *coincidence counting* and the set-up of the positron detection system used in the experiments is described below.

The coincidence system is shown in Figure 4.10. The unit employed two 3"x3" NaI(Tl) detectors, manufactured by Canberra Industries (http://www.canberra.com). The photomultiplier tubes of the detectors must be powered by a HV supply, which usually operates in the 800 V – 1 kV regime, depending on the photomultiplier. In order to detect the annihilation photons, the detectors had to be set-up for this purpose. This is done for each detector on its own, one after the other. This was done using a calibrated ^{22}Na source, a commercially available β^+ emitter. ^{22}Na as well as emitting positrons, which in turn produce annihilation photons, also emits γ-rays of energy 1275 keV. When the output of the amplifier is fed into a cathode-ray oscilloscope (not a digital scope), the annihilation signal appears as a very bright pulse, since this is the event which happens most in the decay of ^{22}Na. Using the controls on the amplifier, it is possible to set the height of the annihilation pulse to the desired level. The photomultiplier saturates above 10 V, the pulse height must be kept under this level. The annihilation pulse height was set to 3 V.

Figure 4.10 (a) The two NaI(Tl) detectors arranged for coincidence counting. The detectors are shielded in lead to reduce effects from background radiation.

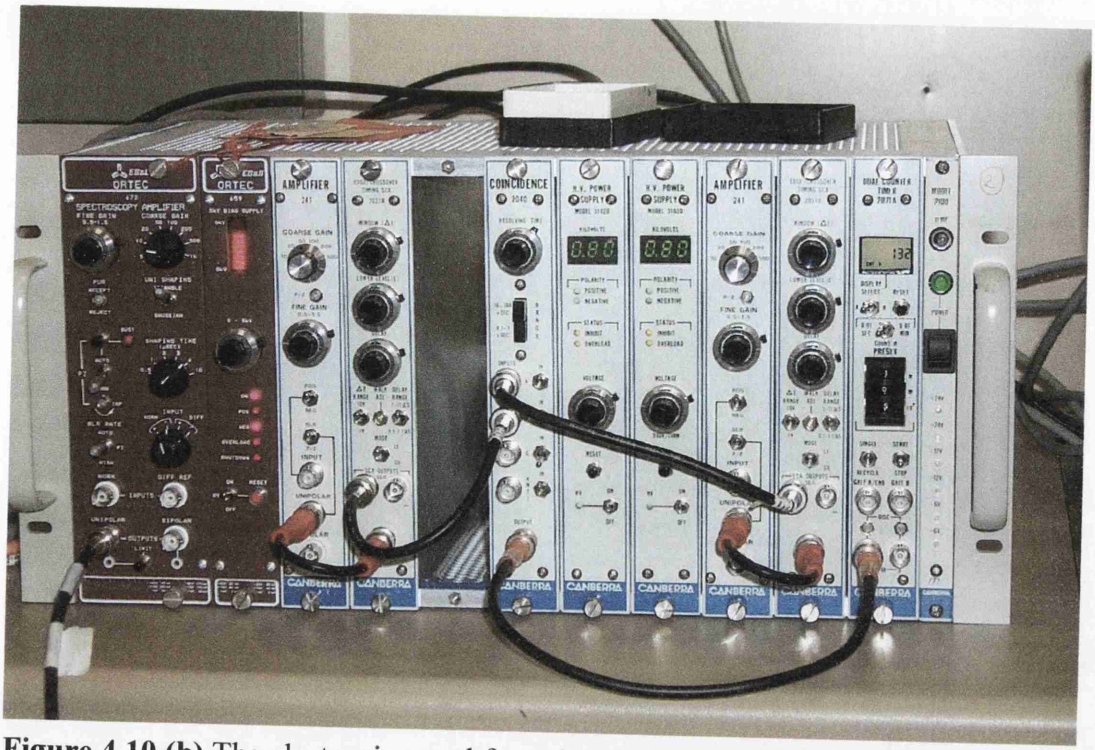

Figure 4.10 (b) The electronics used for coincidence counting. The brown coloured units are not involved in the coincidence system, they are used to operate the Germanium detector (next Section).

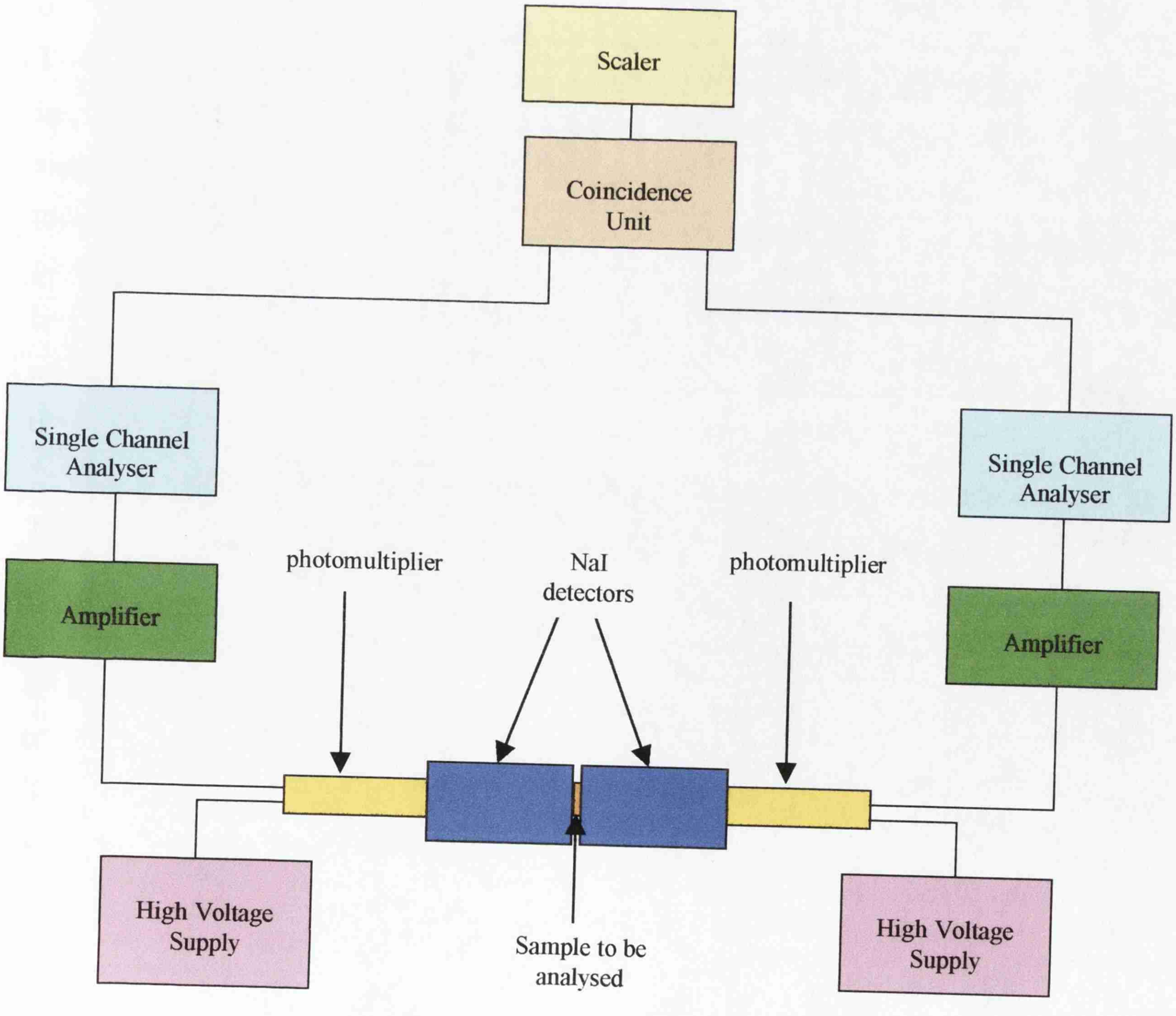

Figure 4.10 (c) Schematic of coincidence system.

The output of the amplifier is fed into a device known as a *Single Channel Analyser* (SCA). This is essentially a pulse height discriminator, and gives an output signal only when the height of an input pulse is within a specified range. Hence the controls on the SCA were set to "look at" the pulse produced from the 511 keV annihilation photons. Depending on the "window" that the SCA looks at, photons from other sources in a similar energy range (e.g. the 1275 keV photon may lose energy through scattering) may produce an output pulse from the SCA. The SCA output is a 5 V logic or "top hat" pulse.

This procedure was carried out for both detectors, i.e. both SCAs gave an output pulse for 511 keV. The outputs from both SCAs were then fed into a *coincidence unit.* A coincidence unit is essentially an AND gate, which operates in a selectable time window. That is when two input pulses are fed into the unit ocurring within a set time, an output logic pulse will be generated. This only occurs when both SCAs give an output pulse. The output of the coincidence unit was then fed into an electronic scaler. This means that a count will only appear on the scaler when two γ-rays of 511 keV are incident on each detector at essentially the same time. This can only occur with significant statistics when a positron emitter is placed between the detectors. This makes this technique extremely suitable when one is interested only in detecting positron annihilation events. The coincidence technique gives extremely low background counting rates, in this case the background was 2 counts in 1000s. When measuring activities in the kBq regime as will be shown in Chapters 5 and 6, this makes the background counting rate statistically insignificant.

The efficiency of the system was also measured using the ^{22}Na source, whose activity was measured by the manufacturer. ^{22}Na has a half-life of 2.6 years, and hence the activity at the time of use can be calculated. The efficiency of the system can then be found by simply observing the number of counts achieved in a set time, and taking the ratio of counts obtained s^{-1} / actual activity. The efficiency of the detector was ~10 %. It is important to periodically check the background counting rate and efficiency of such a system to check for drifts in these values, especially if the system is being used over long periods of time.

Another coincidence system was employed, set-up in exactly the same manner. This system however used two 2”x2” NaI(Tl) detectors, and although the function of the electronics were exactly the same as those described above, they were manufactured by E G & G – ORTEC. The efficiency of this system was 3.4 %, due to the smaller detector size, and the background rate was 26 counts/hour. The specifications of each system are summarised below:

Specifications : ***3”x3” system***

2 CANBERRA 802-3x3 NaI(Tl) DETECTORS
CANBERRA 2100 BIN/POWER SUPPLY
2 CANBERRA 2007 PHOTOMULTIPLIER TUBES/BASES
2 CANBERRA 2005 PRE-AMPLIFIERS
2 CANBERRA 241 AMPLIFIERS
2 CANBERRA 2037A EDGE/CROSSOVER TIMING SINGLE CHANNEL ANALYSERS
CANBERRA 2040 COINCIDENCE ANALYSER
CANBERRA 2071A DUAL COUNTER/TIMER
2 CANBERRA 3102D 0-2kV HV POWER SUPPLIES

2”x2” system

2 ORTEC 2”x2” NaI(Tl) DETECTORS
J&P NIM BIN
2 ORTEC 485 AMPLIFIERS
2 ORTEC 406A SINGLE CHANNEL ANALYSERS
ORTEC 481 COINCIDENCE UNIT
J&P 15 MHz SCALER
BRANDENBURG HV SUPPLY
ORTEC 556 HV SUPPLY

4.5.3 Detection of γ-rays Using an Intrinsic Germanium Detector

Gamma-rays can be detected using NaI(Tl) detectors, and can be used for specific applications such as the detection of annihilation γ-rays described above. However, if one is interested in measuring γ-rays of different energies, i.e. to obtain spectral data from γ-ray emitting sources, then solid-state (semiconductor) detectors offer huge improvements in energy resolution compared to scintillators. A detailed description of semiconductor detectors is given in (Leo 1994, Chapter 10, pp 214-247).

The detector used in the experiments was an intrinsic germanium detector. Put simply, the detector is essentially a semiconductor diode, having a p-i-n (positive-intrinsic-negative) structure in which the intrinsic region is sensitive to ionising radiation, particularly X and γ-rays. Under reverse bias (performed by a HV supply), an electric field extends across the intrinsic or depleted region. When photons interact with the material within the depleted volume of the detector, charge carriers (electrons and holes) are produced and are swept by the electric field to the P and N electrodes. The number of electron-hole pairs produced and hence the charge detected at the electrodes is directly proportional to the energy of the incident radiation. The charge at the electrodes is then converted into a voltage pulse by an integral charge sensitive pre-amplifier.

Because germanium has a relatively low band gap, at room temperature electrons can be excited into the conduction band, generating electron-hole pairs and hence electrical current. The detector must therefore be cooled in order to reduce this thermal generation of reverse leakage current. Otherwise, leakage current induced noise destroys the energy resolution of the detector. Liquid nitrogen which has a temperature of 77 K is used as the coolant and is held in the dewar shown in Figure 4.11 from where it can be supplied to the detector.

Figure 4.11 Liquid nitrogen dewar for Germanium detector.

The pulses obtained from the detector system are then amplified electronically. The height of these pulses is directly proportional to the energy of the incident radiation and hence analysis of these pulse heights can yield spectral data about the γ-ray sources. This is achieved using a multi-channel analyser (MCA) which sorts input pulses into different pulse amplitude channels, or "bins". The MCA used can divide pulse amplitudes into 8192 channels. The MCA is mounted in a PC and the associated software displays the number of counts obtained in a channel as a function of the channel number. Each channel can therefore be thought of as an energy "bin", where the channel number is directly proportional to the γ-ray energy. Figure 4.12 shows a typical γ-ray spectrum obtained using the set-up. The incident source is ^{22}Na. The two γ-ray lines at 511 kev (from β^+ annihilation) and 1275 keV are clearly visible, plus an extra peak at which occurs when the source is close to the detector, and due to the high flux of radiation, the detector sums the 511 and 1275 keV γ-rays.

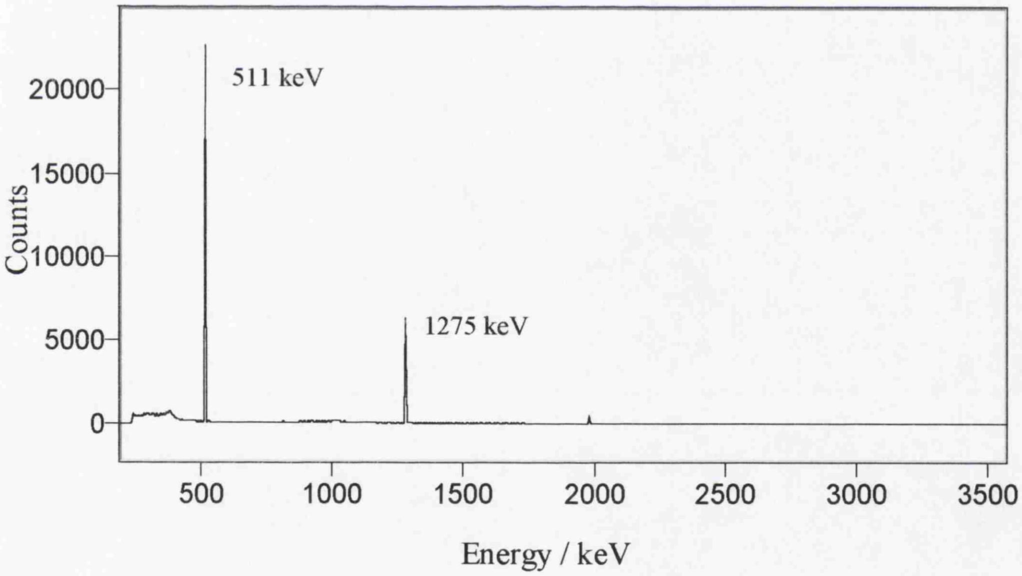

Figure 4.12 Spectrum of ^{22}Na taken with a germanium detector.

The energy axis was calibrated using γ-ray sources of known energy. The calibration sources used were ^{57}Co, ^{22}Na, ^{137}Cs, ^{60}Co and ^{152}Eu which produce γ-rays of energy ranging from 14-1333 keV as shown below in Table 4.1. From this a plot of energy vs channel number can be obtained. The more points on the plot, the more accurate the calibration.

The efficiency of a Germanium detector varies as a function of incident energy. Again, the efficiency can be measured using sources of known activity and energy. Figure 4.13 shows the detector efficiency as a function of energy.

Nuclide	γ-energies (keV)	Relative intensity (%)
^{57}Co	14	9.4
	122	85.2
	136	11.1
^{22}Na	511	181
	1275	99.75
^{137}Cs	662	85.1
^{60}Co	1173	99.86
	1333	99.98
^{152}Eu	112	37
	245	8
	344	27
	779	14
	965	15
	1087	12
	1113	14
	1408	22

Table 4.1 γ-ray energies and intensities of calibration sources for Ge detector

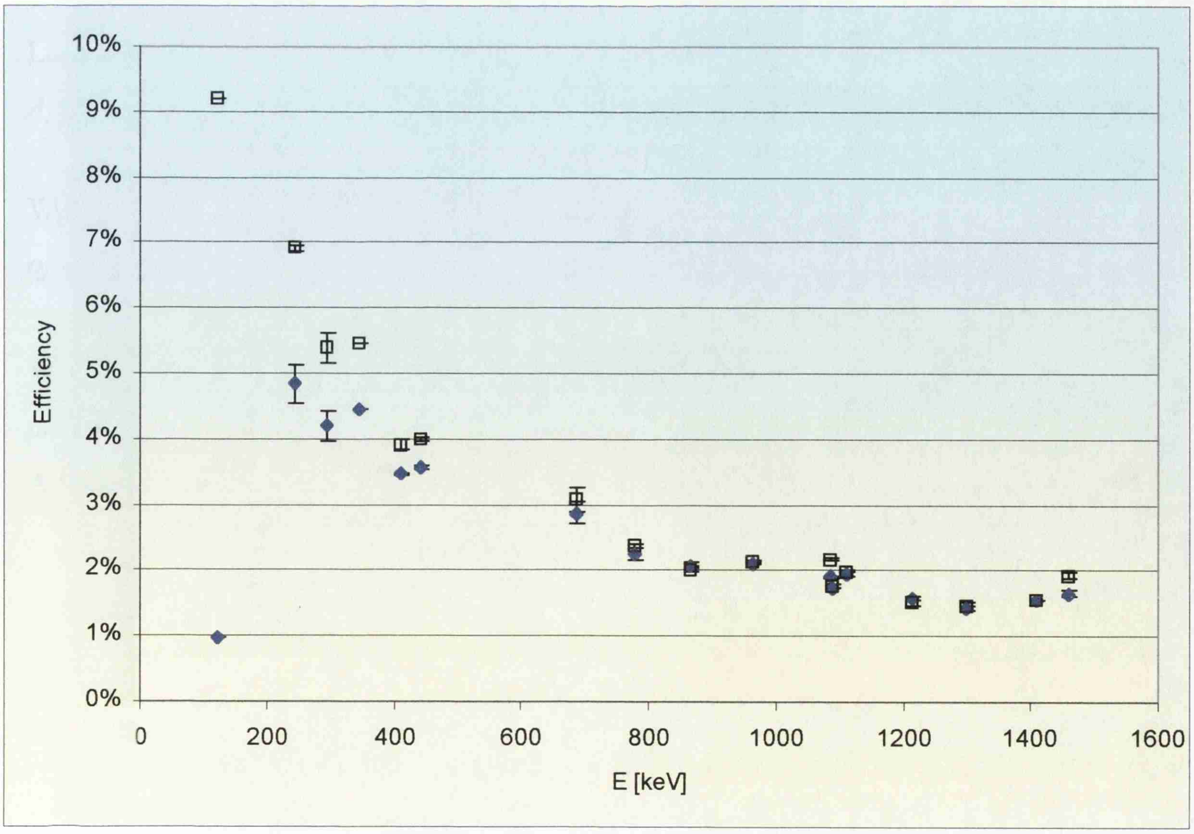

Figure 4.13 Ge-detector efficiency as a function of γ-ray energy.

References

Dilorio, G. J. 1979, *Direct Physical Measurements of Mass Yields in Thermal Fission of Uranium 235* New York: Garland.

Findlay, D. J. S. 1989, "Analytic representation of bremsstrahlung spectra from thick radiators as a function of photon energy and angle", *Nuclear instruments and methods in physics research*, vol. A276, p. 598.

Firestone, R. B., Shirley, V. S., & Chu, C. M. 1998, *Table of Isotopes 8th Edition 1998 update*, 8th edn, Wiley, New York.

IAEA EXFOR www database - experimental nuclear reaction cross-section data – http://www.nds.iaea.or.at/exfor

Krane, K. S. 1988, *Introductory Nuclear Physics* John Wiley and Sons, Inc..

Leo, W. R. 1994, *Techniques for Nuclear and Particle Physics Experiments - A How-to Approach*, 2nd Revised edn, Springer-Verlag Berlin Heidelberg.

Wehr, M. R., Richards Jr, J. A., & Adair III, T. W. 1983, "Nuclear Energy," in *Physics of the Atom*, Fourth edn, Addison-Wesley Publishing Company, pp. 465-512.

Williams, D. R. 1978, *High Resolution γ spectra of 40-44 MeV photon activation products: part 2 the elements Ruthenium to Uranium*, HM Stationery Office, London, AERE-R 9021.

Chapter 5

Gamma-Ray Production and Photo-Nuclear Physics Using Ultra-Intense Lasers

This chapter is concerned with the production of high-energy (up to 25 MeV) gamma-rays via ultra-intense (10^{19} Wcm^{-2}) laser-solid interactions. These high-energy photons are used to induce photo-nuclear reactions in materials, specifically (γ,n) and (γ,fission) reactions. The applications of this new technique, which include the measurement of the temperature of the fast electrons produced in the interaction are described.

5.1 Experimental Set-up

The experiments described in this chapter all employed the ultra-intense chirped pulse amplification (CPA) beam line of the VULCAN Nd: Glass laser (Danson et al. 1998) at the Central Laser Facility of the Rutherford Appleton Laboratory, UK. The beam was incident on a tantalum target, 10x10x1.75 mm thick, and at an angle of 45°. The light was p-polarised, (i.e. the electric field vector was is the direction of the target normal) and the target was maintained in a modest vacuum of $\sim 10^{-5}$ Torr. The experimental arrangement is shown schematically in Figure 5.1.

The VULCAN laser delivered pulses on target of up to 50 J with pulse lengths of about 1 picosecond (10^{-12} sec). A 95% reflecting turning mirror located after the compression gratings was used to steer the beam on target, focused by an F1.5, 225 mm focal length on-axis parabolic mirror. This turning mirror permitted 5% transmission of the laser energy to diagnose the laser pulse (Chapter 3, Section 3.3). The pulse duration was measured by a single shot autocorrelator, and the focal spot quality by an equivalent plane monitor. The main-pulse/pre-pulse contrast ratio (as described in Chapter 3) was measured by a third-order autocorrelator, and found to be $1 : 10^{-6}$. This is sufficient to create a pre-plasma on the target surface, 300 picoseconds before the arrival of the main pulse. The main pulse then interacts with this pre-plasma, and accelerates free electrons into the target (Chapter 2). These fast electrons are then slowed down in the high Z tantalum target, and generate bremsstrahlung radiation as described in Chapter 4. Equivalent plane images showed that the diameter of the focal spot was 9 μm, containing 35% of the laser energy. The focused intensity on target for each shot was monitored by a penumbral imaging camera, and was nominally 10^{19} $\mathrm{Wcm^{-2}}$. The principal diagnostics (Norreys et al. 1999), as shown in Figure 5.1 are described below.

Figure 5.1 Schematic of the experimental set-up in the horizontal plane and the principal diagnostics that were employed.

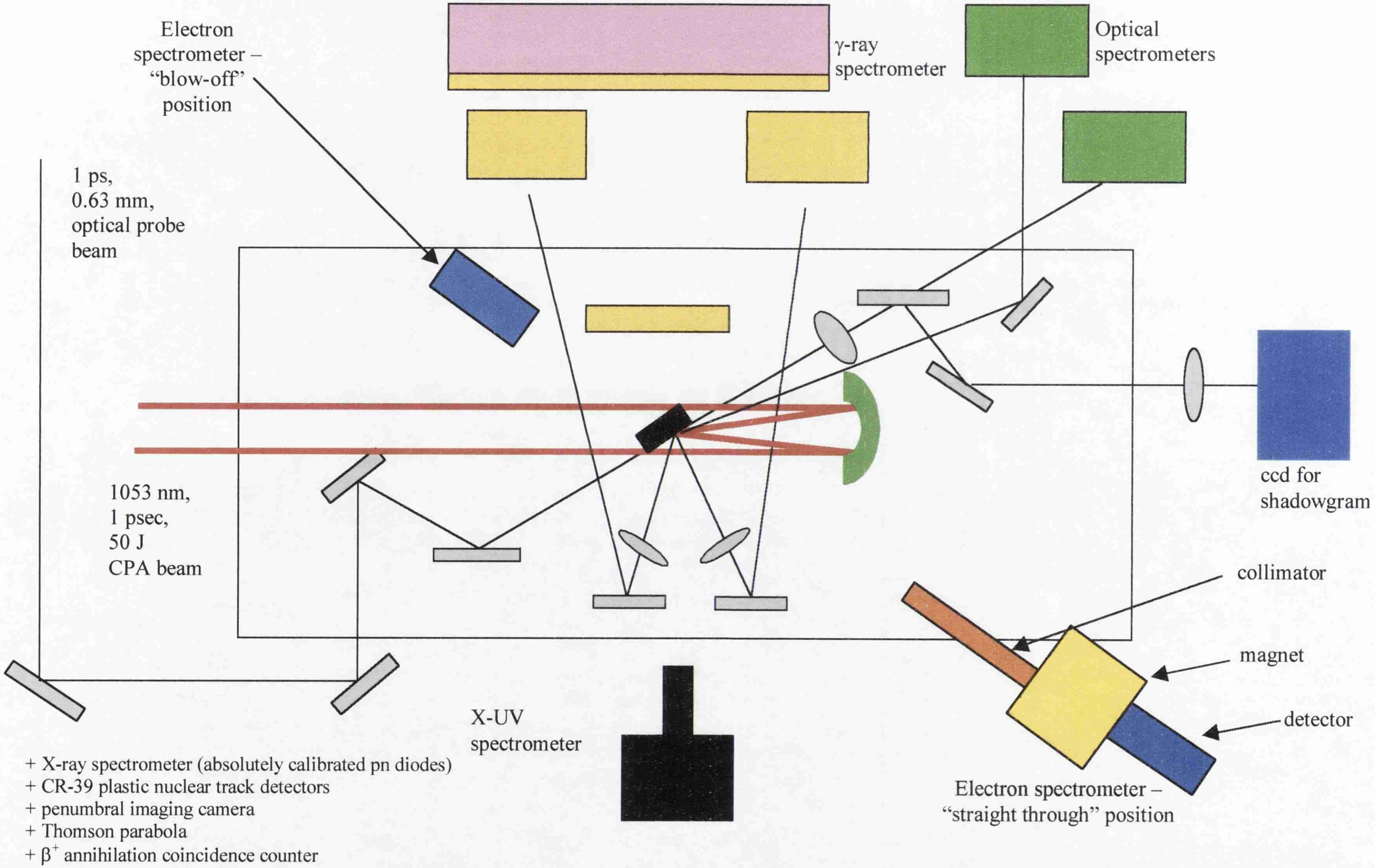

5.1.1 γ-ray bremmstrahlung spectrometer

X-rays from 100 keV to 10 MeV were measured using an array of eight filtered NE102A plastic scintillators each coupled to a Philips XP2012B photomultiplier. Bremsstrahlung emission from the target was collimated within the chamber using a 20 cm thick lead block with eight 1 cm holes drilled through it. The detectors were located outside the chamber at an angle of 125° to the target normal (as illustrated in Figure 5.1) and encased in thick lead shielding drilled with 1 cm holes aligned with respect to the collimator in the target chamber. A lead filter, which was positioned in front of each hole, varied in thickness from 0.1 to 15 cm, thereby enabling the spectrum from 100 keV to 10 MeV to be measured.

Each detector was calibrated at 60 keV, 660 keV, and 1.25 MeV. The detector sensitivity was obtained by extrapolating the mass energy absorption coefficient of the NE102A plastic scintillator. The signals were recorded on digitizing oscilloscopes. An unfolding technique was applied to obtain the spectrum based on an algorithm adopted from the YOGI code (Gorbics, Nash, & Johnson 1981) which was subsequently modified by Carlson and Lorence (Carlson & Lorence 1988) for unfolding bremsstrahlung spectra from flash X-ray machines.

5.1.2 Electron spectrometers

Two electron spectrometers were also deployed, one on each side of the target. The electron spectrometers consisted of a collimating aperture, a magnet, and either a silicon strip detector array, or phosphor/optical film combination. Using a Hall probe, a two-dimensional map of the magnetic field in each spectrometer was calculated so that at any position between the pole pieces the strength of the field was known. The deflection of the electrons at the detector plane as a function of energy was then calculated by solving the relativistic equation of motion from the Lorentz force

$$\frac{d}{dt}(\gamma m_0 \mathbf{v}) = -e\mathbf{v} \times \mathbf{B}\,. \qquad \text{Eqn (5.1)}$$

The electron spectrometer that sampled the "blow-off" plasma (in front of the target, at 15° to the target normal) was a strip detector. An unfolding technique was used to derive the electron spectra (Press et al. 1992). The electron spectrometer detector that was located behind the target in the "straight through" direction (180° to the target normal) consisted of a phosphor/film combination. The response of this detector to electron energy was taken from a calibration performed at the University of California – Los Angeles (UCLA).

5.1.3 Optical probing

A 527 nm pulse, derived from the main beam, was used to transversely probe the blow-off plasma from the target. The pulse length was between 1 and 2 ps. A focused shadowgraphic system was implemented, with an acceptance angle of 0.12 rad. There is a region in the plasma which is inaccessible due to refraction caused by large density gradients (see Chapter 2 pp 27-28 – "critical density"). This is given approximately by

$$\int_l \nabla_\perp n_e dl > 5 \times 10^{20} cm^{-3} \qquad \text{Eqn (5.2)}$$

where *dl* is an element of the optical path (Tatarakis et al. 1998). The field of view was such to allow observation of both the front and rear surfaces of the target.

5.1.4 Positron annihilation coincidence counter

Positrons slow down in solids and annihilate at rest with free electrons to produce two 511 keV gamma rays at 180° to each other. These annihilation γ-rays can be detected with high efficiency and low signal-to-noise ratio using coincidence counting techniques. Two coincidence systems were employed; system 1 employed two 3"x3" NaI scintillation detectors (as described in Chapter 4, Section 4.5), system 2 with two 2"x2" NaI scintillators. The absolute efficiency of each system was measured using a calibrated ^{22}Na source, and found to be 10% for the 3"x3" system, and 3.4% for the 2"x2" system.

5.2 Measurement of the Angular Distribution of the Laser Induced Bremsstrahlung Beam.

When an ultra-intense laser pulse interacts with a solid target, a plasma is formed at the laser-solid interface. Electrons are then accelerated into the target via the mechanisms described in Chapter 2. The acceleration mechanisms are of great interest, and it is important to gain a greater understanding of the different processes involved in plasma particle acceleration.

The first experiment carried out was to measure the angular distribution of the high-energy γ-rays following the laser irradiation of the tantalum bremsstrahlung radiator (Santala et al. 2000). This gives an accurate description of the direction of the fast electrons produced in the interaction, which is of great importance in many areas of plasma physics, including the Fast Ignitor approach to Inertial Confinement Fusion (ICF) (Tabak et al. 1994) and plasma particle accelerators (Tajima & Dawson 1979) (Umstadter et al. 1996) (Modena et al. 1995) (Amiranoff et al. 1998) (Wagner et al. 1997). It was necessary to determine the direction of the bremsstrahlung beam under fixed laser conditions so that targets may be placed in an optimum position, to maximise the number of photo-nuclear reactions taking place. At this stage it is necessary to review the various acceleration mechanisms discussed in Chapter 2.

The principal mechanisms believed to be responsible for fast electron production are classical resonance absorption, Brunel-type "Not-so-resonant", resonance absorption (Brunel 1987), ponderomotive $\mathbf{j} \times \mathbf{b}$ acceleration (Wilks et al. 1992) (Pukhov & Meyer-ter-Vehn 1998) and wakefield acceleration (Tajima & Dawson 1979) (Amiranoff et. al. 1998). The resonance absorption processes accelerate electrons in the direction of the plasma density gradient ∇n_e i.e. the target normal for p-polarised light, while $\mathbf{j} \times \mathbf{b}$ and wakefield acceleration produce electrons mainly in the laser beam propagation direction, $\mathbf{k}_{\mathbf{laser}}$. The dominance of each mechanism is believed to be dependent on the plasma density and laser intensity; for a more detailed account, see Chapter 2.

Pieces of copper were placed around the target (Figure 5.2a). The copper wedges were 10 mm in the radial direction, 15 mm high and 2.5mm thick at midpoint. Each wedge subtended an angle of 10°. Gamma rays above 10 MeV interact with the copper, inducing the photo-nuclear reaction $^{63}Cu(\gamma,n)^{62}Cu$ (Chapter 4, Section 4.3). The reaction cross-section peaks at around 70 mb (1 mb = 10^{-31} m^2) at 17 MeV (Figure 5.3) (Berman & Fultz 1975) (IAEA 2000). The resulting isotope ^{62}Cu has a half-life of 9.74 minutes and is a nearly pure (>99 %) positron emitter (Firestone, Shirley, & Chu 1998). The positrons can be detected using coincidence techniques as described in Chapter 4, Section 4.5.2. The copper slab directly behind the tantalum target acted as an overall activation reference, to determine the shot-to-shot variation in the nuclear activation. The β^+ activity in each copper piece was measured separately, corrected to time zero (time of laser irradiation) to allow for decay, and the angular distributions determined.

It was found that the γ ray beam moves from the target normal to the direction of $\mathbf{k}_{\mathbf{laser}}$ as the plasma scale length (determined by the laser pre-pulse length) is increased. For very large scale-lengths, the angular distribution is random. This has huge implications regarding the competing plasma acceleration mechanisms and hence is addressed in greater detail elsewhere (Santala et. al. 2000). For a fixed pre-pulse, described in Section 5.1, the γ-ray beam was directed along $\mathbf{k}_{\mathbf{laser}}$. Hence, various materials were placed in this position to undergo activation as described below.

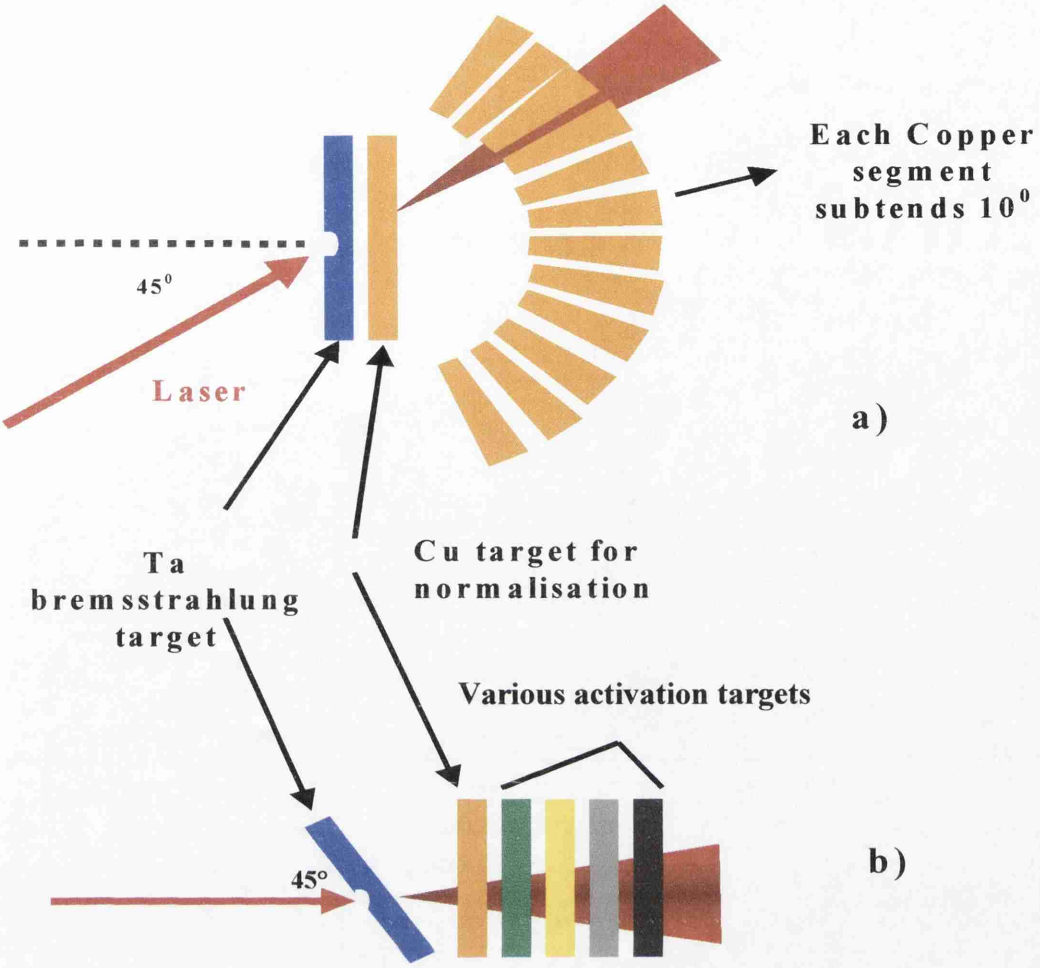

Figure 5.2 Schematic diagrams of the experimental target arrangement. **5.2 (a)** Shows the set-up used to measure the angular distribution of the laser-induced bemsstrahlung beam. **5.2 (b)** Shows the arrangement for producing different radioisotopes, and to measure the temperature of the fast electrons produced in the laser-tantalum interaction.

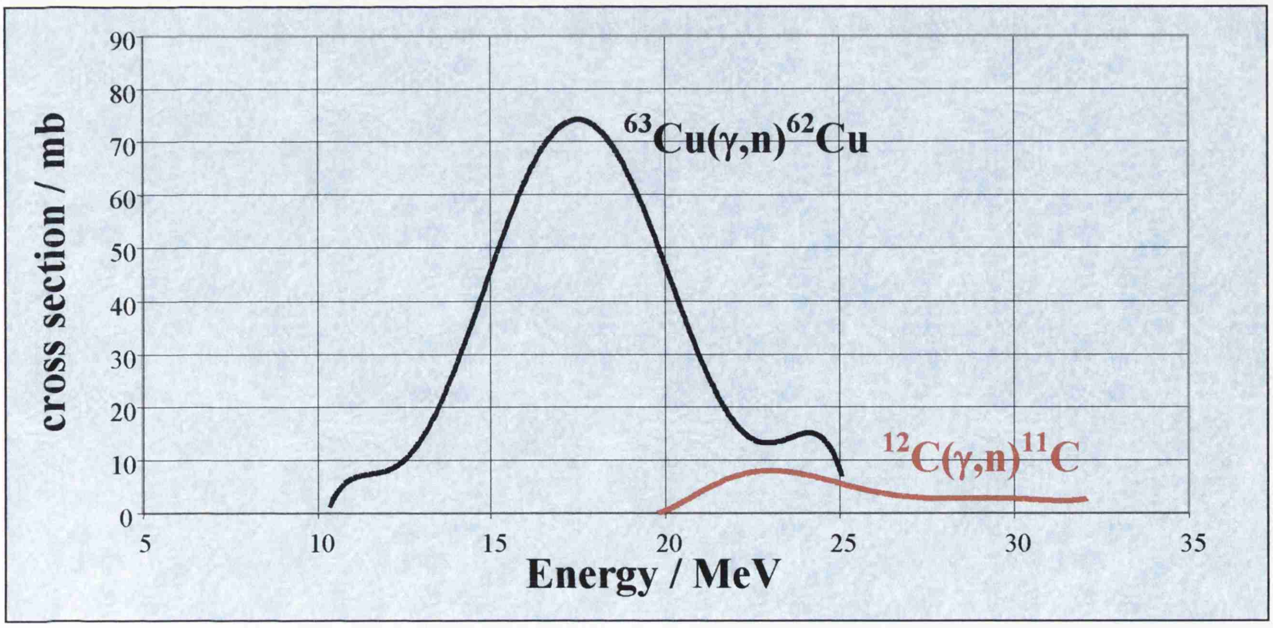

Figure 5.3 Experimental cross sections for the photo-nuclear reactions ^{63}Cu(γ,n)^{62}Cu and ^{12}C(γ,n)^{11}C.

5.3 Laser Production of Radioactive Isotopes

The set-up shown in Figure 5.2b was employed so that various samples could simultaneously undergo photo-nuclear reactions. The tantalum target was irradiated with the VULCAN laser, and the activities induced in each sample was measured in the coincidence counter. Table 5.1 lists the isotopes produced, the half-lives, the reaction thresholds (or Q-values,) and the peak reaction cross-sections. The time taken to extract the activation samples after irradiation was a few minutes, as the chamber must be returned to atmospheric pressure before the samples could be removed. These samples were then transferred to a nuclear laboratory for analysis. Hence, the lifetimes of the activated samples that could be measured were limited to a few minutes or more.

The measured activities were corrected to time zero and knowing the (γ,n) cross-sections (Berman & Fultz 1975;IAEA), the number of high energy photons produced in each pulse could be determined and hence an estimate of the initial number of fast electrons could be made. This will be discussed further in Section 5.4. From the maximum activity sources of ~5 kBq, it can be calculated that in 2π steradians, 10^{8-9} bremsstrahlung photons of energies >10MeV are produced from the suprathermal electrons.

Nuclear Reaction	**Half-life**	**-Q (MeV)**	**Peak σ (mb)**	**Radiation measured**
$^{12}C(\gamma,n)^{11}C$	20.5 mins	18.7	13.1	β^+
$^{39}K(\gamma,n)^{38}K$	7.6 mins	13.7	11	β^+
$^{63}Cu(\gamma,n)^{62}Cu$	9.7 mins	10.9	75	β^+
$^{65}Cu(\gamma,n)^{64}Cu$	12.7 hours	10.9	65	β^+
$^{64}Zn(\gamma,n)^{63}Zn$	38.1 mins	11.9	70	β^+
$^{107}Ag(\gamma,n)^{106}Ag$	24 mins	9.5	155	β^+
$^{141}Pr(\gamma,n)^{140}Pr$	3.4 mins	9.4	335	β^+
$^{181}Ta(\gamma,n)^{180}Ta$	8.2 hours	7.6	367	EC Hf X-Rays
$^{238}U(\gamma,f)^{134}I$ $^{238}U(\gamma,f)^{138}Cs$ $^{238}U(\gamma,f)^{92}Sr$	53 mins 32.3 mins 2.7 hours	7.8	150	847 keV γ 884 keV γ 1436 keV γ 1384 keV γ

Table 5.1 (γ,n) and (γ,f) reactions at laser intensities of ~ 10^{19} Wcm^{-2}

Using the coincidence set-up, the half-lives of the various positron-emitting isotopes produced were measured, and were found to compare well with the accepted values (Figure 5.4). The isotopes produced were ^{38}K, ^{11}C, ^{106}Ag, ^{62}Cu, ^{63}Zn and ^{140}Pr. All of these were produced via (γ,n) reactions. Figure 5.5 shows the cross sections of the various reaction involved.

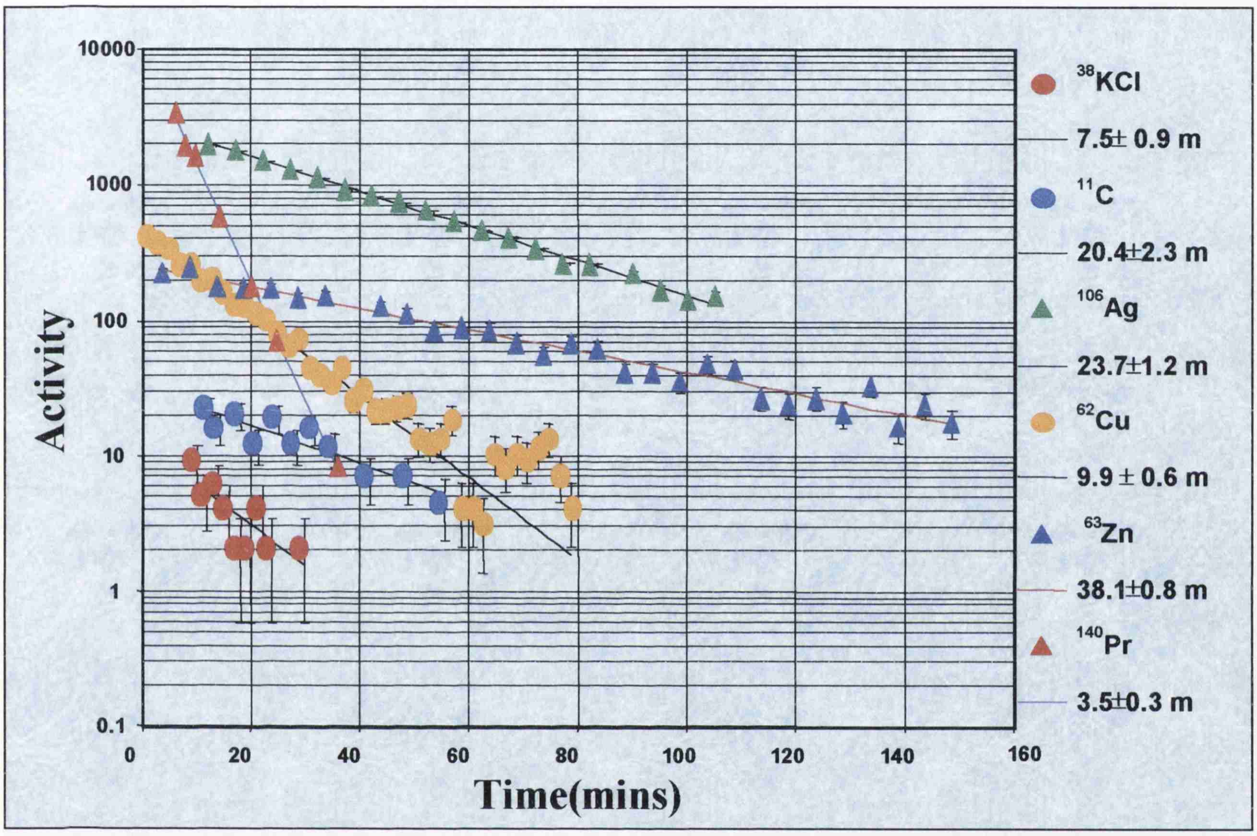

Figure 5.4 The activities of the β^+ emitting radioisotopes listed in Table 5.1 as a function of time. The half-lives measured agree well with the accepted values. The activities shown here are from different laser pulses.

Copper is composed of two stable isotopes, ^{63}Cu (69.1 %) and ^{65}Cu (30.9 %). A (γ,n) reaction on a ^{65}Cu nucleus gives ^{64}Cu, which has a half-life of 12.7 hours, and 19 % of its radioactive decay is via positron emission. Hence an activated copper sample was measured in the coincidence detector for around 30 hours. Figure 5.6 shows the results of this analysis, and the two isotopes, ^{62}Cu (9.74 mins) and ^{64}Cu (12.7 hours) are clearly observed.

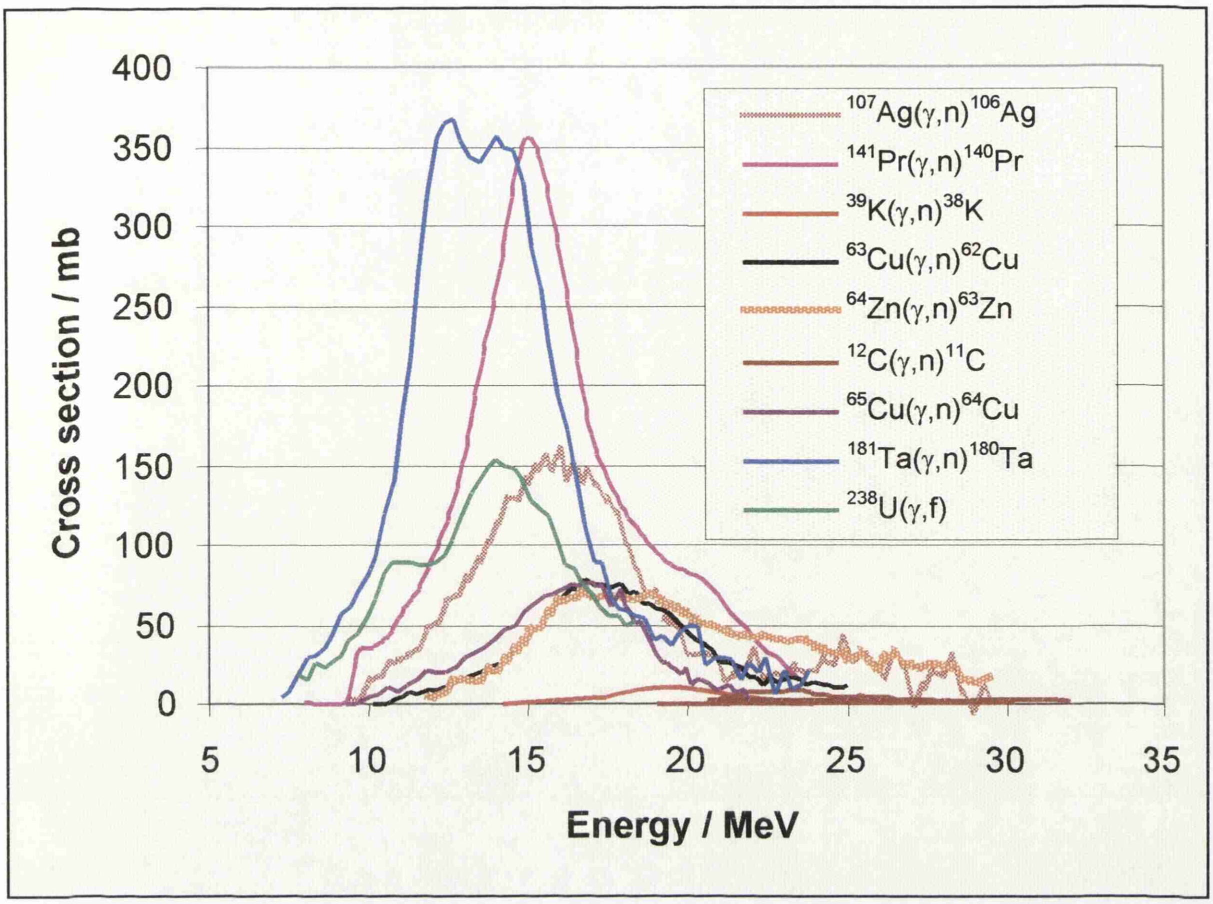

Figure 5.5 Cross sections for the reactions produced in this study.

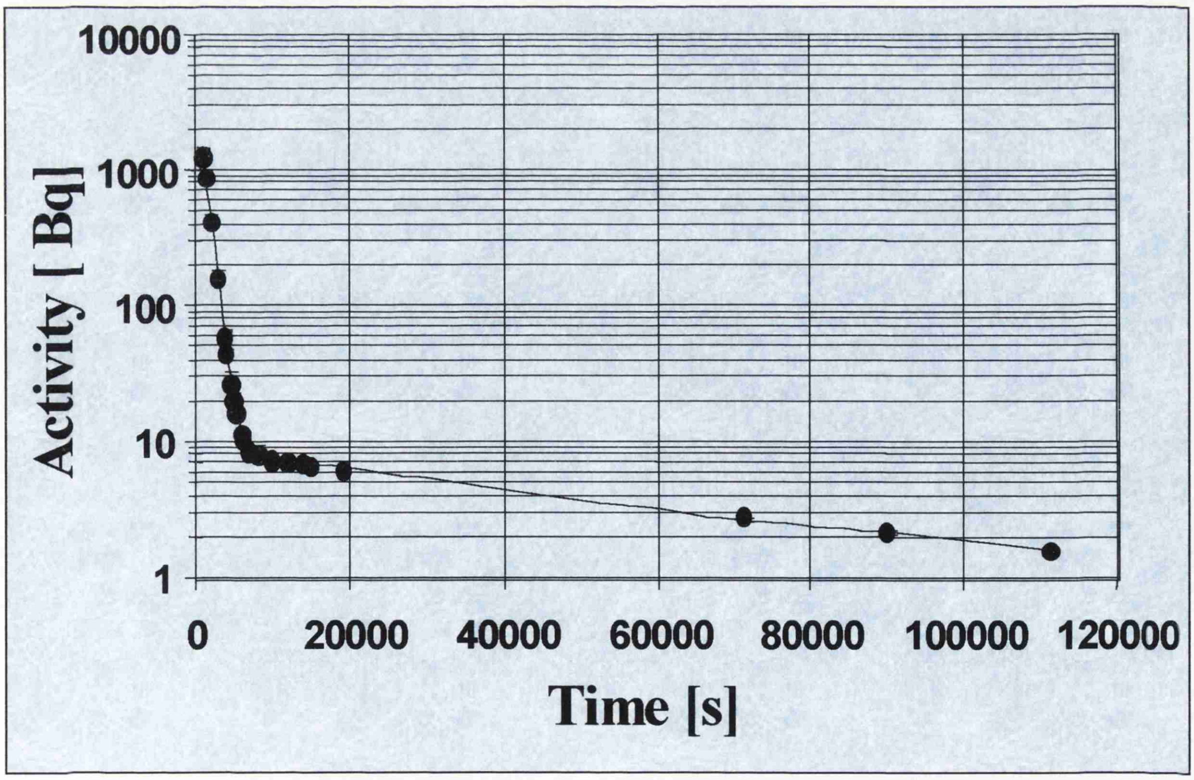

Figure 5.6 The half-lives of the two radioisotopes of Cu produced: ^{62}Cu and ^{64}Cu following the irradiation at laser intensity 10^{19} Wcm^{-2}. The half-lives agree well with the accepted values of 9.7 mins and 12.7 hours.

Since the thresholds (or Q-values) of the various reactions listed in Table 5.1 are different for a given reaction, the measured activities of the isotopes produced can be used to establish the shape of the bremsstrahlung spectrum, and hence the temperature of the fast electrons generated in the laser-solid interaction. This technique is described below in Section 5.4.

5.4 Quantitative Measurement of Fast Electron Temperature in Ultra-Intense Laser-Solid Interactions via Nuclear Activation Techniques

The suprathermal electron temperature T was obtained for a given shot by calculating theoretical values for the activity of the copper sample compared with another sample with a different Q-value in the activation stack for an estimated value of kT (MeV), and comparing this value with the experimental measurement. As an example, the activity ratio of ^{11}C / ^{62}Cu is taken here.

The theoretical ^{11}C / ^{62}Cu activity ratio was calculated in the following way: the relativistic electron distribution is given by (Norreys et al. 1999)

$$N_e(E) = N_0 E^2 e^{-\left(\frac{E}{kT}\right)} \qquad \text{Eqn (5.3)}$$

where $N_e(E)$ is the number of electrons at energy E, N_0 is a constant, E is the electron energy, k is Boltzmann's constant and T is the electron temperature. Figure 5.7 shows this electron distribution for E=0 to 25 MeV, kT=1.63 MeV, N_0=1.

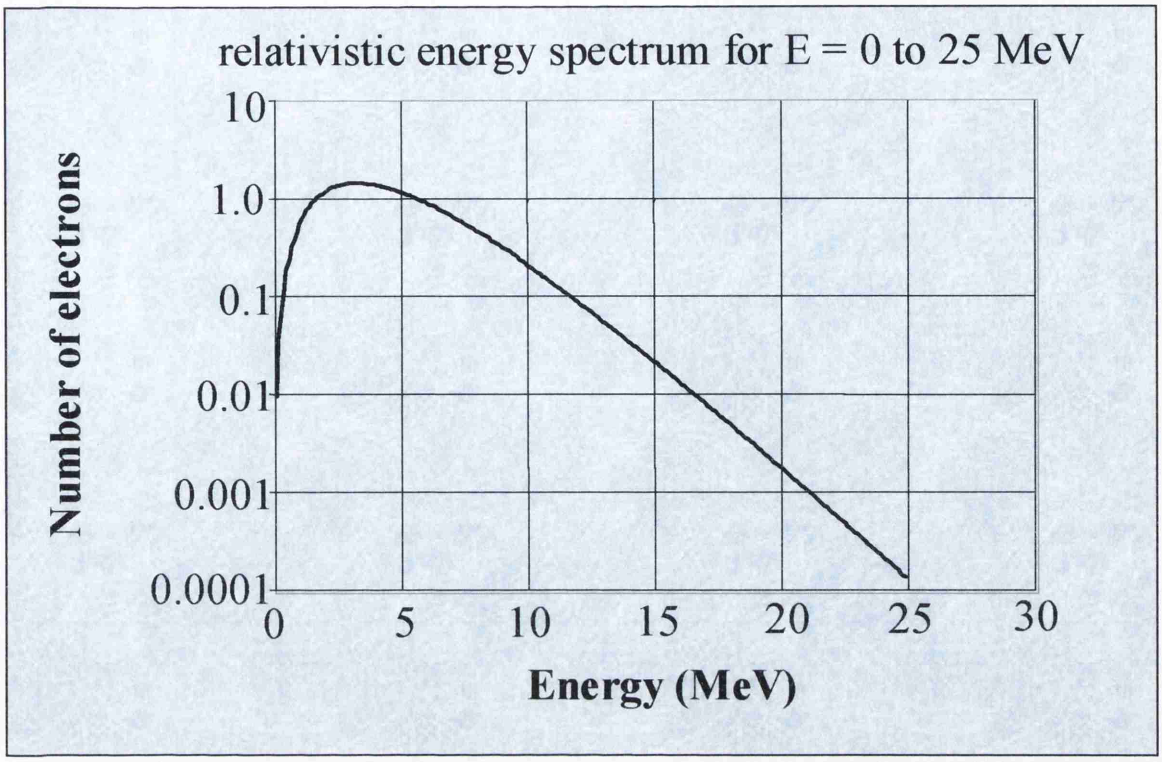

Figure 5.7 The shape of the relativistic electron distribution with $N_0=1$, kT=1.63 MeV.

Electrons of energy E MeV produce a gamma-ray energy spectrum in tantalum. This spectrum was calculated using an analytical representation for bremsstrahlung spectra (Findlay 1989). Examples of gamma-ray spectra produced along the electron (and hence the laser) direction in a tantalum target by 15 MeV and 20 MeV electrons are shown in Figure 5.8

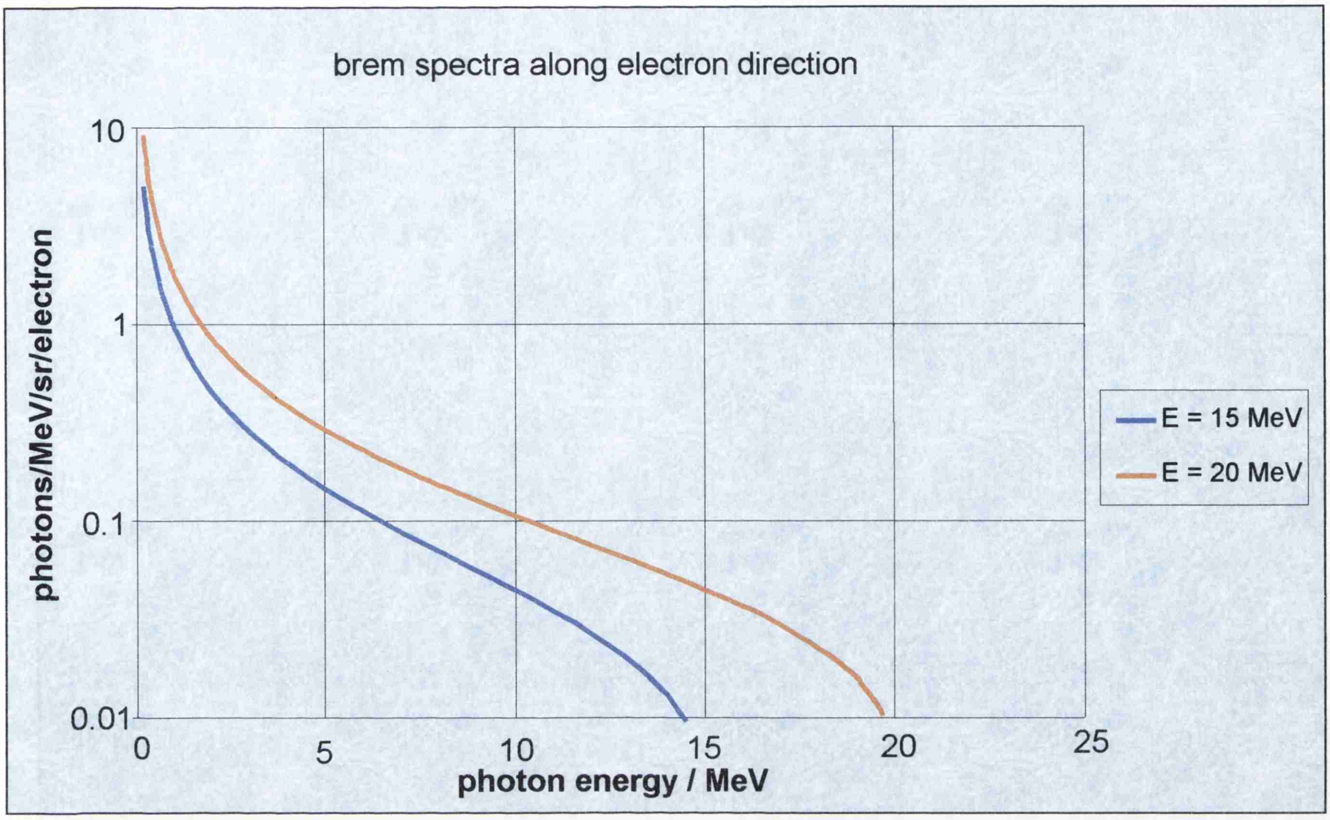

Figure 5.8 Bremsstrahlung spectra along relativistic electron direction for electrons of a) 15 MeV and b) 20 MeV.

The induced activity of a sample when bombarded by high-energy photons may be obtained from

$$A = \left(\frac{\ln(2)}{T_{1/2}} \right) \sum_{E_\gamma} N_\gamma(E_\gamma) \sigma_{\gamma n}(E_\gamma) N \qquad \text{Eqn (5.4)}$$

where $T_{1/2}$ is the half-life of the radioisotope, $N_\gamma(E_\gamma)$ is the number of photons in the energy bin of width 0.5 MeV at energy E_γ, $\sigma_{\gamma n}(E_\gamma)$ is the (γ,n) reaction cross-section at energy E_γ (IAEA) Figure 5.3), and N is the number of nuclei present. The summation in Equation 5.4 extends from the Q-value for the reaction to 25MeV beyond which the cross-section is negligible for the reactions considered. Figure 5.3 shows the cross-sections for the reactions in question.

The total number of photons of energy E_γ incident on both the copper and carbon samples was calculated by integrating over $\theta=0$ to 30.5° for copper, and $\theta=0$ to 14° for the carbon sample, according to the geometry of the system. The activity ratio of ^{11}C/^{62}Cu was then calculated for a given electron temperature kT and compared to the experimental value. The calculation was then repeated with different kT values until the data fitted the experimental ratio.

The calculated $^{11}C/^{62}Cu$ activity ratio is shown as a function of kT in Figure 5.9, with three typical measured activity ratios from different laser pulses, at nominally 10^{19} Wcm^{-2}, plotted as points corresponding to kT values of 1.43, 1.63 and 2.06 MeV. These different temperatures show the shot-to-shot variation from nominally the same intensity. This is a feature that requires further investigation.

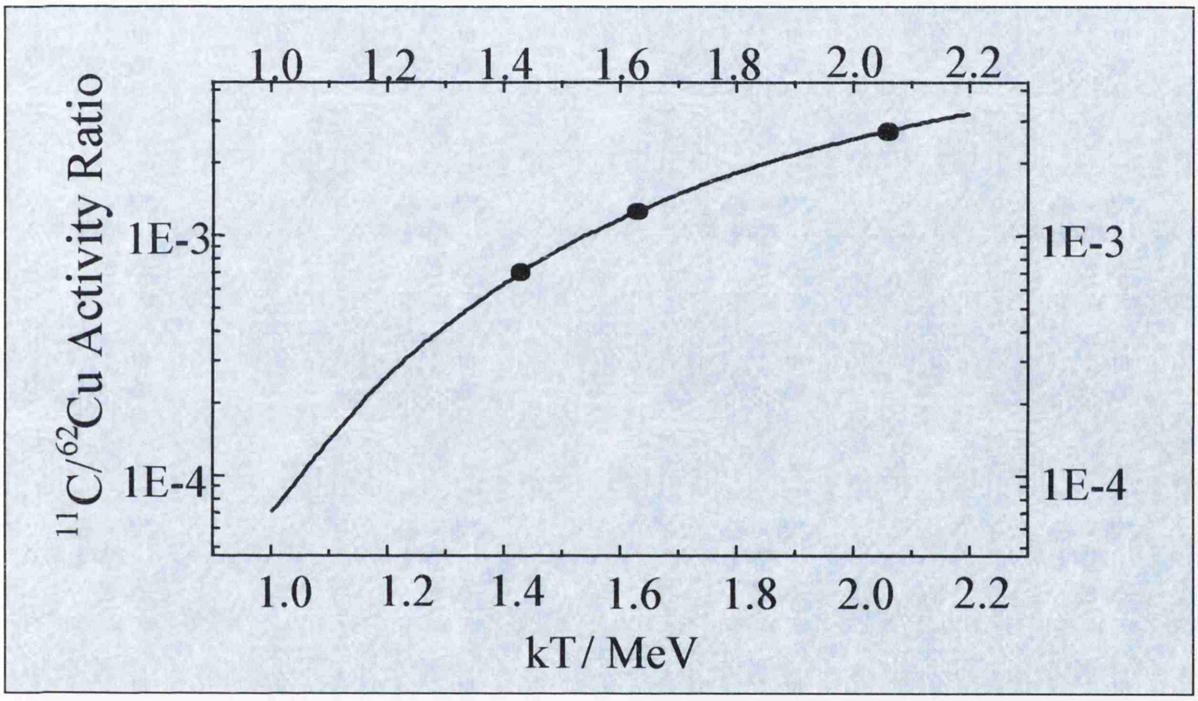

Figure 5.9 Activity ratio as a function of kT with three experimental ratios plotted against their corresponding kT values.

For large-scale, single-shot laser facilities such as VULCAN, this method can be used to calculate the electron temperature between laser pulses, making a shot-to-shot comparison of the electron temperature easily attainable.

5.5 Laser-Induced Nuclear Fission of Uranium-238

A sample of ^{238}U (depleted uranium) of dimensions ~10x10x2 mm (~3 g) was placed behind the tantalum target to undergo irradiation. The ^{238}U sample was shrink wrapped in plastic to contain any gaseous radioactivity and enclosed in an aluminium container.

The tantalum target was irradiated with three consecutive laser pulses, twenty minutes apart, of nominally 10^{19} Wcm^{-2} intensity. The uranium sample was then removed from the target chamber and analysed using the germanium detector arrangement described in Chapter 4, Section 4.5.3. The detector was shielded in lead in order to reduce signals from background radiation and hence to accurately measure the photon emission from the sample.

Both (n,f) and (γ,f) reactions in fissionable materials produce a double headed assymetric fission yield of fragments with maxima at mass numbers A=95 and 140 corresponding to the neutron magic numbers of nucleons 50 and 82 (Wehr, Richards Jr, & Adair III 1983) as discussed in Chapter 4.

The principal fission fragments amount to about 5-6 % of the total fission yield. Evidence for fission events is usually carried out by detecting the characteristic γ-rays (as was applied here) or by detection of fission fragments tracks or fission neutrons. In the case of ^{238}U with a (γ,f) cross section which peaks at around 150 mb, the most abundant isotopes produced include ^{134}I, ^{138}Cs, and ^{92}Sr (Williams 1978) with suitable characteristic γ-rays and half-lives (Table 5.1). The background activity from fissionable materials is normally sufficiently large that careful background measurements must be taken when carrying out fission analysis. For ^{238}U (half-life=4.5×10^9 years) the background activity is 12.3 kBq/g. Figure 5.10 shows two Ge γ-ray spectra in the region of 850 keV and 1400 keV after subtracting background activity.

From the intensity of the ^{134}I γ-ray peak in Figure 5.10, and using the known efficiency of the Ge detector along with the fission yield to that isotope, and the (γ,f) cross section (IAEA) (Table 5.1), it has been estimated that about 10^6 fission events are generated by a laser pulse of $\sim 10^{19}$ Wcm^{-2} in a ^{238}U target of 2 mm thickness. This was the first ever observation of laser-induced fission.

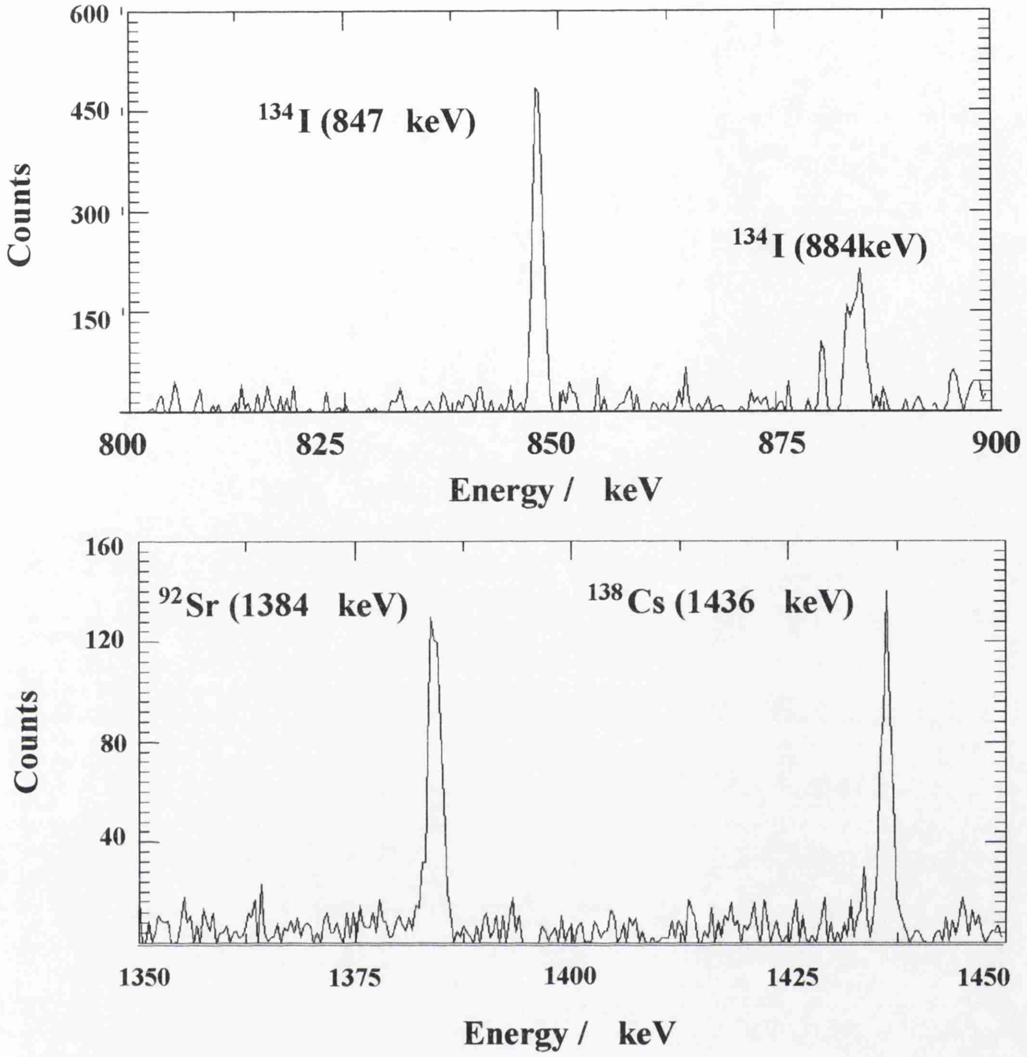

Figure 5.10 Some of the characteristic γ-rays emitted by the three principal fission fragments produced from a (γ,f) reaction.

This provides unambiguous evidence that fission took place in the uranium sample, although it could be argued that the mechanism producing the fission events could also come from neutrons produced in the tantalum bremsstrahlung converter via (γ,n) reactions from the fission process itself. However, the flux of neutrons from the tantalum target is of the order 10^5 neutrons/pulse, and if every fission event produces 2 neutrons, for 10^6 fissions this gives 2×10^6 neutrons. The (n,f) cross section is an order of magnitude greater than the (γ,f) process, but given that 10^9 photons are produced per pulse, it is concluded that photofission is the dominant process.

In addition, the tantalum target was also analysed using the Ge detector. In heavy nuclei such as tantalum, if the nucleus is proton rich, it achieves stability predominately by electron capture. These isotopes are unambiguously identified since they emit the characteristic X-rays of the element of one proton less than the parent. In the case of tantalum, these are halfnium (Hf) X-rays. The low energy γ-ray spectrum from Ta is shown in Figure 5.11. The Hf X-rays are clearly visible, which indicates that the isotope ^{180}Ta was produced, via (γ,n) reactions.

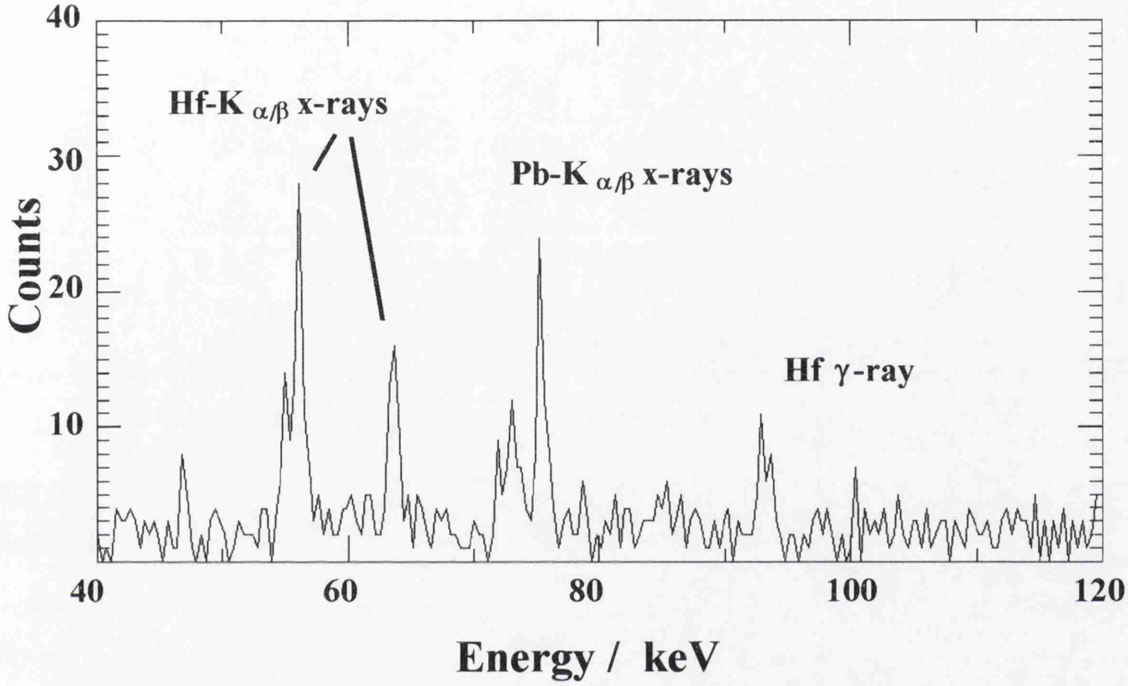

Figure 5.11 The low energy γ-ray spectrum from Ta as measured by an intrinsic Ge detector. The characteristic Hf X-rays from the decay of ^{180}Ta are clearly visible. The Pb X-rays are background peaks.

5.6 Discussion

It has been shown that highly directional high-energy γ-ray (up to 25 MeV) beams can be generated via ultra-intense (~10^{19} Wcm^{-2}) laser-solid interactions. These photons can be used to induce nuclear reactions in various materials. Specifically, (γ,n) reactions were carried out on various materials to produce positron emitting nuclei, and the first laser-driven fission reaction was observed. Proton producing, or (γ,p) reactions have similar threshold or Q-values to (γ,n) reactions, but were not witnessed mainly because of the nuclear Coulomb barrier, which reduces the probability of a (γ,p) event occurring by an order of magnitude with respect to a (γ,n) event.

This is a novel method of performing photo-nuclear physics, and with laser technology advancing at a staggering rate, compact, high-repetition-rate lasers capable of irradiances ~10^{19} $\text{Wcm}^{-2}\mu\text{m}^2$ are beginning to be realised. Hence it may be possible to perform "nuclear physics on a table-top".

In addition, it has been shown that laser-induced photo-nuclear physics can be used to diagnose fundamental parameters in laser-plasma interactions. The direction of the fast electrons in the interaction under varying plasma conditions and the temperature of these electrons has been measured. The ability to quantify these parameters is of utmost importance to plasma acceleration research and the Fast Ignitor approach to Inertial Confinement Fusion. Laser-induced photo-nuclear physics has made this possible.

References

Amiranoff, F., Baton, S., Bernard, D., Cros, B., Descamps, D., Dorchies, F., Jaquet, F., Malka, V., Marquès, J. R., Matthieussent, G., Miné, P., Modena, A., Mora, P., Morillo, J., & Najmudin, Z. 1998, "Observation of laser wakefield acceleration of electrons", *Physical Review Letters*, vol. 81, p. 995.

Berman, B. L. & Fultz, S. C. 1975, "Measurements of the giant dipole resonance with monoenergetic photons", *Review of Modern Physics*, vol. 47, p. 713.

Brunel, F. 1987, "Not-so-resonant, resonant absorption", *Physical Review Letters*, vol. 59, p. 52.

Carlson, G. A. & Lorence, L. J. 1988, "A differential absorption spectrometer for determining flash X-ray spectra from 10 keV to 2000 keV", *IEEE Transactions on Nuclear Science*, vol. 35, p. 1255.

Danson, C., Collier, J., Neely, D., Barzanti, L. J., Damerell, A., Edwards, C. B., Hutchinson, M. H. R., Key, M. H., Norreys, P. A., Pepler, D. A., Ross, I. N., Taday, P. F., Toner, W. T., Trentelman, M., Walsh, F. N., Winstone, T. B., & Wyatt, R. W. W. 1998, "Well characterized 10^{19} Wcm^{-2} operation of VULCAN - an ultra-high power Nd: glass laser", *Journal of Modern Optics*, vol. 45, p. 1653.

Findlay, D. J. S. 1989, "Analytic representation of bremsstrahlung spectra from thick radiators as a function of photon energy and angle", *Nuclear instruments and methods in physics research*, vol. A276, p. 598.

Firestone, R. B., Shirley, V. S., & Chu, C. M. 1998, *Table of Isotopes 8th Edition 1998 update*, 8th edn, Wiley, New York.

Gorbics, S. G., Nash, A. E., & Johnson, T. L. 1981, "Use of an albedo neutron personnel dosimeter for X- and gamma-ray monitoring", *Health Physics*, vol. 40, p. 811.

IAEA. EXFOR www database - experimental nuclear reaction coss-section data. International Atomic Energy Authority – http://iaeand.iaea.or.at/exfor/.

Modena, A., Najmudin, Z., Dangor, A. E., Clayton, C. E., Marsh, K. A., Joshi, C., Malka, V., Darrow, C. B., Danson, C., Neely, D., & Walsh, F. N. 1995, "Electron acceleration from the breaking of relativistic plasma-waves", *Nature*, vol. 377, p. 606.

Norreys, P. A., Santala, M., Clark, E. L., Zepf, M., Watts, I., Beg, F. N., Krushelnick, K., Tatarakis, M., Dangor, A. E., Fang, X., Graham, P., McCanny, T., Singhal, R. P., Ledingham, K. W. D., Creswell, A., Sanderson, D. C. W., Magill, J., Machacek, A., Wark, J. S., Allott, R. M., Kennedy, B., & Neely, D. 1999, "Observation of a Highly Directional γ-ray Beam from Ultra-short, Ultra-intense Laser Pulse Interactions with Solids", *Physics of Plasmas*, vol. 6, p. 2150.

Press, W., Teukolsky, S. A., Vetterling, W. T., & Flanary, B. P. 1992, *Numerical Recipies on the Art of Scientific Computing* Cambridge University Press.

Pukhov, A. & Meyer-ter-Vehn, J. 1998, "Relativistic laser-plasma interaction by multi-dimensional particle-in-cell simulations", *Physics of Plasmas*, vol. 5, p. 1880.

Santala, M. I. K., Zepf, M., Watts, I., Beg, F. N., Clark, E. L., Tatarakis, M., Krushelnick, K., Dangor, A. E., McCanny, T., Spencer, I., Singhal, R. P., Ledingham, K. W. D., Machacek, A., Wark, J. S., Allott, R. M., Clarke, R. J., & Norreys, P. A.

2000, "Effect of the plasma density scale length on the direction of fast electrons in relativistic laser-solid interactions", *Physical Review Letters*, vol. 84, p. 1459.

Tabak, M., Hammer, J., Glinsky, M. E., Kruer, W. L., Wilks, S. C., Woodworth, J., Campbell, E. M., & Perry, M. D. 1994, "|gnition and high gain with ultrapowerful lasers", *Physics of Plasmas*, vol. 1, p. 1626.

Tajima, T. & Dawson, M. 1979, "Laser Electron Accelerator", *Physical Review Letters*, vol. 43, p. 267.

Tatarakis, M., Davies, J. R., Lee, P., Norreys, P. A., Kassapakis, N. G., Beg, F. N., Bell, A. R., Haines, M. G., & Dangor, A. E. 1998, "Plasma fromation on the front and rear of plastic targets due to high intensity laser-generated fast electrons", *Physical Review Letters*, vol. 81, p. 999.

Umstadter, D., Chen, S. Y., Maksimchuk, A., Morou, G., & Wagner, R. 1996, "Nonlinear optics in relativistic plasmas and laser wake field acceleration of electrons", *Science*, vol. 273, p. 472.

Wagner, R., Chen, S. Y., Maksimchuk, A., & Umstadter, D. 1997, "Electron acceleration by a laser wakefield in a relativistically self-guided channel", *Physical Review Letters*, vol. 78, p. 3125.

Wehr, M. R., Richards Jr, J. A., & Adair III, T. W. 1983, "Nuclear Energy," in *Physics of the Atom*, Fourth edn, Addison-Wesley Publishing Company, pp. 465-512.

Wilks, S. C., Kruer, W. L., Tabak, M., & Langdon, A. B. 1992, "Absorption of Ultra-Intense Laser Pulses", *Physical Review Letters*, vol. 69, p. 1383.

Williams, D. R. 1978, High Resolution γ spectra of 40-44 MeV photon activation products: part 2 the elements Ruthenium to Uranium, HM Stationery Office, London, AERE-R 9021.

Chapter 6

Proton Generation and Proton Induced Nuclear Physics

This Chapter is concerned with the use of the VULCAN laser beam to generate beams of energetic protons of energies up to 37 MeV. These protons can then induce nuclear reactions in materials, to produce β^+ emitting nuclei of relevance to the nuclear medicine community. The possibility of using ultra-intense lasers to produce commercial quantities of short lived positron emitting sources for Positron Emission Tomography is discussed. In addition, the possibility of using lasers to generate proton beams for oncology is also addressed.

6.1 Introduction

In the last chapter, it was shown that beams of energetic γ-rays can be generated when the VULCAN laser pulse interacts with thick, high-Z targets. These laser-generated γ-rays were then used to produce radioactive nuclei (decaying by electron capture/positron emission) via (γ,mn) reactions (m=1,2,3,....). The development of this technique for "table-top" production of radio-nuclides is the natural extension of this work.

One of the potential applications of this new technology is to produce short lived (2 minutes-2 hours) positron emitters for Positron Emission Tomography (PET) (See Chapter 1, pp 16 for more information on PET).

The main positron emitting nuclei used in PET are ^{11}C, ^{13}N, ^{15}O and ^{18}F, with the latter being the most widely used positron source. These sources are usually produced using energetic protons generated by cyclotrons or van de Graffs via (p,n) and (p,α) reactions. The reactions used, the half-life of the product and the peak reaction cross sections are listed in Table 6.1. The reason that proton induced nuclear reactions are favoured is because the isotope produced has a different atomic number from the reactant, and hence these can be separated using fast chemistry. This makes it possible to produce carrier free sources allowing patients to be injected with the minimum of foreign material.

Nuclear reaction	Half-life	-Q (MeV)	Peak cross-section (mb)	Radiation measured
$^{11}B(p,n)^{11}C$	20.34 mins	2.76	430	β^+ 99%
$^{14}N(p,\alpha)^{11}C$	20.34 mins	2.92	250	β^+ 99%
$^{16}O(p,\alpha)^{13}N$	9.96 mins	5.22	140	β^+ 100%
$^{15}N(p,n)^{15}O$	123 seconds	3.53	200	β^+ 100%
$^{18}O(p,n)^{18}F$	109.7 mins	2.44	700	β^+ 97%

Table 6.1 PET isotope production reaction data.

At the moment, only a few hospitals in the UK have the facilities to produce these positron emitting sources. This is mainly due to the size and cost of the present systems used to produce the proton beams. This is one of the main reasons that ^{18}F, with its half life of ~2 hours is the most widely used, since it is possible to produce this isotope off-site, then transport it to nearby hospitals. The other isotopes are also extremely useful, although their use is limited since their short lifetimes make them difficult to transport since most of the activity will have decayed away during transit. However, it was shown theoretically in Chapter 2 that beams of energetic protons can be generated in ultra-intense laser-solid interactions. This chapter reports on the generation of proton beams up to 37 MeV using the VULCAN laser. These proton beams are then used to produce the PET isotopes ^{11}C and ^{13}N. Activities of 200 kBq have been measured from a single laser pulse of 10^{20} Wcm^{-2} interacting with a thin aluminium target. Various methods of increasing the induced activity and the possibility of developing this technique for the table-top laser production of PET isotopes commercially is discussed.

6.2 Experimental Set-up

The experiment used the ultra-intense CPA beam-line of the VULCAN Nd: Glass laser (Danson et al. 1998;Danson et al. 1999) (Chapter 3) incident on a thin 25 μm aluminium foil target, at 45° incidence with p-polarised light within an evacuated target chamber held at a modest vacuum of about 10^{-5} Torr. The experimental arrangement was essentially the same as that shown in Figure 5.1, pp 100, except that this time, the system delivered pulses of energies up to 120 J, duration 0.9-1.2 ps. When focused to a spot size of 6 μm using a F4, 450 mm focal length off-axis parabola (Chapter 3, pp 57), intensities up to 10^{20} Wcm^{-2} were achieved.

The VULCAN laser has a pre-pulse associated with it, with intensity roughly 10^{-6} that of the main pulse, arriving 300 ps before the main pulse. This is sufficient to ionise the target surface, generating a plasma that expands out in front of the target, which is known as "blow-off" plasma, consisting of electrons and ions. The type of ion depends on the target. The main pulse then interacts with this plasma, and causes electrons to be accelerated into the target (See Chapter 2 for a more detailed account). Proton beams are then produced in front of the target in the "blow-off" direction, and behind the target in the "straight through" direction (since the fast electrons exiting the rear of the target set up electrostatic fields due to space charge effects), as described in Chapter 2, Section 2.9 (in particular, see Figure 2.4, pp 39).

6.3 Results and Discussion

To characterise the proton beams, and to produce radioisotopes, different activation samples were placed in the target chamber, behind the target, in the straight through direction at a distance of 10 mm from the target, and in front of the target, directed along the target normal, at a distance 50 mm from the target, in the blow-off direction, as shown in Figure 6.1.

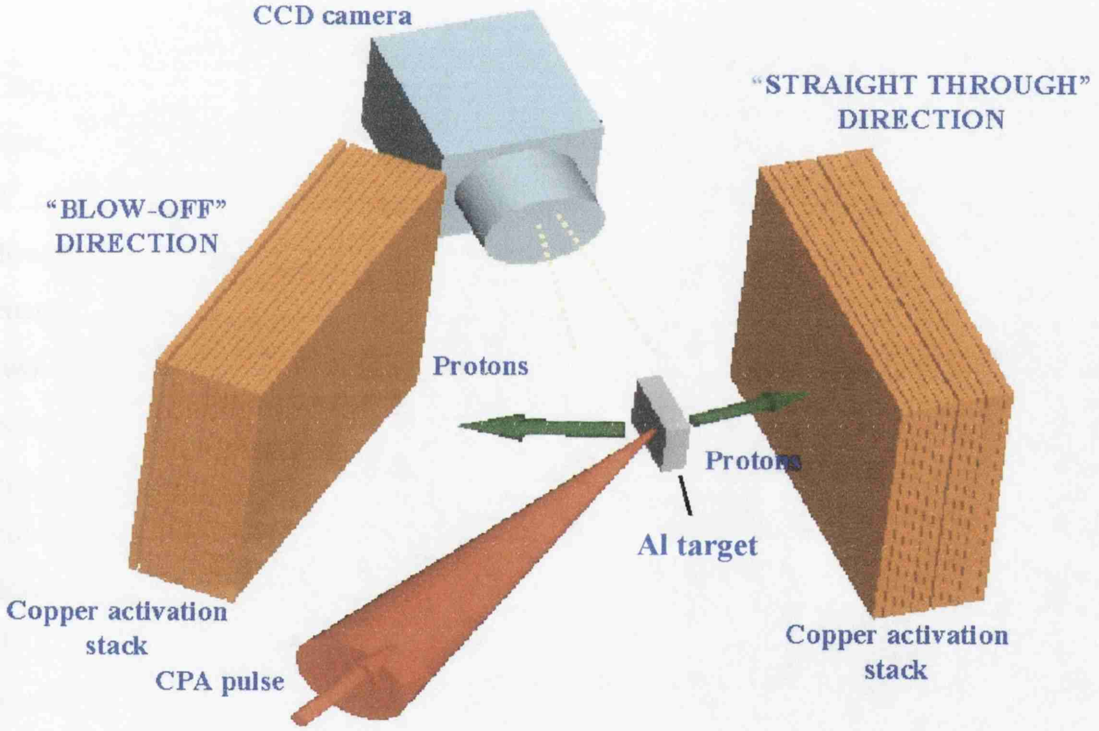

Figure 6.1 Target and activation sample arrangement, showing "blow-off" and "straight through" directions.

The time taken to extract the samples from the target chamber after laser irradiation was a few minutes, as the chamber must be returned to atmospheric pressure before the samples could be removed. These samples were then transferred to a nuclear laboratory for analysis limiting the lifetimes of the activated samples that could be measured to a few minutes or more. These practicalities are a temporary inconvenience, and will be resolved in future experiments.

The energy spectra of the accelerated protons were determined by placing activation stacks in both the blow-off and straight through directions. These consisted of nine pieces of copper foil, 100 μm thick, plus a 1 mm thick piece.

Previous results from Clark *et al.* (Clark et al. 2000a) show that the protons are emitted in the straight through direction in a cone half angle of 30°. The protons in the blow-off direction are emitted in a cone half angle of 20°. The copper activation stacks were positioned such that all the protons were incident on the stacks and hence a spatially integrated measurement was made.

Copper undergoes the nuclear reaction ^{63}Cu(p,n)^{63}Zn when bombarded with protons of energies greater than 4.15 MeV. The resulting Zn isotope is radioactive, and decays via β^+ emission with a characteristic half-life of 38.1 minutes. To recap, positrons slow down in solids and annihilate at rest with free electrons, producing two photons of energy 511 keV, at 180° to each other. These annihilation photons were detected using two 3"×3" NaI scintillation detectors, set up to detect 511 keV photons and operated in coincidence, as described in Chapter 4, Section 4.5. The efficiency of the system was again measured using a calibrated ^{22}Na source, and hence the absolute activity, i.e. the number of (p,n) reactions induced in each copper piece in the stack could be determined. Knowing the ^{63}Cu(p,n)^{63}Zn cross section, which is shown in Figure 6.2 (IAEA), the number of protons incident on each piece of copper in the stack can be found and hence a proton energy spectrum can be built up.

Each piece of copper in the stack represents an energy "bin", because protons are slowed down in copper. Figure 6.3 shows typical energy spectra of the emitted protons from the front and rear of the target. It is clear that more energetic protons are observed in the straight through direction, having energies up to a diagnostic limit of 37 MeV. The proton beam in the blow-off direction has a maximum energy of 25 MeV.

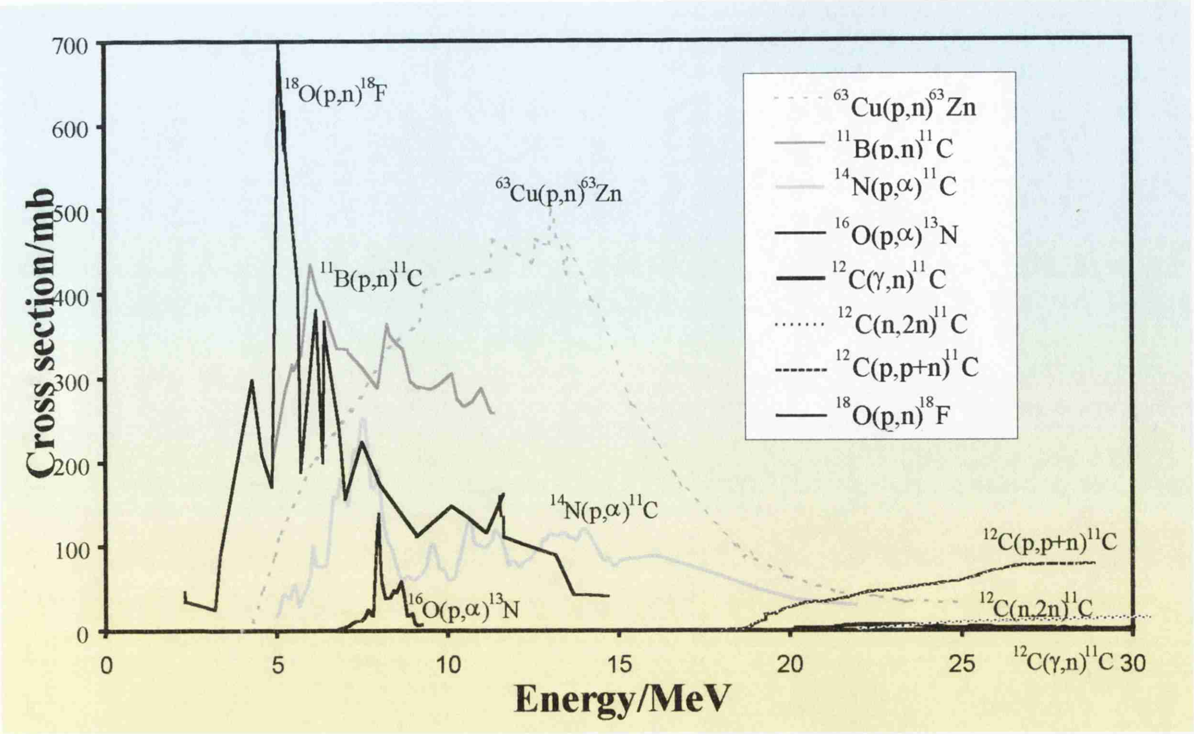

Figure 6.2 Experimentally measured cross-sections for the nuclear reactions discussed.

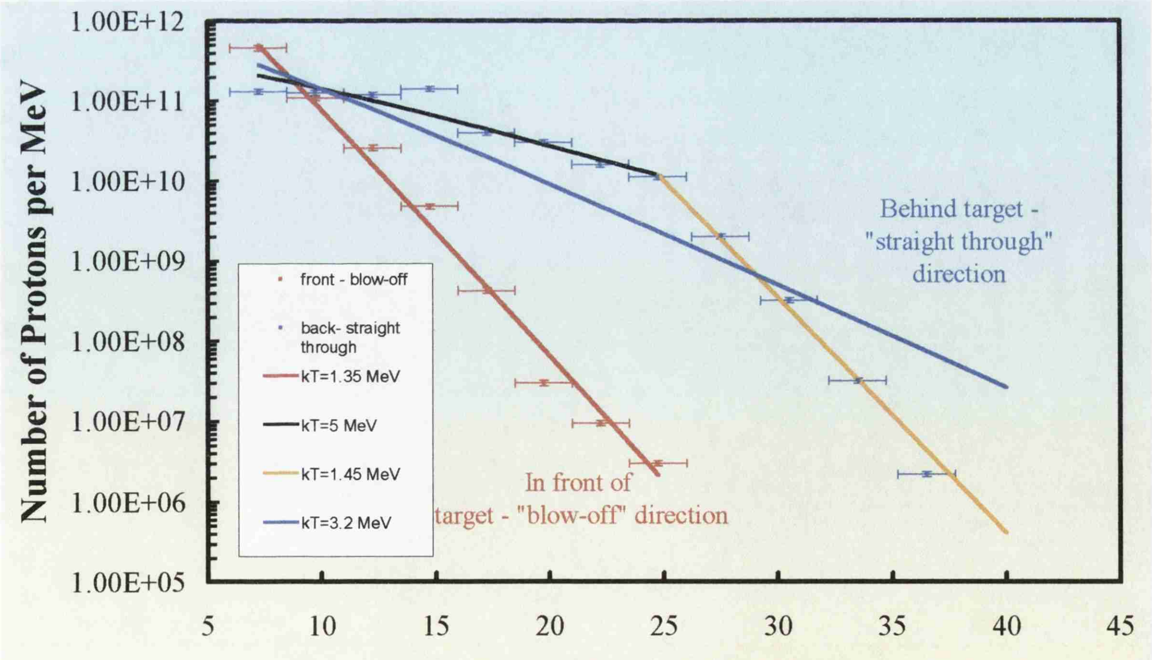

Figure 6.3 Proton energy spectra obtained from copper activation stacks in front of and behind the target.

A Maxwellian distribution expressed in terms of energy, $E^{1/2}\exp(-E/kT)$ (Diver 2001) where E is the proton energy, k is the Boltzmann constant and T is the proton temperature was fitted to the data. For the "blow-off" spectrum, a reasonable fit was obtained and the temperature was found to be 1.35 MeV. For the spectrum in the "straight through" direction, the best fit to the data yielded a temperature of 3.2 MeV, although it can be seen that the Maxwellian does not provide an overall fit to the data points. It can be seen that there are two gradients present, and these were fitted with Maxwellians also. The temperatures for these were found to be 1.45 and 5.00 MeV. The higher energy portion of this spectrum has a similar temperature to that of the "blow-off" spectrum. However, if the data presented is truly a superposition of two Maxwellians of temperature 5.00 and 1.45 MeV, then there should be a greater flux of lower energy protons to account for the 1.45 MeV component, and the proton energies should extend to higher energies due to the 5 MeV component. The sudden change in temperature at around 25 MeV is a feature that requires further investigation, but for the purposes of this study it is sufficient to state that in the "straight through" direction, around 8×10^{12} protons are produced with a maximum energy of 37 MeV.

Care must be taken when taking measurements of the induced activity in the copper pieces to account for competing reactions. The reaction ^{63}Cu(p,p+n)^{62}Cu takes place for proton energies above 10.9 MeV. The isotope ^{62}Cu can be distinguished from ^{63}Zn as it has a much shorter half-life of 9.8 minutes, compared to 38.1 minutes for ^{63}Zn. The cross section for this reaction is similar to that of the ^{63}Cu(p,n)^{63}Zn, but takes place at higher energies (IAEA). The typical decay of a copper activation sample is shown in Figure 6.4. When more than one isotope is present in a sample, the decay equation is defined by

$$A_t = A_{0_1} e^{-\lambda_1 t} + A_{0_2} e^{-\lambda_2 t} + \ldots. \qquad \text{Eqn (6.1)}$$

Where A_{01} is the activity of isotope (1) at t=0, A_{02} is the activity of isotope (2) at t=0, λ_1 and λ_2 are the decay constants of isotopes (1) and (2) respectively ($\lambda=\ln(2)/t_{1/2}$). The equation follows this form for the number of isotopes present in the sample.

The average half life of the decay plot shown in Figure 6.4 is 34.6 minutes. Since there are no likely products with this half-life, it must be assumed that there is more than one isotope present. A fit was made using the above equation, with $\lambda_1=\ln(2)/(9.8*60)\ s^{-1}$ (^{62}Cu) and $\lambda_2=\ln(2)/(38.1*60)\ s^{-1}$ (^{63}Zn). A best fit was found for $A_{01}/A_{02}=3/1$. The contribution from the reaction ^{63}Cu(p,p+n)^{62}Cu was accounted for when calculating the proton energy spectrum.

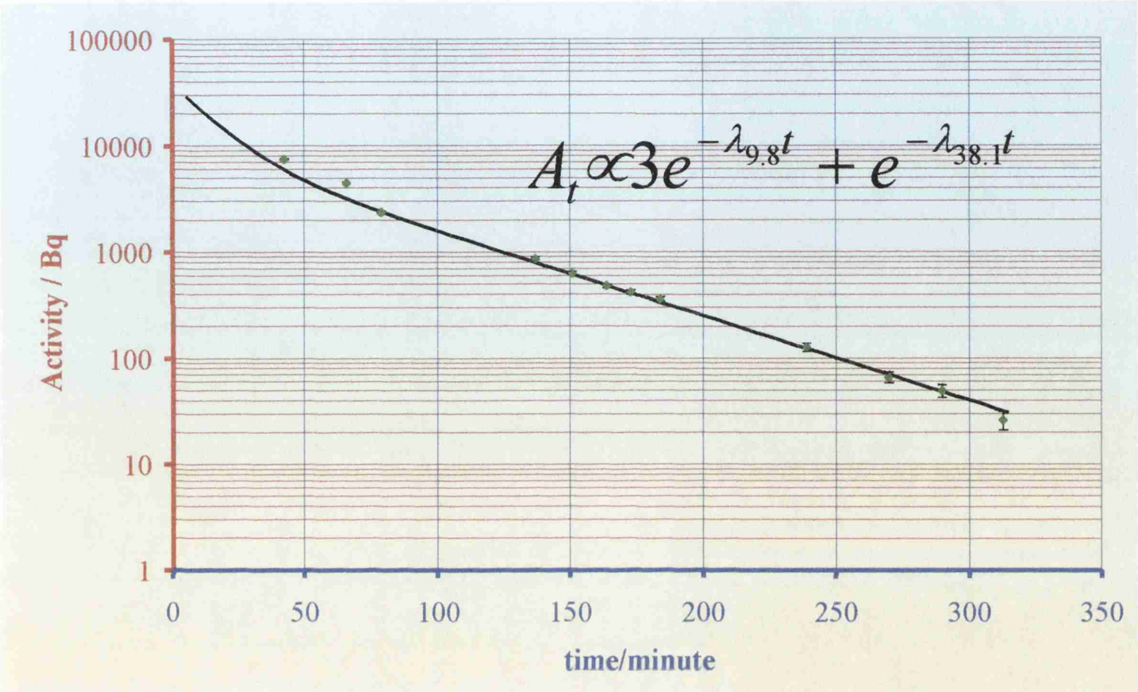

Figure 6.4 Typical decay curve of a copper activation stack. It is clear that two isotopes are present, ^{62}Cu and ^{63}Zn, and their relative abundance is 3:1.

It can be seen from the spectra shown in Figure 6.3 that around 8 × 10^{12} protons are produced in the straight through direction (around 5 × 10^{12} in the blow-off). As stated previously, these protons are present as hydrocarbon or water impurity layers on the rear target surface. Preliminary static SIMS surface analysis (Vickerman & Lockyer 2001) have revealed that a hydrocarbon layer of about 5 nm is present on the surfaces of the aluminium targets. A simple calculation assuming that the impurity layer consists of water molecules shows that to produce 10^{12} protons, the area involved must be greater than 150 × 150 μm^2, which is a factor of 100 greater than the laser focal spot region.

Different samples were placed in the target chamber and were bombarded with energetic protons from the intense laser-solid interaction. Samples were chosen to produce radioisotopes suitable for PET.

First, a boron sample of circular geometry with diameter 50 mm and thickness 3 mm was placed in front of the target, in the blow-off direction, prior to the laser irradiation. The induced activity in the boron sample was then measured in the coincidence system following laser irradiation. From the decay curve obtained (Figure 6.5) it is clear from the measured half-life of 20.3±0.4 minutes that the isotope produced was ^{11}C (accepted value 20.34 minutes) which is used in medical imaging for PET. The ^{11}B nuclei undergo (p,n) reactions to form ^{11}C, and the cross-section for this reaction is shown in Figure 6.2. By extrapolating this decay curve, it can be seen that the activity at t=0, i.e. at the time of laser irradiation was 200 kBq.

A sample of silicon nitride (SiN_4) of dimensions 20 × 20 mm^2 and thickness 1.75 mm was placed in front of the target. The silicon nuclei, when bombarded with protons in the present energy range, produce isotopes with lifetimes of a few seconds and a small amount of the 2.5 min ^{30}P isotope. Hence because of the finite transfer time of a few minutes they could not be detected in our current arrangement and can therefore be neglected.

The activity of the silicon nitride sample as a function of time was measured following laser irradiation, again using the coincidence unit. The results are shown in Figure 6.5. As with the boron activation, the isotope ^{11}C was produced (measured half-life 20.1±0.5 minutes), but this time via the reaction $^{14}N(p,\alpha)^{11}C$. The activity at t=0 (laser irradiation) was two orders of magnitude lower than the boron activation, at 2 kBq, but this is not surprising since the cross-section for this reaction is much lower (Figure 6.2).

A sample of silicon oxide (SiO_2) of dimensions 50 × 50 mm^2 and thickness 1.5 mm was placed in front of the target to undergo nuclear activation, and its activity measured as a function of time, again using the coincidence set-up. Again the silicon nuclei produced no measurable isotopes, but from the decay curve shown in Figure 6.6 it is clear that two isotopes are present. From the half-life measurements of 10.0±1.5 and 20.5±2 min, the isotopes were identified to be ^{13}N and ^{11}C, with accepted half-lives of 9.97 and 20.34 min, respectively.

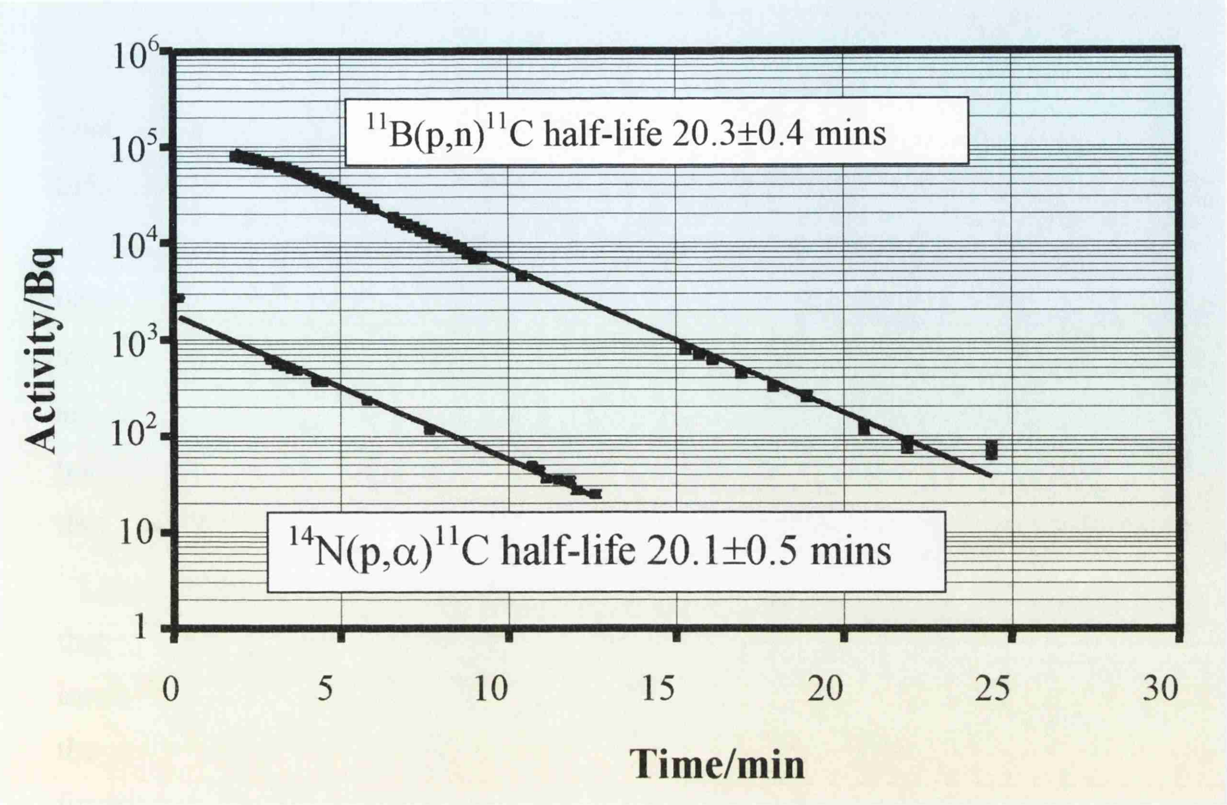

Figure 6.5 Decay curves for the activated boron and silicon nitride samples, showing that the isotope ^{11}C was produced via the reactions $^{11}B(p,n)^{11}C$ and $^{14}N(p,\alpha)^{11}C$.

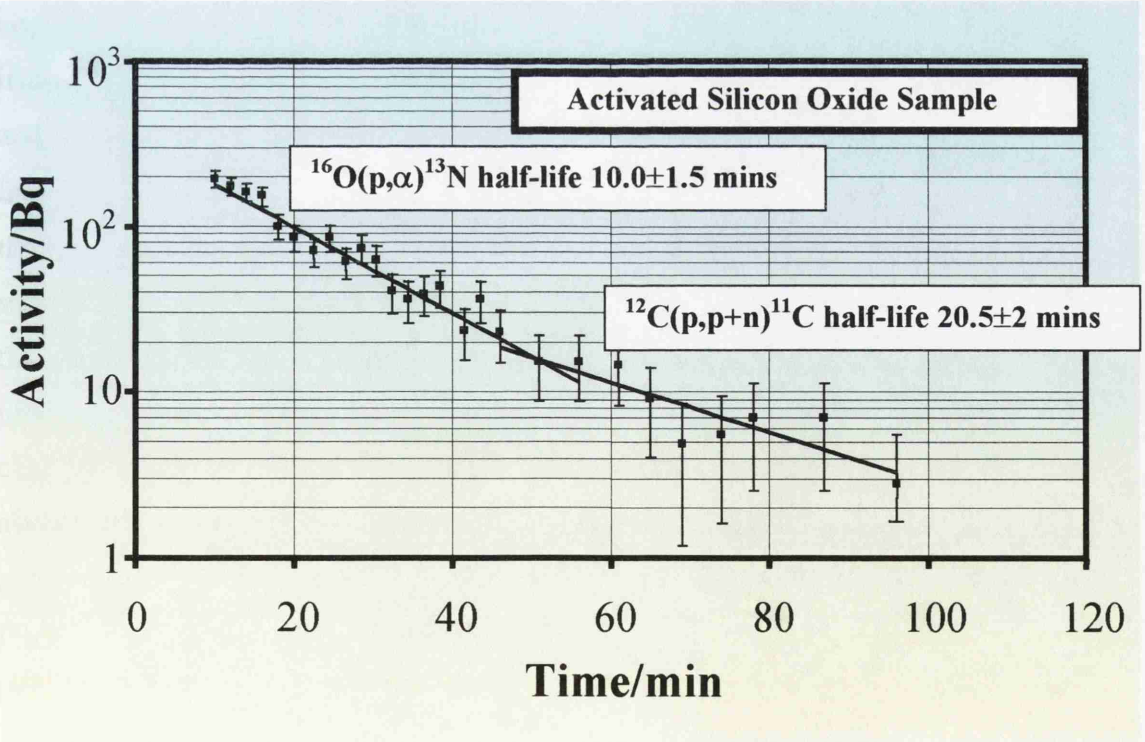

Figure 6.6 Decay curve for the silicon oxide sample. Two isotopes are present, ^{13}N from $^{16}O(p,\alpha)^{13}N$ reactions and ^{11}C, most likely from $^{12}C(p,p+n)^{11}C$ reactions. The carbon nuclei are present due to hydrocarbon impurities on the surface of the SiO_2 sample.

The ^{13}N component is produced via the reaction $^{16}O(p,\alpha)^{13}N$ and the cross section for this reaction is shown in Figure 6.2. It is believed that the ^{11}C content is produced from ^{12}C nuclei, which are present due to hydrocarbon impurities on the surface of the silicon oxide. Although the target is thin (125 μm) aluminium (Z=13) and the activation sample of silicon oxide is also composed of low Z materials, some high energy γ-rays are produced via bremsstrahlung. Neutrons are also produced from the (p,n) reactions taking place, however by analysing reaction cross-sections (Figure 6.2) it can be seen that the reaction $^{12}C(p,p+n)^{11}C$ is most likely, rather than the reactions $^{12}C(\gamma,n)^{11}C$ or $^{12}C(n,2n)^{11}C$. Furthermore, the fluxes of neutrons and γ-rays are considerably less than that of protons since they are produced via secondary processes. The presence of two isotopes of different atomic number presents no problems for applied purposes, since the nitrogen and carbon components can be separated via fast chemistry. Even so, future experiments will be conducted using "clean" activation samples that have been heated prior to use in order to remove all surface impurity layers.

Finally, the induced activity in copper was measured as a function of laser intensity. A copper sample of thickness 2 mm was placed in the blow-off direction prior to laser irradiation. The activity of the sample was then measured in the coincidence counter, and this process was repeated for five different laser pulses, with intensities ranging from 2×10^{19} Wcm^{-2} to 10^{20} Wcm^{-2}. The results are shown in Figure 6.7. It can be seen that as the laser intensity increases, the proton production rate flattens out, i.e. there is a saturation effect present. It is thought that this factor is dependent on the target, since the protons are generated from very thin hydrocarbon and water impurity layers on the target surfaces. Further experiments are required to fully analyse this effect, using well characterised targets, and also different materials, e.g. plastic (CH) targets, targets with absorbed hydrogen and cluster targets, in order to determine the optimum target for proton production. Also the proton production rate will be measured systematically as a function of target thickness in future experiments. Preliminary studies of target thickness dependence have been carried out by Maksimchuk *et al.* (Maksimchuk et al. 2000) where the energy of the protons only was measured as a function of target thickness.

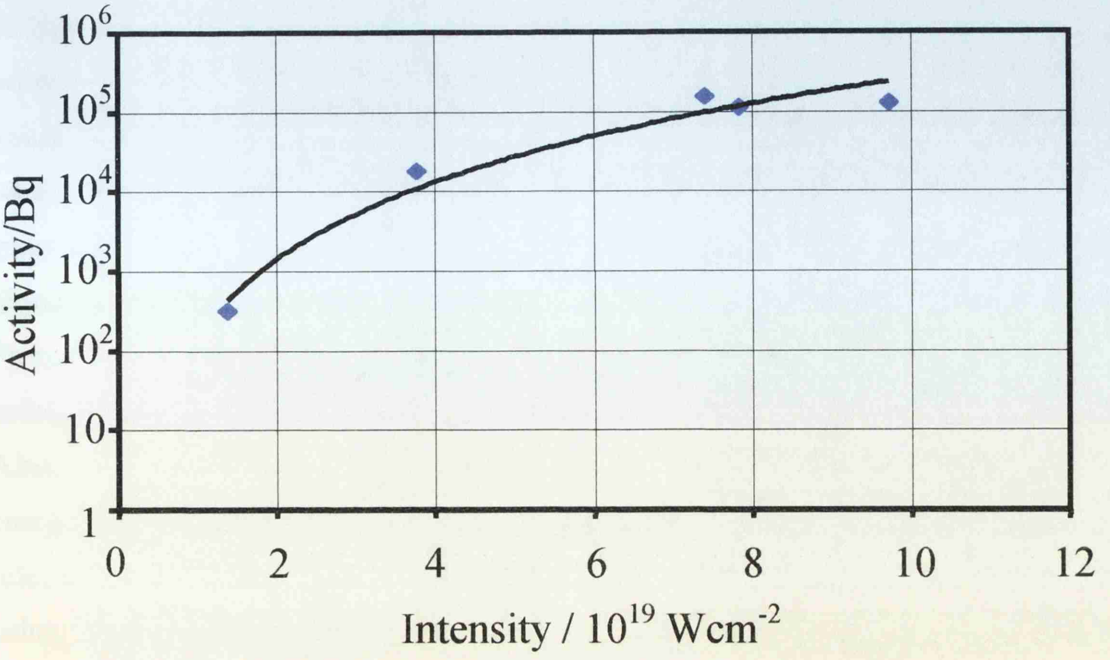

Figure 6.7 Induced activity as a function of laser intensity. The "flattening out" of the curve is apparent with increasing intensity, indicating a saturation effect.

6.4 Conclusions

It has been shown that protons of energies up to 37 MeV can be generated when an ultra-intense laser interacts with solid targets. These energetic protons can then be used to trigger (p,n) and (p,α) reactions in various materials, to produce radioisotopes that are used in nuclear medicine, specifically PET. Activities of 2×10^5 Bq of the isotope ^{11}C have been measured.

Although ^{11}C is a useful isotope for PET, the favoured isotope at the moment is ^{18}F. The reaction usually employed to produce this isotope is ^{18}O(p,n)^{18}F. The cross-section for this reaction is shown against the ^{11}B(p,n)^{11}C reaction in Figure 6.2. The integrated cross-section for the ^{18}F producing reaction is about half that of the ^{11}C reaction, hence it is feasible that the VULCAN laser could produce 10^5 Bq of ^{18}F per shot, operating at 10^{20} Wcm^{-2}.

A typical patient dose for PET is 200 MBq although up to 800 MBq sources are necessary to allow time for fast chemistry to be performed on the sample to separate the tracer from the inactive carrier. Assuming that a VULCAN type laser could deliver 10 Hz, then the integrated activity after 500 s is about 10^9 Bq. If this source was generated by a 1 J pulse typical of table-top lasers then a kHz repetition rate would be required since it is predicted that the proton flux would be reduced by x100 in this case. Further improvement in the production rate will be achieved by optimising the laser pre-pulse, and as stated previously, the target material, thickness and surface treatment. Also, it has been shown that the proton spectrum from the rear of the target is more energetic, which could also lead to higher activities since the cross-sections for the relevant reactions extend to this current limit of 37 MeV. One possible drawback of using higher energies is that unwanted isotopes may be produced via higher-order reactions. Yamagiwa and Koga (Yamigiwa & Koga 1999) have estimated that ^{18}F yields as high as 10^{14} Bq – two orders of magnitude higher than that obtainable with a standard cyclotron – can be generated if the laser intensity were increased to 10^{21} Wcm^{-2}, at 1 μm wavelength.

At present a smaller scale laser operating at 1 kHz and 0.3 J per pulse is proposed (Ross 2001) which would approach the required irradiance on target to provide sufficiently intense ^{18}F sources. The proposed design contains an Nd: YLF laser system (100 ps modelocked oscillator and several diode-pumped amplifiers) operating at a wavelength of 1.047 μm and generating 1 J pulses at 1 kHz repetition rate using a total peak pump power of 100 kW (quasi-cw). The output of this laser is used to pump an optical parametric chirped pulse amplifier (OPCPA) (Ross et al. 1999) which amplifies chirped pulses at a wavelength of 2 μm up to an energy of 0.3 J. These pulses are compressed to 30 fs and focused to a sub-10 μm spot size to generate intensities of 10^{19} Wcm^{-2}. Although this laser is based on existing technology and the basis of the proton generation process has been established, the complete system will operate in a regime at the forefront of laser physics and technology. A full study of such a system is the basis of a new research proposal (Ross 2001), which will seek funding from the "Physics for Healthcare" scheme. A laser with a pulse energy of 0.3 J is expected to produce proton fluxes of ~3 × 10^{-3} that of a VULCAN type laser, although this is compensated by the much improved 1 kHz repetition rate. Part of this study involves using the ASTRA Ti: Sapphire laser to investigate proton production from a table-top laser. This laser is under continual development, and when complete should yield intensities in excess of 10^{19} Wcm^{-2} at 800 nm wavelength. Preliminary results of experiments conducted using this system are reported in Chapter 7.

Finally, it has been shown that beams of cyclotron produced energetic protons can be used to treat tumours, with greater efficiency than conventional X-radiotherapy, because protons have more suitable dE/dx curves (energy loss per unit distance travelled through a medium) than X or γ-rays. Protons with their characteristic "Bragg Peak" (Indiana University;Wilson 1946) deposit almost all of their energy just before coming to rest in materials. Figure 6.8 shows the depth-dose curve of a 200 MeV proton in water compared to that of a 20 MeV electron and an 8 MeV X-ray. This means that proton beam energies can be tuned efficiently to treat the tumour, once the position of the tumour is determined by techniques such as PET. The red curve in Figure 6.8 shows the "summed over Bragg peaks" (SOBP) distribution for a spectrum of proton energies, selected to deposit energy over a range of 5 cm. The energy required for proton oncology is typically 150 MeV.

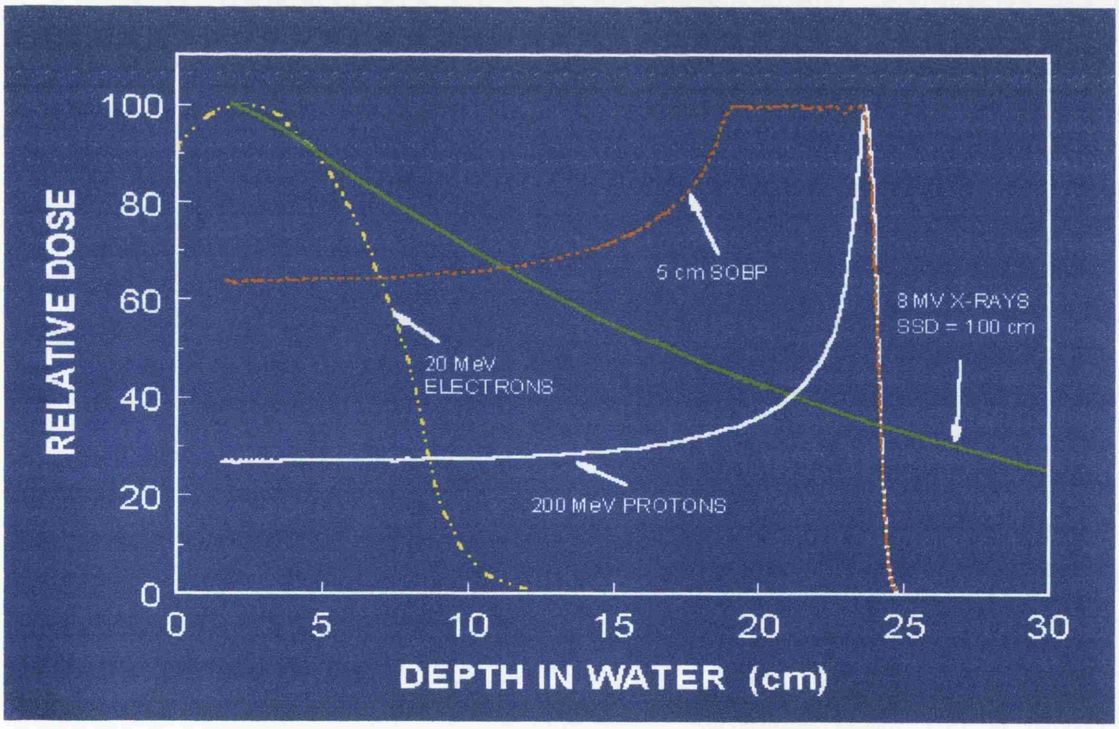

Figure 6.8 Depth –dose curves for protons, electrons and X-rays. The red curve shows the "summed over Bragg peaks" distribution for a spectrum of proton energies, selected to deposit their energy in a range of 5 cm.

It has been shown by Clark *et al.* (Clark et al. 2000b) that the irradiance required to generate protons of 150 MeV required for proton oncology is 5×10^{21} $Wcm^{-2}\mu m^{2}$. (Esirkepov et al. 1999) have shown theoretically that ions of energies as high as 1 GeV can be generated at 2×10^{21} $Wcm^{2}\mu m^{2}$. These intensities, however, require energies of 100 J in 30 fs in a 10 μm diameter focal spot with lasers operating at 1 μm wavelength. These parameters are extreme but one possible development of an oncology laser might be based on an upgrade of the PET laser described above. This laser will operate at 2 μm rather than 1 μm, and consequently the energy required to reach an irradiance of 5×10^{21} $Wcm^{-2}\mu m^{2}$ is reduced to 25 J per pulse, since a λ=2 μm laser gives a factor of ~4 increase in $I\lambda^{2}$ compared to a 1.053 μm beam at the same I. This is a significant energy saving compared to 100 J for a Nd: glass or Ti: sapphire laser, but is still two orders of magnitude larger than the 0.3 J level of the PET laser.

In summary, it has been shown that high-intensity lasers can be used to produce short-lived positron-emitting nuclei. A possible extension of this work is to generate proton beams using a table-top laser, and preliminary results of this using the ASTRA laser, a system still under development are shown in the next chapter.

References

Clark, E. L., Krushelnick, K., Davies, J. R., Zepf, M., Tatarakis, M., Beg, F. N., Machacek, A., Norreys, P. A., Santala, M. I. K., Watts, I., & Dangor, A. E. 2000a, "Measurements of energetic proton transport through magnetized plasma from intense laser interactions with solids", *Physical Review Letters*, vol. 84, p. 670.

Clark, E. L., Krushelnick, K., Zepf, M., Beg, F. N., Tatarakis, M., Machacek, A., Santala, M. I. K., Watts, I., Norreys, P. A., & Dangor, A. E. 2000b, "Energetic heavy-ion and proton generation from ultra-intense laser-plasma interactions with solids", *Physical Review Letters*, vol. 85, p. 1654.

Danson, C., Collier, J., Neely, D., Barzanti, L. J., Damerell, A., Edwards, C. B., Hutchinson, M. H. R., Key, M. H., Norreys, P. A., Pepler, D. A., Ross, I. N., Taday, P. F., Toner, W. T., Trentelman, M., Walsh, F. N., Winstone, T. B., & Wyatt, R. W. W.

1998, "Well characterized 10^{19} Wcm^{-2} operation of VULCAN - an ultra-high power Nd: glass laser", *Journal of Modern Optics*, vol. 45, p. 1653.

Danson, C. N., Allott, R. M., Booth, G., Collier, J., Edwards, C. B., Flintoff, P. S., Hawkes, S. J., Hutchinson, M. H. R., Hernandez-Gomez, C., Leach, J., Neely, D., Norreys, P. A., Notley, M., Pepler, D. A., Ross, I. N., Walczak, J. A., & Winstone, T. B. 1999, "Generation of focused intensities of $5\text{x}10^{19}$ Wcm^{-2}", *Laser and Particle Beams*, vol. 17, p. 341.

Diver, D. 2001, *A Plasma Formulary for Physics, Technology and Astrophysics* Wiley-VCH.

Esirkepov, T. Z., Sentoku, Y., Mima, K., Nishihara, K., Califano, F., Pegoraro, F., Naumova, N. M., Bulanov, S. V., Ueshima, Y., Liseikina, T. V., Vshvkov, V. A., & Kato, Y. 1999, "Ion acclereration by superintense laser pulses in plasmas", *JETP Letters*, vol. 70, p. 82.

IAEA. EXFOR nuclear reaction database – http://iaeand.iaea.or.at/exfor/.

Indiana University Cyclotron Facility Website –
http://www.Iucf.indiana.edu/MPRI/about.htm

Maksimchuk, A., Gu, S., Flippo, K., & Umstadter, D. 2000, "Forward ion acceleration in thin films driven by a high-intensity laser", *Physical Review Letters*, vol. 84, p. 4108.

Ross, I. N. 2001, "Feasibility study of high repetition-rate, ultra-intense lasers for energetic proton production in nuclear medicine, to be published.

Ross, I. N., Matousek, P., Towrie, M., Langley, A. J., Collier, J., Danson, C., Hernandez-Gomez, C., Neely, D., & Osvay, K. 1999, "Prospects for a multi-PW source using optical parametric chirped pulse amplifiers", *Laser and Particle Beams*, vol. 17, p. 331.

Vickerman, J. & Lockyer, N. It is a pleasure to acknowledge discussions and preliminary measurements of hydrocarbon layers on metal surfaces with Prof. J Vickerman and Dr.N Lockyer, Department of Chemistry, UMIST. 2001.

Wilson, R. R. 1946, *Radiology*, vol. 47, p. 487.

Yamigiwa, M. & Koga, J. 1999, "MeV ion generation by an ultra-intense short-pulse laser: application to positron emitting radionuclide production", *Journal of Physics D*, vol. 32, p. 2526.

Chapter 7

Proton Production from ASTRA – A High-Power, Compact, High Repetition Rate Laser – Preliminary Results

This Chapter reports preliminary results of proton generation using the ASTRA Ti: sapphire laser system – a much smaller scale facility than VULCAN with a much higher repetition-rate. A brief description of the operating characteristics of ASTRA is provided. The system is currently under development, and at the time these experiments were conducted, was operating at ~6 × 10^{17} Wcm^{-2}μm^{2}, compared to 10^{19-20} Wcm^{-2}μm^{2} for VULCAN. The implications these early results have on future experiments are discussed.

7.1 Introduction

The last chapter reported results of the production of proton beams using the large-scale, low-repetition rate laser system, VULCAN. A natural extension of this work is to generate similar beams using high repetition-rate table-top lasers. In order to achieve this, smaller scale systems must be able to achieve intensities similar to that of VULCAN.

With the extraordinary advancement of laser technology, lasers of this type are beginning to become a reality. Some of these systems are listed in Table 1.1, pp 10. One such candidate is the ASTRA Ti: sapphire laser system at the Rutherford Appleton Laboratory, UK. This is a system under continual development, and when completed will achieve intensities in excess of 10^{19} Wcm^{-2} at 800 nm with a rep-rate of 2 Hz.

When the experiments described below were conducted, ASTRA was operating at an intensity ~10^{18} Wcm^{-2}. The results described however are important to test the feasibility of using such a system for proton production, given the differences in such a system compared to VULCAN; most notably that the pulse energy is much lower than VULCAN, and the pulse length is much shorter, as will be shown below.

This chapter describes briefly the operation of the ASTRA system, and then reports preliminary results of proton production experiments on the laser. A short discussion follows on the implications the results found have on future possibilities.

7.2 Experimental

ASTRA is a high-power, ultra short pulse titanium-sapphire laser facility (Hooker & Marshall 1999;Langley et al. 1999a;Langley et al. 1999b;Langley et al. 2000). A floor plan of the system is shown in Figure 7.1.

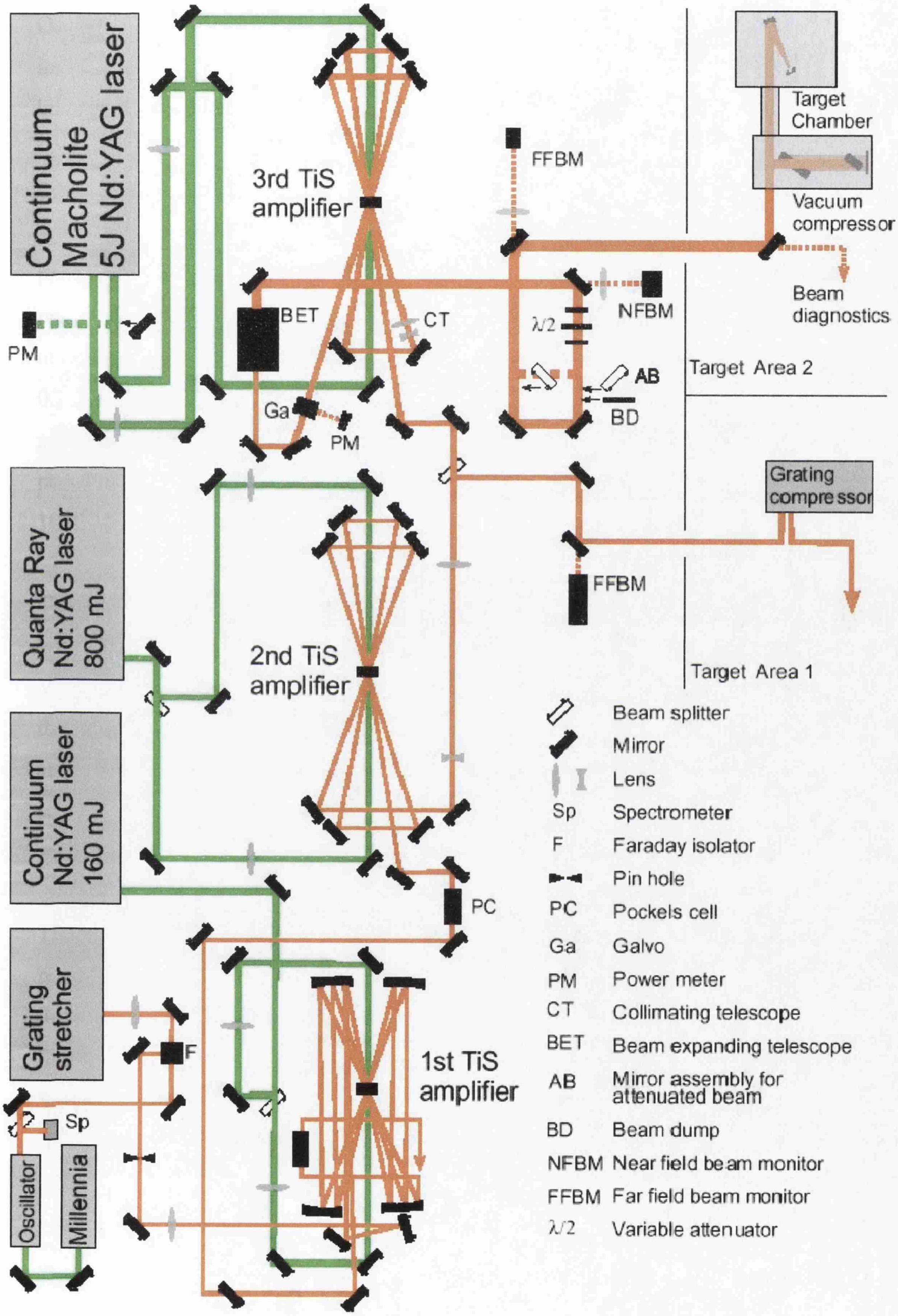

Figure 7.1 Floor plan of the ASTRA Ti:sapphire laser facility.

The ASTRA system, in common with other high-power lasers, has a MOPA (Master Oscillator – Power Amplifier) architecture, similar to that of VULCAN. For further information, see Chapter 3. Because the source pulses are so short, it uses the well-known technique of Chirped Pulse Amplification (Chapter 3, pp 51-55 and references therein) to prevent damage to the amplifiers and adverse nonlinear effects. Single pulses from the oscillator, of 20 fs duration and energy 5 nJ, are stretched to 530 ps then amplified in the 1st amplifier to around 1 mJ. After spatial filtering to clean up the beam profile, the energy is boosted to 200 mJ in the second power amplifier before half of the pulse is split off and sent to the terawatt target area, TA1, for use in experiments. The other half is amplified further in the third power amplifier, reaching pulse energies up to 0.5 J on target (when development is completed), and is subsequently used for plasma physics experiments in the multi-terawatt target area TA2. In each target area, the pulses are recompressed to a duration of about 70 fs before use. Pulses are available at 10 Hz in TA1 and up to 2 Hz in TA2.

This overview, although it describes the main features of ASTRA is somewhat simplistic, and for more information one should consult the above references. The VULCAN laser was described in more detail since most of the results reported in this thesis were generated using this system. However, the concepts discussed in Chapter 3 are general for high-power lasers and the main features of ASTRA (front end oscillator, stretcher, amplifiers, compressor) are similar to VULCAN, albeit on a smaller physical scale.

The pulse exiting the third amplifier is roughly circular in shape, diameter 60 mm. The beam diagnostics in place are a joulemeter which measures a leakage beam after the third amplifier. This is cross-calibrated periodically with a direct measurement of the full beam energy using a calorimeter, in a similar fashion to that described in Chapter 3, Section 3.3.1, pp 58-59. The pulse length was measured using an autocorrelator (Chapter 3, Section 3.3.2, pp 59-61), positioned after the compressor. A systematic measurement of the pulse contrast ratio has not as yet been conducted, although a pre-pulse of 2×10^{-5} that of the main pulse arriving on target 13 ns before the main pulse has been measured, originating from the finite opening and closing time of the galvo whose purpose it is to select single pulses. Work is currently underway to reduce this pre-pulse and hopefully eliminate it. Preliminary measurements of contrast ratio (the ratio of the main pulse intensity to the intensity of the amplified spontaneous emission, ASE) show that it is at least 1: 10^{-4}, although at the moment it is unknown how long this is present during the interaction. A full characterised measurement of the pulse profile, including pre-pulses and ASE, and optimisation of these features is part of the ongoing development programme of the ASTRA system. A diagnostic capable of measuring ASE levels is a third-order autocorrelator, such as the system described in Chapter 3, Section 3.3.4, pp 63-66.

To give an idea of the physical scale of the system, Figure 7.2 shows one of the CPA compression gratings. The white light from the flash of the camera can be seen to be dispersed into its spectral components following interaction with the grating. Figure 7.3 shows the high-power target interaction chamber of the ASTRA laser.

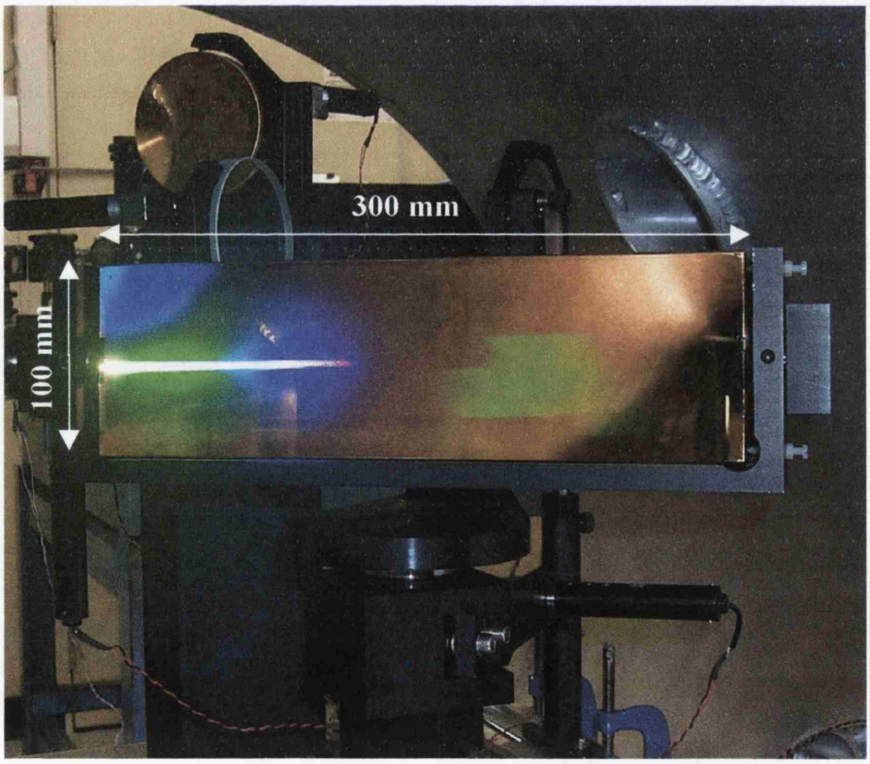

Figure 7.2 One of the compression gratings in ASTRA TA2. The white light from the flash of the camera can be seen to be dispersed into its spectral components.

Figure 7.3 Tom McCanny of the University of Glasgow working on the ASTRA TA2 interaction chamber.

At the time the experiments were conducted, the system delivered pulses on target of 150 mJ, duration 70 fs at a rate of 1 Hz with a wavelength centred at 800 nm, and when focused to a spot size of 12 μm (measured by passing a CW beam of similar wavelength to ASTRA down the system and placing a CCD camera at the focal spot, calibrated using a grating with line spacing of known dimensions) using a F3 off-axis parabolic mirror, yielded intensities of 10^{18} Wcm^{-2} (irradiance ~6 × 10^{17} Wcm^{-2}μm^{2}). The pre-pulse, as described above is sufficient to ionise the target surface, producing a pre-plasma with a density scale length ~1.40 mm which expands out in front of the target prior to the arrival of the main pulse (assuming that the plasma expands thermally at a rate of 10^{7} cms^{-1}). The main pulse/ASE contrast ratio, or "pedestal") at 1: 10^{-4} would almost certainly enhance this effect, and is present throughout the interaction. The pre-pulse and ASE intensity was not sufficient to create a crater in the target however, although this effect was observed for the main pulse interaction.

The laser light was incident on either 18 μm thick magnetic TDK tape, or 23 μm thick CH tape, at 45° incidence, with p-polarised light within an evacuated target chamber. The pressure of the vacuum was nominally 10^{-4} Torr. The experimental set-up is shown

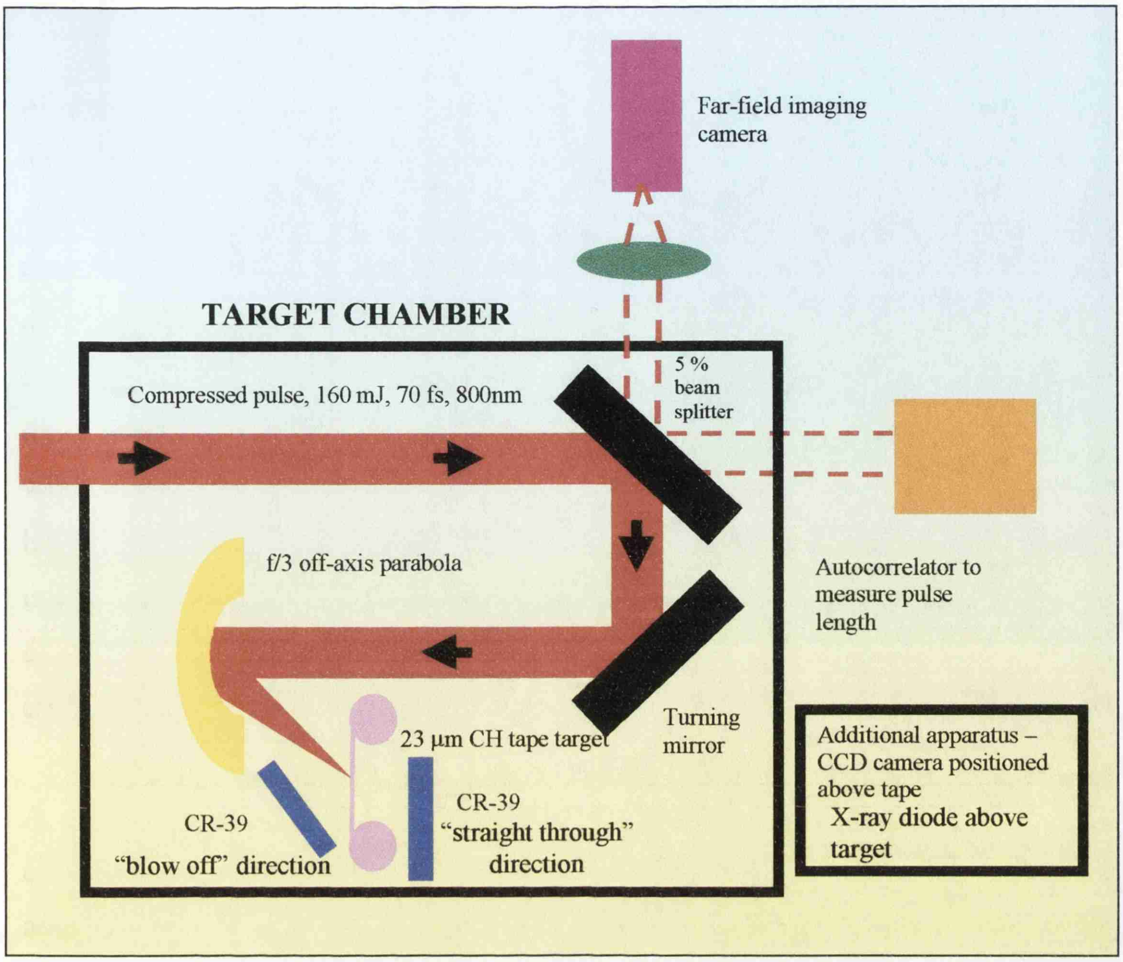

Figure 7.4 Schematic of the experimental set-up.

in Figure 7.4. Two 95 % reflecting turning mirrors were used to steer the beam on target, prior to focusing. The first turning mirror permitted 5 % transmission of the laser energy to allow measurements of the pulse duration to be taken by a single shot autocorrelator (see Chapter 3, pp 59 and references therein), and to view the far-field image of the laser-focus via a CCD camera. This is a technique known as retro-reflection, and can provide information about the best focal spot since light is reflected from the target back down the chain, so the camera sees an image of the focal spot. Due to the use of a focusing lens to view the image on the CCD camera, it does not however yield the actual physical dimensions of the spot, and only yields information about the best spot once this has been found using other techniques. The focal spot dimensions was measured using a CW beam of similar wavelength to ASTRA and a CCD camera at the focal spot as described above. The position of best focus was found using an X-ray diode, positioned above the target, the signal of which maximises when at best focus, since this is when the X-ray flux from the interaction is greatest. This technique is slightly ambiguous however, since the signal produced is the sum of all photons produced in the interaction. It can yield information about X-ray flux, but does not give an indication of the dimensions of the X-ray source. A better technique is to use an X-ray pinhole camera which actually measures the dimensions of the X-ray spot size. This diagnostic is in place in VULCAN. This again highlights the need for better and more diagnostics for ASTRA, but is typical for a new system under development. VULCAN on the other hand is a well-established operation which has been developing its diagnostics for many years. When ASTRA development is complete, it is hoped that it will have diagnostics in place on a par with that of VULCAN. It must be stressed again however that the present experiment is an important one in order to test the viability of using table-top lasers for the kind of work carried out on VULCAN in Chapter 6, and even though some information about the pulse is unknown, it was still possible to estimate the intensity on target with a sufficient degree of confidence.

A second CCD camera was positioned above the tape target in order to view plasma emission from the laser-solid interaction. A tape target was used so that the tape was advanced after every laser pulse, and hence the laser interacted with a fresh piece of target for every shot. This tape target is shown in Figure 7.5.

CR-39 is a plastic nuclear track detector which is sensitive to ions with energies greater than 100 keV / nucleon. When a nucleon is incident on a piece of CR-39, it causes structural damage just before it comes to rest, which after etching with sodium hydroxide, produces a pit of definite dimensions. The heavier the incident ion, the greater the pit size. CR-39 is not sensitive to electrons, or other ionising radiation such as X-rays, since their dE/dx curves (energy loss/unit thickness as they pass through matter) do not have an ion-like Bragg Peak and hence do not cause structural damage (see Chapter 6, pp 132, Figure 6.8). Pieces of CR-39 were placed in the target chamber, behind the target, in the "straight through" direction at a distance 40 mm from the target, and in front of the target, directed along the target normal, at a distance 180 mm from the target, in the "blow-off direction".

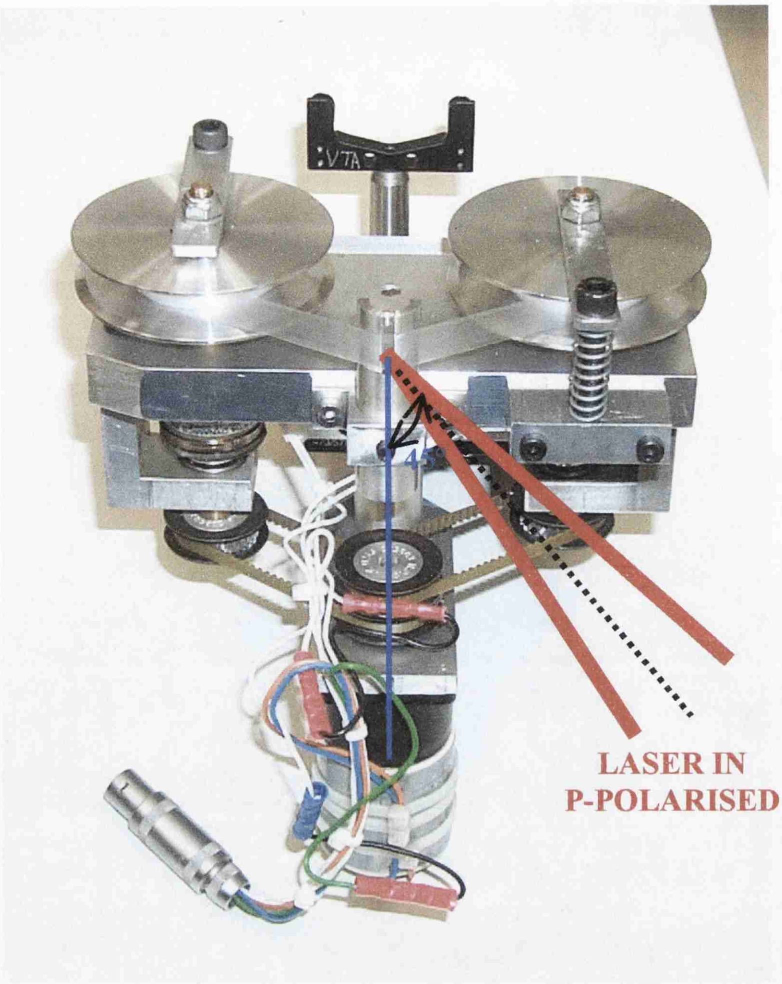

Figure 7.5 Tape drive target used in the experiments.

7.3 Results and Discussion

The first experiment carried out was to observe proton and possibly heavier ion emission from the laser-solid interaction. Laser pulses were incident on 18 μm thick TDK tape for this experiment. This magnetic tape was composed of a 12 μm thick CH layer, plus a 6 μm thick layer of fine grained ferric (iron) particles.

When the CR-39 samples were analysed, it was found that when the grained ferric particle layer faced the straight through direction, the CR-39 sample showed evidence of protons, carbon ions and larger pits which are believed to be iron ions. A magnified image of the CR39 is shown in Figure 7.6. Pits of three different sizes are evident, corresponding to protons (smallest), carbon (medium) and iron (largest) ions. The CR-39 samples in the blow-off position did not contain these iron pits, only protons and

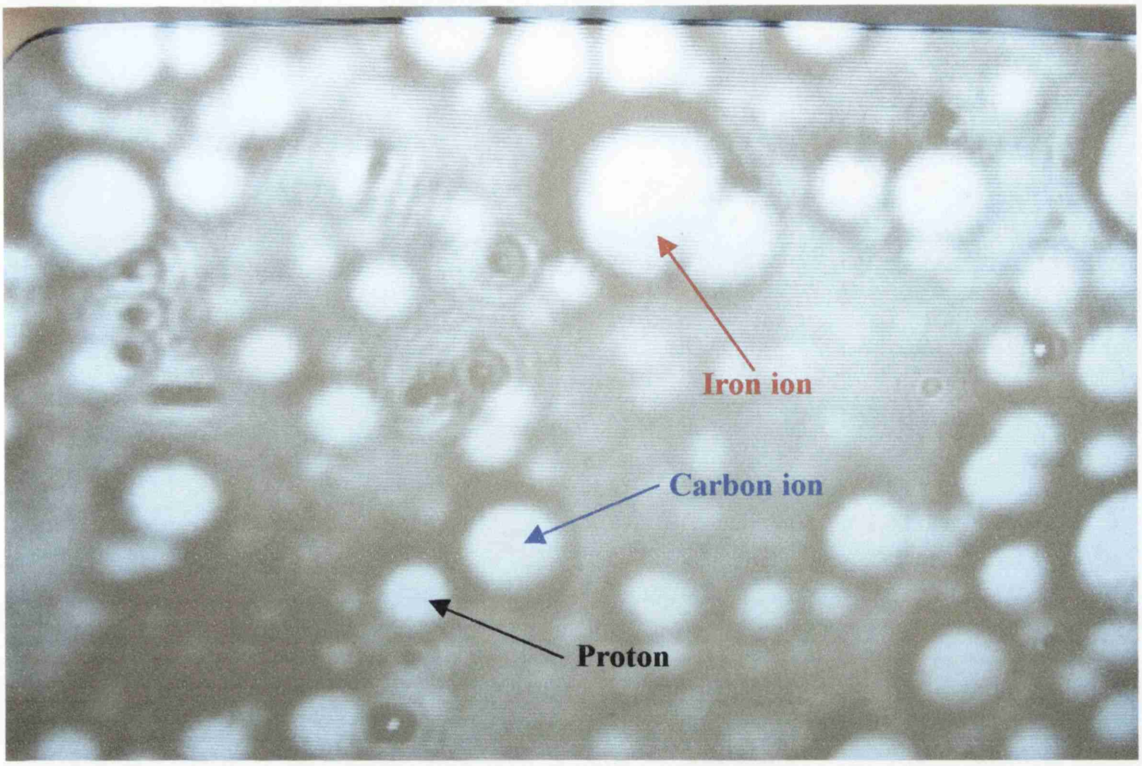

Figure 7.6 Magnified image of CR39. Proton, carbon and iron ion pits are evident.

carbon ions. This is in agreement with the picture described in Chapter 2, Section 2.9, pp 37-39 (Wilks et al. 2001), where the fast electrons produced in the interaction travel through the target and ionise the rear surface, then drag ions in their wake via charge separation as they leave the target. If, however, protons originate from the front of the target and travel through the target and out the rear as described by Clark *et al.* (Clark et al. 2000), and Maksimchuk *et al.* (Maksimchuk et al. 2000) then they would need energies of at least 1.5 MeV to traverse the target, assuming that the 6 μm ferric layer consists purely of iron atoms. Table 7.1 lists the various ions, and their approximate abundance / sr / laser pulse.

Ion species	**Position**	**Abundance / sr / shot**
Protons	Blow-off	7.9×10^5
Carbon	Blow-off	4.2×10^4
Protons	Straight-through	3.6×10^6
Carbon	Straight-through	1.3×10^6
Iron	Straight-through	5.6×10^5

Table 7.1 Detected ions above 100 keV/nucleon, and their relative abundance/sr/shot.

Once evidence for proton emission was established, the next experiment was to obtain an estimate of the energies of the protons being emitted. This was achieved by covering the CR-39 in mylar filters of varying thickness, ranging from 3 μm to 12 μm, and directing the laser at a 23 μm CH tape target. Thicker filters stop protons of higher energy, and the stopping distances of protons of various energies in mylar is well known (National Institute of Standards and Technology Physics Laboroatory), and so using filters of various thickness, it was possible to build up a spectrum of the protons emitted in the laser-solid interaction. Figure 7.7 shows a typical spectrum of protons emitted in the "straight through" direction. This shows a maximum proton energy of around 600 keV, and a mean energy of about 250 keV. This energy range is roughly as expected for a system operating at an intensity of 10^{18} Wcm^{-2}, and an irradiance of 6×10^{17} Wcm^{-2}μm^2 (λ=800 nm) and in reasonable agreement with previous observations on the VULCAN laser (Fews et al. 1994).

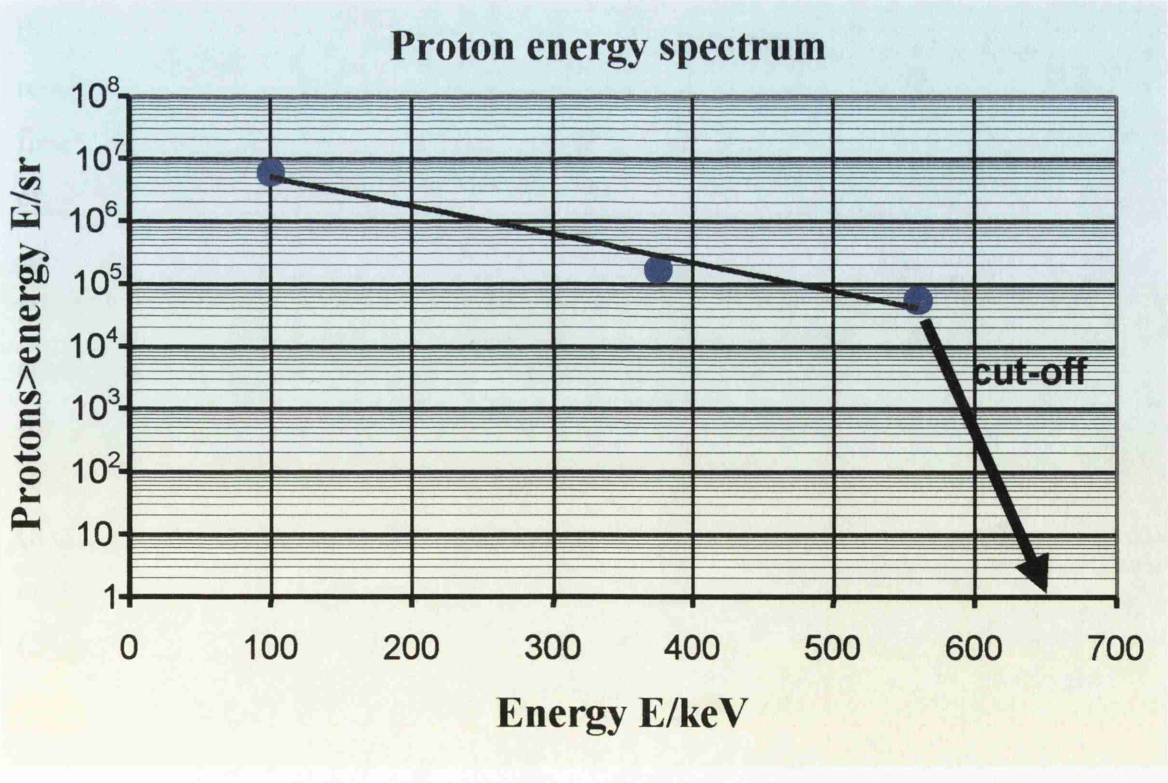

Figure 7.7 Spectrum of proton energies emitted in the "straight through" direction. This shows an energy cut-off at about 600 keV, and a mean energy of 250 keV.

No iron ions were produced since the target in this case consisted of pure CH. Carbon ions were not observed either, since their much shorter stopping distances meant that they would all be stopped in the thinnest 3 μm layer.

In the blow-off direction, no protons were seen that could penetrate the 3 μm mylar filter. This means that no protons above ~300 keV were produced in the blow-off direction. This is in agreement with other results (Chapter 6, pp 124, Figure 6.3) which showed that the energies of the protons emitted in the blow-off direction were much lower, and with Maksimchuk *et al.* (Maksimchuk et al. 2000) who observed that the energies of the protons emitted in the blow-off direction were about half that of those emitted in the straight-through direction.

An important quantity to measure is the conversion efficiency of the energy in the laser pulse to the total energy (average energy × total number) of the protons produced in the interaction. For the present experiment, this was estimated to be ~0.0002 %. This is very small compared to VULCAN, where for the experiments described in Chapter 6, the efficiency was ~13 %. In light of this difference, a plot was produced incorporating results from other laser systems around the world and is shown in Figure 7.8. This is a first-order, mostly qualitative result, since the points on the plot are from different experiments and hence different laser intensities (ranging from ~6×10^{17} Wcm^{-2}μm^{2} to ~10^{20} Wcm^{-2}μm^{2}). The target type and thickness also varies for each point shown. Even so, for this first-order plot, it is clear that there is a correlation between the conversion efficiency and the energy in the laser pulse. The data points shown are from the present experiment (ASTRA), the experiments described in Chapter 6 (VULCAN), the Trident laser at Los Alamos, USA (Roth 2001), the CUOS in Michigan, USA (Maksimchuk, Gu, Flippo, & Umstadter 2000), three points again from VULCAN (Zepf et al. 2001), the LULI system in France (Roth 2001), the Petawatt at LLNL, USA (Snavely et al. 2000) and one more point from VULCAN (Fews et al. 1994).

This measurement shows the importance that the pulse energy may play in the role of proton generation. It may mean that there is a certain minimum pulse energy required to produce enough protons to generate commercial amounts of PET isotopes. This could be a key factor in the future design of a PET laser. Further experiments must be carried out to fully quantify this dependence, which would involve collaboration between many different research groups, and as much consistency between experiments as possible. This may well be one of the most important measurements to make in the feasibility study of using table-top lasers for PET isotope production.

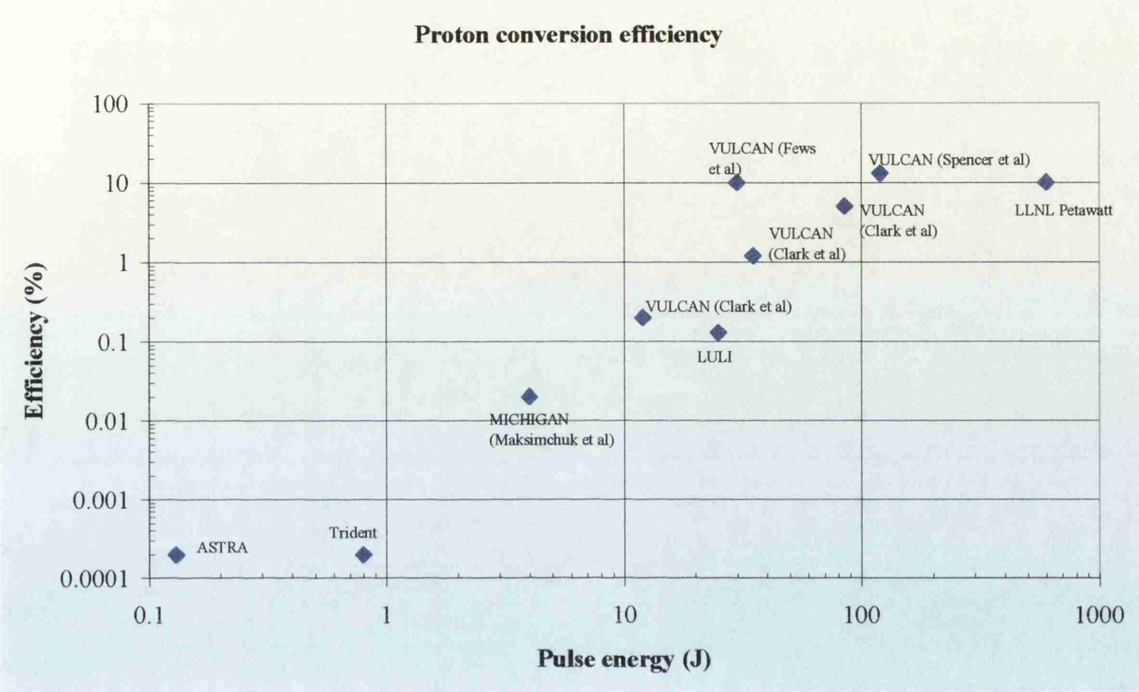

Figure 7.8 Proton conversion efficiency versus pulse energy. Even though this is a first-order measurement, a strong dependence on the conversion efficiency with pulse energy is clear.

Finally, a CCD camera positioned above the tape target was used to take images of plasma emission from the laser-solid interaction. Figure 7.9 shows a typical emission profile. It is clear that there are several plasma "jets" going off in several directions, both from the front of the target, and from the back. This is indicative of several competing electron acceleration mechanisms (Chapter 2). This occurs when the plasma density scale-length is relatively long, which is brought about by a long laser pre-pulse (Santala et al. 2000).

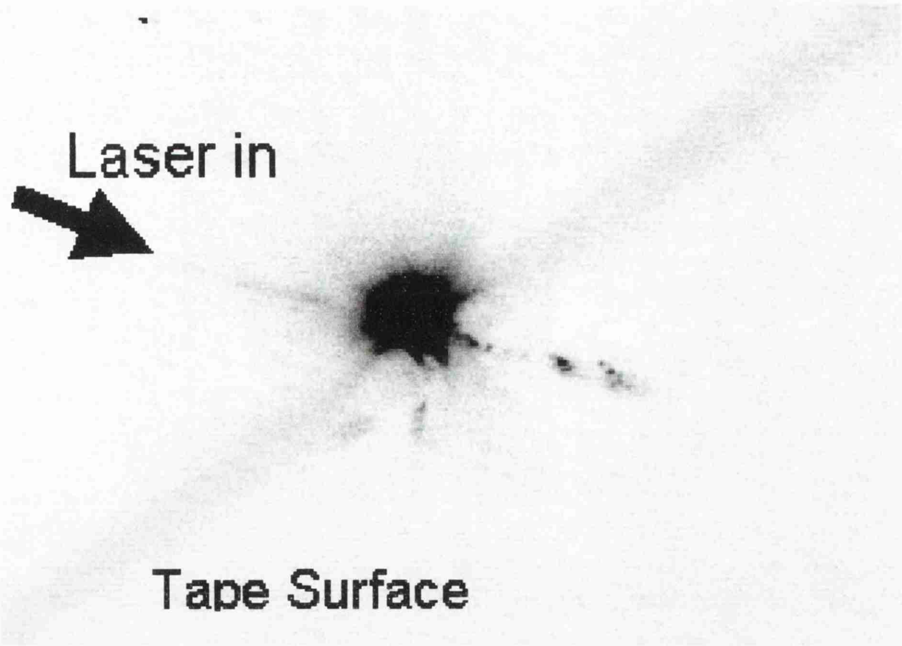

Figure 7.9 Image of plasma emission from the laser-solid interaction. It is clear that there are several plasma jets present.

7.4 Conclusions

Preliminary measurements of proton production from a high-power, high repetition-rate laser interacting with solid targets have been made. It has been shown that protons, as well as heavier ions such as carbon and iron are emitted during such an interaction, although of all the particles produced protons are most abundant. The energies of these protons have been measured and are found to have a mean energy of 250 keV and a cut-off energy of 600 keV when a laser pulse of irradiance ~6 × 10^{17} $\mathrm{Wcm^{-2}\mu m^2}$ is incident on target. The conversion efficiency of laser pulse energy to protons was found to be ~0.0002 %, much lower than VULCAN. A possible correlation between conversion efficiency and pulse energy was found, and highlights the need for further investigations of this effect. The plasma was also imaged, and found to produce plasma (electron and ion) "jets" in all directions, both in front of and behind the target.

As stated throughout this chapter, these results are very much preliminary, but are encouraging nonetheless, since ASTRA will be capable of intensities in excess of 10^{19} $\mathrm{Wcm^{-2}}$ when development is complete. A systematic study of proton production on this system is necessary, and will be conducted in the near future. It is important to fully investigate the effect that a very much reduced energy per pulse (0.5 J compared to 120 J) and shorter pulse length (~70 fs compared to 1 ps) has on both the proton flux and energies (especially in light of Figure 7.8), for comparable intensities.

For the results reported here, 600 keV is well below the threshold for any of the nuclear reactions performed in Chapter 6 to occur. It has been calculated that to produce ^{11}C activities ~5 × background (as measured by the coincidence unit described in Chapters 4,5 and 6) via the reaction $^{11}B(p,n)^{11}C$, at least 10^6 protons above 3 MeV are required. When the laser irradiance is increased by 1.5 orders of magnitude, it is hoped that this flux will be reached and that a full study of the feasibility of using small-scale, high repetition rate lasers for the production of radionuclides for PET, and other applications can be conducted. These early results indicate much promise for the future, although only further, systematic experiments and physical results will prove this.

References

Clark, E. L., Krushelnick, K., Davies, J. R., Zepf, M., Tatarakis, M., Beg, F. N., Machacek, A., Norreys, P. A., Santala, M. I. K., Watts, I., & Dangor, A. E. 2000, "Measurements of energetic proton transport through magnetized plasma from intense laser interactions with solids", *Physical Review Letters*, vol. 84, p. 670.

Fews, A. P., Norreys, P. A., Beg, F. N., Bell, A. R., Dangor, A. E., Danson, C., Lee, P., & Rose, S. J. 1994, "Plasma ion emission from high intensity picosecond laser pulse interactions with solid targets", *Physical Review Letters*, vol. 73, p. 1801.

Hooker, C. J. & Marshall, A. 1999, "Astra development phase 2, design considerations for a multi-terawatt amplifier", *Central Laser Facility, Rutherford Appleton Laboratory Annual Report 1998-99* p. 190.

Langley, A. J., Divall, E. J., Girard, N., Hooker, C. J., Hutchinson, M. H. R., Lecot, A., Marshall, A., Neely, D., & Taday, P. F. 1999b, "Development of a multi-terawatt, femtosecond laser facility - ASTRA", *Central Laser Facility, Rutherford Appleton Laboratory Annual Report 1998-99* p. 186.

Langley, A. J., Girard, N., Mohammed, I., Ross, I. N., & Taday, P. F. 1999b, "Astra Development Phase 1 - a femtosecond terawatt laser", *Central Laser Facility, Rutherford Appleton Laboratory Annual Report 1998-99* p. 187.

Langley, A. J., Girard, N., Mohammed, I., Ross, I. N., & Taday, P. F. 1999a, "Astra Development Phase 1 - a femtosecond terawatt laser", *Central Laser Facility, Rutherford Appleton Laboratory Annual Report 1998-99* p. 187.

Maksimchuk, A., Gu, S., Flippo, K., & Umstadter, D. 2000, "Forward ion acceleration in thin films driven by a high-intensity laser", *Physical Review Letters*, vol. 84, p. 4108.

National Institute of Standards and Technology Physics Laboroatory. Stopping power & range tables for protons http://physics.nist.gov/PhysRefData/Star/Text/PSTAR.html.

Roth, M. 2001, private communication.

Santala, M. I. K., Zepf, M., Watts, I., Beg, F. N., Clark, E. L., Tatarakis, M., Krushelnick, K., Dangor, A. E., McCanny, T., Spencer, I., Singhal, R. P., Ledingham, K. W. D., Machacek, A., Wark, J. S., Allott, R. M., Clarke, R. J., & Norreys, P. A. 2000, "Effect of the plasma density scale length on the direction of fast electrons in relativistic laser-solid interactions", *Physical Review Letters*, vol. 84, p. 1459.

Snavely, R. A., Key, M. H., Hatchett, S. P., Cowan, T. E., Roth, M., Phillips, T. W., Stoyer, M. A., Henry, E. A., Sangster, C., Singh, M. S., Wilks, S. C., Mackinnon, A. J., Offenberger, A. A., Pennington, D. M., Yasuike, K., Langdon, A. B., Lasinski, B. F., Johnson, J., Perry, M. D., & Campbell, E. M. 2000, "Intense high-energy proton beams from petawatt-laser irradiation of solids", *Physical Review Letters*, vol. 85, p. 2945.

Wilks, S. C., Langdon, A. B., Cowan, T. E., Roth, M., Singh, M. S., Hatchett, S. P., Key, M. H., Pennington, D. M., Mackinnon, A. J., & Snavely, R. A. 2001, "Energetic proton generation in ultra-intense laser-solid interactions", *Physics of Plasmas*, vol. 8, p. 542.

Zepf, M., Clark, E. L., Krushelnick, K., Beg, F. N., Dangor, A. E., Santala, M., Tatarakis, M., Watts, I., Norreys, P. A., Clarke, R. J., Davies, J. R., Sinclair, M., Edwards, R., Goldsack, T., Spencer, I., & Ledingham, K. W. D. 2001, "Fast particle generation and energy transport in laser-solid interactions", *Physics of Plasmas*, vol. 8, p. 2323.

Chapter 8

Electron Temperature Measurements using Higher-Order Photo-Nuclear Reactions

Measurements of the temperature of the fast electrons generated in the ultra-intense laser-solid interaction are made by inducing (γ,n) and (γ,3n) reactions in a tantalum target, and then detecting the products via γ-ray spectroscopy using a germanium detector.

8.1 Introduction

It was shown in Chapter 5, Section 5.4 that photo-nuclear reactions can be used to measure the temperature of the fast electrons produced in the laser-solid interaction. This was done using copper and carbon samples, and was made possible because the Q-values and cross sections for the reactions ^{63}Cu(γ,n)^{62}Cu and ^{12}C(γ,n)^{11}C are different.

To recap, photo-nuclear reactions occur when the energy of the incident photon is sufficient to excite a nucleon (most likely a neutron due to its charge neutrality) such that it can escape from the nucleus. Higher energy photons can release more than one nucleon, and these reactions are known as higher-order photo-nuclear reactions. Examples of these are (γ,2n), (γ,3n), (γ,n+p). The Q-values of these reactions can be calculated from the masses of the target and product nuclei as before.

If you have a spectrum of photons like that obtained in the experiments described in Chapter 5, then it is possible to induce (γ,n) and higher order reactions in the same material. Hence you have two (or more) reactions with different Q-values and cross sections in the same material, therefore you have a mechanism for temperature measurements similar to that of the copper/carbon set-up. The difference being that you can obtain measurements from one sample, meaning that issues such as the angular distribution of the photons can be neglected. In addition, it is a less complicated set-up, and temperature measurements can be made while other experiments are being conducted. Since the higher the incident energy, the higher order the reaction, this technique should not be limited by photon energy, since with thoughtful target selection, one simply chooses a higher order reaction to look at. The copper/carbon (γ,n) technique has an upper limit of ~ 35 MeV, the extent of the cross section for ^{12}C(γ,n)^{11}C. Higher order reactions are therefore a useful route to electron temperature measurements provided the energy of the photons produced are high enough.

This chapter describes the application of higher order reactions in tantalum to measure the electron temperature on VULCAN. The products decay by electron capture and do not emit positrons, so the analysis is slightly more complicated than that of the positron coincidence counting described in Chapter 5. The analysis involves γ-ray spectroscopy using the germanium detector described in Chapter 4, Section 4.5.3.

8.2 Experimental

The experiment used the ultra-intense CPA beam-line of the VULCAN Nd: glass laser system (Danson et al. 1998;Danson et al. 1999) (Chapter 3) incident on a 1.75 mm thick 10×10 mm tantalum target, at 45° incidence with p-polarised light within an evacuated target chamber held at a modest vacuum of about 10^{-5} Torr. The experimental arrangement and principal diagnostics employed were the same as those described in Chapter 5, Section 5.1 and shown in Figure 5.1, pp 100. The system delivered pulses of energies up to 120 J, duration 0.9-1.2 ps. When focused to a spot size of 6 μm using an F4, 450 mm focal length off-axis parabola (Chapter 3, pp 57), intensities of up to 10^{20} Wcm^{-2} were achieved.

The main pulse/pedestal contrast ratio (as described in Chapter 3) was measured by a third-order autocorrelator and found to be 1: 10^{-6}. This is sufficient to ionise the target surface, producing a plasma which expands out from the target surface, 300 ps before the arrival of the main pulse. The main pulse then interacts with this pre-plasma and accelerates electrons into the target via the mechanisms described in Chapter 2. These relativistic electrons with an energy distribution proportional to $E^2e^{-E/kT}$ (where E is the electron energy, k is the Boltzmann constant and T is the electron temperature) are slowed down in the high Z tantalum target (Z=73) and generate bremsstrahlung radiation as described in Chapter 4. The bremsstrahlung photons then interact with the tantalum nuclei, and induce photo-nuclear reactions. The electrons themselves can take part in nuclear reactions, but the cross-sections for these reactions are much lower than those of photo-nuclear reactions. Hence γ-ray induced nuclear reactions are the dominant mechanism.

Once the tantalum was irradiated with the VULCAN pulse, the target chamber was restored to atmospheric pressure and the tantalum target was extracted. The time taken to restore the chamber to atmospheric pressure was a few minutes, after which the sample was transferred to a nuclear laboratory for analysis. This limited the lifetimes of the unstable isotopes produced to a few minutes or more. The γ-radiation emitted from the tantalum target was measured in the germanium detector which is described in Chapter 4. The detector was calibrated using sources of known energy and efficiency, as described in Section 4.5.3.

8.3 Results and Discussion

The tantalum target was composed 100 % ^{181}Ta, the stable tantalum isotope. The two reactions of interest are shown below:

$$^{181}\mathrm{Ta}(\gamma,n)^{180}\mathrm{Ta}$$
$$^{181}\mathrm{Ta}(\gamma,3n)^{178}\mathrm{Ta}.$$

^{180}Ta decays via electron capture with a half-life of 8.1 hours to an excited state of ^{180}Hf, which then achieves stability via the emission of a γ-ray of 93 keV (in 1.5 ns). Hf X-rays are also emitted in the decay (K_α=55.7 keV, K_β=63.2 keV). The competing decay to EC is β^-, again with a characteristic half-life of 8.1 hours. This produces an excited state of ^{180}W, which achieves stability via the emission of a γ-ray of 103 keV (in 1.2 ns) plus Hf X-rays (Firestone, Shirley, & Chu 1998).

^{178}Ta decays via EC with a characteristic half-life of 2.1 hours to excited states of ^{178}Hf which then achieves stability via the emission of a number of γ-rays of various energies, plus Hf X-rays. The Q-values, half-lives, peak cross sections and principal radiations of these reactions are summarised in Table 8.1. The cross sections for these reactions are shown in Figure 8.1 (IAEA).

The product of the reaction ^{181}Ta(γ,2n)^{179}Ta (Q=14.2 MeV) has a half-life of 600 days, which is too long for the type of analysis undertaken in this study, and the principal radiation is Hf X-rays, making it impossible to distinguish from other (γ,mn) reactions (m=1,3,4…). This was why this reaction was not studied in detail in the present case, although the cross-section for this reaction is shown in Figure 8.1 for comparison with the (γ,n) and (γ,3n) processes.

Reaction	Half-life	-Q (MeV)	Peak σ (mb)	Principal radiations
^{181}Ta(γ,n)^{180}Ta	8.1 hours	7.6	360	Hf X-rays γ-rays 93 keV (4 %) 103 keV (0.6 %)
^{181}Ta(γ,3n)^{178}Ta	2.1 hours	22.1	20	Hf X-rays γ-rays 89 keV (54 %) 93 keV (14 %) 214 keV (75 %) 328 keV (120 % complex) 426.5 keV (97 %)

Table 8.1 Nuclear reaction data for the reactions studied.

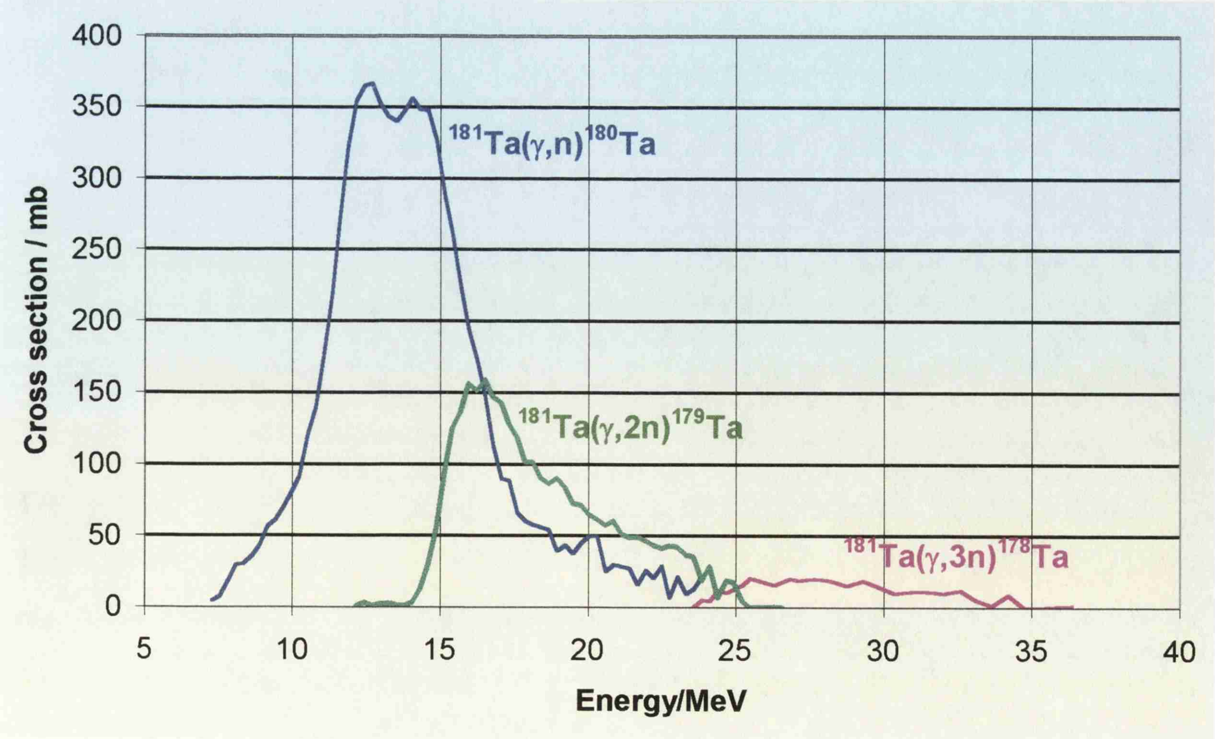

Figure 8.1 Experimentally measured cross sections (IAEA) for the reactions studied.

The tantalum sample was analysed using the germanium detector which was shielded in lead, coupled to a multi-channel analyser (MCA). This set-up makes it possible to measure the energies and the relative intensities of the γ-rays emitted from the sample. The tantalum target was counted in the germanium detector for 1 hour. It is also important to measure the contribution from background radiation. The background spectrum was taken over 12 hours to improve the counting statistics, then the overall count rate was divided by 12 to show its strength relative to the tantalum signal. Figure 8.2 shows a typical spectrum obtained, with the background contribution overlapped.

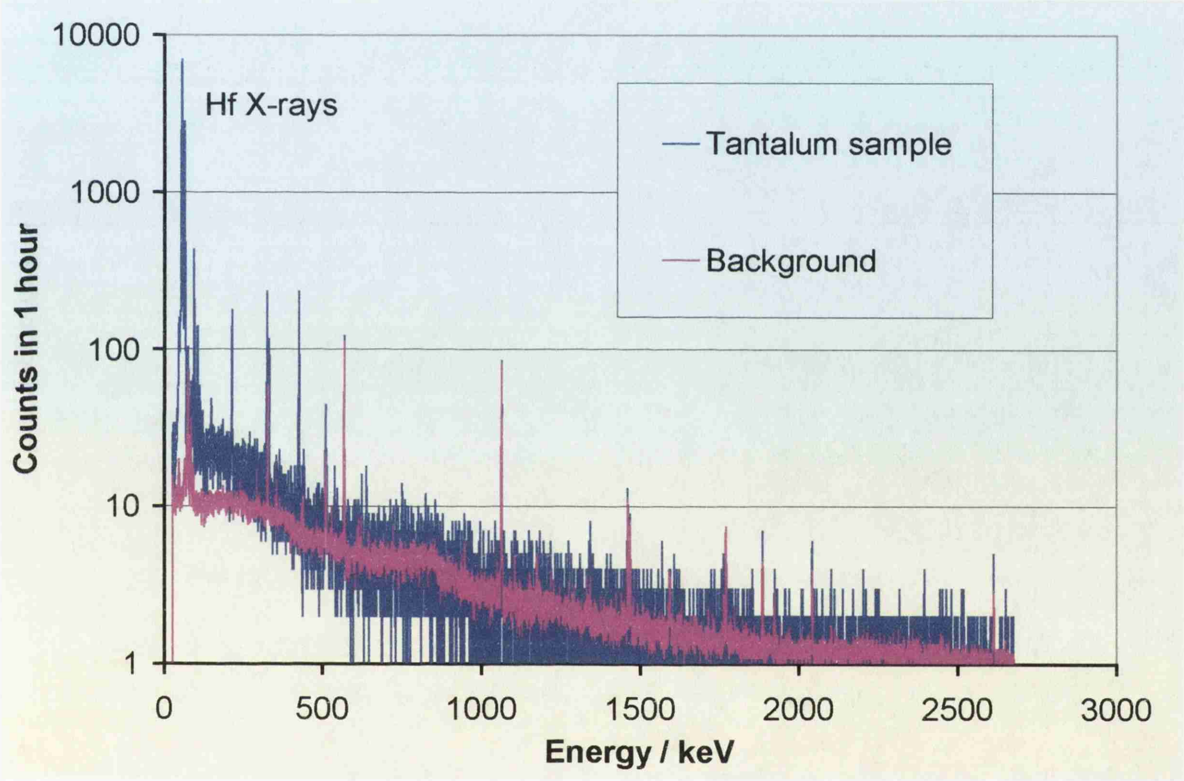

Figure 8.2 Tantalum spectrum with background signal overlapped. The spectrum is dominated by the huge Hf X-ray signal.

The spectrum is dominated by the huge contribution from the emission of Hf X-rays. This makes it difficult to observe the characteristic γ-rays for the (γ,n) and (γ,3n) reactions, although it is clear that there are other smaller peaks. It is more instructive to zoom in on regions of interest in the spectrum.

Figure 8.3 shows the region 40-70 keV. The measured energies of the peaks are 55.7 and 63.5 keV, which indeed correspond to the K_α and K_β X-rays of Hf (accepted values

55.7 and 63.2 keV). However, both ^{180}Ta and ^{178}Ta emit these X-rays, meaning that it is difficult to distinguish the contribution from either isotope. These peaks provide definite evidence however of at least ^{180}Ta. The fact that these peaks are resolved shows the advantages of a germanium detector over NaI(Tl) when studying γ-ray spectra. A scintillation detector is not capable of resolving peaks this close in energy, rather they would appear as one peak.

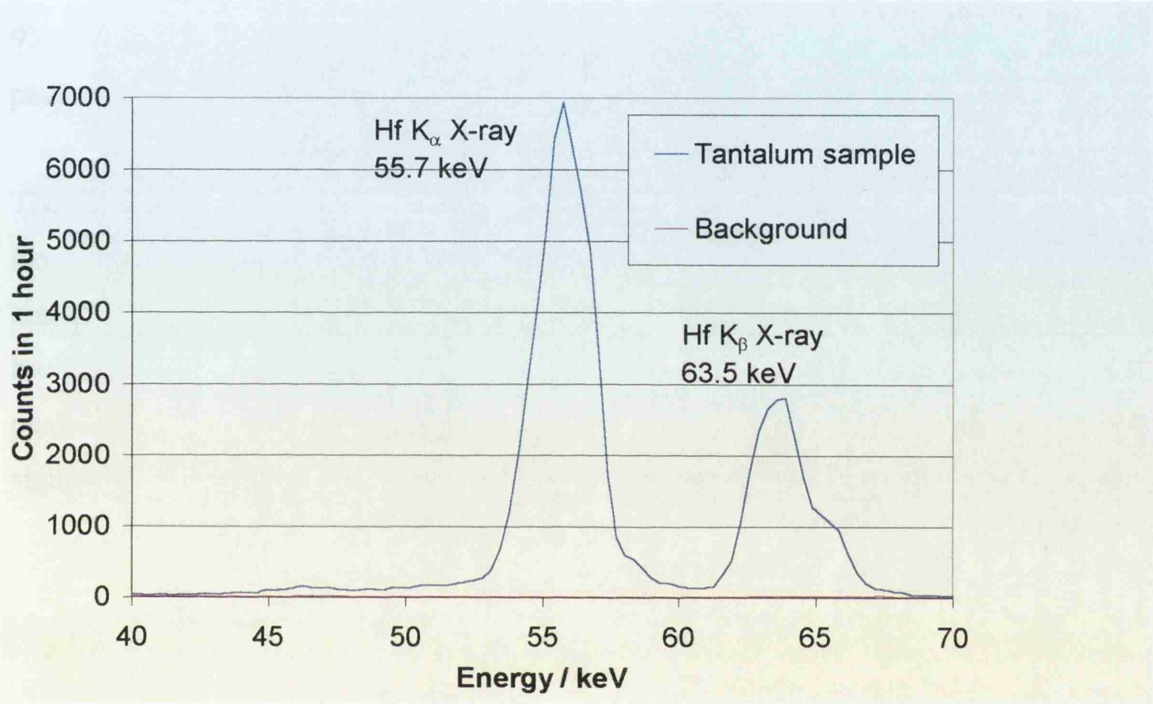

Figure 8.3 Hf K_α and K_β lines. This provides evidence of at least ^{180}Ta.

As well as the X and γ-ray energies emitted, isotopes can also be identified by their characteristic half-lives. This will be discussed later, but for the moment, let us concentrate on the most interesting features of Figure 8.2.

Figure 8.4 shows the spectrum expanded to the region 0-500 keV, and looking at the peaks which were previously swamped by the X-ray signal. Many lines are observed, but most notably the 93.6 keV peak (accepted value 93.3 keV) which is emitted by both ^{180}Ta and ^{178}Ta, and 103.3 keV (accepted value 103 keV) which is emitted by ^{180}Ta.

A strong case for the presence of ^{178}Ta can be made by taking a closer look at a very interesting feature of the decay scheme for this isotope (Firestone, Shirley, & Chu

1998), shown in Figure 8.5. There is a cascade of transitions from the 8+ level to 6+, 4+, 2+, then to the ground state via the emission of γ-rays of energies 426.5, 325.7, 213.6 and 93.2 keV. The intensities of these peaks are all equal, and these peaks are evident in Figure 8.4 (experimentally measured values 426.0, 325.3, 213.4 and 93.6 keV). This gives an automatic efficiency calibration, and a useful cross-calibration with the efficiency measurement shown in Figure 4.13. In addition, the observation of these peaks is a unique fingerprint and evidence of the presence of ^{178}Ta. Even though the 93.6 keV peak has a contribution from ^{180}Ta, the observation of the other three lines provides proof of the presence of ^{178}Ta.

The 328 keV peak is also characteristic of ^{178}Ta, but unfortunately sits exactly on a peak from background contributions, making it difficult to distinguish. There is so much activity in this region that it is difficult to say if the 328 keV signal is real or background since the peaks at 325.3 and 331.5 keV also interfere and overlap. The peaks at 111.0, 121.0 and 148.4 are as yet unidentified, but since this study requires signals from ^{180}Ta and ^{178}Ta, they can for the moment be overlooked.

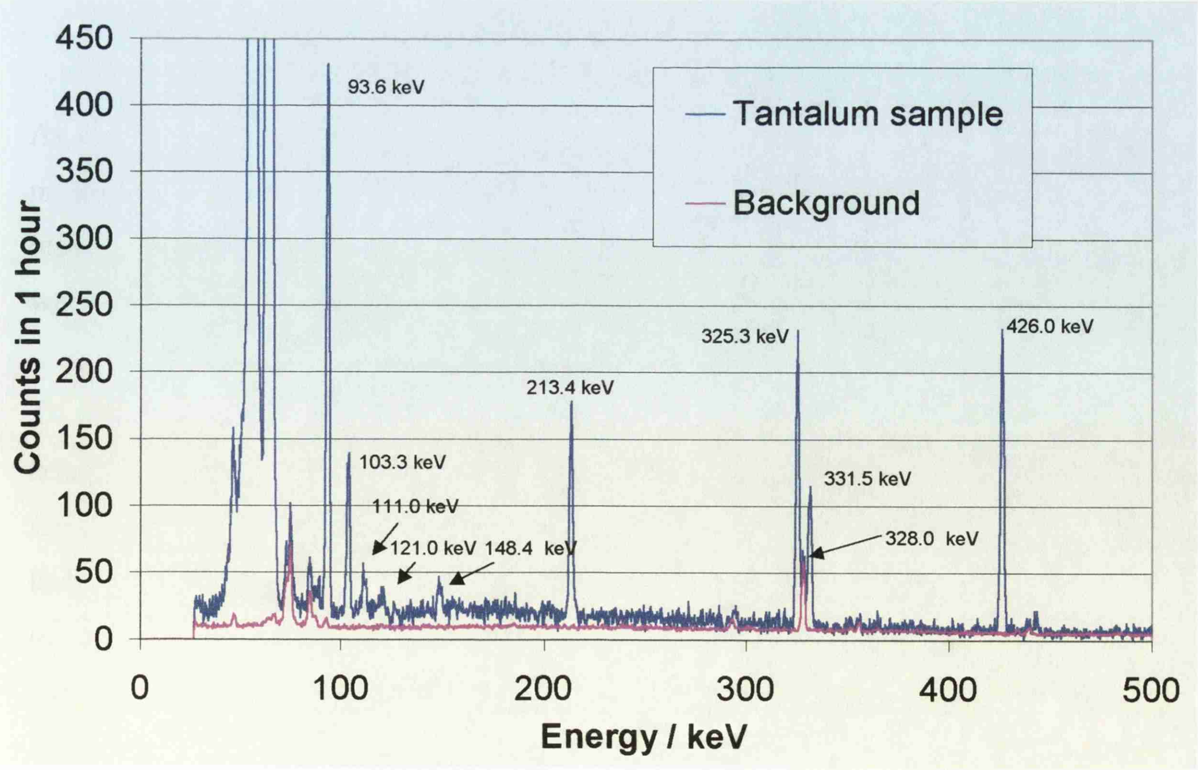

Figure 8.4 Tantalum spectrum in the region 0-500 keV. Many γ-ray lines are evident.

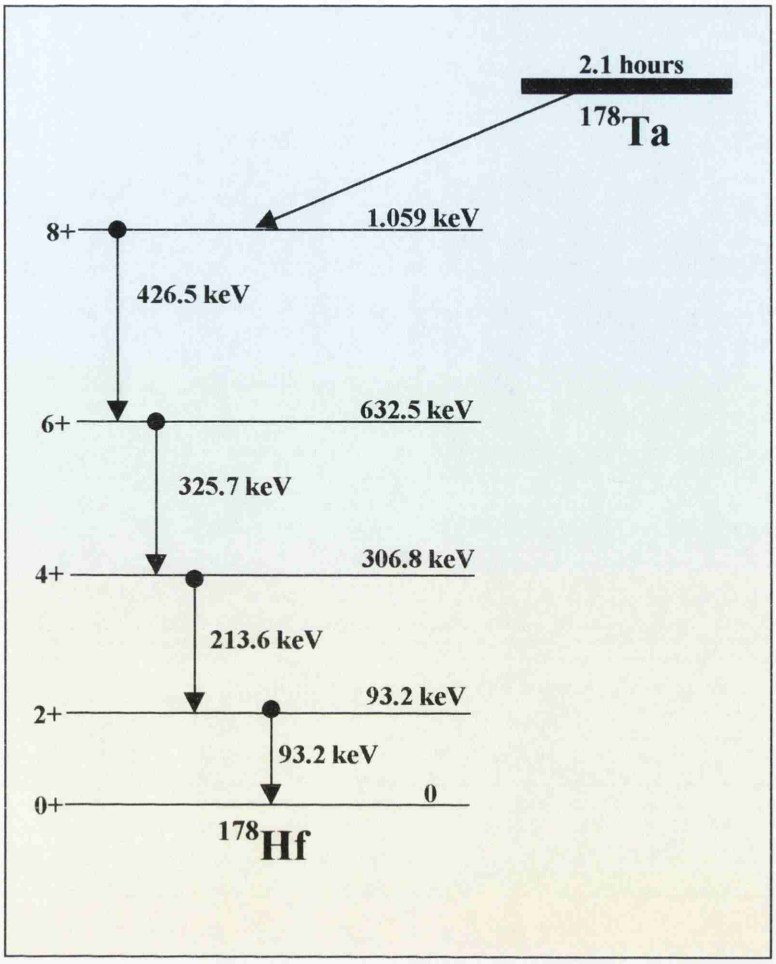

Figure 8.5 Portion of the decay scheme for ^{178}Ta. There are many other transitions, but this cascade yields an unambiguous fingerprint of ^{178}Ta, as well as a detector efficiency calibration since the intensities of these γ-rays are all equal.

As well as looking at the energies of the γ-rays emitted, another way of identifying the presence of a particular radioisotope is to measure the decay of the sample. Since radioisotopes all have characteristic half-lives, a positive measurement of this coupled with the energy measurements makes for a strong case of identification.

To measure the decay of the γ-ray activity of the sample, 4 measurements lasting one hour were taken. The areas of the peaks were then measured as a function of time. The most interesting peaks are at 103 keV (^{180}Ta) and 426 keV (^{178}Ta) since these are unique to the two isotopes in question, and occur in areas of the spectrum which are isolated so do not have contributions from other sources. Figures 8.6 and 8.7 shows the decay of these peaks over time, and Figure 8.8 displays the peak area measurement (activity) against time. From this decay data, the half-lives of the peaks were established and found to be 7.4±0.3 hours for the 103 keV peak . The accepted value for ^{180}Ta is 8.1

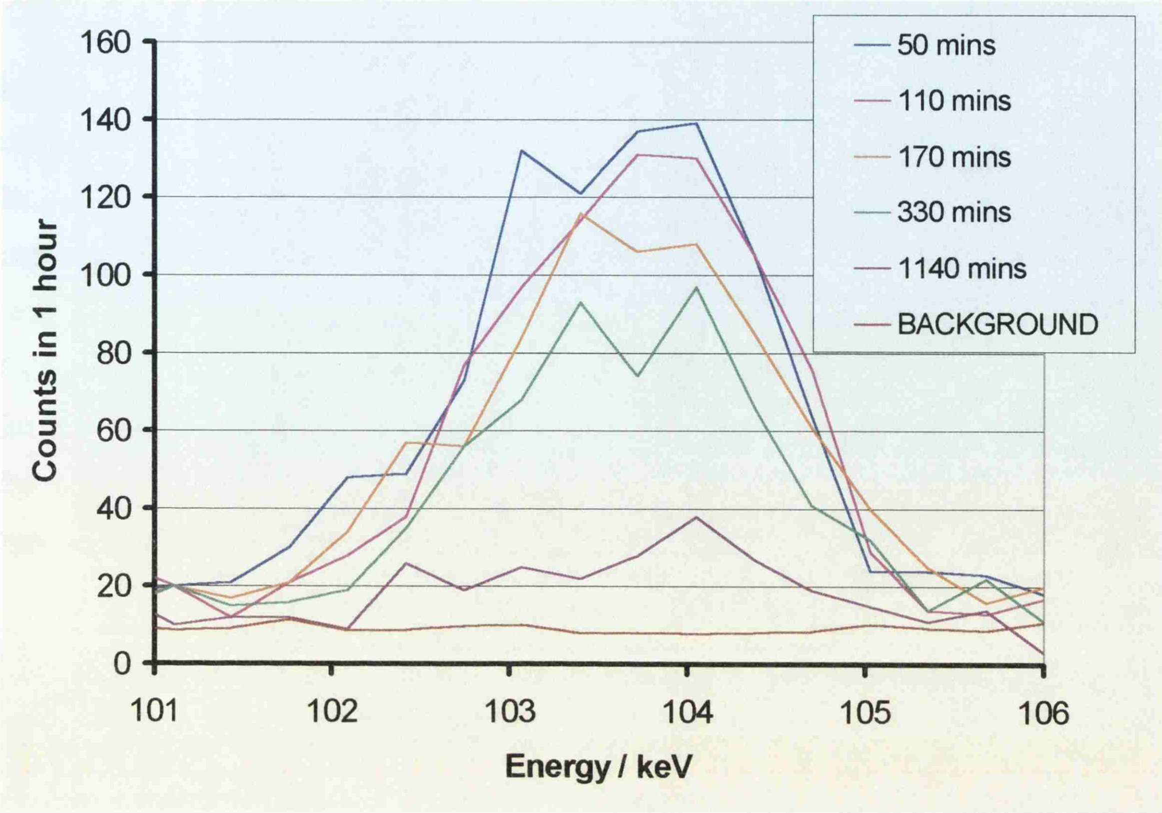

Figure 8.6 Decay of the 103.3 keV peak (^{180}Ta) over time.

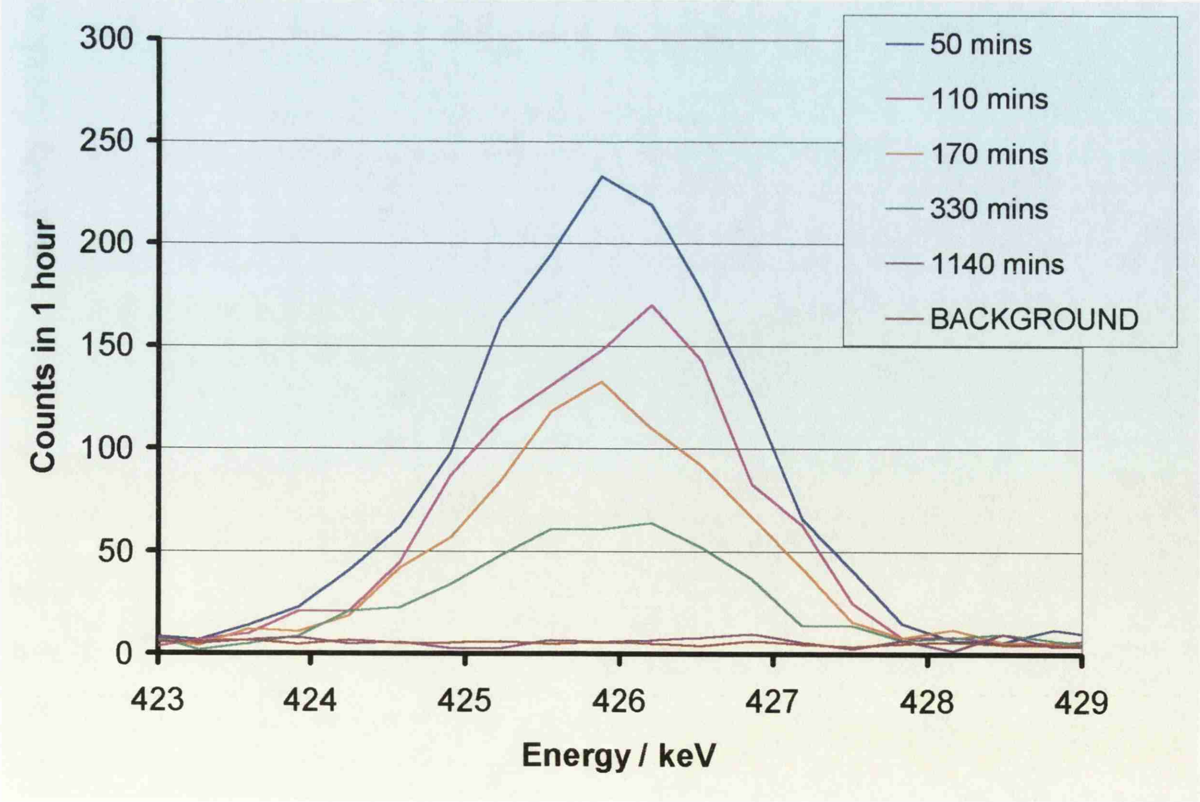

Figure 8.7 Decay of the 426 keV peak (^{178}Ta) over time.

hours. The decay was only measured over 1 half life – to yield more accurate results the decay should have been monitored for longer, but this was not possible due to experimental constraints. The half-life measurement obtained however, coupled with the energy measurement of the peak is enough to positively identify the source of this peak as ^{180}T, produced via the reaction ^{181}Ta(γ,n)^{180}Ta. The half-life of the 426 keV peak was measured and found to be 2.2±0.2 hours (accepted value 2.1 hours for ^{178}Ta). This provides unambiguous evidence that the source of this peak is ^{178}Ta, produced via the reaction ^{181}Ta(γ,3n)^{178}Ta. The result obtained is closer to the accepted value than the previous peak, because the decay was monitored for almost 10 half-lives, as opposed to just one for the previous measurement.

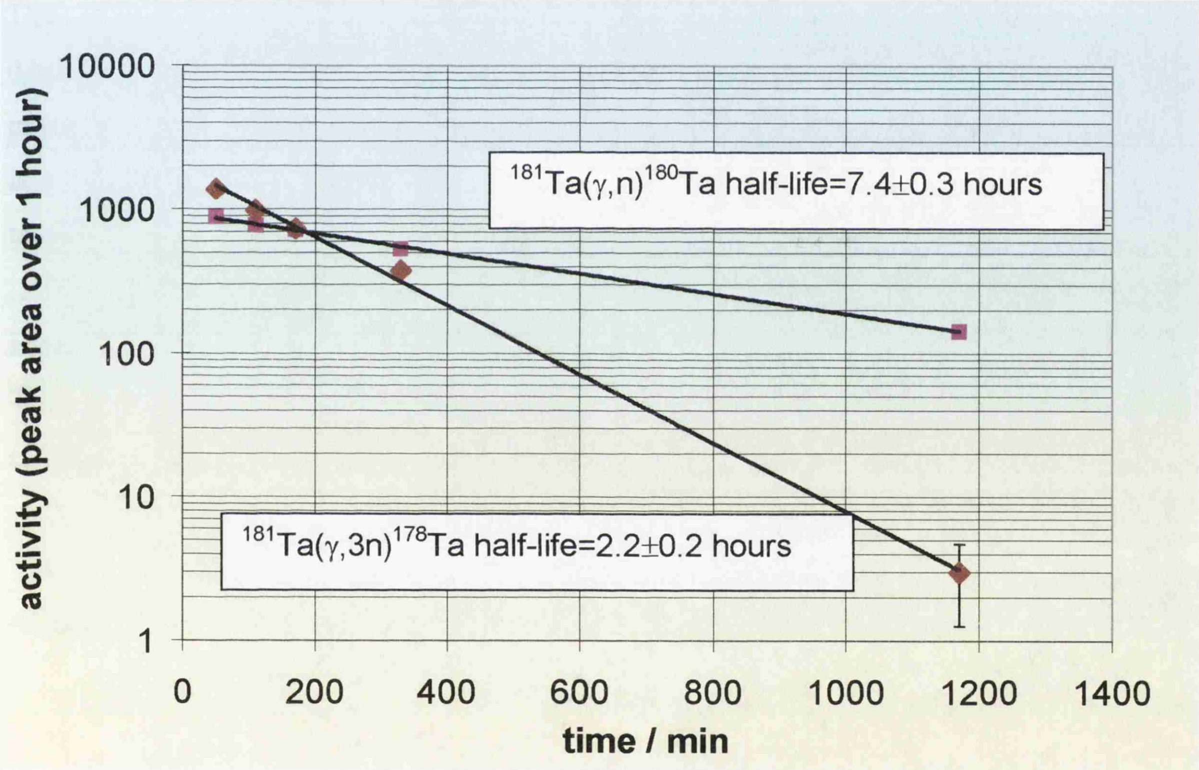

Figure 8.8 Decay plots of the two peaks in question. Half life measurements confirm the presence of ^{180}Ta and ^{178}Ta.

Now that the presence of ^{180}Ta and ^{178}Ta was established, the activity ratio of these isotopes was measured. This was done by measuring the area of the peaks in question and taking into account their relative intensities which are 0.6 % for the 103 keV peak and 97 % for the 427 keV peak (Firestone, Shirley, & Chu 1998). In addition, the efficiency of the detector had to be included in the calculation, since this varied with incident energy (see Chapter 4, Figure 4.13, pp 96). The experimentally measured ^{178}Ta/^{180}Ta activity ratio was found to be 1.55×10^{-2}.

Another useful measurement to make is the relative intensities of the Hf-X rays to the 103 keV peak. This was done for the spectrum taken after 20 hours, once the bulk of the contribution from the 2.1 h ^{178}Ta component had decayed away. The measured ratio, taking into account the detector efficiency was found to be 0.8 %. This is in reasonable agreement with the 0.6 % from "Table of Isotopes" (Firestone, Shirley, & Chu 1998), even though an efficiency calibration was not made at such low energies.

The theoretical ^{178}Ta/^{180}Ta activity ratio was calculated in a manner similar to that described in Chapter 5, Section 5.4. To recap, the relativistic electron distribution is given by $N_e(E)=N_0E^2\exp(-E/kT)$ where $N_e(E)$ is the number of electrons at energy E, N_0 is a constant, E is the electron energy, k is Boltzmann's constant and T is the electron temperature.

Electrons of energy E MeV produce a γ-ray spectrum in tantalum via bremsstrahlung. This spectrum was calculated using the analytical expression developed by Findlay (Findlay 1989).

The induced activity of a sample when bombarded by high-energy photons may be obtained from

$$A = \left(\frac{\ln(2)}{T_{1/2}} \right) \sum_{E_\gamma} N_\gamma(E_\gamma)\sigma(E_\gamma)N \qquad \text{Eqn (8.1)}$$

where $T_{1/2}$ is the half-life of the radioisotope, $N_\gamma(E_\gamma)$ is the number of photons in the energy bin of width 0.5 MeV at energy E_γ, $\sigma(E_\gamma)$ is the photo-nuclear reaction cross section at energy E_γ (see Figure 8.1) (IAEA) and N is the number of nuclei present / cc. The activity ratio of ^{178}Ta/^{180}Ta was then calculated as a function of kT. The results are shown in Figure 8.9. The experimentally measured activity ratio of 1.55×10^{-2} corresponds to kT=4.5 MeV on this plot. The intensity on target was $\sim 10^{20}$ Wcm^{-2}. This is in reasonable agreement with the electron spectrum reported by Cowan *et al.* (Cowan et al. 2000) – a rough analysis of this spectrum shows that the temperature is

~3.5 MeV for a similar intensity. In addition, the measured *proton* kT in chapter 6 was ~3 MeV, and on the Petawatt the measured proton kT is 5-6 MeV (Roth 2001). Also, recall from Chapter 2 that the calculated ponderomotive potential for $I\lambda^2=10^{20}$ $Wcm^{-2}\mu m^2$ is 4 MeV.

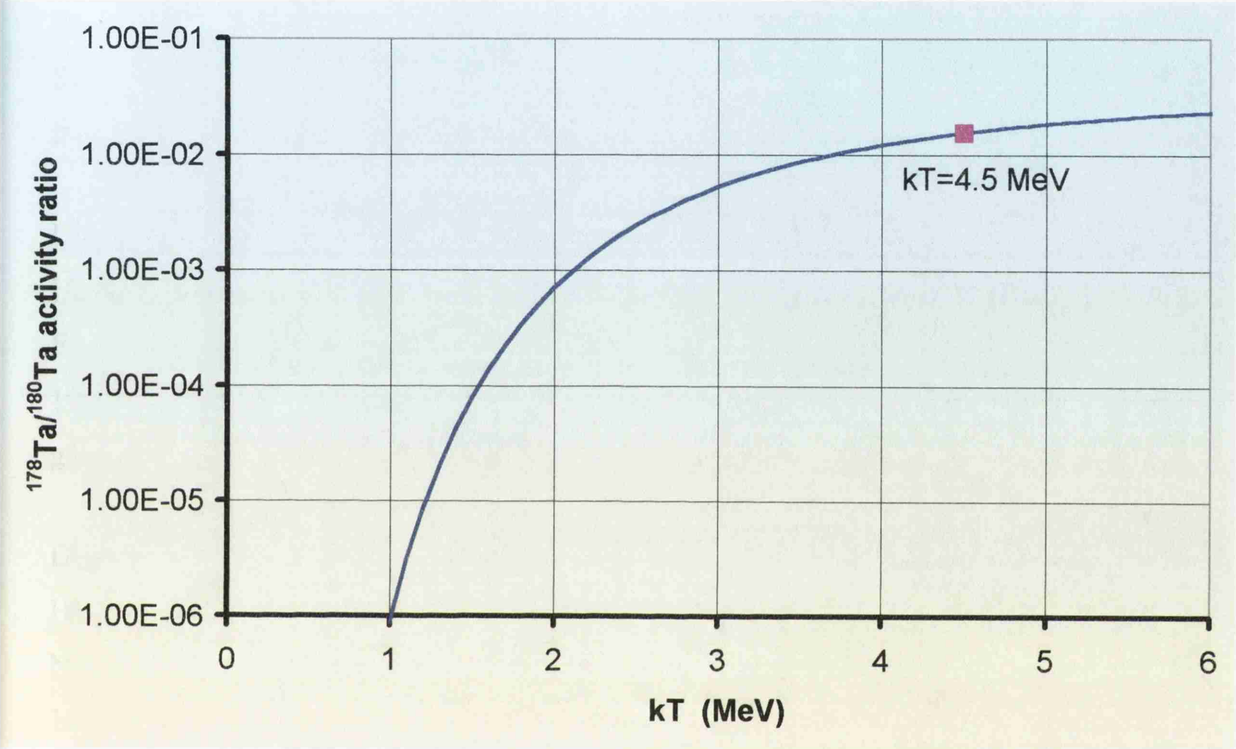

Figure 8.9 Theoretical ^{178}Ta/^{180}Ta activity ratio as a function of kT. The experimentally measured ratio corresponds to the kT value of 4.5 MeV.

8.3 Summary

It has been shown that higher-order photo-nuclear reactions can be used to measure the electron temperature when an ultra-intense laser pulse interacts with a solid tantalum target. Analysis of the specific peaks described is recommended since they are unambiguous for the isotopes ^{180}Ta and ^{178}Ta. For higher laser intensities and hence higher electron and photon energies, this technique should still be applicable since one simply looks for evidence of higher order reactions using the same spectroscopic technique. In addition, other materials such as gold may prove useful. This technique can provide temperature information on a shot-to-shot basis, even while other experiments (e.g. angular distribution measurements) are being conducted.

References

Cowan, T. E., Hunt, A. W., Phillips, T. W., Wilks, S. C., Perry, M. D., Brown, C., Fountain, W., Hatchett, S. P., Johnson, J., Key, M. H., Parnell, T., Pennington, D. M., Snavely, R. A., & Takahashi, Y. 2000, "Photonuclear fission from high energy electrons from ultra-intense laser-solid interactions", *Physical Review Letters*, vol. 84, p. 903.

Danson, C., Collier, J., Neely, D., Barzanti, L. J., Damerell, A., Edwards, C. B., Hutchinson, M. H. R., Key, M. H., Norreys, P. A., Pepler, D. A., Ross, I. N., Taday, P. F., Toner, W. T., Trentelman, M., Walsh, F. N., Winstone, T. B., & Wyatt, R. W. W. 1998, "Well characterized 10^{19} Wcm^{-2} operation of VULCAN - an ultra-high power Nd: glass laser", *Journal of Modern Optics*, vol. 45, p. 1653.

Danson, C. N., Allott, R. M., Booth, G., Collier, J., Edwards, C. B., Flintoff, P. S., Hawkes, S. J., Hutchinson, M. H. R., Hernandez-Gomez, C., Leach, J., Neely, D., Norreys, P. A., Notley, M., Pepler, D. A., Ross, I. N., Walczak, J. A., & Winstone, T. B. 1999, "Generation of focused intensities of $5x10^{19}$ Wcm^{-2}", *Laser and Particle Beams*, vol. 17, p. 341.

Findlay, D. J. S. 1989, "Analytic representation of bremsstrahlung spectra from thick radiators as a function of photon energy and angle", *Nuclear instruments and methods in physics research*, vol. A276, p. 598.

Firestone, R. B., Shirley, V. S., & Chu, C. M. 1998, *Table of Isotopes 8th Edition 1998 update*, Wiley, New York.

IAEA. EXFOR www database – http://iaeand.iaea.or.at/exfor/.

Roth, M. 2001 – private communication.

Chapter 9

Conclusions and Future Experiments

The results found are put into context, and some experiments for the immediate future are outlined.

9.1 Conclusions

It has been shown the VULCAN ultra-intense laser can be used to perform nuclear physics. This is possible because electron and proton beams of energies up to ~40 MeV are generated when this laser is focused on to a solid target. The purpose of this section is to put the results found into context. In order to do this, it is first necessary to summarise the results obtained.

Using the VULCAN laser, the first ever laser-induced fission reaction has been performed and detected, and isotopes used in Positron Emission Tomography have been produced. In addition, nuclear techniques have been used to measure a fundamental parameter in laser-matter interactions, namely the temperature of the fast electrons produced in the interaction. The angular distribution of the electrons has been measured using nuclear techniques. Nuclear effects were also used to measure the abundance and energies of protons produced in the interaction.

So there is a new way of performing nuclear physics – a light source. This is an extraordinary light source however, and there are not many like it in the world. That is, you cannot use any laser to perform nuclear physics. So what makes these findings so interesting? With the way laser technology is advancing, many more systems around the world may soon be capable of this. Also, the acceleration mechanisms are like no other found on Earth. The particles used to induce nuclear effects were accelerated to MeV energies on a micron scale, not metres like that of conventional particle accelerators. Laser-plasma acceleration is more akin to the acceleration of cosmic rays, as described in Chapter 1. It is the author's view that the results described herein mark only the beginning of a new field of science - laser induced nuclear physics.

What do the findings of this study mean, and what place do they have in the grand scheme of things?

Laser induced nuclear physics has enabled the use of nuclear diagnostics in laser-plasma interactions. These can be applied to any laser-plasma interaction where the particle energies produced are sufficient to induce nuclear effects. These diagnostics are in use in many systems around the world now, and will only become more relevant as more and more systems around the world become capable of generating particles in the nuclear regime. As the leading systems become more and more powerful as predicted, these nuclear diagnostics will be developed further and may become the most important type of laser-plasma diagnostic.

Laser induced nuclear fission has been demonstrated. At the present time, this has only been achieved on VULCAN and the Petawatt at LLNL (Cowan et al. 2000a) – large scale research facilities. As stated previously, this is of course extremely interesting from a proof-of-principle point of view, since this idea was first postulated thirteen years ago (Boyer, Luk, & Rhodes 1988). What does inducing fission using a laser have over established techniques such as neutron sources? There has been an undercurrent throughout this thesis that laser technology is moving at a staggering rate; lasers are getting more powerful and achieving these increased powers while at the same time taking up less room. What would it take to induce photo-fission like that described in Chapter 5 using a table-top laser? First of all, the system would have to justify itself to be table-top. It would then have to be capable of producing electrons in excess of 8 MeV. Theoretically, the temperature of fast electrons and hence their energy distribution scales as $I\lambda^2$. It is then feasible that a table-top laser operating at an irradiance 10^{19} $\mathrm{Wcm^{-2}\mu m^2}$ could induce fission, as this was seen on VULCAN. Note however that most high-power small scale systems are generally based on Ti: sapphire technology and operate at wavelengths of ~800 nm. This would mean that the focused intensity would have to be $\sim 1.6 \times 10^{19}$ $\mathrm{Wcm^{-2}}$ to make up for the loss due to the λ^2 dependence.

How many fission events would be produced? It is extremely difficult to predict this, since the process is complicated – electron generation, bremsstrahlung conversion, photo-fission. It was shown tentatively in Chapter 7 that there is a dependence on proton conversion efficiency to pulse energy. This may also be true of electron conversion efficiency. As stated previously, more experiments are required to confirm this effect. However, the author predicts that less photo-fission events would occur for a table-top laser operating at 10^{19} $\mathrm{Wcm^{-2}\mu m^2}$. As a rough estimate, since 10^6 fissions were generated from a single VULCAN pulse, it may be reasonable to assume that around 10 fissions are produced per pulse on a table-top system. The deficit again being balanced by the Hz – kHz repetition rates of table-top lasers. Of course, only experimental evidence can establish this.

It is of course possible in the present study that neutrons emitted in fission events led to subsequent fissions. The object of the experiment though was to prove that a laser could be used to induce fission, and so this possibility was deemed not as relevant as the fact that fission occurred. However, this fact could prove extremely important for table-top lasers. If less photo-fission events are produced, then thoughtful target design could enable efficient production of neutrons which could then induce further fission events. As with commercial nuclear reactors, it does not take many fissions to start a chain reaction, since it is sustained by the arrangement of the fuel, moderator and control rods. In other words, lasers could be used as a fission ignition device. Again, the feasibility and usefulness of laser-induced nuclear fission and its possible table-top extension will only be verified via further investigation.

Laser production of positron emitting isotopes has been demonstrated. Again this is interesting from a proof-of-principle point of view. In addition, photo-nuclear reactions enabled quantitative measurement of the fast electron temperature, and proton induced nuclear reactions in copper and measurement of the induced positron activity enabled measurements of the abundance and energies of the proton beams to be made. One major possible application though is the use of proton induced nuclear reactions for the production of PET isotopes as described in Chapter 6.

PET isotopes are usually generated using proton beams generated using cyclotrons. What advantages does generating the same isotopes using a laser have? It is possible that since the accelerator is a light beam, less nuclear radiation shielding will be required. In addition, it is hoped that a laser accelerator would require less maintenance, and be less expensive, which ties in with the shielding aspect. A compact laser source would occupy less room than a cyclotron. One possible goal of this study would be to make laser systems compact, affordable, safe and reliable enough for use on-site in hospitals. As stated previously, many hospitals with PET scanners do not have the isotope production facilities on-site, rather they are produced somewhere else and transported, which limits the use of very short-lived isotopes. Possibilities of future commercial applications and outlines of what is required in the future have already been discussed in Chapters 6 and 7.

I was fortunate enough to be invited to the PET facility at the University of Aberdeen, for this I must thank Dr. A. Mannivanan. The purpose of this visit was to show the staff there recent results and the potential of using lasers to produce PET isotopes. This is another offshoot of this study, that researchers involved in many diverse fields are coming together in collaboration. At the time of writing, collaboration between laser, plasma, nuclear and medical physicists is developing; I only use the above visit as an example as it highlights the need for such collaboration.

Following a conversation with Dr. Maurice Dodd, an expert in PET isotope production, the requirements of PET facilities was made clearer. In order to produce usable quantities of ^{18}F via the reaction $^{18}O(p,n)^{18}F$, the cyclotron at Aberdeen generates 10^{14} protons per second of energy 5 MeV. This is because the ^{18}F production cross section peaks at 5 MeV (see Chapter 6, pp 124, Figure 6.2). This is one of the main differences between the cyclotron and the laser-plasma accelerator used in this study; cyclotrons generate beams of monoenergetic protons in a DC beam (protons/second) whereas the laser accelerator produces a spectrum of proton energies in picosecond-femtosecond bursts, but the total flux is defined by the laser repetition rate.

In light of this, let us dilute the requirement to 10^{14} protons in the energy range 3-15 MeV, the range across which the $^{18}O(p,n)^{18}F$ cross section extends. Above this, higher order reactions come into play, generating unwanted isotopes. These isotopes can be separated via fast chemistry, but their original production is inefficient. Can lasers fulfil this requirement? It is the author's opinion that in the future, yes they will. From the results shown in Chapter 6 (pp 124, Figure 6.3) it can be seen that 3×10^{12} protons are produced in the straight through direction per pulse, and 1.5×10^{12} in the blow-off per pulse, in the range 5-15 MeV. The fact that there are two proton beams present which can induce nuclear reactions may be advantageous in itself, since two different samples could be produced from one run. Yamigiwa and Koga (Yamigiwa & Koga 1999) have shown theoretically that at laser irradiances of 10^{21} $Wcm^{-2}\mu m^2$, the ^{18}F yield is two orders of magnitude greater than that of a standard cyclotron.

In the near future, these irradiances will only be achieved using large-scale laser systems like VULCAN, which is currently being upgraded to achieve this. But what about using table-top lasers for PET isotope production? From the tentative plot shown in Chapter 7, pp 148 Figure 7.8, the proton flux is greatly reduced with the lower ~few 100 mJ pulse energies typical of table-top systems. The advantage of course is that table-top lasers have high repetition rates and can hence integrate over many shots. The results from VULCAN have been tentatively scaled to table-top systems in Chapter 6, Section 6.4. At the time of writing, there is insufficient data to show whether a table-top laser can achieve PET requirements, without even answering the question of pulse energy to proton conversion efficiency. Again, only further experiments will provide answers, and of course this should be fully explored. The word "preliminary" as applied to Chapter 7 can not be stressed enough.

Another interesting concept brought up in Chapter 6 was the use of lasers for proton oncology. This requires protons of energy typically 150 MeV. What came out of my visit to Aberdeen and other meetings with medical physicists (organised by my supervisor Prof. K.W.D. Ledingham) was that 150 MeV cyclotrons are extremely expensive and bulky, and hence there is only one in existence in the UK, at the Clatterbridge Oncology Centre. VULCAN, when upgraded to 10^{21} $\mathrm{Wcm^{-2}\mu m^{2}}$ is predicted to be able to produce protons of this energy, but again along with a range of other energies. However, there may not be as much of a requirement to reduce the size and cost of proton oncology lasers since oncology cyclotrons are also bulky and expensive. This application appears extremely promising.

In summary, the concept of laser induced nuclear physics is one that fires the imagination, and it is a field in its infancy. As with many areas of study, as the technology develops, the new results found may be totally unexpected and unpredictable. The author, for one, will be keeping a close eye on what happens in the future.

9.2 Future Experiments

Whereas the previous section discussed the results obtained and what they might imply, this section outlines some possible future experiments that could follow this study with current technology and that which will be available in the next year.

9.2.1 Proton Production on ASTRA

At the time of writing, ASTRA is now operating at 300 mJ, 70 fs at 800 nm. When focused to a spot size of 5 μm, intensities of $\sim 2 \times 10^{19}$ $\mathrm{Wcm^{-2}}$ and an irradiance in excess of 10^{19} $\mathrm{Wcm^{-2}\mu m^{2}}$ is available. A full systematic study of proton production on this system will be conducted, addressing the issues of target type and thickness, and how the reduced pulse energy and pulse length affects the proton production rate. The system also has improved beam diagnostics, so it will be easier to estimate and maximise the intensity on target. A third-order autocorrelator will be employed to measure the ASE level, and the effect this has on the experiment will be investigated. More precise proton diagnostics will be incorporated, such as a Thomson Parabola spectrometer (Clark et al. 2000;Wehr, Richards Jr, & Adair III 1983) to measure the proton flux and energies. With luck, nuclear diagnostics will be employed if the proton flux and energies enable this. The main goal of this experiment is to obtain some quantitative results based on the ideas introduced in Chapter 7.

9.2.2 Laser Production of Positron Beams

In recent years positron beam physics has become an active and diverse field with a number of applications, e.g. surface studies, positronium spectroscopy and positron interactions with ions and Rydberg atoms.

Of course, positron emitting isotopes were produced in this study, but their lifetimes are such that they could not be used for the above studies. More useful would be to produce positron beams directly in the laser-solid interaction.

When high energy photons > 1.022 MeV pass through solids, considerable energy is lost through pair creation with a cross section which increases with Z^2 (atomic number of target) and with log E_γ (photon energy). Results from the Petawatt at LLNL (Cowan et al. 2000b) have shown that $\sim 10^8$ positrons with maximum energy ~10 MeV are produced when a laser of 6×10^{20} $Wcm^{-2}\mu m^2$ is incident on a gold target. Gahn *et al.* (Gahn et al. 2000) have demonstrated positron production using a terawatt, 10 Hz system and measured $\sim 10^6$ positrons with maximum energy ~5 MeV.

Positron production experiments have been planned on VULCAN, and will be carried out in the very near future. An electron-positron spectrometer has been designed and built for this purpose, incorporating strong magnetic fields and plastic scintillator detectors. It is hoped that this design will yield precise quantitative results. Detecting positrons in the interaction will prove difficult, considering that electrons, ions and γ-rays are also produced in the interaction.

Another interesting experiment which will be conducted on VULCAN is to split the high-intensity beam in two, and to focus these two beams on either side of a high Z target. It is hoped that in doing this, the fast electrons generated will be confined by their self-generated magnetic fields, increasing the probability of positron production by electron-ion collisions, and not by bremsstrahlung pair production. This electron-positron plasma could yield some very interesting results, and may attract interest from the astrophysics community.

When the VULCAN laser is upgraded to 10^{21} $Wcm^{-2}\mu m^2$ in 2002, these experiments will be repeated at this intensity to investigate how the positron production rate and their energies scale with intensity.

9.2.3 Laser Production of Elementary Particles

Pions are the lightest of the elementary particles and can be produced when γ-rays >140 MeV interact with solid targets. Karsch *et al.* (Karsch et al. 1999) have shown theoretically that a laser of irradiance 10^{21} $Wcm^{-2}\mu m^2$ incident on a tungsten target of 8 mm thickness will produce photons well in excess of this (up to 500 MeV). In addition, they also calculated the yields of pions at this irradiance and predicted that several thousand pions could be produced with a single laser pulse, as well as the expected electrons, ions, γ-rays and electron-positron pairs.

As with positron detection, pion detection will prove a difficult task. The π^0 has a lifetime of about 8×10^{-17} s and so cannot be detected within the time of the laser pulse laser pulse (10^{-12} s) and most π^- are absorbed in the target. The positive pions decay to muons in about 2×10^{-8} s, and this also cannot be observed within the huge γ-ray flash produced via bremsstrahlung. However the above authors (Karsch et al. 1999) suggest that a muon decays rather slowly (2×10^{-6} s) to a positron and subsequently to two 511 keV γ-rays which can be detected by a delayed coincidence in suitable detectors arranged round the target. However, it may prove difficult to distinguish these positron annihilation photons from bremsstrahlung photons, and from 511 keV photons produced via annihilation of positrons generated by other mechanisms such as pair production and electron-ion collisions as described above.

It is possible to detect the production of pions and hence the number of γ-rays >140 MeV by activation techniques, analagous to those employed in Chapters 5, 6 and 8. By placing an aluminium sample after the high Z target, the following reaction takes place for γ-rays in excess of 140 MeV:

$$^{27}\mathrm{Al} + \gamma(140\ \mathrm{MeV}) \rightarrow {}^{27}\mathrm{Mg} + \pi^+.$$

The ^{27}Mg can be detected unambiguously by its two characteristic γ-rays (844 and 1014 keV) and its 9.5 min half-life, using germanium spectroscopy as demonstrated throughout this study. Care would have to be taken to eliminate the possibility of competing reactions, such as $^{27}\mathrm{Al(n,p)}^{27}\mathrm{Mg}$, since neutrons can be generated via neutron-producing nuclear reactions. Perhaps a neutron absorber between the target and the aluminium which would hopefully not attenuate the γ-rays by a significant amount could achieve this.

9.2.4 Heavy Ion Production and Heavy Ion Nuclear Physics

Measurements of heavy ion production, specifically carbon and lead ions have been made on VULCAN (Clark et al. 2000). Generation of nuclear events with these ions has also been studied on VULCAN at a preliminary stage (Santala et al. 2000).

Heavy ion physics is interesting from a number of points of view. Oncologists are interested in using heavy ions to treat tumours, especially carbon ions since their Bragg peaks are even more attractive than that of protons. Heavy ion accelerators are even more rare than 150 MeV proton cyclotrons. In addition, heavy ion interaction physics is very much in vogue at the moment in the nuclear community. Lasers could prove an attractive method of heavy ion production as an injector for a heavy ion accelerator, and for this reason many more experiments are planned on VULCAN to investigate this. Again, this will attract input from oncologists and nuclear physicists.

9.3 Close

This outlines only a fraction of the plans for the immediate future, since interest in this field in growing at an incredible rate. New and exciting experiments are envisaged, such as the idea that at 10^{28} $\mathrm{Wcm^{-2}\mu m^{2}}$, electron-positron pairs can be produced from the vacuum – akin to the birth of the Universe. Whether the future of the findings of this study lie in large scale systems such as VULCAN, or table-top systems, or hopefully both, only time will tell. Researchers from diverse fields of science are coming together to take the idea of laser induced nuclear physics further into the new millennium. In undertaking this study, I felt a sense of being in the right place at the right time, and that this was only the beginning. As to what the future holds, it remains to be seen, but I wait with baited breath. After all, when you're dealing with the brightest light sources on Earth, how can there be a dull moment?

References

Boyer, K., Luk, T. S., & Rhodes, C. K. 1988, "Possibility of Optically Induced Nuclear Fission", *Physical Review Letters*, vol. 60, p. 557.

Clark, E. L., Krushelnick, K., Zepf, M., Beg, F. N., Tatarakis, M., Machacek, A., Santala, M. I. K., Watts, I., Norreys, P. A., & Dangor, A. E. 2000, "Energetic heavy-ion and proton generation from ultra-intense laser-plasma interactions with solids", *Physical Review Letters*, vol. 85, p. 1654.

Cowan, T. E., Hunt, A. W., Phillips, T. W., Wilks, S. C., Perry, M. D., Brown, C., Fountain, W., Hatchett, S. P., Johnson, J., Key, M. H., Parnell, T., Pennington, D. M., Snavely, R. A., & Takahashi, Y. 2000a, "Photonuclear fission from high energy electrons from ultra-intense laser-solid interactions", *Physical Review Letters*, vol. 84, p. 903.

Cowan, T. E., Roth, M., Johnson, J., Brown, C., Christl, M., Fountain, W., Hatchett, S. P., Henry, E. A., Hunt, A. W., Key, M. H., Mackinnon, A. J., Parnell, T., Pennington, D. M., Perry, M. D., Phillips, T. W., Sangster, T., Singh, M. S., Snavely, R. A., Stoyer, M. A., Takahashi, Y., Wilks, S. C., & Yasuike, K. 2000b, "Intense electron and proton beams from petawatt laser-matter interactions", *Nuclear instruments and methods in physics research*, vol. A455, p. 130.

Gahn, C., Tsakiris, G. D., Pretzler, G., Witte, K. J., Delfin, C., Wahlström, C.-G., & Habs, D. 2000, "Generating positrons with femtosecond laser pulses", *Applied Physics Letters*, vol. 77, p. 2662.

Karsch, S., Habs, D., Schätz, T., Schramm, U., Thirolf, P., Meyer-ter-Vehn, J., & Pukhov, A. 1999, "Particle physics with petawatt class lasers", *Laser and Particle Beams*, vol. 17, p. 565.

Santala, M. I. K., Zepf, M., Beg, F. N., Clark, E. L., Dangor, A. E., Krushelnick, K., Tatarakis, M., Watts, I., Ledingham, K. W. D., McCanny, T., Spencer, I., Allott, R. M., Clarke, R. J., Norreys, P. A., & Machacek, A. 2000, “Observations of heavy ion fusion during high intensity laser plasma interactions using nuclear activation techniques”, *Rutherford Appleton Laboratory Central Laser Facility Annual Report 1999/2000,* pp 25.

Wehr, M. R., Richards Jr, J. A., & Adair III, T. W. 1983, *Physics of the Atom*, Fourth edn, Addison-Wesley Publishing Company, pp. 51-54.

Yamigiwa, M. & Koga, J. 1999, "MeV ion generation by an ultra-intense short-pulse laser: application to positron emitting radionuclide production", *Journal of Physics D*, vol. 32, p. 2526.